Fabric Development, Electrical Conductivity and Graphite Formation in graphite-bearing Marbles from the Central Damara Belt, Namibia

Dissertation
zur Erlangung des Doktorgrades
der Mathematisch-Naturwissenschaftlichen Fakultäten
der Georg-August-Universität zu Göttingen

vorgelegt von
Jens Martin Walter
aus Windhoek/Namibia

Göttingen, 2004

D 7

Referent:	Prof. K. Weber
Korreferent:	Dr. B. Leiss
Tag der mündlichen Prüfung:	29.06.2004

ABSTRACT

Graphite-bearing marbles occur in crustal-scale dome structures of the central parts of the Damara Belt in north-western Namibia. They have been reported to show significant anomalies of high electrical conductivity in magnetotelluric profiles. This work presents conductivity measurements on a sample scale of different types of these graphite-bearing marbles. As the graphite-bearing marbles also form distinct shear zones along reactivated rims of the dome structures, these different types of graphite-bearing marbles were distinguished by their macro- and microscopic fabric characteristics. The investigation and classification of the different fabrics is the basis for understanding the conductivity potentials of the different types of graphite-bearing marbles. The classification was made using qualitative optical microscopy, cathodoluminescence microscopy (CL), scattered electron microscopy (SEM), bulk and local texture analysis and the quantification of the calcite-graphite ratios. Several studies were made to verify the tectono-metamorphic development of the different fabrics, and to characterise the modes of graphite formation within these marbles. These include Raman spectroscopic measurements, energy dispersive X-ray analysis (EDX) and investigations of the stable isotopes.

Fabric investigations and field work show that the graphite-bearing marbles are abnormally coarse-grained. The large grain-size of the marble is according to these investigations related to the regional intrusion of granitic melts into high-grade metamorphic rocks. Calcite-graphite thermometry by carbon isotopes indicates regional peak temperatures of around 760° C. The coarse-grained marbles were subsequently deformed in brittle-ductile shear zones along the reactivated rims of the dome structures, producing complex fabrics. The studied shear zones are composed of a mylonitic core zone and a brittle-ductile deformed boundary zone. Part of the deformation in the shear zones was by pressure solution, which resulted in the formation of graphitic stylolites. The graphitic stylolites form network structures of varying degrees of intensity. On a sample scale, the graphite networks show resistivities of 400 to 540 Ω m. These networks are responsible for the anomalies of high electrical conductivity, measured in the magnetotelluric profiles. Many of the graphitic stylolites are cut by microveins. It is proposed that these veins were generated as tension fractures and hydrofractures during the Cretaceous break-up of Gondwana and the subsequent uplift to surface levels.

Graphite was most probably formed during metamorphism, which also lead to the abnormal grain-coarsening of the marbles. The graphite is of uniform high crystallinity across all types of graphite-bearing marbles. Since carbon isotopes of graphite were equilibrated with the calcite marble host rock, no isotopic indications about the origin of the graphite are preserved in the marbles. Qualitative optical microscopy and EDX investigations show, that the graphite is commonly epitaxial-intergrown with mica minerals. The fine-grained graphitic stylolites formed as a residue of pressure solution of calcite. The calcite-graphite ratios indicate, that both calcite and graphite were subject to pressure solution deformation. The calcite textures correspond to so-called ‘low-temperature’ pure shear textures, both in the mylonitic core zones as well as in the brittle-ductile boundary zones. The intensity of lattice-preferred orientations is generally very high and varies strongly with the grain size of the investigated samples. The mylonitic core zones show a complex pattern of different domains of lattice preferred orientation within microscopic scales. Graphite also shows a strong lattice-preferred orientation in the mylonitic core zones with the basal plains oriented parallel to the foliation.

The abnormal grain-coarsening resulted from a combination of regional and contact metamorphism. The complex brittle-ductile deformation fabrics were formed subsequently in a seismic-aseismic transition zone with isochronous brittle, ductile and pressure solution deformation. The graphitic stylolites developed during this deformation, are responsible for crustal anomalies of high electrical conductivity in the measured magnetotelluric profiles.

CONTENTS

ACKNOWLEDGEMENTS III

1 INTRODUCTION 1
1.1. AIMS OF THIS WORK 1
1.2. GEOLOGICAL SETTING 1
1.3. LOCATION AND DESCRIPTION OF THE FIELD AREAS 4

2 STRUCTURAL AND TEXTURAL ANALYSIS 6
2.1. REGIONAL DEFORMATION AND STRUCTURES 6
2.2. CHARACTERISATION OF THE DIFFERENT TYPES OF MARBLES 13
2.3. MICROSTRUCTURES 14
2.3.1. COARSE-GRAINED MARBLE HOST ROCK 15
2.3.2. BRITTLE-DUCTILE DEFORMED MARBLE 17
2.3.3. DUCTILE DEFORMED MARBLE 23
2.3.4. CATHODOLUMINESCENCE INVESTIGATIONS 25
2.3.5. INVESTIGATIONS BY SCANNING ELECTRON MICROSCOPY 26
2.3.6. QUANTITATIVE CALCITE-GRAPHITE RATIOS 28
2.3.6.1. ANALYTICAL TECHNIQUES 30
2.3.6.2. MEASUREMENTS AND RESULTS 31
2.4. TEXTURE ANALYSIS 35
2.4.1. TEXTURE ANALYSIS BY NEUTRON DIFFRACTION 35
2.4.1.1. ANALYTICAL TECHNIQUE 35
2.4.1.2. TEXTURE TYPES OF CALCITE 36
2.4.1.3. SAMPLES AND MEASUREMENTS 38
2.4.2. TEXTURE ANALYSIS BY ROTATING POLARIZER STAGE 45
2.4.2.1. ANALYTICAL TECHNIQUE 46
2.4.2.2. SAMPLES AND MEASUREMENTS 49
2.5. DISCUSSION 49

3 GRAPHITE CRYSTALLINITY MEASUREMENTS 56
3.1. ANALYTICAL TECHNIQUES 56
3.2. SAMPLES MEASURED 58
3.3. RESULTS AND QUANTIFICATION 59
3.4. DISCUSSION 62

4 CONDUCTIVITY MEASUREMENTS 64
4.1. PRINCIPALS OF ELECTRICAL CONDUCTIVITY 64
4.1.1. ELECTRONIC CONDUCTIVITY 68
4.1.2. IONIC OR ELECTROLYTIC CONDUCTIVITY 68
4.1.3. ELECTRICAL CONDUCTIVITY OF ROCKS 70
4.1.4. IMPEDANCE SPECTROSCOPY 72
4.1.4.1 POLARISATION EFFECTS AND ELECTRICAL CONDUCTIVITY 72

4.1.4.2. THEORY OF COMPLEX IMPEDANCE 74
4.2. ANALYTICAL TECHNIQUES 78
4.3. SAMPLES MEASURED 79
4.4. MEASUREMENTS AND RESULTS 80
4.5. DISCUSSION 85

5 STABLE ISOTOPE ANALYSIS 93
5.1. STABLE ISOTOPES OF MARBLES AND GRAPHITE 97
5.2. CHARACTERISATION OF THE GRAPHITE-BEARING MARBLES 100
5.3. CALCITE-GRAPHITE THERMOMETRY 102
5.4. DISCUSSION 105

6 MOBILISATION AND PRECIPITATION OF GRAPHITE 111
6.1. THERMODYNAMICS AND MODELS 111
6.2. IMPLICATIONS OF CARBON ISOTOPES 113
6.3. IMPLICATIONS OF GRAPHITE CRYSTALLINITIES 114
6.4. IMPLICATIONS OF REGIONAL METAMORPHISM 115
6.4. IMPLICATIONS OF THE SEM DATA 115
6.6. DISCUSSION 116

7 REGIONAL IMPLICATIONS 117
7.1. REGIONAL METAMORPHISM 117
7.2. DEFORMATIONAL PATH 118
7.3. DISCUSSION 119

8 CONCLUSIONS 121

REFERENCES 123

APPENDICES 134
I. STRUCTURAL AND TEXTURAL ANALYSIS 134
II. GRAPHITE CRYSTALLINITY MEASUREMENTS 135
III. CONDUCTIVITY MEASUREMENTS 169
IV. STABLE ISOTOPIC ANALYSIS 270

ACKNOWLEDGEMENTS

Writing a PhD thesis is a long and sometimes stony path of rewarding scientific progress and inevitable detours and scientific setbacks. In this process, the personal and scientific gain and progress is also based on the profound experience and knowledge, shared in discussions and laboratory setups.

First of all I want to thank Prof. Dr. Klaus Weber, my supervisor, for the initiation of the project WE 488 50-1 together with Dr. Bernd Leiss and Dr. Georg Nover. The funding of this project by the Deutsche Forschungsgemeinschaft (DFG) enabled this research. He participated in this work by fruitful discussions and observations, especially in the field. I am also very appreciative for adjuvant comments on the manuscript.

Secondly I want to express my gratitude to Dr. Bernd Leiss, my co-supervisor for his effective support and his readiness for valuable discussions. The co-operation with him was a great personal gain and a great pleasure. His constructive comments on the manuscript are also grateful acknowledged.

Special thanks also go to Dr. Klaus Ullemeyer for stimulating discussions in the field and afterwards. Furthermore, I especially want to thank him for his uncomplicated helpfulness in the organisation of the textural measurements and during the analysis of the textural data. His profound scientific attitude always had been exemplary for me.

Furthermore, I want to thank Dr. Georg Nover from the Mineralogisch-Petrologisches Institut of the Universität Bonn for the excellent co-operation regarding the electrical conductivity measurements at his institute and afterwards.

I also want to thank Dr. Axel Vollbrecht for our prolific discussions regarding the microstructural analysis. Likewise, I want to thank Prof. Dr. Agust Gudmundsson and Dr. Sonja Brenner for their enlightening discussions with me about tensile- and hydrofractures. I also want to thank Prof. Dr. Agust Gudmundsson for his general support of this work. The stimulating discussions about the isotope geothermometry with Prof. Dr. Jochen Hoefs are also gratefully acknowledged.

I am also very grateful to Dr. Thomas Kenkmann from the Institut für Mineralogie at the Museum für Naturkunde, Humboldt-Universität Berlin for his uncomplicated and effective co-operation concerning the raman measurements at his institute.

I also want to thank Percy-Constatin von Samson-Himmelstjerna for his support in solving high-grade polynomial functions. As time becomes a very important matter during the accomplishment of a thesis, his little program helped me solving hundreds of these polynomial functions in a reasonable time.

Additionally the readiness of Dr. Sonja Brenner for proof-reading the manuscript for spelling is very much appreciated.

The helpfulness regarding professional photos from the spherical graphite structures by Günther Schnorrer of our institute is also greatly appreciated. Likewise, I want to thank Michael Sosnitza for the many hours he spent in finding the optimal preparation of my samples.

After all I want to express my love and sincere gratefulness to my wife Mariele and my little daughter Franziska for their tolerance for late working hours and their love. They always stood beside me and without their support this work would not have been possible in this form.

Göttingen,
June 2004 Jens M. Walter

CHAPTER 1

INTRODUCTION

This PhD thesis originates in the discovery of (subsurface) anomalies of high electrical conductivity in magnetotelluric profiles. These were measured by Ritter et al. (2003) and Weckmann et al. (2003) in the central Damara Belt of north-western Namibia. Questions about the correlation of potential electrical conductivities on sample scale with different fabric types of the graphite-bearing marble, led to the initiation of this work. Furthermore, precipitation and mobilisation mechanisms of graphite seem to have played an important role during the formation of the different fabrics. The work on this PhD thesis was accomplished at the Geowissenschaftliches Zentrum der Universität Göttingen (GZG).

1.1. AIMS OF THIS WORK

Previous works by Ritter et al. (2003) and Weckmann et al. (2003) show, that anomalies of high electrical conductivity correlate with graphite-bearing marbles. As these are also surface anomalies, one aim of the present work is to correlate different potentials of electrical conductivity on a sample scale with different types of marbles.

The different types of graphite-bearing marbles can be distinguished based on their fabrics and microfabrics. Consequently, another aim of this thesis is to characterise and to understand the formation of the associated fabric types. The marbles are located in the central parts of the Damara Orogen, so that their fabric development must be correlated with the regional tectono-metamorphic history of the area.

Graphite is the most important factor for the conductivity of marbles as well as to distinguish between the different types of fabrics. The third aim of this work is therefore to explore the conditions of formation, mobilisation and precipitation of graphite during the tectonic and metamorphic history of the graphite-bearing marbles. Consequently, the geological fieldwork was made primarily to understand the geological setting, as well as the structural, metamorphic and deformational history of the area.

1.2. GEOLOGICAL SETTING

The areas of investigation are located in the north-western Damara Belt in Namibia. The Damara Orogenesis forms a part of the neoproterozoic Pan-African orogenic belts (Fig. 1.1), which amalgamated Gondwana and eventually Pangea. The Damara Orogen is subdivided into the northern Kaoko Belt, the central Damara Belt, and the southern Gariep

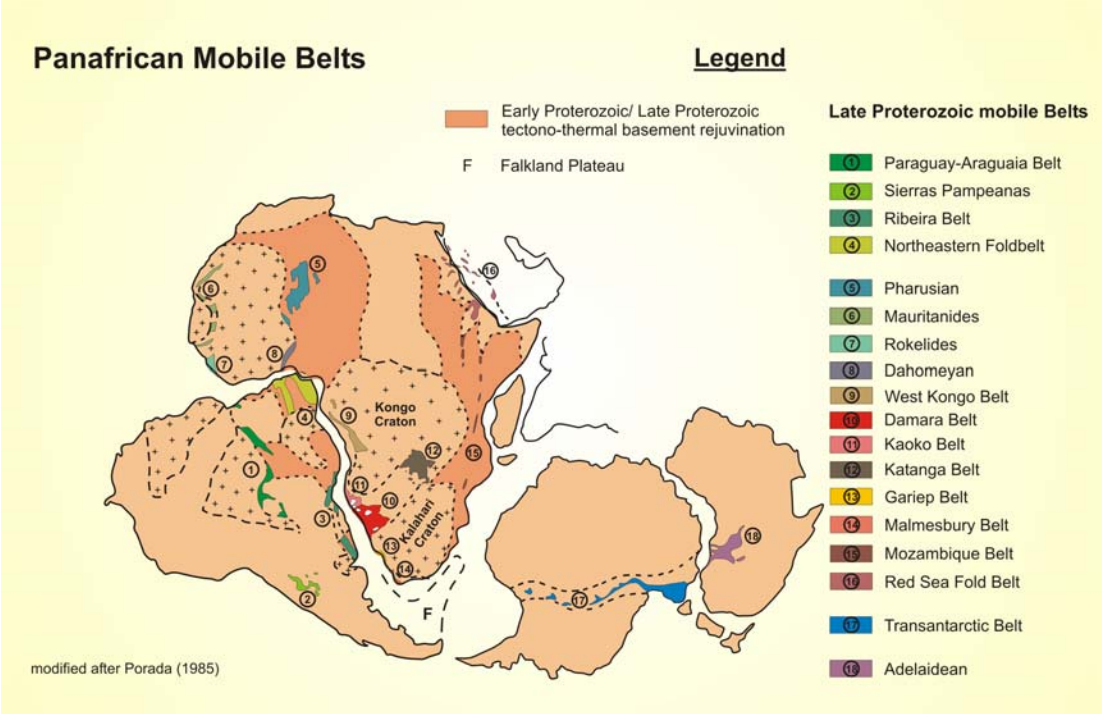

Fig 1.1 *Panafrican Mobile Belt System with Neoproterozoic Orogenic Zones amalgamating Gondwana after Porada (1985).*

Belt (Fig. 1.1 and 1.2). The Damara Belt developed during the north-westward subduction of the southern Kalahari Craton and the northern Congo Craton. Therefore, structures are trending parallel to a general strike of north-east to south-west. This is also reflected by the boundaries of the tectono-stratigraphic zones, postulated by Miller (1983) throughout the Damara Orogen (Fig. 1.2). The Kaoko Belt and Gariep Belt formed during the subsequent collision of the Kalahari and Congo Cratons with the Rio De La Plata Craton in Brazil.

The areas of investigation are situated within the Central Zone (CZ) of the Damara Belt, which is shown in Figure 1.2. The CZ is characterised by the highest metamorphic grades within the Damara Belt, and the intrusion of syn- to post-tectonic granitic magmas. South of the CZ, metamorphic grades increase up to sillimanite-in, whereas the CZ was dominated by partial melting during the peak metamorphism (Hartmann et al., 1983). The Okahandja Lineament (OL) in the south marks the boundary between the CZ and the Southern Zone (SZ).

It is postulated that the suture zone of the continental collision is located in the SZ (Kasch, 1983; Miller, 1983; Kukla, 1992). In these models, the CZ either includes a backarc, and further north a back-arc basin, or is a part of the active margin. In this case, it

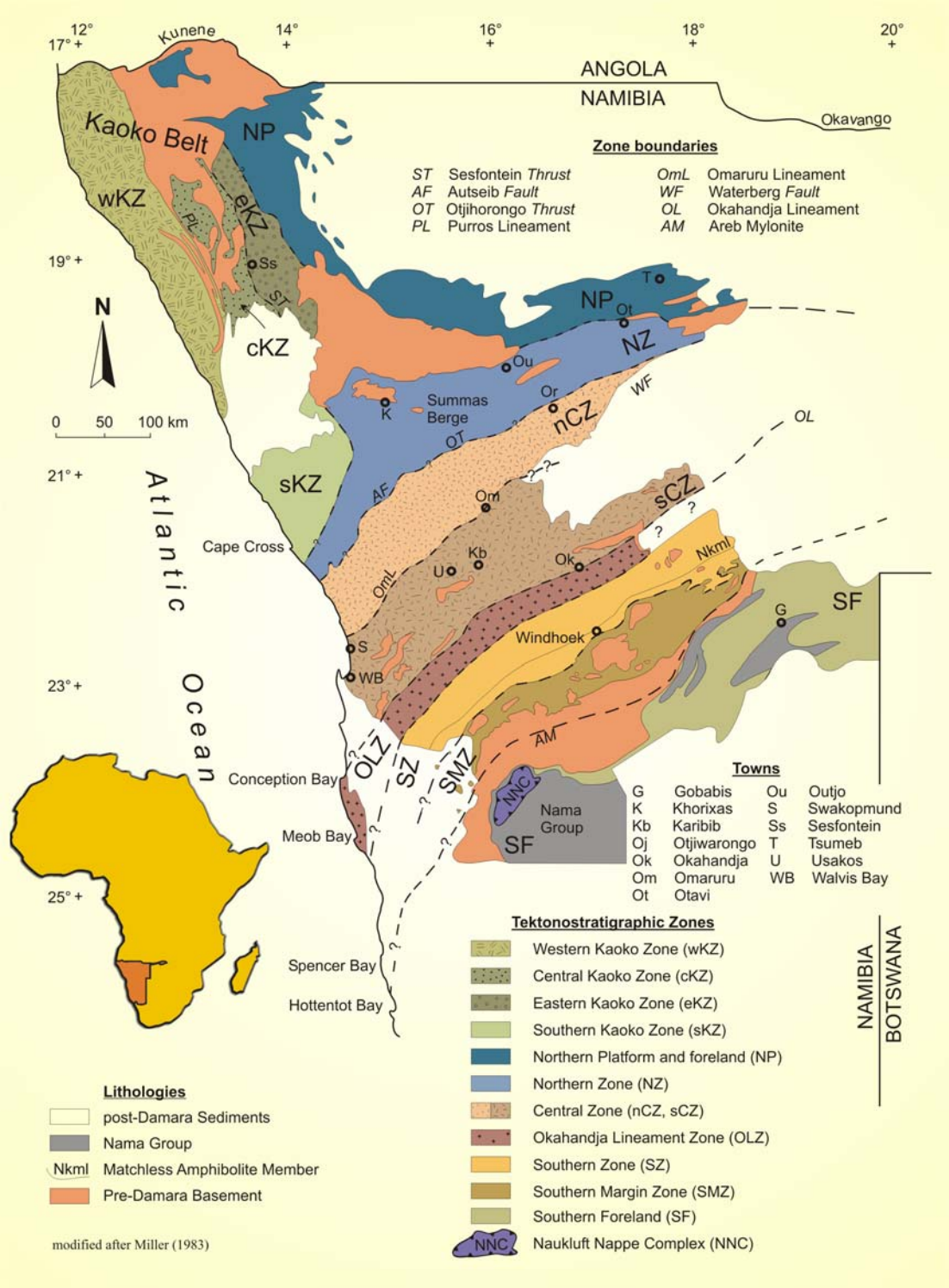

Fig 1.2 *Tectonostratigraphic zones of the Kaoko Belt and Damara Belt after Miller (1983).*

is assumed, that the CZ was subsequently stacked with the subducted Kalahari Craton. However, there is no clear geological evidence for a subduction zone in the Damara

Orogen (Jung & Mezger, 2003). The main reasons for this are a lack of eclogites, blueschists, a HP/LT regime and no igneous rocks with a clear subduction zone signature. Recently Jung & Mezger (2003) argue, that the large volumes of granite in the CZ are the products of collisional orogenic processes. In general, the characteristics of the Damaran intrusives contrast with the Cordilleran-type plutonism, both in spatial distribution and the overall chemistry. However, similarities were found to the proportions and patterns of Himalayan plutons (Jung & Mezger, 2003).

As shown in Fig. 1.2, the CZ itself is subdivided into the northern Central Zone (nCZ) and the southern Central Zone (sCZ) by the Omaruru Lineament (OmL). The nCZ can be distinguished from the sCZ, by its higher stratigraphic level (Miller, 1983). Crustal-scale dome structures in the nCZ, comprising complex refolded fold structures are mainly the effects of magmatic intrusion. Dome structures of the sCZ, comprising mainly basement and lower stratigraphic cores, are much more elongated along the strike (Miller, 1983).

In the area of the magnetotelluric profile, the exact position of the OmL shear zone is still a matter of debate. Recent apatite fission track data of Raab et al. (2002) indicate that the OmL was reactivated after the Cretaceous break-up of Gondwana. According to this data, the OmL shear zone is located in the southern part of the magnetotelluric profile. This location of the OmL shear zone is also supported by (Weckmann et al., 2003).

1.3. LOCATION AND DESCRIPTION OF THE FIELD AREAS

The areas of investigation are situated in the CZ of the Damara Belt in north-western Namibia. The magnetotelluric profile was measured in an area about 235 to 280 km north-west of the capital city Windhoek. The profile is located parallel to the road D 1930 west and north-west of the town of Usakos. The magnetotelluric profile was measured along this road from north to south, crosscutting the Damaran Autseib Fault and Omaruru Lineament (OmL), as postulated by Ritter et al. (2003) and Weckmann et al. (2003) (Fig. 3.1 a). The second area of investigation is situated approximately 90 km north-east of the first area, and locates on the road C 35 between Omaruru and Kalkfeld on the farm Epako Süd.

The vegetation and morphology of the area north-west of Usakos is mainly controlled by the climate of the Namib Desert. The Namib is one of the oldest deserts of the world, and is assumed to have developed 10 to 15 Ma ago, because of the upwelling of the cold Benguela current. The desert extends parallel to the Namibian coast and about 80 to 150 km inland. The area of investigation is thus barren. A sparse bush savannah

dominates with *acacia tortilis* (umbrella thorn), *acacia karoo* (sweet thorn), *acacia reficiens* (false umbrella thorn) and *acacia erioloba* (camelthorn tree), being the main species. After sporadic rainfalls, grass savannahs dominate the area with *stipagrostis uniplumis* (silky bushmen grass) as the main species. The average precipitation in this area ranges between 0 to 150 mm per year, with a rainfall variability of 70 to 80 %.

The second area of investigation, near the town of Omaruru has an annual rainfall of 100 to 350 mm, with a rainfall variability of 40 to 50 %. Apart from mesozoic dykes, granite ring complexes and deeply cut river canyons, there are hardly any elevation differences in the field areas. Some graphite-bearing carbonates however, crop out in morphological elevations. The mean elevation along the southern part of the magnetotelluric profile is around 950 m above sea level, whereas it is around 1340 m above sea level at the farm Epako Süd.

The area along the magnetotelluric profile was commercially farmed after the Second World War, primarily by white famers. This farming was generally not very successful because of erratic and sparse rainfall. Since Namibia was formerly under the administration of the Apartheidsregime in the Republic of South Africa, this area became expropriated and made a part of the homeland of the Damaran people. They took over the farms for substantial farming. Traditionally the Damaran people do not own ground privately, and normally they are very friendly. Access to the outcrops is thus normally easy. The area between Omaruru and Kalkfeld however, is still farmed commercially, so that permission is needed to access that part of the field areas.

In the field areas the vegetation is normally very sparse. The fluvial and calcrete sediments are also thin or absent. Therefore, the outcrops are generally good and many large structures can easily be followed over long distances with the help of aerial photographs and satellite images.

CHAPTER 2

STRUCTURAL AND TEXTURAL ANALYSIS

Detailed field investigations show that the graphite-bearing marbles have a complex deformational and metamorphic history. A first step to reveal the tectono-metamorphic evolution is therefore the microstructural and textural analysis regarding the field relationships and deformational structures. Textural analysis includes bulk and single-grain crystallographic orientation studies of the calcite-marbles. The structural and textural analysis forms the basis for a classification of the graphite-bearing marbles for further investigations of the graphite-bearing marbles.

2.1. REGIONAL DEFORMATION AND STRUCTURES

The sampling sites are located in the main magmatic province of the nCZ in the Damara Belt (Fig. 2.1). As shown in Figure 2.1, the plutonic rocks of the CZ consist mainly of monzogranite with minor granodiorite. Other intrusives are syenogranite, syenite and diorite. The sampling sites show that the graphite-bearing marbles are situated at the contact to these intrusions.

The satellite image of the southern part of the magnetotelluric profile in Figure 2.2 shows that the general geological structures are composed of a sequence of dome structures (D). Furthermore, a variety of magmatic intrusions are observable in the satellite image (I). The mesozoic dykes (MD) result from the Cretaceous break-up of Africa and South America.

It follows from Figure 2.2 that two kinds of dome structures have developed in this area. One type has developed by refolding large scale mostly isoclinal D1 folds into heteroaxial folds. This refolding event may either have developed within a transtensional deformation regime or during a second phase of deformation (D2). These dome structures are mainly developed in the north-western part of the displayed area. A compilation of models for the formation of structural dome structures is found in Soula et al. (2001).

The second type of dome structures formed during the post D1 intrusion of granitic melt into the large scale, mostly isoclinal fold structures. The dome structures comprise mica schists, quartzites, and granitic intrusions next to calcite and calc-silicate marbles which commonly include graphite. The granite intrusions also form dome structures with marble, quarzite and mica shist along their rims.

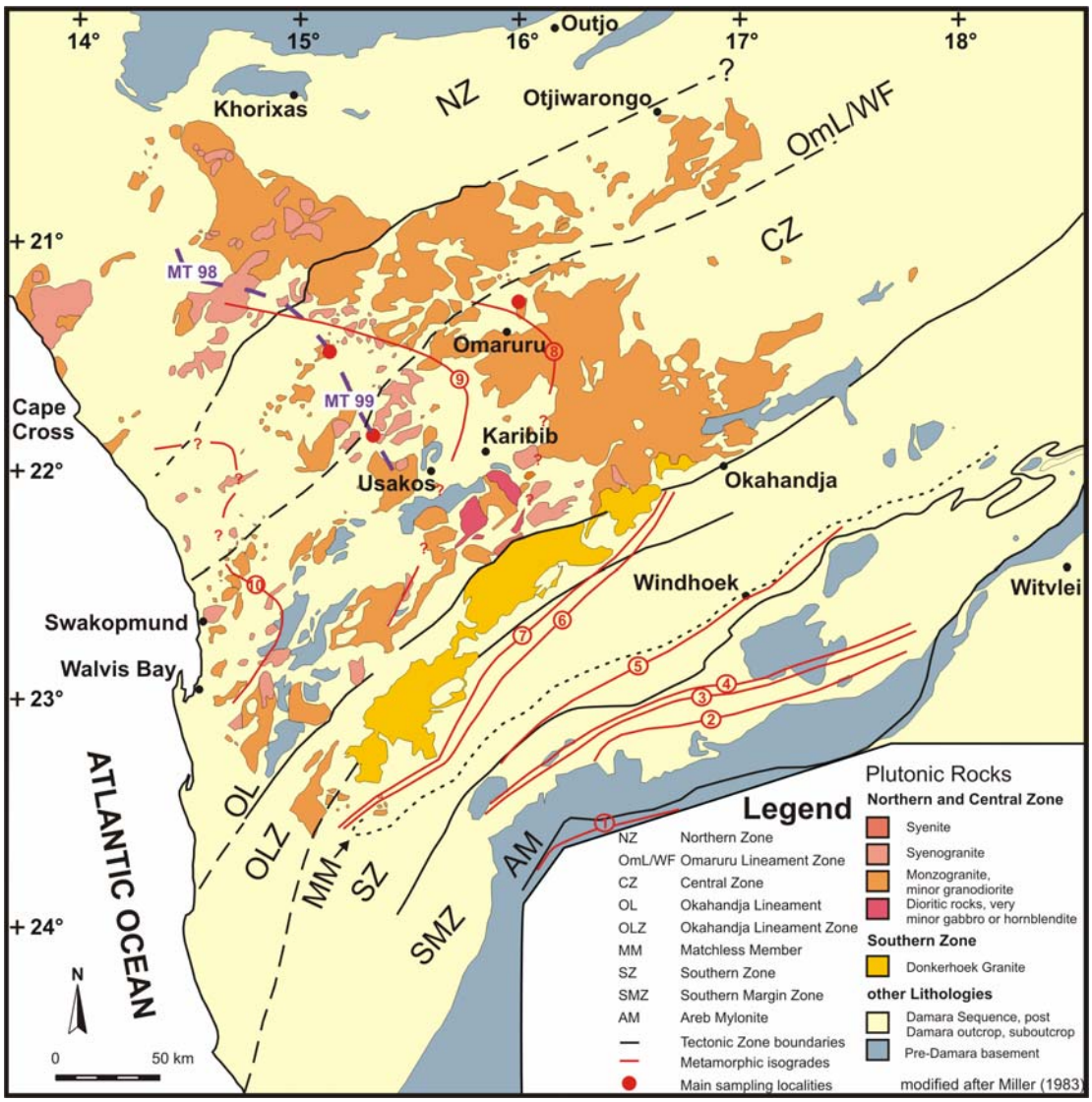

Fig 2.1 *Distribution of Damaran intrusives within the Damara Belt after Miller (1983). The map also shows the course of the magnetotelluric profiles measured by Ritter et al. (2003) and Weckmann et al. (2003). The metamorphic isograds throughout the Damara Belt increase after Hartmann et al. (1983) in metamorphic grade from south to north and within the CZ from east to west. The metamorphic isograds are characterised as follows: 1: biotite-in; 2: garnet-in; 3: staurolite-in; 4: kyanite-in; 5: cordierite-in; 6: andalusite ↔ sillimanite; 7: sillimanite-in due to the breakdown of staurolite; 8: partial melting due to: muscovite + plagioclase + quartz + H_2O ↔ melt + sillimanite; 9: K-feldspar- and cordierite-in; 10: partial melting due to: biotite + K-feldspar + plagioclase + quartz + cordierite ↔ melt + garnet.*

It is obvious from the field investigations that a regional phase of static recrystallisation postdates the formation of the dome structures. This resulted in the abnormal grain-coarsening of large parts of the calcite-marbles. This triggered a comprehensive blastesis of the calcite-marble resulting in an abnormal grain growth of

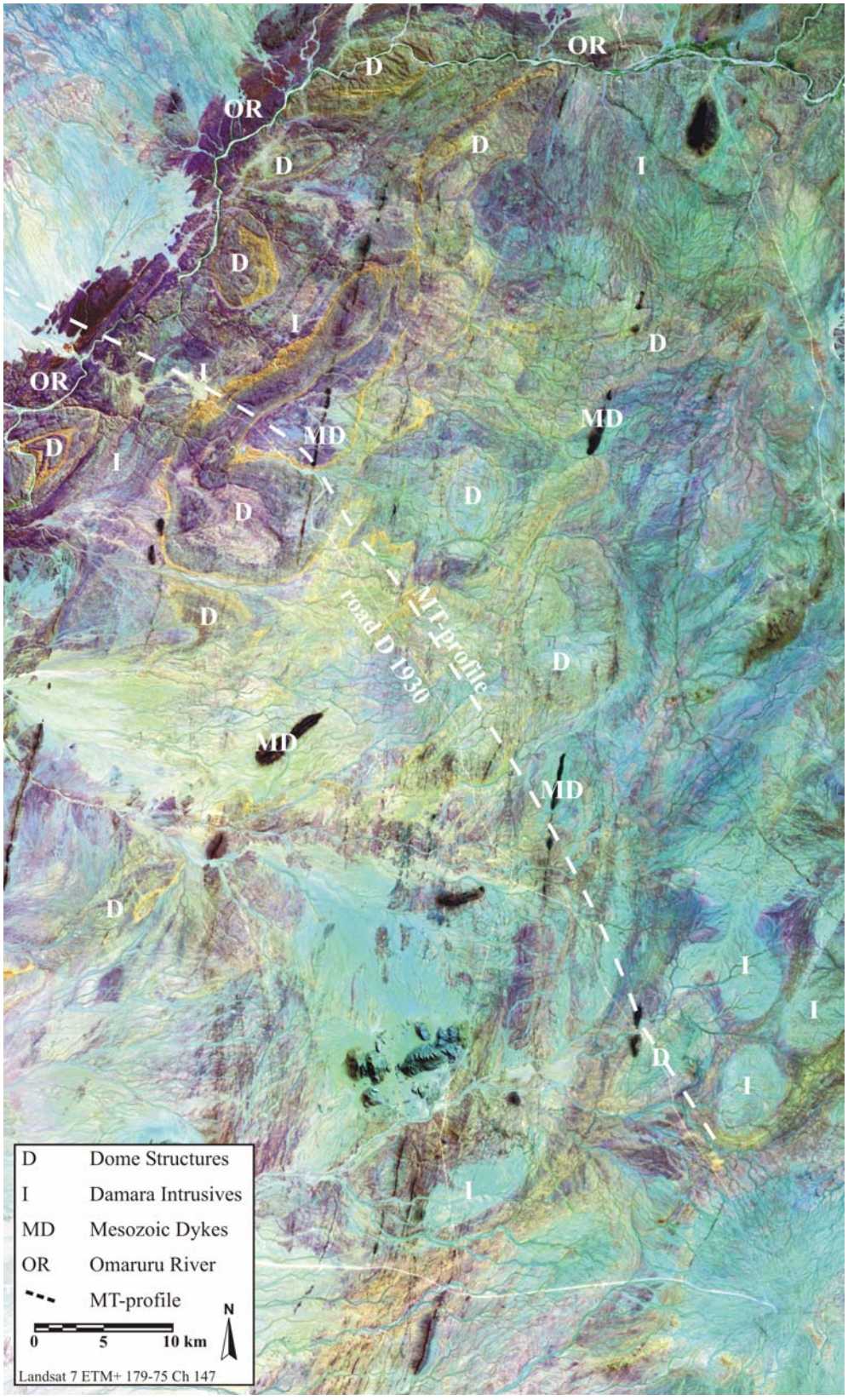

Fig 2.2 *Landsat satellite image of the area of the southern part of the magnetotelluric profile.*

rhombohedral calcite crystals of up to decimeter in diameter in size (Fig. 2.3 a, b). In a regional context, this abnormal grain growth in the calcite-marble occurs only within the magmatic province of the northern Central Zone. This observation is in accordance to Covey & Rutter (1989) who observed isolines of grain coarsening around a magmatic intrusion on Naxos.

Figure 2.1 also displays the generell pattern of the metamorphic isograde of the Damara Belt after Hartmann et al. (1983). They increase in metamorphic grade from the SMZ and SZ to the CZ across the Damara Belt and within the CZ from east to west. As described above, the CZ is characterised by partial melting during peak metamorphism (Hartmann et al. 1983). Depending on the amount of crustal fluids, a amphibolite- to granulite facies metamorphic grade has dominated the central and western parts of the CZ (Jung et al., 2000a).

The regional peak metamorphism of the central and western CZ dates at about 540 to 520 Ma (Kröner, 1982; Haack & Martin, 1983; Steven et al., 1993; Jung et al., 2000a; Jung et al., 2000b; Jung & Mezger, 2003). Jung & Mezger (2003) suggested that the growth of metamorphic garnet ceased at about 510 Ma in the western CZ at temperatures of about 600 to 700° C. The granitic intrusions in the Central Zone are dated between 563 Ma (Hawkesworth et al., 1981; Jacob et al. 2000) and Ar/Ar biotite and hornblende cooling ages of 461 ± 9 and 465 ± 1 Ma (Tack & Bowden, 1999).

The main phase of intrusions started with the intrusion of the Salem granites with Rb/Sr intrusion ages of about 550 Ma (Haack et al., 1983; Miller, 1983) and whole rock Rb/Sr isochron ages of 563 ± 63 Ma (Hawkesworth et al., 1981). Recent SHRIMP dating by Jacob et al. (2000) give intrusion ages in the area of Karibib of 563 ± 4 to 539 ± 6 Ma and a later phase of intrusions at 500 ± 10 to 494 ± 8 Ma. Marlow (1983), Miller (1983) and Haack & Gohn (1988) published Rb/Sr intrusion ages ranging between 530 and 460 Ma, which coincide with Rb/Sr datings of 512 to 468 Ma by Steven et al. (1993). West of Omaruru Rb/Sr ages of 507 ± 44 and 510 ± 48 Ma are reported by Jung et al. (1998), whereas Pb/Pb ages give slightly higher intrusion ages of 521 to 528 Ma and 496 to 490 Ma, respectively.

The extend of the abnormal grain growth and blastesis of the calcite-marble is therefore related to the combination of an amphibolite- to granulite-facies grade metamorphism and the intrusion of granitic melts. Figure 2.3 c shows the apophysic granite intrusions, which developed during the intrusion of highly mobile melts into the graphite-bearing calcite-marble in a high-temperature metamorphic regime. The granitic

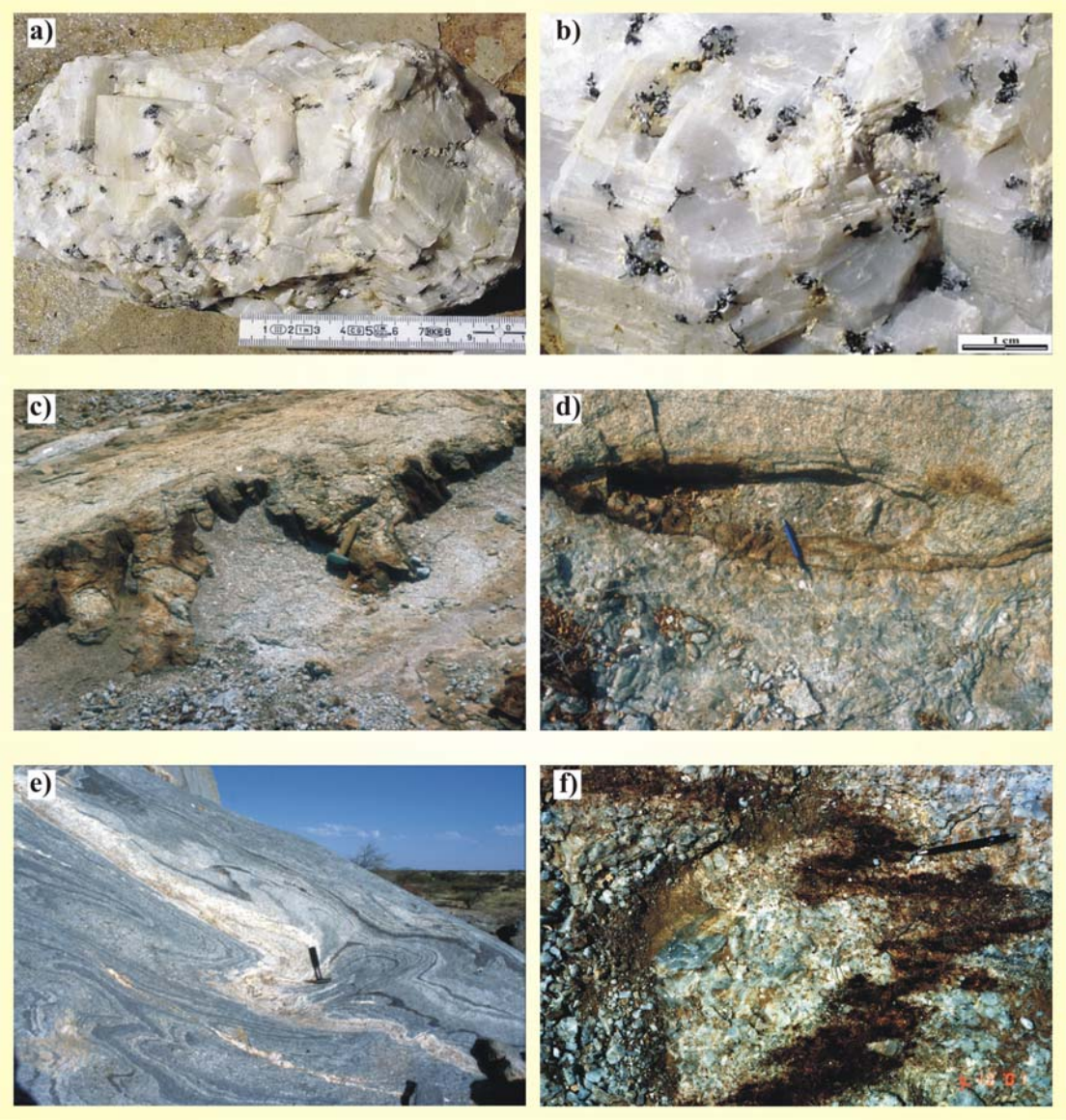

Fig 2.3 *Fabrics of the graphite-bearing marble and the granitic intrusions.* ***a)*** *Abnormally grain-coarsened blastic calcite-marble with disseminated graphite nests.* ***b)*** *Rhombohedral calcite blasts with disseminated graphite nests.* ***c)*** *Apophysic intrusion of highly mobile granitic melts into the calcite-marble.* ***d)*** *Xenolith of calcite-marble in a granitic body.* ***e)*** *Intensively folded impure marbles which show no grain coarsening effects. The calc-silicate layer is more competent than the marble and therefore affects the development of fold structures in the marble. The fold axis mainly dip to NE.* ***f)*** *Folded calc-silicate layer embedded in grain-coarsened calcite marble. The deformation of the calc-silicate layer predates the blastic abnormal grain-coarsening by static recrystallisation.*

intrusions display abnormal grain coarsening within calcite-marble xenoliths (Fig. 2.3 d). They also show a blastic fabric of calcite rhombohedral crystals. Extensive parts of this marble consist of pure grain coarsened calcite-marbles with graphite occuring in disseminated nests as shown in Figure 2.3 a, b.

Parts of this marble rich in impurities do not show any grain-coarsening fabric and often include calc-silicates. These domains of the marble are characterised by intensive folding (Fig. 2.3 e), which result from a complex deformation (Klein, 1980). This deformation is probably related to the development of the dome structures. This is also documented by folded calc-silicate layers which are imbedded in grain-coarsened calcite-marble (Fig. 2.3 f).

On the satellite image in Figure 2.2, the calcite-marbles appear within the dome structures in yellowish colours. Where they occur along the outer rims of the dome structures, these calcite-marbles were subsequently mylonitically and cataclastically deformed. These zones of brittle and ductile deformation developed in a preferred orientation parallel to the general north-east to south-west strike of the Damaran structures. They appear in a 3 to 10 m broad shear zone, including a distinct mylonitic core with adjacent zones of brittle and ductile deformation which are mutually overprinted.

The mylonite core zones are up to 1 m in width and are characterised by the concentration of graphite parallel to the mylonitic foliation (Fig. 2.4 a). The adjacent domains of brittle-ductile deformation did not overprint the distinct mylonitic core zones and are characterised by a variety of deformation fabrics (Fig. 2.4 b to h). Figure 2.4 b, c show the development of graphitic stylolites from single disseminated graphite nests of the grain-coarsened host rock. During deformation the graphite nests became deformed and graphite was reduced in grain size. In addition, graphite was enriched along interconnecting stylolite seams during progressive pressure solution. These graphitic stylolites commonly developed a high angle orientation between individual stylolites. The degree of network intensity of the graphitic stylolites varies within this zone as shown in Figure 2.4 b to f.

According to their orientation with respect to the mylonitic core zone, some of the stylolites develop into ductile shear bands as shown in Figure 2.4 d to f. With increasing stylolite network intensity, the amount of ductile shear bands developed from the graphitic stylolites increases as also shown in Figure 2.4 d to f. Figure 2.4 f shows that one set of these ductile shear bands are developed as subsidiary synthetic Riedel shear bands.

Cataclastic breccia zones often overprint the graphitic network structures (Fig. 2.4 g). The calcite breccia occurs macroscopically in a very fine to ultra fine-grained matrix of calcite (Fig. 2.4 h). These different fabrics of brittle-ductile deformation occur next to the mylonitic core zone in domains of different deformation characteristics. The occurrence of these different deformational domains alternate within the brittle-ductile boundary zones lateral and perpendicular to the mylonitic core zone in an irregular complex pattern. Therefore, the degree of network intensity varies extensively along the strike of the shear

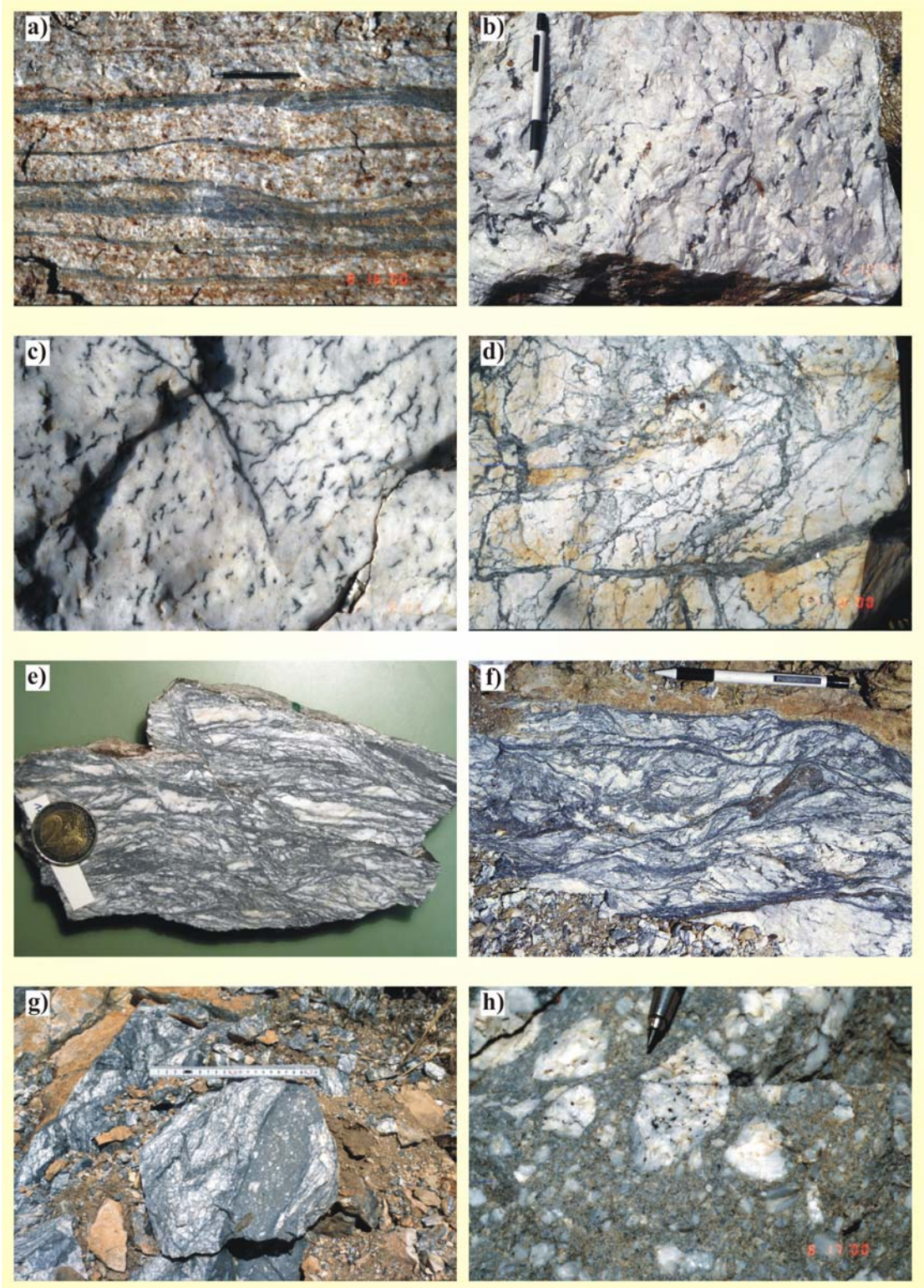

Fig 2.4 *Fabrics of the mylonitically and brittle-ductile deformed graphite-bearing marble.* ***a)*** *Mylonite of the mylonitic core zones with graphite concentrated parallel to the foliation.* ***b)*** *Deformed graphite nests and short stylolitic seams developed from the graphite nests* ***c)*** *Increased pressure solution and brittle-ductile*

deformation resulted in graphitic stylolites which connected to form the graphite network structures. ***d)*** *Graphite network structures with higher network intensities and some graphite stylolites already developed into ductile shear bands.* ***e)*** *Very high graphite network intensity with a close band of ductile shear bands developed in preferred orientation.* ***f)*** *High network intensity with a set of conjugated ductile shear bands with the development of synthetic Riedel shears.* ***g)*** *Cataclastic vein developed in domains within the graphite network structures.* ***h)*** *Cataclastic breccia in a matrix of ultra fine-grained calcite-marble.*

zones. The cataclastic breccia zones also occur in irregular intervals along the shear zones. They are restricted to the brittle-ductile domains since they do not overprint the mylonitic core zones.

These shear zones are of Damaran age, as the mesozoic dykes resulting from the cretaceous break-up of Gondwana are not affected by the deformation of the investigated shear zones. Fieldwork revealed, that the mesozoic dykes intrude the graphite network structures independent of the deformational fabric of the shear zones. Therefore, these shear zones may not be related to the shear zones and structural lineaments that have been postulated as reactivated shear zones after the break-up of Gondwana as described by Raab et al. (2002).

2.2. CHARACTERISATION OF THE DIFFERENT TYPES OF MARBLES

Within the range of the described shear zones along the rims of the dome structures three types of graphite-bearing marbles can generally be distinguished macroscopically. The first type is characterised by the blastic, abnormally grain-coarsened marble, which is the host rock of the described shear zones. Type 2 and type 3 represent the brittle-ductile deformed marble and the mylonitically deformed marble respectively.

Type 1:

This type is the marble host rock adjacent to the shear zones. This marble host rock is composed of domains of pure calcite-marble with disseminated nests of graphite. Other domains additionally contain phases like calc silicates, phyllosilicates, dolomite and quartz. The domains of nearly pure calcite-marble are abnormally grain-coarsened to a large extent, and generally characterised by a blastic fabric of rhombohedral calcite crystals (Fig. 2.3 a, b). The size of the calcite crystals are from 0,5 to about a decimeter in diameter. Graphite occurs in single graphite nests disseminated throughout these marbles (Fig. 2.3 b). In this type of graphite-bearing marble the graphite crystals and flakes are mostly well crystallised and of up to 2 mm in size.

The other domains of graphite-bearing marble host rock containing calc-silicates, phyllosilicates, dolomite and quartz show grain coarsening fabrics to a much less extent. In

some domains they are not affected by grain growth. These marbles still show prior deformation structures like extensive folding and often contain layers of calc-silicates. In this study, the marble host rock is referred to as the abnormally grain coarsened calcite-marble because this is the dominating type within the marble host rock.

Type 2:

The second type of graphite-bearing marble occurs in the boundary zone of brittle-ductile deformation within the investigated shear zones. In this zone network structures of graphitic stylolites, single ductile shear bands and cataclastic breccia are observable (Fig. 2.4 b to h). The thickness of the graphitic stylolites and shear bands, as well as the graphite network intensity varies quite extensively. From the investigation of the macroscopic structures shown in Figure 2.4 b to h, it is obvious that the deformational structures are mutually overprinted.

Pressure solution resulting in the formation of graphitic stylolites occurred during the brittle-ductile deformation and is restricted to this domain of the shear zone. The stylolites themselves are again overprinted by ductile shearing and cataclastic deformation. In general, a grain size reduction of the calcite-marble and the graphite is associated with the brittle-ductile deformation. Graphite is generally ultra fine-grained in the stylolites as well as in the cataclastic zones and ductile shear bands.

Type 3:

The third type also occurs in the mylonitic core zones of the shear zones and is characterised by pure ductile deformation (Fig. 2.4 a). This mylonitic core zone is up to 1 m wide and is unaffected by the brittle deformation of the adjacent boundary zone of brittle-ductile deformation. This mylonitic core zone is continuously existent within the investigated shear zones, whereas the boundary zone of brittle-ductile deformation varies lateraly along the shear zone. As shown in Figure 2.4 a, graphite is concentrated parallel to the mylonitic foliation.

2.3. MICROSTRUCTURES

The microstructures will be investigated according to the macroscopic classification of the graphite-bearing marbles by the three different types. The classification of the microstructures has been performed by qualitative optical microscopy. The microstructural investigation will be the basis for the general interpretation of the progression of the deformational processes within the macroscopically differentiated domains of deformation. Additionally the microstructural analysis should reveal some information about the

abnormally grain-coarsened host rock, with respect to the graphite formation within the disseminated nests.

2.3.1. COARSE-GRAINED MARBLE HOST ROCK

The microstructures of the calcite-marble host rock are characterised by the blastic fabric of the abnormally grain coarsened calcite marble. As shown in Figure 2.5 a to d, two sets of calcite twins are developed in the rhombohedral calcite crystals. These twin lamellae intersect each other at an angle of 80°. At the intersection between the twin lamellae, the elder generation of calcite twins are rotated and dislocated by the younger generation (Fig. 2.5 a). Likewise, the twin lamellae are fractured and slightly dislocated by the the development of the rhombohedral plains (Fig. 2.5 b).

These sets of twins are recrystallised in parts again by the host crystal and therefore are partially extinct (Fig. 2.5 c). Figure 2.5 d shows, that the twin lamellae are recrystallised in lobate and bulging fronts of recrystallisation. The twins are recrystallised in the orientation of the host crystal at a late stage during the abnormal grain growth and static recrystallisation.

The rhombohedral calcite crystals show inclusions of graphite, muscovite and quartz as accessory minerals. Graphite, muscovite and quartz had been overgrown by statically recrystallising calcite during abnormal grain-coarsening and are incorporated in the calcite crystals. Graphite occurs in graphite nests which are disseminated throughout the calcite crystals (Fig. 2.5 e, f). In general, the graphite flakes in the nests are oriented as shown in Figure 2.5 e. The graphite crystals in the nests are locally oriented radial forming spherical structures (Fig. 2.5 f). Some of these radial graphite nests have a single mineral grain in the centre of the radial graphite structure.

As shown in Figure 2.5 g, h, graphite and muscovite are partially epitaxially intergrown on their basal plains. Figure 2.5 h shows that the growth of graphite is also to some extent controlled by the two sets of twins developed in the calcite host crystal. Additionally, in the investigated rhombohedral calcite crystals no fluid inclusions are observable.

Nevertheless, fluid inclusions within more impure and less grain-coarsened grey marbles are reported in the same area of the dome structures (Gross et al., 1999). However, the fluid inclusions occur as secondary fluid inclusions trails and are probably of cretaceous age. These grey marbles occur in small lenses of some meters within the abnormally grain-coarsened marble.

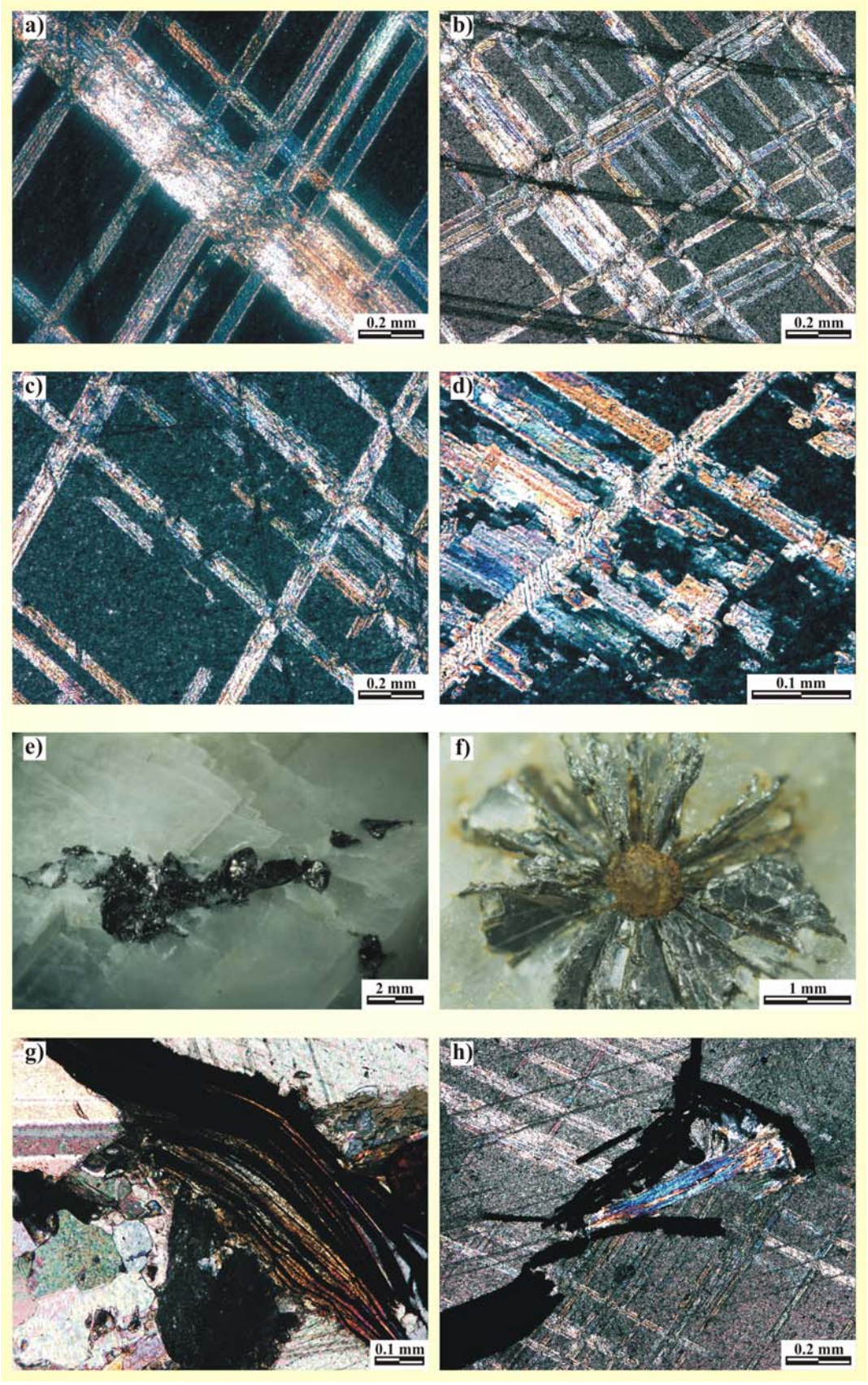
a)
0.2 mm
b)
0.2 mm
c)
0.2 mm
d)
0.1 mm
e)
2 mm
f)
1 mm
g)
0.1 mm
h)
0.2 mm

Fig 2.5 *Microstructures of the undeformed grain-coarsened host rock. Figures a to d and g to h are microphotographs in crossed polarised light, whereas Figures e and f are microphotographs in reflected light.* ***a)*** *Two sets of intersecting calcite twins. The younger set of twins rotated and dislocated the older twins at the points of intersection (sample Elim Sp).* ***b)*** *The rhombohedral plains fractured and slightly dislocated the twin lamellae (sample Elim Sp).* ***c)*** *Twin lamellae have been recrystallised by the host crystal and therefore are partially extinct (sample Elim Sp).* ***d)*** *Twin lamellae that have been partially recrystallised by interlobate fronts of recrystallisation (sample Elim Sp).* ***e)*** *Graphite nest with graphite flakes as they occur commonly throughout the grain-coarsened graphite-bearing marble (sample Elim Sp).* ***f)*** *Nest of radial graphite with mineral core in the center occuring in the grain-coarsened calcite-marble (sample Omaruru Sp).* ***g)*** *Epitaxial intergrown basal plains of graphite and muscovite (sample 13.8.97/3A from C. Gross Univ. Göttingen).* ***h)*** *Epitaxial intergrown graphite and muscovite. (sample Elim Sp).*

2.3.2. BRITTLE-DUCTILE DEFORMED MARBLE

The calcite-marble of the brittle-ductile domains shows a variety of microstructures in the boundary zone of brittle-ductile deformation ranging from brittle to crystal-plastic deformation structures. The microstructural investigations revealed that despite pronounced differences in the macroscopic fabrics shown above, the microstructures of the different fabrics are very similar. The cataclastic breccia zones are exceptional in some respects, as the cataclastic microfabric dominates in these samples.

Figures 2.6 a to d display a general overview of the microstructures representative for the different macroscopic fabrics shown in Figure 2.4 b to h. Therefore, they are arranged in an order of increasing graphite network intensity from Figure 2.6 a to c. Figure 2.6 d represents the microfabrics of a cataclastic breccia zone. The fabrics and microfabrics described are identical for all investigated localities shown in Figure 2.1.

Figure 2.6 a shows an overview of the microstructures of a sample with a low degree of network intensity of graphitic stylolites. The macroscopic fabric is similar to the fabrics shown in Figure 2.4 b and c. The grain size of the calcite crystals ranges between 5 to 10 mm for the host crystals and between 50 to 200 μm for the calcite grains in the fracture zones. The orientations of the host crystals are still similar, which implies that these result from one single calcite crystal as observable in the abnormally grain-coarsened and undeformed marble host rock. The fracture zones show, that this sample had already been deformed.

The microstructures of a sample with an intermediate degree of graphite network intensity are shown in Figure 2.6 b, which applies to the macroscopic fabric shown in Figure 2.4 d. It is obvious, that the grain size is generally reduced with an increasing degree of graphite network intensity. The calcite host crystals are reduced to grain sizes of

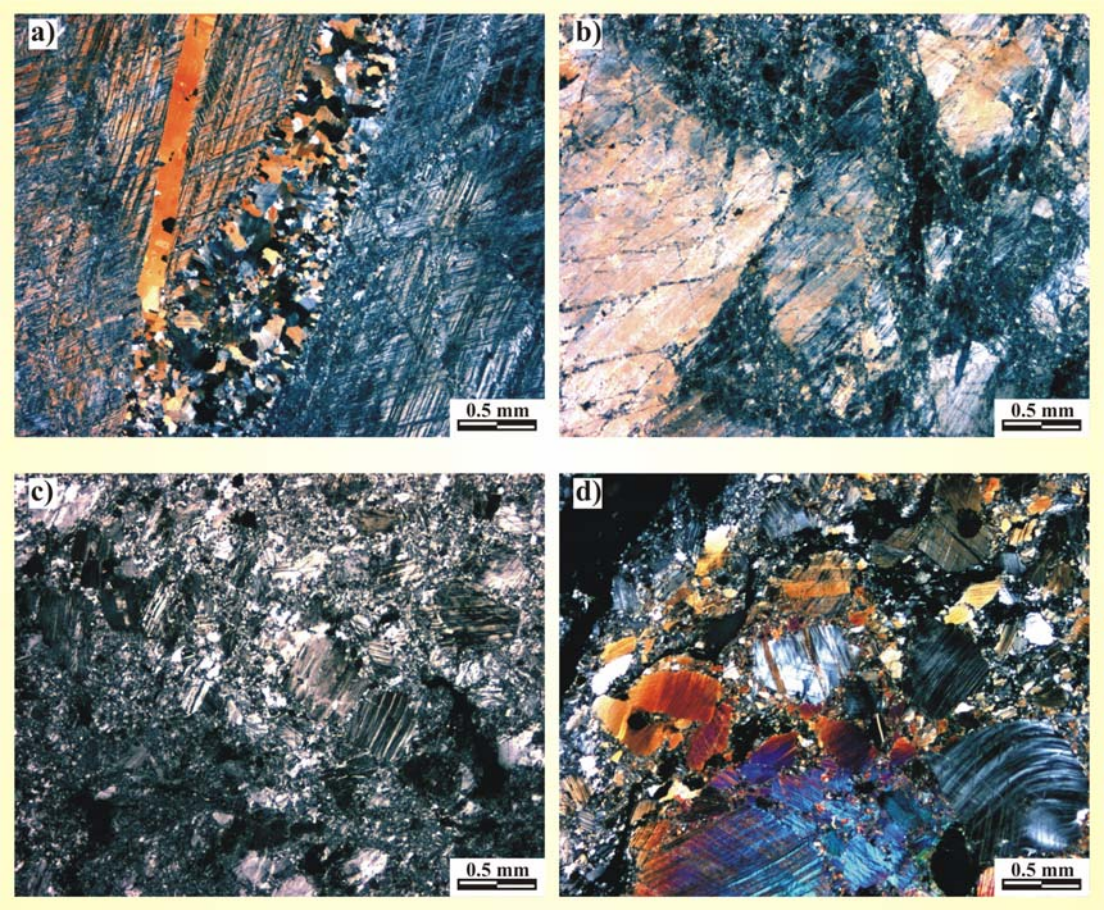

Fig 2.6 *General overview of brittle-ductile deformed marbles. The samples increase in network intensity from a to c. Figure d represents purely cataclastic deformation. All figures represent microphotographs in crossed polarised light.* ***a)*** *Microstructures of a sample with a low degree of network intensity of graphitic stylolites. The macroscopic fabric is similar to the macroscopic fabric shown shown in Figure 2.4 b,c (sample 17/08/00/15).* ***b)*** *Microstructures of a sample with an intermediate degree of graphite network intensity as shown in Figure 2.4 d (sample 17/08/00/19).* ***c)*** *Overview of the microstructures of a sample with a high degree of graphite network intensity. The macroscopic fabric is similar to the fabric shown in Figure 2.4 e, f (sample 17/08/00/17).* ***d)*** *Microstructures of a cataclastic breccia zone as shown in Figure 2.4 g, h (sample17/08/00/16)*

about 0.5 to 3 mm and in the matrix to about 10 to 100 µm. The orientation of these calcite host crystals varies already to a greater extent than in Figure 2.6 a.

Figure 2.6 c shows microstructures of samples with a high degree of graphite network intensity. The macroscopic fabric is equivalent to the fabric shown in Fig. 2.4 e, f. It is obvious that the grain sizes of the calcite host crystals and the matrix are reduced to a great extend compared to Figure 2.6 a, b. The grain size of the calcite host crystals are reduced to 0.1 to 0.5 mm and the grain size of the matrix ranges from 10 to about 100 µm.

Additionally, similarities in orientation between the host crystals as obvious in Figure 2.6 a are not observable anymore.

The microstructures of the cataclastic breccia zone show a different distribution of grain sizes. The macro- and microscopic fabrics give an impression, that the distribution of grain sizes is scale invariant as it is the similar in every dimension. This excludes the ultra fine-grained matrix, which shows recrystallisation fabrics. According to the microstructures in Figure 2.6 c there is a great variety in crystallographic orientation of the bigger calcite clasts compared to the fabric of the only slightly deformed sample shown in Figure 2.6 a.

The microstructurs of these samples show a strong cataclastic deformation, wheras the other samples of the brittle-ductile boundary zones rather show fine-grained inter- and intracrystalline fracture-zones. In these fracture zones the graphitic stylolites have developed. Locally an overprinting of the cataclastic microfabric by dynamic and static recrystallisation is observable in these samples.

From Figure 2.6 a to c it is obvious that the only difference in microstructures is the distribution of grain sizes, which can be correlated directly to the macroscopic fabrics. Therefore, the microstructures will be described independently of the degree of graphite network intensity. Nevertheless, the microstructures of the graphite network fabrics are distinguished from the cataclastic breccia zones.

Nearly all calcite grains show intensive twinning, often in two sets of twin lamellae which intersect each other. Figure 2.7 a shows two sets of twins are developed, whereas the older set of twins is often overprinted by intensive twinning of the second set of twins. The twin lamellae vary quite extensive in thickness within one set of twins. The twin lamellae are often bent or kinked (Fig. 2.7 b). As shown in this Figure, the degree of bending and kinking depends on the thickness of the twins. Thick twins are folded whereas thinner twins are already kinked.

Figure 2.7 c shows, that kink bands are sometimes strongly developed with a great variety of thickness. In some samples, higher metamorphic temperatures are indicated by a kink bands that are irrregular in shape, thickness and orientation (Fig. 2.7 d). It is obvious in all samples, that the kink bands develop also from deformation bands shown in Figure 2.7 e. The deformation bands are often developed in irregular shapes. In other cases, the deformation bands are in regular shape and show a preferred orientation within distinct domains of a grain (Fig. 2.7 f).

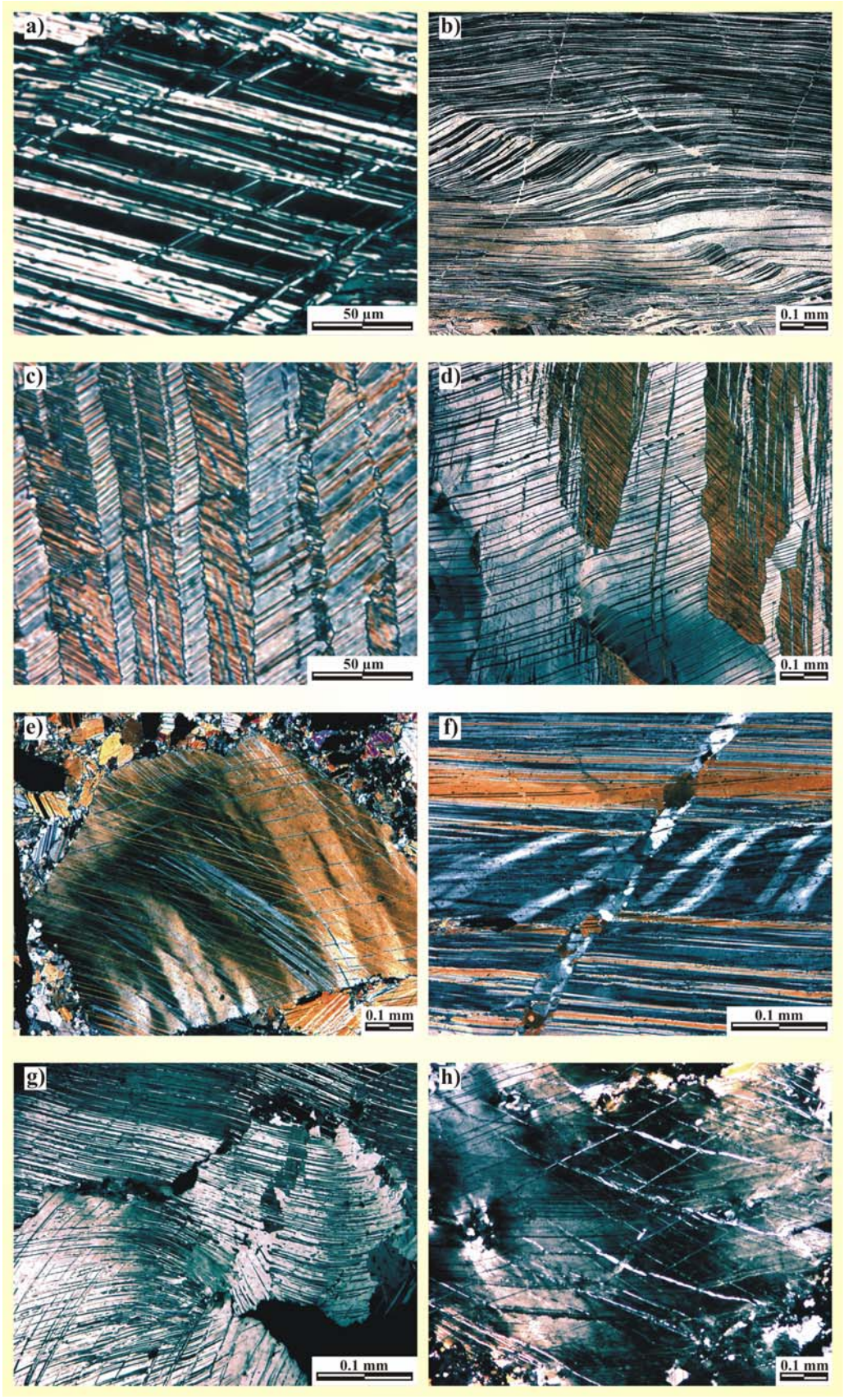
a)
50 µm
b)
0.1 mm
c)
50 µm
d)
0.1 mm
e)
0.1 mm
f)
0.1 mm
g)
0.1 mm
h)
0.1 mm

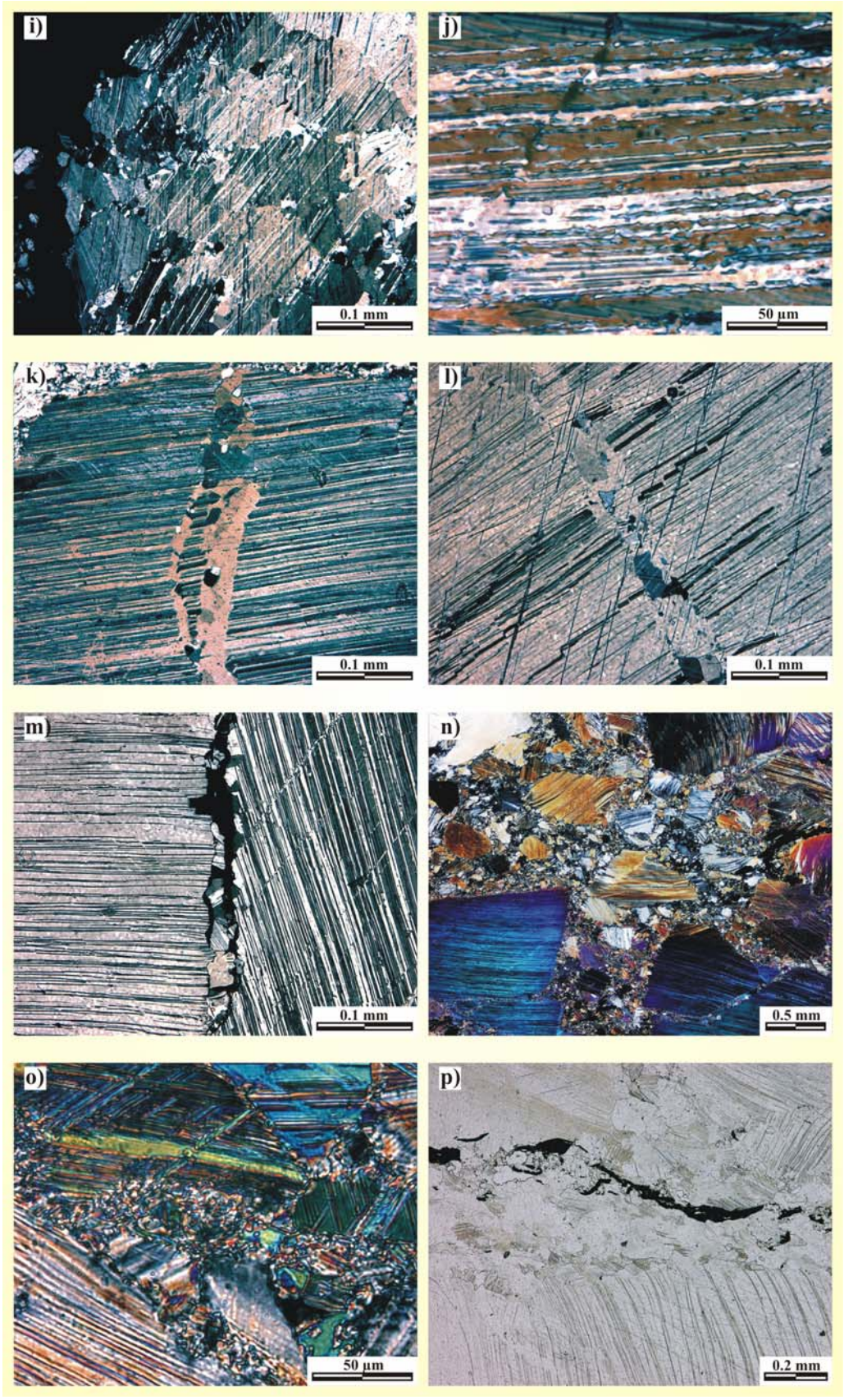
i)
0.1 mm
j)
50 µm
k)
0.1 mm
l)
0.1 mm
m)
0.1 mm
n)
0.5 mm
o)
50 µm
p)
0.2 mm

Fig 2.7 *Microstructures of the brittle-ductile deformed marbles. Figures a to o represent microphotographs in crossed polarised light, whereas Figure p is a microphotograph in plain polarised light.* ***a)*** *Intensive twinning of the calcite crystals with an extensive difference in the thickness of the twins. Often two sets of twins are developed, where the first set of twins has been overprinted by the younger genereation of twins (sample 17/08/00/19).* ***b)*** *Calcite twins are bent or kinked depending on their thickness (sample 3.10.01/3).* ***c)*** *Intensive kinking of the calcite twins (sample 17/08/00/15).* ***d)*** *Kink bands at higher metamorphic temperatures (sample 3.10.01/3).* ***e)*** *Deformation bands in varying extent are developed in the calcite host crystals (sample 17/08/00/16).* ***f)*** *Deformation bands developed in distinct parts of the grain which are free from intensive twinning (sample 3.10.01/3).* ***g)*** *Flexural slip in the calcite crystals with a thickening of the flexured twins (sample 17/08/00/16).* ***h)*** *Undulous extinction due to polygonisation within the calcite crystals (sample 17/08/00/16).* ***i)*** *Subgrain rotation recrystallisation of the calcite crystals (sample 17/08/00/16).* ***j)*** *Ultra fine-grained recrystallisation along the twins of a calcite crystal (sample 3.10.01/3).* ***k)*** *Intracrystalline multiple crack-seal vein filled mainly with breccia of the host crystal (sample 17/08/00/16).* ***l)*** *Intracrystalline crack-seal vein filled with breccia of different orientation (sample 17/08/00/16).* ***m)*** *Open fracture of a younger generation filled with fine-grained breccia (sample 17/08/00/16).* ***n)*** *Purely cataclastic microfabric of a breccia zone, which shows the same microstructures than the brittle-ductile deformed samples (sample 17/08/00/16).* ***o)*** *The purely cataclastic microstructures are scale invariant (sample 17/08/00/16).* ***p)*** *Graphite stylolites are developed in fine-grained fracture zones with ultra fine-grained graphite as residue of the pressure solution (sample 3.10.01/3).*

Another deformation structure observed is flexural slip within the crystal lattice, which leads to a thickening of calcite twins in the area of bending and flexural slip (Fig. 2.7 g). The deformation of the calcite crystals also lead to polygonisation as shown in Figure 2.7 h and eventually to subgrain rotation recrystallisation (Fig. 2.7 i). Higher metamorphic temperatures within distinct shear zones are indicated by ultra fine-grained recrystallisation along the twin lamellae (Fig. 2.7 j).

Intracrystalline fracturing is also observable in all investigated samples of the boundary zone of brittle-ductile deformation. Figure 2.7 k indicates a vein of multiple crack and seal events. In this vein, breccia of the same orientation as the host rock is still observable. The fluid inclusions in the matrix of the vein shows, that the sealing was controlled by fluids percolating the fractures.

The vein in Figure 2.7 l shows that the fracture had been filled with breccia, now partially in different orientation to the host crystal. The pore space between the fracture breccia has crystallised in the same orientation as the host crystal. Even the twins have developed again across the vein in the same orientation as in the host crystal. Figure 2.7 m shows an open fracture of a younger generation, which is also filled with breccia of the host crystal. This breccia, as well as the breccia in the sealed veins are slightly recrystallised.

Also the ultra fine-grained matrix of the cataclastic zones shown in Figure 2.7 n and o is recrystallised as shown in Figure 2.7 o. Both Figures show, that the cataclastic microfabric and especially the distribution in grain size is scale invariant up to the recrystallised ultra fine-grained matrix. In the brecciated cataclastic zones more brittle microstructures dominate with kinking, flexural slip within the crystal lattice, the devolopment of deformation bands and polygonisation.

Graphite in the brittle-ductile deformed graphite-bearing marble is also ultra fine-grained with grain sizes of 1 to 5 μm. As shown in Figure 2.7 p, graphite is concentrated in the fine-grained fracture zones as residue in stylolitic seams. These graphitic stylolites occur between the grain boundaries of the fine-grained and ultra fine-grained calcite crystals. Within zones of intensive pressure solution the graphitic stylolites are interconnected around calcite grain boundaries and form the graphitic network structures. The thickness of the graphitic stylolites varies from 20 to about 100 μm. The graphitic stylolites develop only in the fine-grained zones between the coarser-grained calcite host crystals. Therefore, the degree of graphite network intensity is dependent on the grain size distribution in the samples. The graphitic stylolites are never developed as intracrystalline stylolites.

2.3.3. DUCTILE DEFORMED MARBLE

The ductile deformed marble of the mylonitic core zone commonly shows a fine-grained dynamically recrystallised matrix and porphyroclasts of calcite, quartz and plagioclase. Graphite either occurs concentrated in layers or is disseminated within the matrix. The grain size of the matrix varies from 10 to 100 μm, whereas the grain size of the graphite ranges from 5 to 70 μm. The porphyroclasts show grain sizes of up to 1 mm.

The calcite porphyroclasts are commonly twinned. As shown in Figure 2.8 a some porphyroclasts have two sets of twins developed. The twins are commonly bent or show kink bands as shown in Figure 2.8 b. The porphyroclasts display undulose extinction (Fig. 2.8 a) and are recrystallised along the grain boundaries. The grain sizes of the recrystallised grains vary in domains around the clast as shown in Figure 2.8 b.

The porphyroclast in Figure 2.8 c shows subgrain rotation recrystallisation which caused a rotation and bending of the unrecrystallised twin lamellae within the subgrain domain. This porphyroclast also shows recrystallisation along the grain boundary. The recrystallised grains are commonly free of twins along the rim of the porphyroclast. Subgrain rotation recrystallisation and the formation of new grains also occurs along twin lamellae within the porphyroclasts as shown in Fig 2.8 d.

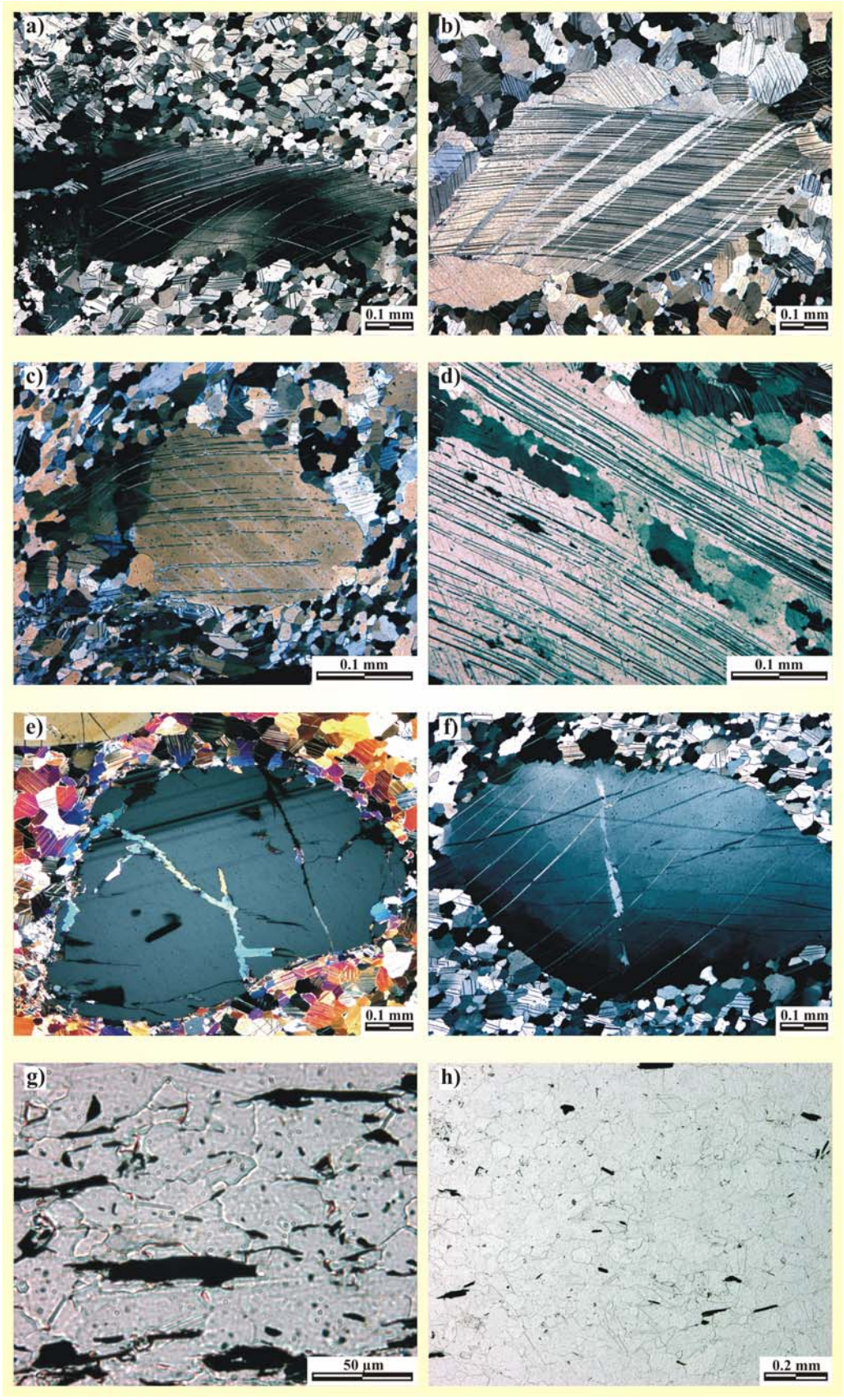
a)
0.1 mm
b)
0.1 mm
c)
0.1 mm
d)
0.1 mm
e)
0.1 mm
f)
0.1 mm
g)
50 µm
h)
0.2 mm

Fig 2.8 *Microstructures of the mylonitic core zone. Figures a to f are photomicrographs in crossed polarised light and Figures g and h are photomicrographs in plain polarised light.* ***a)*** *Twinned calcite porphyroclast with two sets of twins developed. It shows undulous extinction and is recrystallised along the grain boundary (sample 11/08/00/03).* ***b)*** *Calcite porphyroclast with kink bands and recrystallisation along the grain boundary (sample 16/08/00/02).* ***c)*** *Calcite porphyroclast with subgrain rotation recrystallisation and recrystallisation along the grain boundary (sample 12/08/00/04).* ***d)*** *Calcite porphyroclast with subgrain rotation recrystallisation and the formation of new grains along the twin lamellae (sample 12/08/00/04).* ***e)*** *Fractured plagioclase porphyroclast with healed calcite veins and an ultra fine-grained rim of recrystallised calcite around the grain boundary (sample 3.10.01/4).* ***f)*** *Calcite porphyroclast with a vein developed. Recrystallisation along the grain boundaries occurred in different grain size domains (sample 11/08/00/03).* ***g)*** *Graphite concentrated in layers in preferred orientation of the basal plains parallel to the foliation (sample 11/08/00/03).* ***h)*** *Graphite disseminated in the fine-grained dynamically recrystallised matrix with a preferred orientation of the basal plains parallel to the foliation (sample 11/08/00/06).*

The quartz and plagioclase porphyroclasts are often fractured and sealed with calcite veins as shown in Figure 2.8 e. This plagioclase porphyroclast shows an ultra fine-grained rim of recrystallised calcite along the grain boundary, which is very common in the marble mylonites. Also the calcite porphyroclasts show veins of recrystallised intracrystalline fractures as shown in Figure 2.8 f. This porphyroclast is recrystallised along domains of the grain boundary, whereas other domains do not show any recrystallisation of the grain boundaries of the porphyroclast.

Graphite occurs in the dynamically recrystallised matrix of the marble mylonites. As shown in Figure 2.8 g, h it either occurs concentrated in graphitic layers or disseminated throughout the matrix. The graphite is not interconnected in the graphitic layers and shows a preferred orientation with the basal planes parallel to the foliation (Fig. 2.8 g). Graphite disseminated throughout the marble mylonites, also shows a preferred orientation parallel to the foliation. In both cases graphite mainly occurs on the calcite grain boundaries.

2.3.4. CATHODOLUMINESCENCE INVESTIGATIONS

For cathodoluminescence microscopy (CL) investigations thin sections are carbon coated. By the irradiation with electrons, the distribution of trace elements like manganese (Mn) and iron (Fe) is dectected. Mn is the most important activator element for the luminescence, whereas Fe inhibits bright luminescence colours. For calcite the luminescence colours range from dark read to bright yellow. By CL investigations, fluid-controlled recrystallisation processes can be visualized.

The investigation by CL revealed that the brittle-ductile deformed marble shows consistent CL colours for the calcite host crystals, the fracture zones, the stylolites and the crack-seal

veins (Fig. 2.9 a, b). Local differences in intensity as shown in Figure 2.9 a, are related to effects on luminescence intensities due to differences in grain geometry and lattice orientations. This is also observable in Figure 2.9 c, where the coarse-grained host crystal shows a slightly darker CL colour than the fine-grained matrix (Fig.2.9 d).

Figure 2.9 c to h show additionally a younger generation of microveins, which display different CL colours than the older fabric of brittle-ductile deformation. These younger veins occur in different generations, which all show a preferred orientation. They postdate the brittle-ductile deformation as they cut the graphitic stylolites, the brittle-ductile fracture zones and the veins regardless of the orientation of the previous deformational structures. Figure 2.9 d shows that these younger microveins cut the coarse-grained host crystals as well as the matrix.

Graphitic stylolites are also opened and crystallised with calcite by these younger microveins (Fig. 2.9 e). It is also commonly observable that the microveins either cut the graphitic stylolites or end when a stylolite is reached by the vein (Fig. 2.9 e to h). The stylolites are not inevitably reactivated by the younger microveins as shown in Figure 2.9 g, h. A microvein has developed parallel to a graphitic stylolite cutting other stylolites of the graphite network structure and a domain of coarse-grained calcite crystals.

2.3.5. INVESTIGATIONS BY SCANNIG ELECTRON MICROSCOPY

Investigations by Scanning Electron Microscopy (SEM) and Energy Dispersive X-ray Analysis (EDX) were conducted to characterise the different types of graphite-bearing marbles described above. EDX investigations reveal the qualitative composition of a sample by the composition of existing elements. Figure 2.10 shows the qualitative composition of the measured arrays in the left column. The according SEM phase contrast image is shown in the right column.

The measurement and composition of the calcite-marble is shown by the representative Figure 2.10 a, b. The area scan of Figure 2.10 b shows, that the marble is mainly composed of calcite (Fig. 2.10 a). Quarz, plagioclase and muscovite occur in concentrations of about 0.5 Vol % and were also detected in the measurements. However, as these phases are only accessory minerals, the composition shown in Figure 2.10 a is representative for all three types of the investigated graphite-bearing marbles.

The quantitative composition of graphite within the abnormally grain coarsened marble host rock (type 1) is shown in Figure 2.10 c to f. According to the measurement spots shown in the phase contrast images (Fig. 2.10 d, f) the composition of the graphite

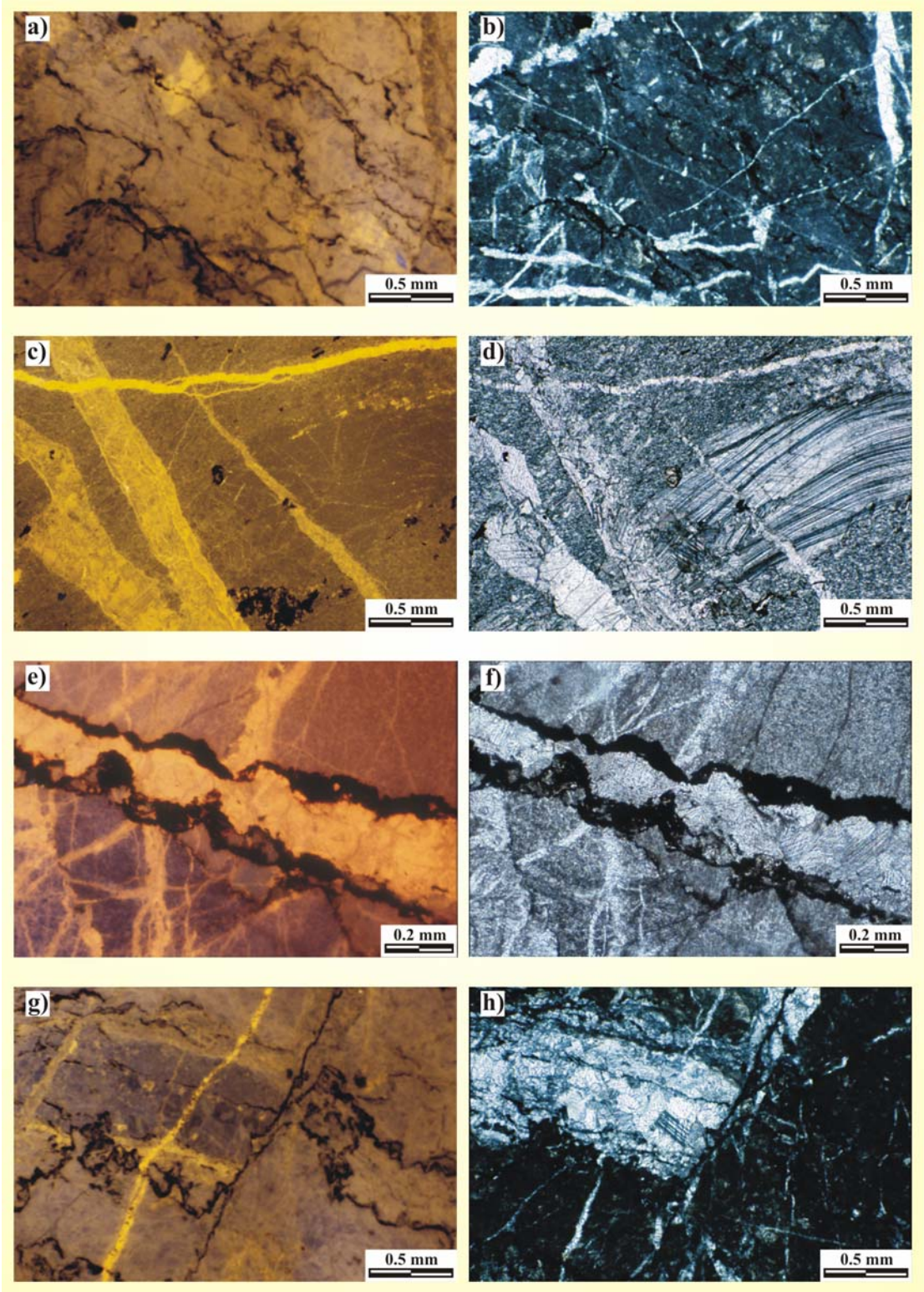

Fig 2.9 *Cathodoluminescence microscopy investigations of microveins in the brittle-ductile deformed marble* ***a)*** *Microphotograph of uniform CL colours of the graphitic stylolites (sample 17/08/00/08a).* ***b)*** *Normal polarised microphotograph of the same section as in Figure a), which shows the calcite matrix with*

microveins and stylolites of the brittle-ductile deformation (sample 17/08/00/08a). ***c)*** *Microphotograph in CL colours of two generations of younger microveins cutting coarse-grained host crystals and the fine-grained matrix. They are distinguished from the older deformational structures by the different CL colours (sample 12/08/00/04).* ***d)*** *Microphotograph in crossed polarised light of the sampe section as Figure c (sample 12/08/00/04).* ***e)*** *Microphotograph in CL colours of a reactivated graphitic stylolite mineralised as calcite vein. Microveins end at stylolites (sample 17/08/00/08b).* ***f)*** *Crossed polarised light microphotograph of the section shown in e (sample 17/08/00/08b).* ***g)*** *Microvein parallel to a stylolite cutting other stylolites and a domain of coarse-grained calcite crystals. Microphotograph in CL colours (sample 17/08/00/08a).* ***h)*** *Section of g under crossed polarised light (sample 17/08/00/08a).*

varies quite extensively between different graphite flakes within one radial graphite structure. The composition shown in Figure 2.10 c results from a spot measurement of a graphite flake, that has grey colours in the phase contrast image (Fig. 2.10 d). This measurement shows a strong C peak accompanied by Ca and O peaks which are most probaly resulting from calcite.

In contrast, the white domains in the phase contrast image of this radial graphite structure (Fig. 2.10 f) show a completely different quantitative composition of graphite (Fig. 2.10 e). Additional phases like Fe, Ti, K, Si, Al, Mg and Cl are detected in this part of the radial graphite structure. These phases may be related to the epitaxial intergrowth of mica minerals and graphite on the basal plains.

These phases are also detected in the graphitic stylolites of the brittle-ductile deformed graphite bearing marbles (type 2) as shown in Figure 2.10 g to j. The spot measurements of the phase contrast images in Figure 2.10 h, j indicate that the graphite stylolites also display different colours in the phase contrast image.

As the EDX measurements in Figure 2.10 g, i show, this difference in phase contrast colours is not only related to the measurement of fine-grained calcite within the stylolites. The additional phases Fe, Ti, Al, Mg, P, Ca, O are similar to the phases detected in the undeformed radial graphite structure. From their composition, they may be related to mica and calcite minerals. Therefore, the undeformed and the retrograde deformed graphite shows a similar composition in accessory minerals.

2.3.6. QUANTITATIVE CALCITE-GRAPHITE RATIOS

As the graphitic stylolites are formed by pressure solution, it is necessary to quantify this influence on the development of the microstructures by calculating the quantitative calcite-graphite ratios. These were approached by two methods: Firstly by the evaluation of the content of graphite in samples with a known volume. Secondly by scanning polished sample surfaces and counting the ratio between white calcite and black

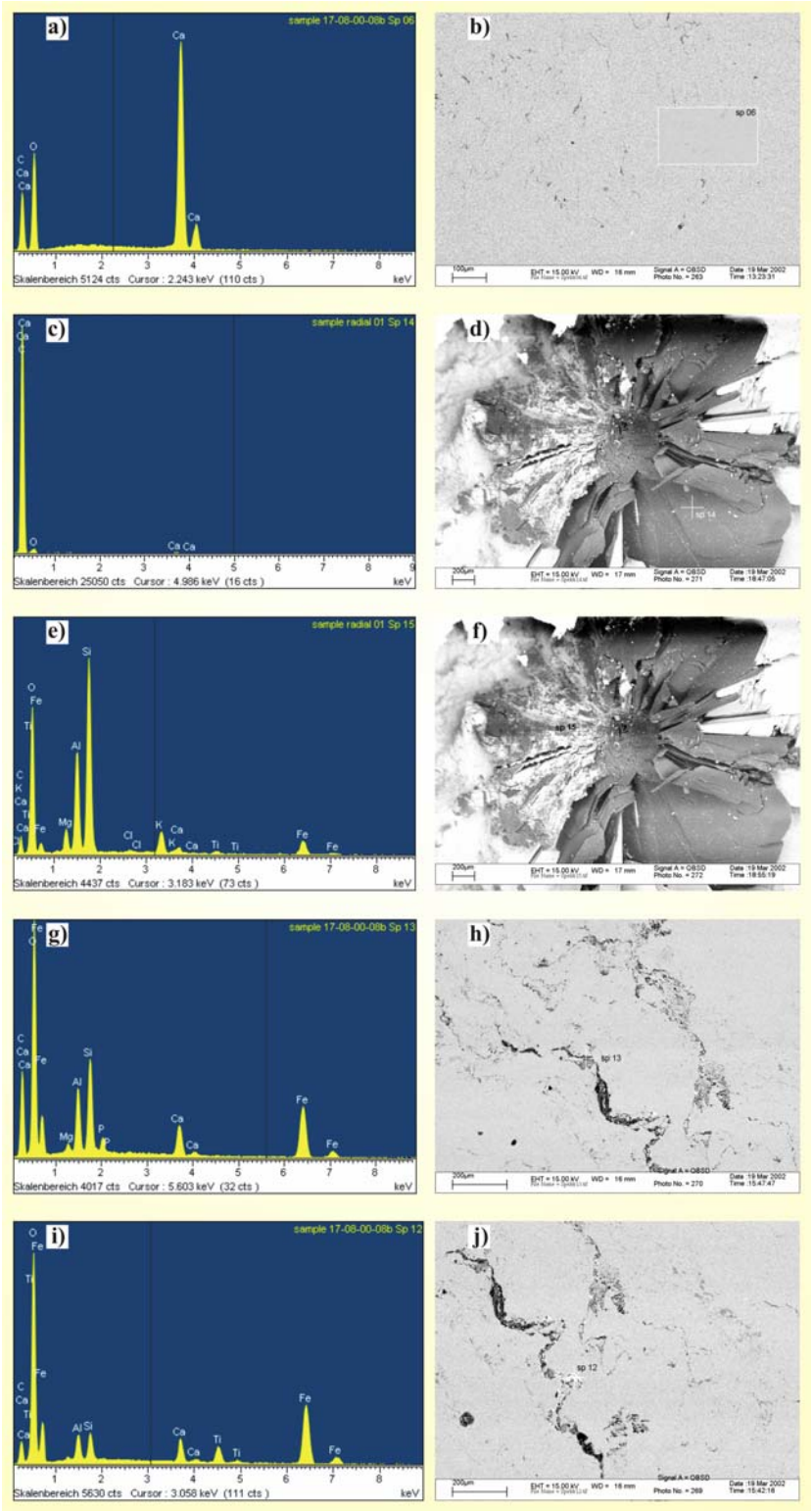

Fig 2.10 *SEM and EDX investigations of the different types of graphite-bearing marbles. Figures a, c, g and i are the EDX diagrams and Figures b, d, h and j represent the phase contrast images.* ***a)*** *Representative plot of*

the qualitative composition of a type 2 graphite-bearing marble (sample 17/08/00/08b). ***b)*** *Phase contrast image with the measured area marked by the white box (sample 17/08/00/08b).* ***c)*** *Qualitative composition of a graphite flake (type 1 graphite-bearing marble) with grey colours in the phase contrast image (sample radial 01).* ***d)*** *Phase contrast image of the radial graphite structure with the locality of the spot measurement marked by a + (sample radial 01).* ***e)*** *Qualitative composition of a different graphite flake (type 1 graphite-bearing marble) with a white colour in the phase contrast image (sample radial 01).* ***f)*** *Spot measurement in the white domains of the graphite flakes is marked by a + (sample radial 01).* ***g)*** *Qualitative composition of a graphitic stylolite from a type 2 graphite-bearing marble (sample 17/08/00/08b).* ***h)*** *The spot of the measurement is marked on the phase contrast image (sample 17/08/00/08b).* ***i)*** *Qualitative composition of a white domain of a graphitic stylolite from a type 2 graphite-bearing marble (sample 17/08/00/08b).* ***j)*** *Phase contrast image with the locality of the spot measurement marked (sample 17/08/00/08b).*

graphite pixels in a predefined area. This area was constant for all samples. This was done to evaluate whether it is possible to estimate the amount of pressure solution by macroscopic optical methods.

2.3.6.1. ANALYTICAL TECHNIQUES

For quantifying the calcite-graphite ratio by the content of graphite, the different sample volumes were obtained of samples with varying degrees of graphite network intensity. This was done by measuring the water displacement of the samples, which then was used to calculate the sample volume by the density of the displaced water. In a second step, the samples were excavated and the volume of the permeable pore space was measured by the oven-dry mass, the saturated mass and the flotation mass. The porosity then was substracted from the calculated volume of the samples.

Afterwards the graphite bearing marbles were dissolved in concentrated hydrochloric acid. After calcite was dissolved, the graphitic residue was then treated with hydrofluoric acid to dissolve accessory silicate minerals. As the graphitic residue still contained Ca-Fluorides, it had to be boiled in hydrochloric acid. After the graphite has been rinsed with demineralised water, the volumetric content of graphite for each sample had been calculated from the graphite density.

For the second method of quantifying the calcite-graphite ratios, polished surfaces of the same samples were scanned on a flat bed scanner with a resolution of 600 dpi. An area of 50 cm^2 was selected for all samples, to evaluate the content of graphite statistically. This was done by calculating the ratio between black pixels of the graphitic stylolites and the white pixels of calcite.

The evaluation of both methods is based on the assumption that the graphite in the undeformed and therefore unaltered host rock must have a statistically constant volume,

because it is disseminated thoughout the host rock in graphite nests. Under this precondition, the amount of pressure solution of calcite may be calculated for the samples, where the volumetric content of graphite is higher than in the undeformed host rock. Likewise, for lower volumetric contents of graphite pressure solution of graphite has to be assumed. As shown in Figure 2.3 a, b this assumption is only true for a sample volume that eliminates statistically local differences in the concentration of disseminated graphite nests in the undeformed host rock. Whether this critical sample volume of the undeformed host rock has been reached in the investigated samples, has not been evaluated in detail. It is assumed however, that the sample volume is statistically appropriate.

2.3.6.2. MEASUREMENTS AND RESULTS

The results of the measurement of the concentration of graphite are shown in table 2.1. The table shows the samples sorted from the lowest to highest volumetric content of graphite. The volumetric content of graphite in the undeformed host rock is around 0.098 Vol %, whereas the highest concentration of graphite are observable in the brittle-ductile boundary zone with 0.442 Vol %. This table also reveals that there are seven samples, which show a lower volumetric content of graphite than the undeformed host rock. The lowest value measured is 0.018 Vol % of graphite.

According to this data it can be assumed, that pressure solution has occurred for calcite as well as for graphite. From the obtained values, the calculated pressure solution of graphite amounts to a maximum of 5.44 %. Likewise, the pressure solution of calcite can be calculated to about 4.51 %. For a simultaneous pressure solution of both mineral phases, the amount of graphite pressure solution must be substracted from the field of calcite pressure solution. A maximal amount of pressure solution of calcite of 24.56 % is in this case implied by the data.

The quantitative calcite-graphite ratios obtained from the same samples by macroscopic optical methods are shown in table 2.2. The proportion of graphite pixels from the measured area is given as a percentage. The samples are sorted from the lowest proportion to the maximum proportion of graphite obtained from the measured samples.

Compared to the volumetric contents of graphite (table 2.1), it becomes obvious from table 2.2 that the samples with a lower volumetric content than the undeformed host rock imply macroscopically an exceeding concentration of graphite. This is related to a high portion of dark and/or black arrays within the samples, due to fine-grained calcite, which also appears in darker colours. The macroscopic fabrics of the measured samples are shown in Figure 2.11 a to p.

sample	sample volume [cm^3]	content of graphite [cm^3]	volumetric content of graphite [Vol %]
17/08/00/04	2397.876	0.439	0.018
17/08/00/17	2292.347	0.527	0.023
17/08/00/13	745.192	0.344	0.046
17/08/00/15	599.671	0.360	0.060
17/08/00/19	675.834	0.450	0.067
17/08/00/10	366.988	0.262	0.071
17/08/00/12	381.800	0.367	0.096
17/08/00/20	1158.106	1.545	0.098
18/08/00/02	385.824	0.387	0.100
12/08/00/02	295.190	0.300	0.102
12/08/00/03	288.253	0.302	0.105
3.10.01./4	295.132	0.319	0.108
15/08/00/01	422.667	0.585	0.139
17/08/00/11	131.691	0.249	0.189
3.10.01./3	224.579	0.545	0.243
17/08/00/05	881.652	3.398	0.301
17/08/00/21	936.970	4.141	0.442

Table 2.1 *Quantitative calcite-graphite ratios calculated from the sample volume and the graphite content of the sample. The sample in orange is the host rock sample, whereas the samples in grey show pressure solution of graphite. The samples in peach colours show pressure solution of calcite as well.*

Table 2.1 and Figure 2.11 a to p indicate, that pressure solution of graphite occurs in samples with a broad variety of graphite network intensity. The samples of Figure 2.11 b, d with short graphitic stylolites and a very low occurrence of interconnected stylolites, definitely experienced graphite pressure solution. Likewise, the samples of Figure 2.11 k, l with an intermediate to high degree of graphite network intensity show graphite pressure solution. Furthermore samples with a very high degree of graphite network intensity as shown in Figure 2.11 m, o and p also clearly show graphite pressure solution.

sample	Proportion of Graphite [%]	sample	Proportion of Graphite [%]
17/08/00/20	0.23	17/08/00/11 1	5.72
17/08/00/13	0.39	17/08/00/11 2	6.57
18/08/00/02	1.99	17/08/00/17	16.09
17/08/00/15	2.54	17/08/00/19	17.6
12/08/00/03	2.84	17/08/00/04	19.08
12/08/00/02	3	17/08/00/21	22.31
15/08/00/01	4.34	17/08/00/12	29.93
17/08/00/05	4.68	17/08/00/10	32.5

Table 2.2 *Quantitative calcite-graphite ratios calculated from the area percentage of graphite on defined sample surfaces. Analogue to table 2.1 the sample in orange is the host rock. Samples in grey colours show pressure solution of graphite and the samples in peach colours show pressure solution of calcite.*

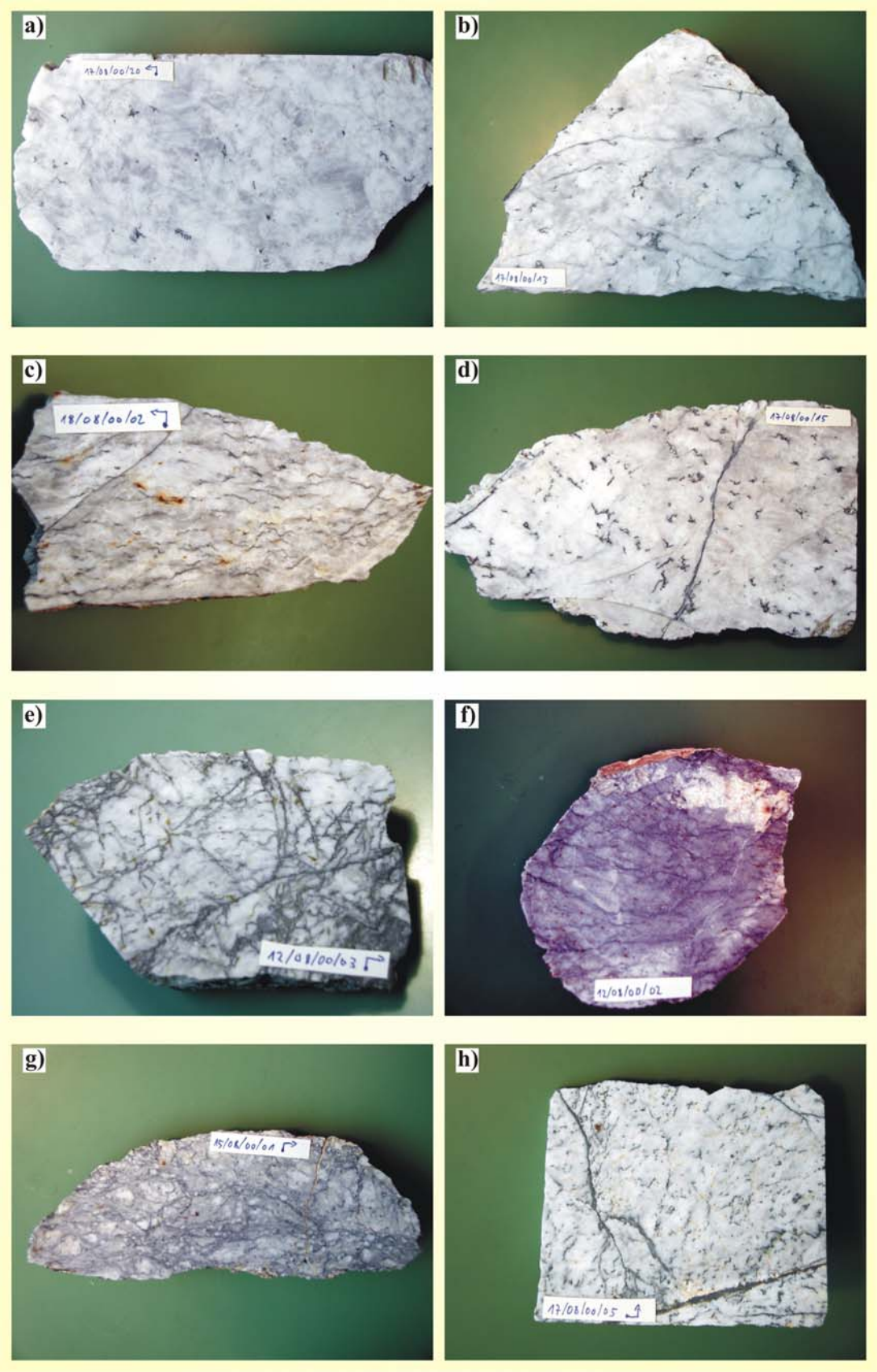
a)
b)
c)
d)
e)
f)
g)
h)

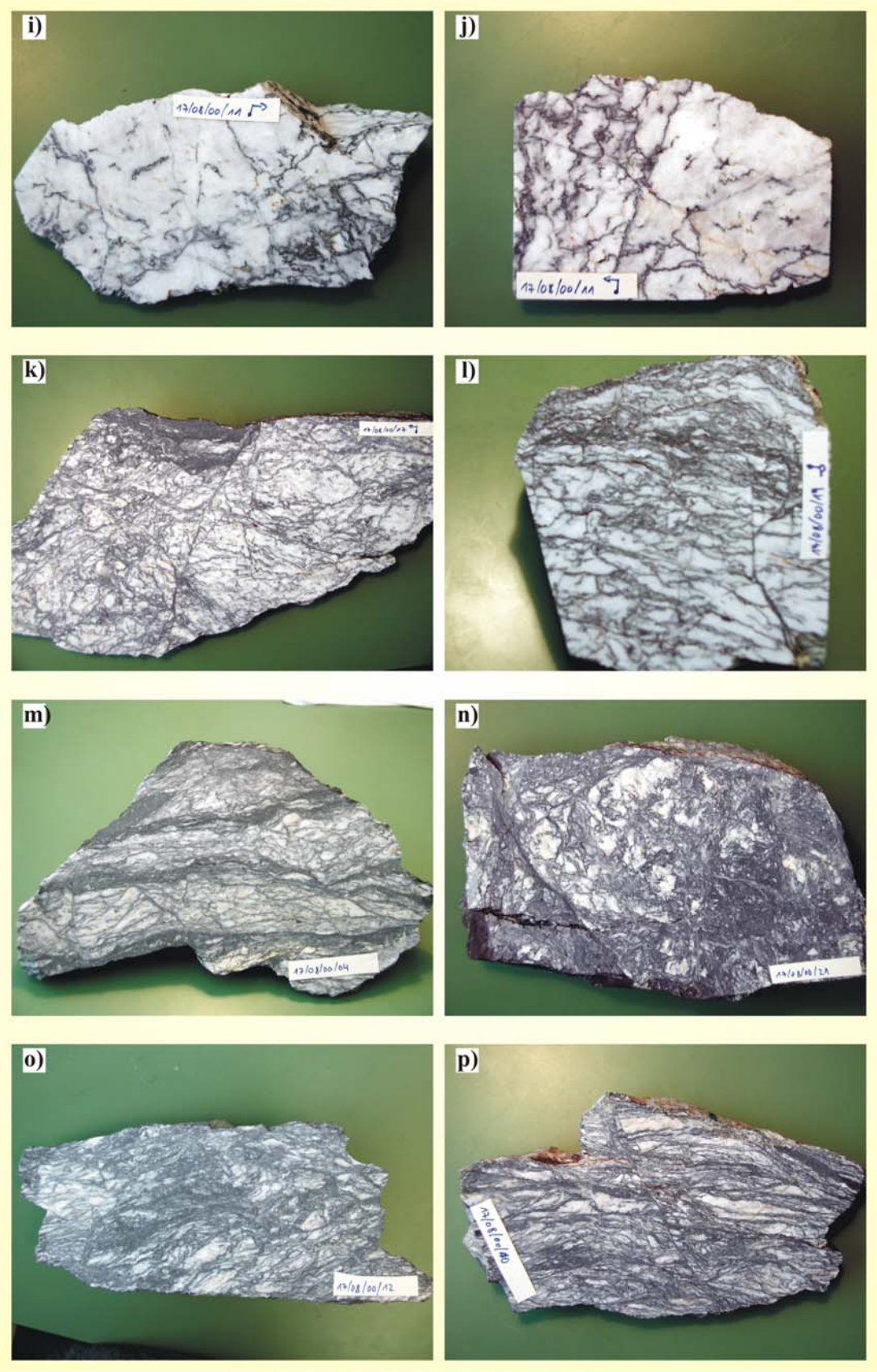
i)
j)
k)
l)
m)
n)
o)
p)

Fig 2.11 *Samples with different degrees of graphite network intensity used to quantify the calcite-graphite ratios by optical methods. The calcite-graphite ratios are shown in table 2.2* ***a)*** *sample 17/08/00/20* ***b)*** *sample 17/08/00/13* ***c)*** *sample 18/08/00/02* ***d)*** *sample 17/08/00/15* ***e)*** *sample 12/08/00/03* ***f)*** *sample 12/08/00/02* ***g)*** *sample 15/08/00/01* ***h)*** *sample 17/08/00/05* ***I)*** *sample 17/08/00/11 1* ***j)*** *sample 17/08/00/11 2* ***k)*** *sample 17/08/00/17* ***l)*** *sample 17/08/00/19* ***m)*** *sample 17/08/00/04* ***n)*** *sample 17/08/00/21* ***o)*** *sample 17/08/00/12* ***p)*** *sample 17/08/00/10*

2.4. TEXTURE ANALYSIS

In this study texture analysis is referred to as the quantification and analysis of crystallographic orientations of the mineral phases in the investigated samples. The texture analysis measurements were restricted to samples from the investigated shear zones, as the undeformed host rock is to coarse-grained to obtain statistically reprentative results. Texture analysis was conducted by neutron diffraction and the rotating stage polarizor.

2.4.1. TEXTURE ANALYSIS BY NEUTRON DIFFRACTION

For the texture analysis by neutron diffraction, the texture diffractometer SKAT (Ullemeyer et al., 1998) at the pulsed reactor IBR-2 in Dubna (Russia) was used. From the obtained time-of-flight (TOF) spectra, experimental pole figures were extracted, which represent the bulk texture of the samples.

2.4.1.1. ANALYTICAL TECHNIQUE

For the measurements with the texture diffractometer SKAT cylindrical samples of 40 mm in length and diameter were prepared. An exposition time of 15 min per sample position was selected. A measuring grid of 5°x5° and a simultaneous application of 19 detectors, resulted in measuring times of 16 hours per sample. Neutron diffraction enables texture measurements of the whole sample volume with an high d-resolution ($\Delta d/d \approx 0.5$ % at d = 2 Å), where d is the lattice spacing. The high d-resolution is necessary to identify individual Bragg peaks of the polyphase diffraction patterns. From the obtained TOF spectra (Fig. 2.12), experimental pole figures were calculated after the background subtraction, by integrating over all intensities at a pre-defined interval.

The experimental pole figures are plotted in equal area projection and the lowest contour represents 1.0 multiples of random distribution (m.r.d.). The contour intervals for the pole figures are uniform for all plotted samples. For the calcite pole figures in Figure 2.14 the contour intervals for the c-axes are 0.5 m.r.d. The a-axes pole figures are contoured at 0.2 m.r.d exept for sample 17/08/00/15 where it is 0.4 m.r.d. For the r- and f-plains the contour intervals are 0.1 m.r.d., except for samples 17/08/00/16b and 17/08/00/15 where it is 0.2

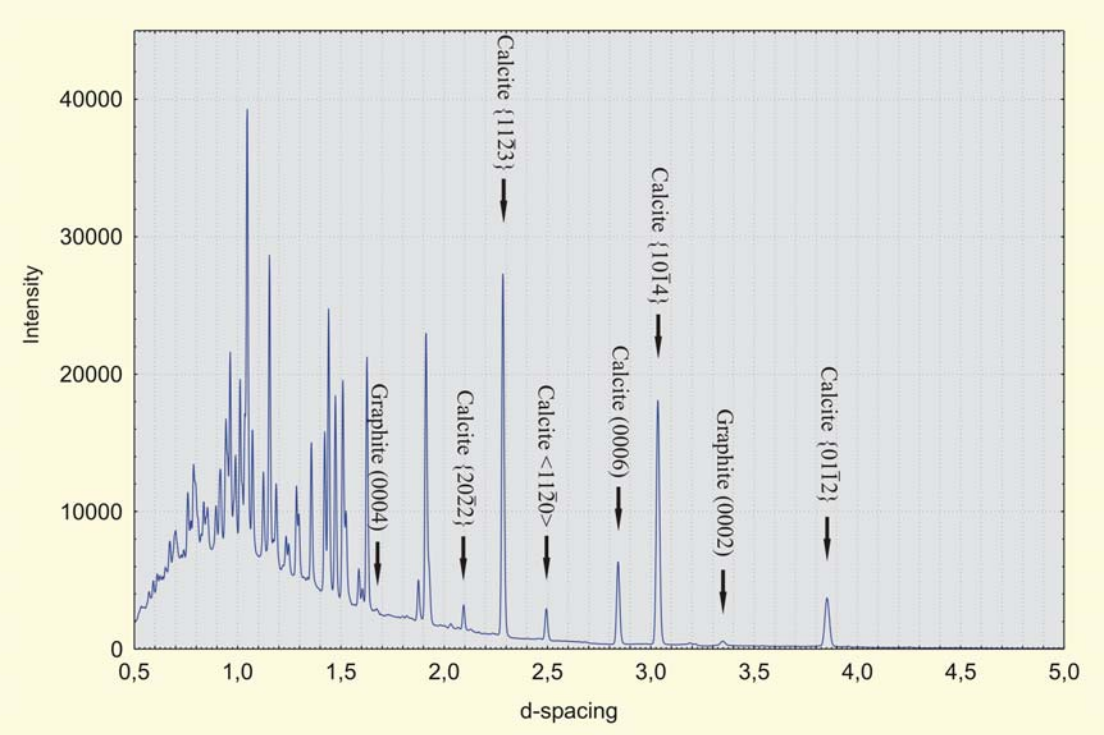

Fig 2.12 *Sumarised TOF neutron diffraction pattern. From the labelled peaks of calcite and graphite the pole figures were calculated.*

m.r.d. and 0.4 m.r.d. respectively. For the graphite pole figures in Figure 2.15, the contour intervals of the c-axes of the (0002) and (0004) Bragg reflections are 1.0 m.r.d. The dotted lines represent additional intermediate contours in samples of low texture intensities. The pole figures are oriented normal to the foliation and parallel to the lineation, where it was obtainable. The relative maxima are given for all pole figure in Figures 2.14 and 2.15.

2.4.1.2. TEXTURE TYPES OF CALCITE

For calcite, high-temperature and low-temperature texture types are distinguished for pure shear and simple shear deformation (Wenk et al., 1987). The different texture types of calcite are plotted in a compilation by Leiss & Molli (2003) after Wenk et al. (1987) (Fig. 2.13). The transition between different texture types in dependence of the temperature and deformation regime, is due to different critical shear stresses for the intracrystalline slip systems at different temperatures during deformation (e.g. De Bresser & Spiers, 1997). As these critical shear stresses are not only dependent on the temperature but also on the stress and strain rate, the simple correlation for calcite textures shown in Figure 2.13 is doubted by Leiss & Molli (2003).

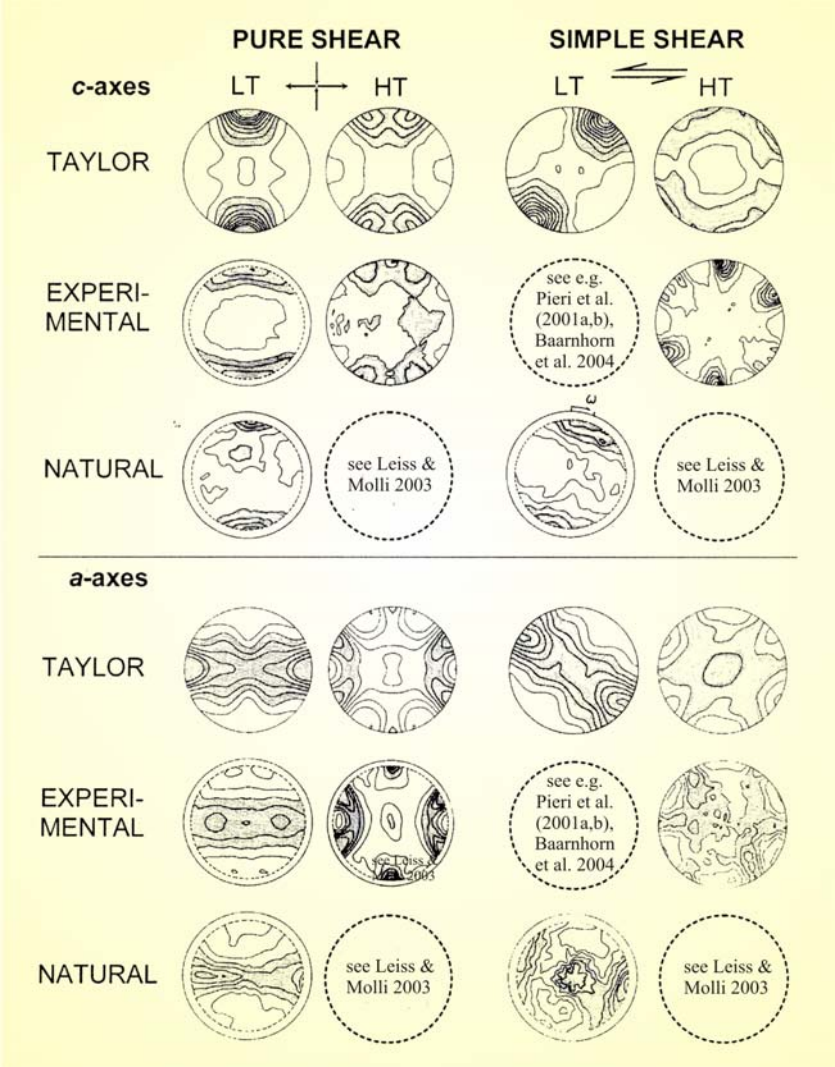

Fig 2.13 *Calcite texture types for different deformation regimes at different temperatures. The textures are represented by c-axes and a-axes after Wenk et al. (1987) and Leiss & Molli (2003).*

According to the the compilation of texture types in Figure 2.13, c-axes pole figures with one maximum normal to the foliation are related to ´low-temperature´ pure shear deformation. In this case the a-axes pole figures show a girdle distribution parallel to the lineation. This is the most common texture type for calcite as also described by Wenk et al. (1987) and Bestmann et al. (2000) The ´high-temperature´ pure shear calcite textures show a c-axes double maximum normal to the foliation and fixed maxima of the a-axes at 45° to the lineation. These types of ´high-temperature´ pure shear textures have recently been reported in the literature by Leiss & Molli (2003). However, these 'high-temperature' texture types occur in a low-temperature deformation structure.

Simple shear low-temperature calcite textures show a maximum normal to the foliation, which is rotated against the sense of shear for both the c-axes and a-axes (Fig. 2.13). The a-axes again form a girdle distribution. These textures have recently been obtained in experimental data of Pieri et al. (2001a,b) and Barnhoorn et al. (2004).

The high-temperature variation of simple shear textures for calcite again exists in a double maximum for the c-axes, which is also rotated against the shear sense from the position normal to the foliation (Fig. 2.13). The a-axes form distinct maxima, which are rotated correspondingly to the c-axes. These pole figures were also recently reported from natural samples by Leiss & Molli (2003).

The relationship between temperature, deformational regime and texture type as shown in Figure 2.13, is not as clearly documented in natural samples. After Leiss & Molli (2003), high-temperature texture types also occur in low-temperature deformation structures.

After Wenk et al. (1987), the most common texture type of calcite is the single maximum texture as shown in the low-temperature pure shear type of Figure 2.13. This single maximum may be rotated against or according to the sense of shear as shown by the low-temperature simple shear texture type in Figure 2.13. Bestmann et al. (2000) also shows, that the single maximum texture type is common across different stages of mylonitisation. A spectrum of different texture types of natural samples are shown and characterised by Leiss & Ullemeyer (1999), Weiss et al. (1999), Leiss & Weiss (2000) with respect to their implications on the physical properties of carbonate rocks.

2.4.1.3. SAMPLES AND MEASUREMENTS

The measured samples cover a broad range of shear zones and were selected due to different macroscopic fabrics. The sample localities are shown in Fig. 2.1. Corresponding coordinates are listed in the appendix. The calcite pole figures of the measured samples are shown in Figure 2.14. They are classified between mylonitic samples of the mylonitic core zones and the samples of the brittle-ductile boundary zone. The pole figures of the samples 11/08/00/03 to 16/08/00/02 represent the mylonitic samples, whereas the brittle-ductile deformed marbles are the samples 17/08/00/15 to 17/08/00/16b.

The samples of the brittle-ductile boundary zone were selected to cover a broad range of different macroscopic fabrics. The pole figures from sample 17/08/00/15 to sample 17/08/00/01 are sorted according to increasing degree of graphite network intensity. The pole figures of sample 17/08/00/16a represent the textures of the

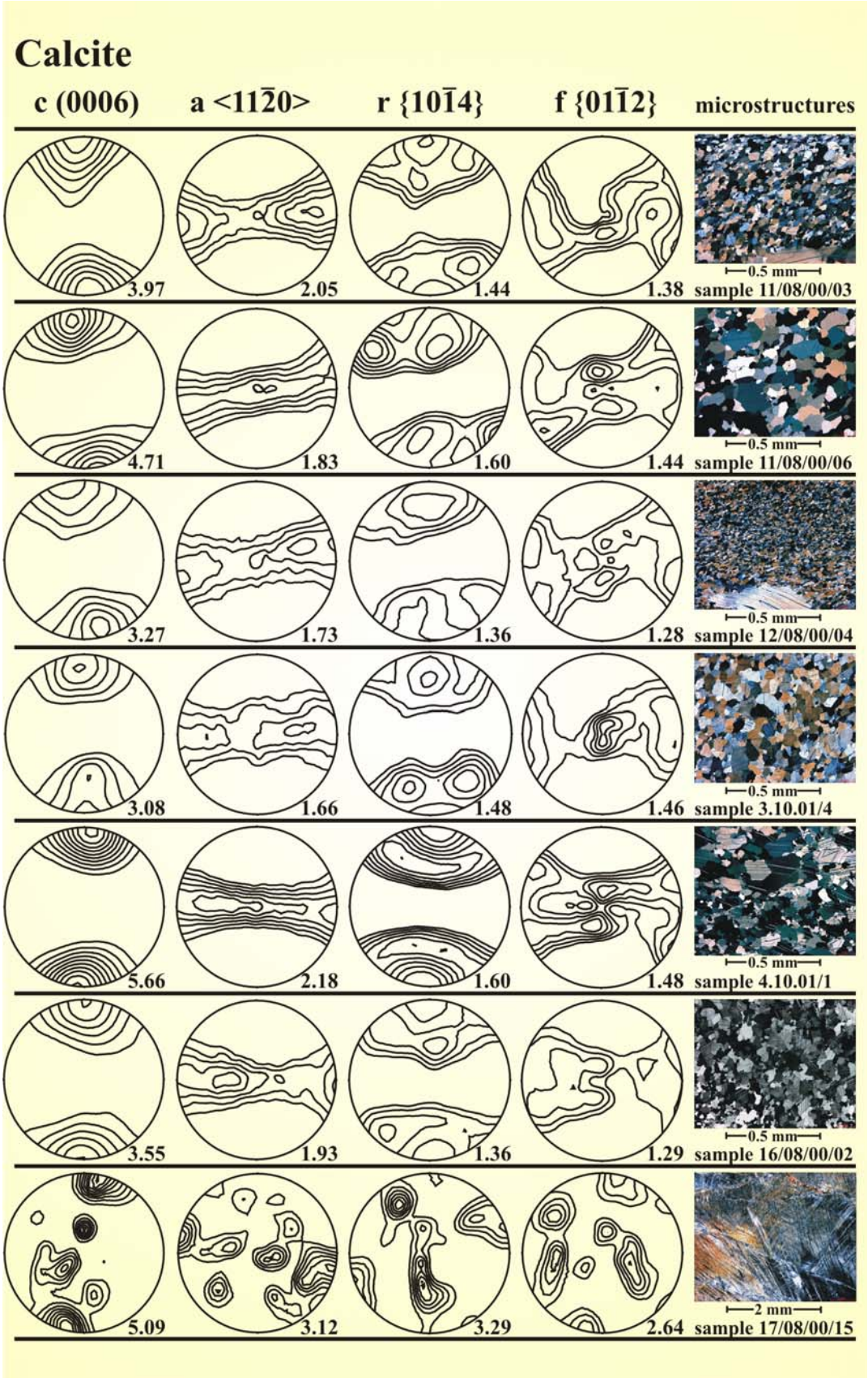
Calcite
c (0006)
a <11$\bar{2}$0>
r {10$\bar{1}$4}
f {01$\bar{1}$2}
microstructures
3.97
2.05
1.44
1.38
0.5 mm
sample 11/08/00/03
4.71
1.83
1.60
1.44
0.5 mm
sample 11/08/00/06
3.27
1.73
1.36
1.28
0.5 mm
sample 12/08/00/04
3.08
1.66
1.48
1.46
0.5 mm
sample 3.10.01/4
5.66
2.18
1.60
1.48
0.5 mm
sample 4.10.01/1
3.55
1.93
1.36
1.29
0.5 mm
sample 16/08/00/02
5.09
3.12
3.29
2.64
2 mm
sample 17/08/00/15

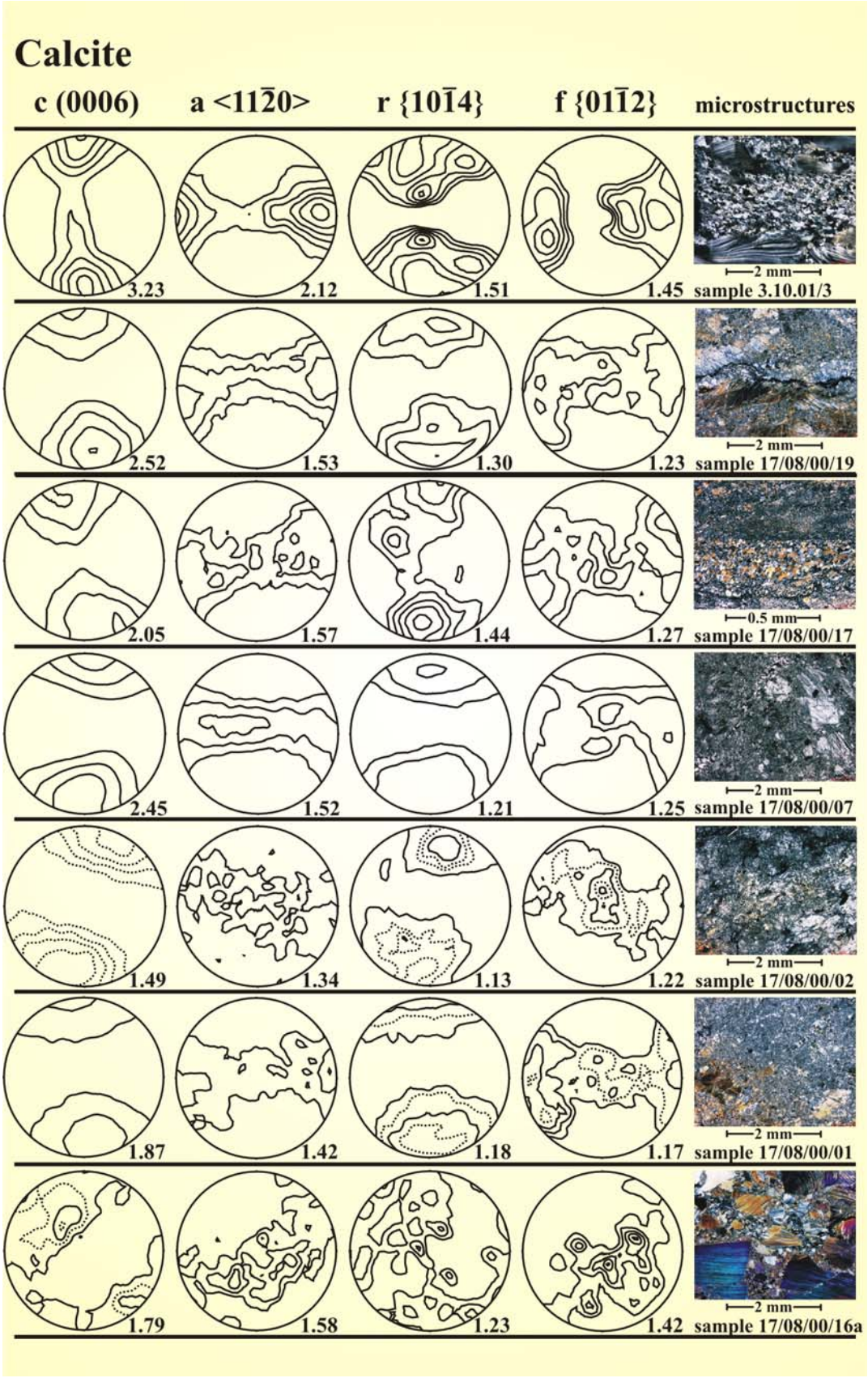
Calcite
c (0006)
a <11$\bar{2}$0>
r {10$\bar{1}$4}
f {01$\bar{1}$2}
microstructures
3.23
2.12
1.51
1.45
2 mm
sample 3.10.01/3
2.52
1.53
1.30
1.23
2 mm
sample 17/08/00/19
2.05
1.57
1.44
1.27
0.5 mm
sample 17/08/00/17
2.45
1.52
1.21
1.25
2 mm
sample 17/08/00/07
1.49
1.34
1.13
1.22
2 mm
sample 17/08/00/02
1.87
1.42
1.18
1.17
2 mm
sample 17/08/00/01
1.79
1.58
1.23
1.42
2 mm
sample 17/08/00/16a

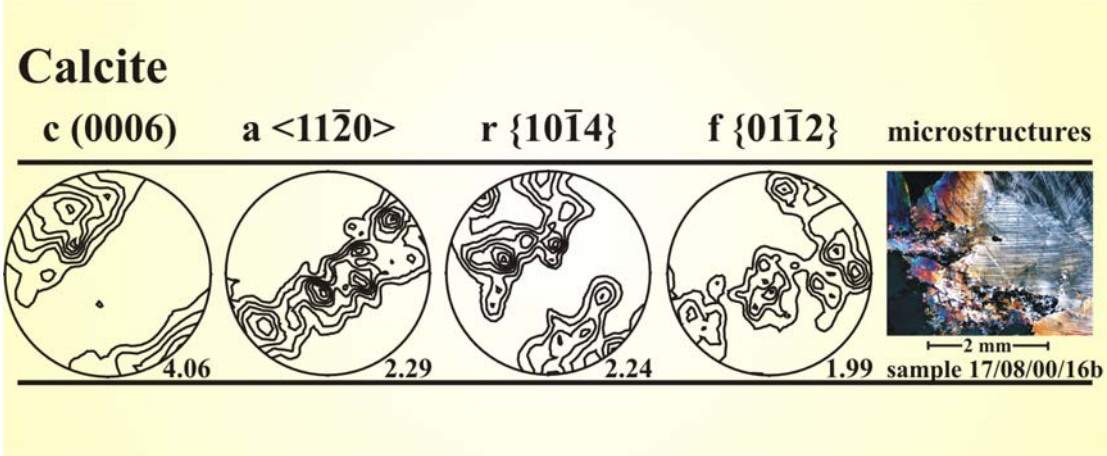

Fig 2.14 *Calcite textures of mylonitically and brittle-ductile deformed graphite-bearing marble. The pole figures of the samples 11/08/00/03 to 16/08/00/02 represent the mylonitic samples, and the samples 17/08/00/15 to 17/08/00/16b represent the brittle-ductile boundary zone. The samples 17/08/00/16a and 17/08/00/16b are from a purely cataclastic domain. Sample 17/08/00/16a represents the matrix and sample 17/08/00/16b represents the texture of a clast.*

macroscopic matrix of a cataclastic breccia zone and the pole figures of sample 17/08/00/16b represent the textures of a macroscopic clast. The microstructures show, that the investigated clast also consists of brecciated domains. However, the general grain size distribution is clearly different between these to samples.

Sample 17/08/00/15 represents the domains of low graphite network intensity, which is characterised by short graphitic stylolites. The macroscopic fabric of this sample is shown in Figure 2.11 d. Samples 3.10.01/3, 17/08/00/19 and 17/08/00/17 show fabrics of intermediate to high to degrees of graphite network intensity. The macroscopic fabrics of the latter are shown in Figure 2.11 k, l. Sample 17/08/00/07 to sample 17/08/00/01 are characterised by the highest degrees of graphite network intensity.

The pole figures of the c-axes of the mylonitic samples show a single maximum normal to the foliation, which shows the tendency for a girdle maximum in some samples (11/08/00/03, 12/08/00/04, 3.10.01/4, 16/08/00/02). The pole figures of the a-axes form a girdle parallel to the lineation. The samples which show a tendency for a c-axes girdle have some distinct maxima within the a-axes girdle, whereas the other samples show a-axes girdles without distinct maxima. The latter therefore underwent a rotation in the a-axes. This is related to compression normal to the foliation, which implies pure shear deformation. The r- and f-plains show distinct maxima and small circle girdle distribution.

The intensities of the textures of the mylonitic samples are generally very high. From the microstructural overview images in Figure 2.14 it is obvious, that the intensity of the textures is directly related to the grain size of the mylonitic samples. Fine-grained

mylonites show less high intensities than coarser-grained mylonites. This effect is also observable in the brittle-ductile deformed samples.

Sample 17/08/00/15 is the least deformed and most coarse-grained sample and it shows the highest intensities of the brittle-ductile deformed marbles. This is statistically also related to the single-crystal orientations of the single coarse grained calcite crystals, as they represent larger volume fractions compared to fine-grained samples. Nevertheless, the accordance of the crystallographic orientation between the single calcite crystals is obvious in the pole figures. Also the girdle alignment of the a-axes maxima is parallel to the mylonitic foliation, which indicates a consistent preferred lattice orientation in these samples. This relationship will have to be discussed later in this chapter.

With increasing degrees of network intensity an obvious decrease in grain size is observable in the microstructures of the brittle-ductile boundary zone. The textures all form single maxima normal to the foliation in the c-axes pole figures. Some of these maxima form girdles like in sample 3.10.01/3 and other maxima are rotated around an axis parallel to the foliation. This may either be related to the heterogeneities in deformation as shown in Figure 2.4 f or to a rotation within or against the sense shear. Due to the heterogenous deformation it is also possible that the foliation is not perfectly parallel to an E-W axis of the pole figure. This is related to the complex deformation it was not in all cases possible to identify the exact foliation during sample preparation.

The textures of the cataclastic samples show, that the lattice preferred orientations are strongly diminished by the cataclastic deformation as obvious from the texture of the cataclastic matrix of sample 17/08/00/16a. In contrast, the texture of the coarse-grained clast of sample 17/08/00/16b again shows very high intensities. The rotation of the single maximum in the c-axes may be related to a rotation of the clast during the event of cataclastic deformation in the breccia zones.

For the c-axes textures of graphite, a strong lattice preferred orientation in the mylonitic samples is obvious (Fig. 2.15). The single maxima normal to the foliation shows that the basal plains of graphite are oriented parallel to the foliation. The highest texture intensities of graphite are rather related to the coarser-grained samples as also observed for the calcite textures. Two mylonitic samples display a slight girdle distribution of the c-axis orientation distribution. In these samples the c-axes and their equivalent basal planes are partially rotated in the direction normal to the foliation.

The samples from the brittle-ductile deformed boundary zone show no real preffered lattice orientations with the exeption of sample 3.10.01/3. This may be related to

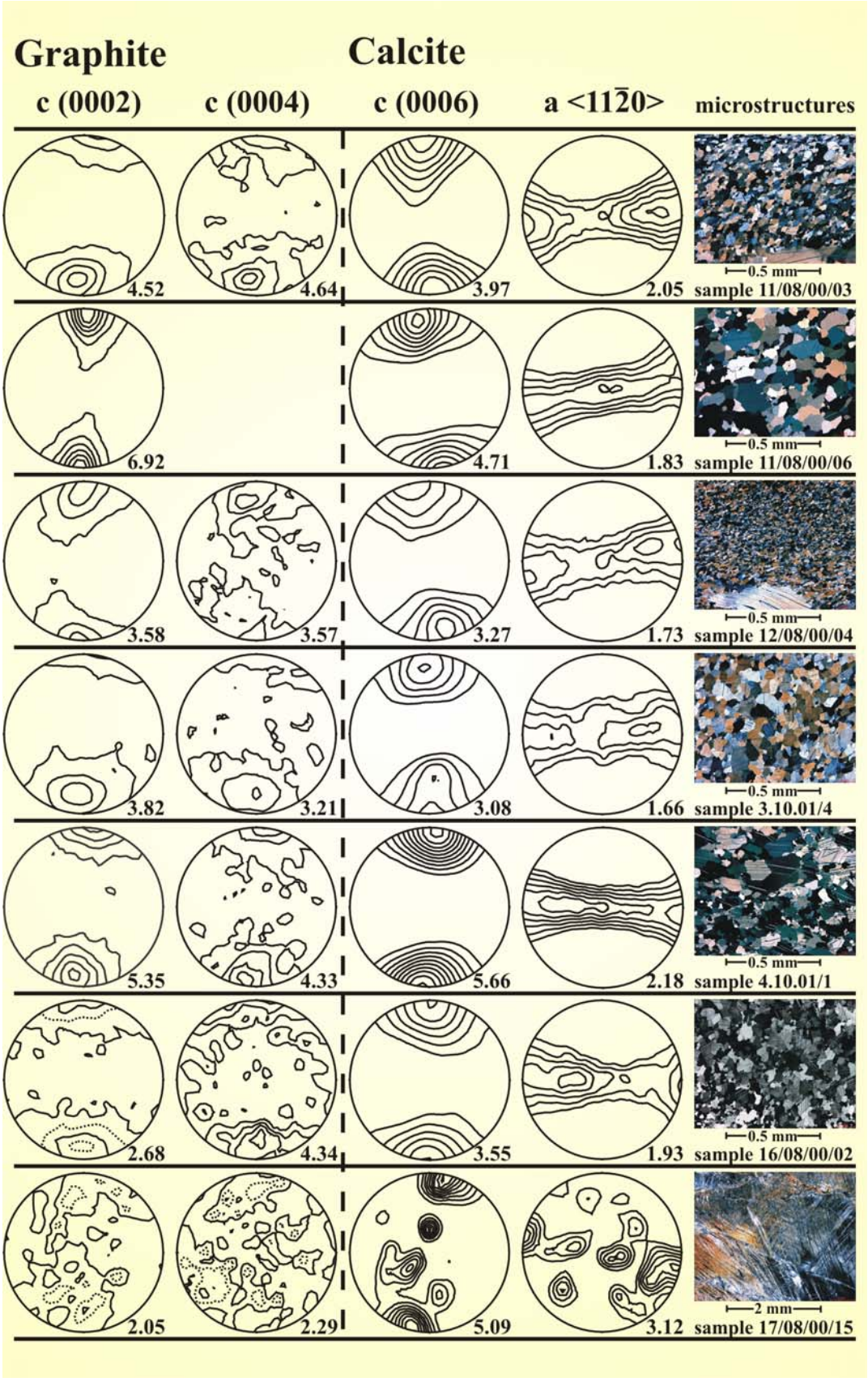
Graphite
Calcite
c (0002)
c (0004)
c (0006)
a <11$\bar{2}$0>
microstructures
4.52
4.64
3.97
2.05
0.5 mm
sample 11/08/00/03
6.92
4.71
1.83
0.5 mm
sample 11/08/00/06
3.58
3.57
3.27
1.73
0.5 mm
sample 12/08/00/04
3.82
3.21
3.08
1.66
0.5 mm
sample 3.10.01/4
5.35
4.33
5.66
2.18
0.5 mm
sample 4.10.01/1
2.68
4.34
3.55
1.93
0.5 mm
sample 16/08/00/02
2.05
2.29
5.09
3.12
2 mm
sample 17/08/00/15

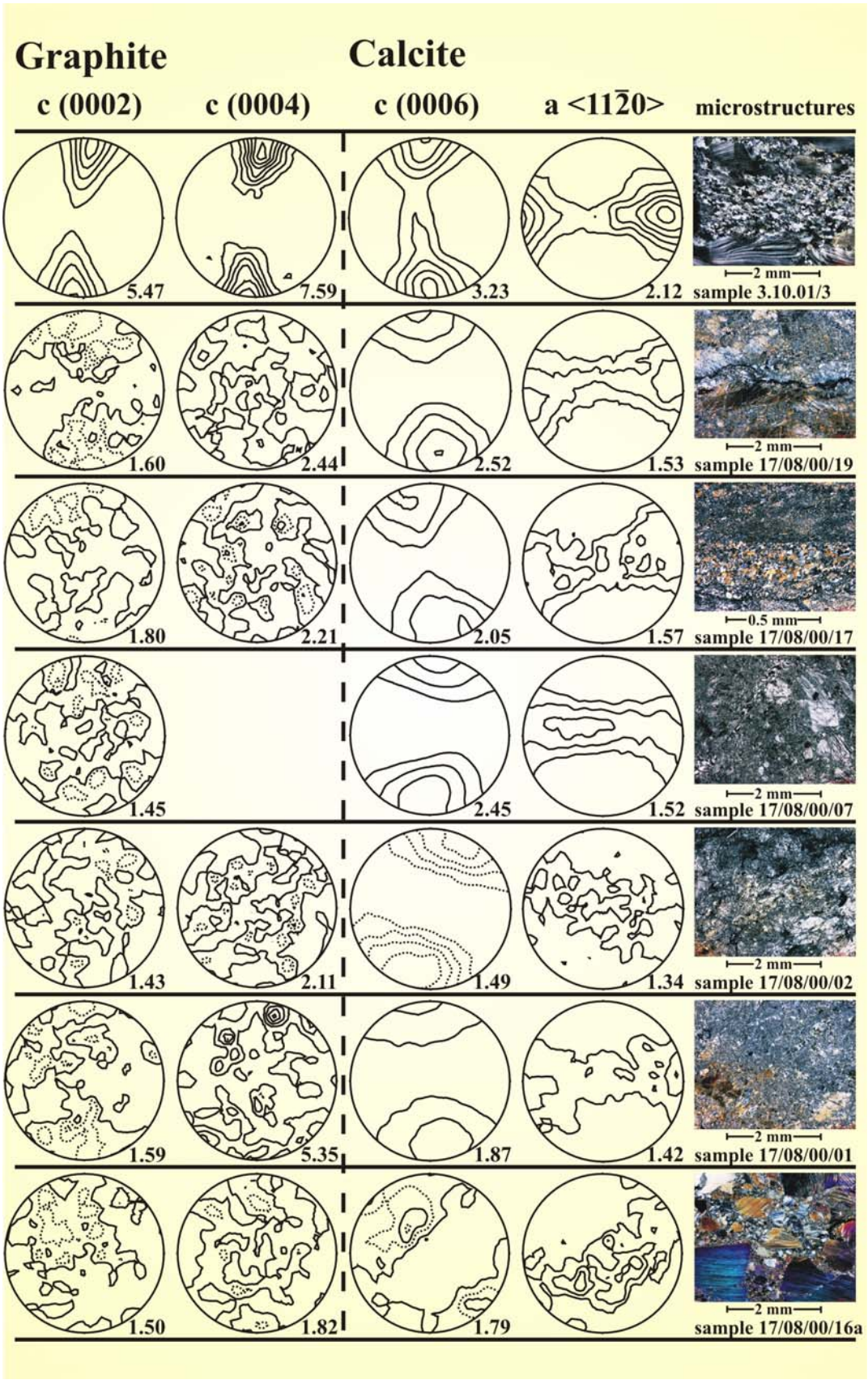
Graphite
Calcite
c (0002)
c (0004)
c (0006)
a <11$\bar{2}$0>
microstructures
5.47
7.59
3.23
2.12
2 mm
sample 3.10.01/3
1.60
2.44
2.52
1.53
2 mm
sample 17/08/00/19
1.80
2.21
2.05
1.57
0.5 mm
sample 17/08/00/17
1.45
2.45
1.52
2 mm
sample 17/08/00/07
1.43
2.11
1.49
1.34
2 mm
sample 17/08/00/02
1.59
5.35
1.87
1.42
2 mm
sample 17/08/00/01
1.50
1.82
1.79
2 mm
sample 17/08/00/16a

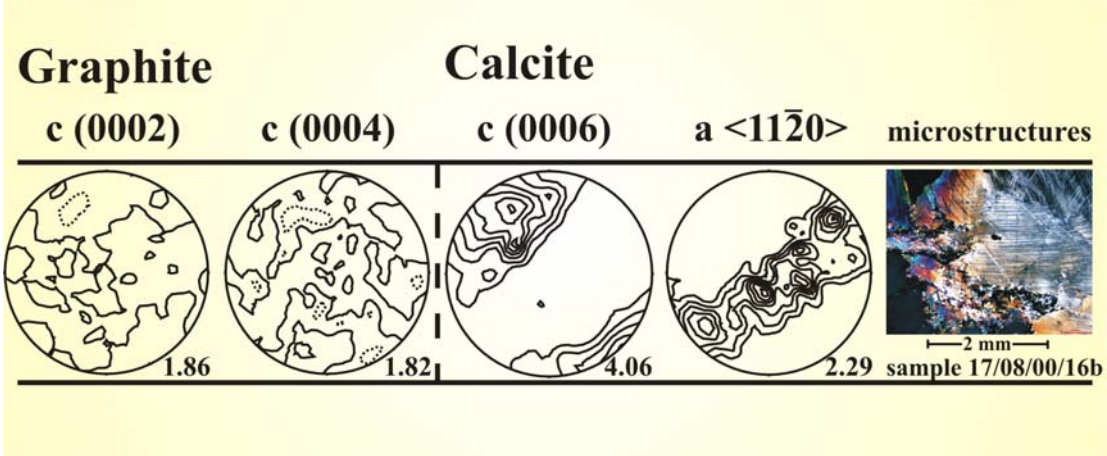

Fig 2.15 *Graphite and Calcite textures of mylonitically and brittle-ductile deformed graphite-bearing marble. The graphite c(0004) pole figures are missing where the peak intensities were to low to extract the pole figures. Sample 17/08/00/16a represents the matrix of a cataclastic breccia zone, whereas sample 17/08/00/16b is derived from a macroscopic clast of the cataclastic breccia zone.*

a strong influence of the cataclastic and pressure solution deformation in these samples. Sample 3.10.01/3 however is characterised by a strong influence of mylonitic deformation and therefore by dynamic recrystallisation. Therefore a strong texture is observable in this sample from the brittle-ductile boundary zone.

From the texture analysis of the investigated samples, it is not possible to evaluate whether the mutual influence between the calcite and graphite textures is existent. In the samples from the brittle-ductile boundary zone this influence is not existent as the graphite textures show no to very weak preferred orientations. In the mylonitic samples and the mylonitically overprinted sample of the brittle-ductile zone a girdle maximum is either existent in both phases or only in one of both phases. Also the texture intensity of both phases is not directly related, although a dependence of the texture intensity of both phases may is also observable in the samples.

2.4.2. TEXTURE ANALYSIS BY ROTATING POLARIZER STAGE

The rotating polarizer stage microscope enables the 2-dimensional measurement of crystallographic orientations in microscopic scales. These are local textures allow qualitative texture measurements on a grain scale within different domains of a sample. With these measurements the degree of homogeneity of the global textures of a sample can be evaluated. For the graphite-bearing marbles these investigations were conducted to verify, whether the texture is different between the coarse-grained and the fine-grained

domains of the matrix. Secondly this method was used to measure the texture of the individual porphyroclasts in the samples of the mylonitic core zones.

2.4.2.1. ANALYTICAL TECHNIQUE

The applicated rotating polarizer stage was designed by Fueten & Goodchild (2001). It is mounted on a standard petrographic transmitted light microscope. Therefore, normal polished thin sections for quartz and ultrathin sections (< 15 μm thickness) for carbonates are suitable for the measurements.

The microscope of the rotating polarizer stage was modified to include two rotating polarisers, which are oriented 90° to each other. The sample position is fixed between the rotating polarisers, which enables the gathering of information for every pixel in a stable position. The rotating polarisors are computer-controlled and at incremental steps a frame is captured by a video device and a frame grabber card. The different frames are then piled to form a composite picture of the thin section. This composite data set image (see upper images in Figures 2.16 and 2.17) contains the information of every pixel for every step. The maximum resolution is 0.9° per step. Therefore, 200 steps are needed for a rotation of the polarisers of 180° at maximum resolution.

For uniaxial minerals like quartz and calcite, the maximum intensity gathered during the rotation is a function of the angle between the light path of the microscope and the c-axis. This information is then used to calculate the trends of the c-axes, either per grain or across a grid for the composite data image as shown in the second image of Figure 2.16 and 2.17. The principles of the rotating polarizer stage are described by Fueten & Goodchild (2001) and Heilbronner (2000).

This data is then extracted and plotted into a pole figure of equal area projection as shown in Figures 2.16 and 2.17. As it is not possible to gain the plunge of the c-axis with this method, the measurements are displayed as 2-dimensional vectors. These are plotted as linears in the equivalent pole figure. One half of a pole figure is sufficient to cover the whole range of directional data. In the pole figures of the data from the rotating polarizer stage a circular array of about 5 to 10° is visible, where no data is plotted. This is due to normalisation problems. Likewise a tendency of distortion of the data along small circles is observable in the data.

The software of the rotating polarizer stage also enables the plot of an ‘Achsenverteilungsanalyse (AVA)’, which is shown in the third image of Figures 2.16 and 2.17. In these plots, the direction of every pixel is coloured according to a predefined

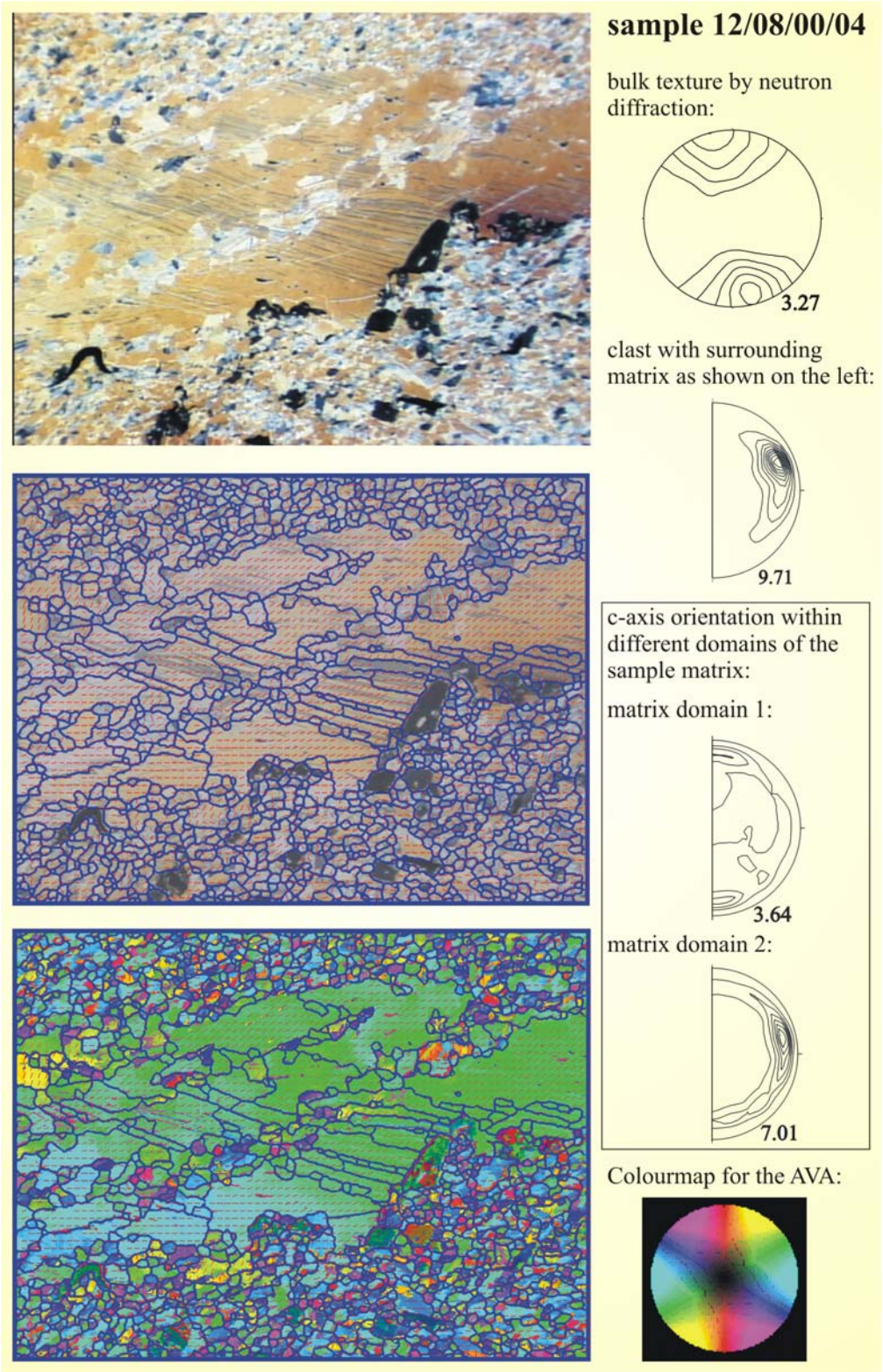

Fig 2.16 *Rotating polarizer stage data shows the heterogeneities in c-axes orientation of this mylonitic sample within the matrix and the porphyroclasts.*

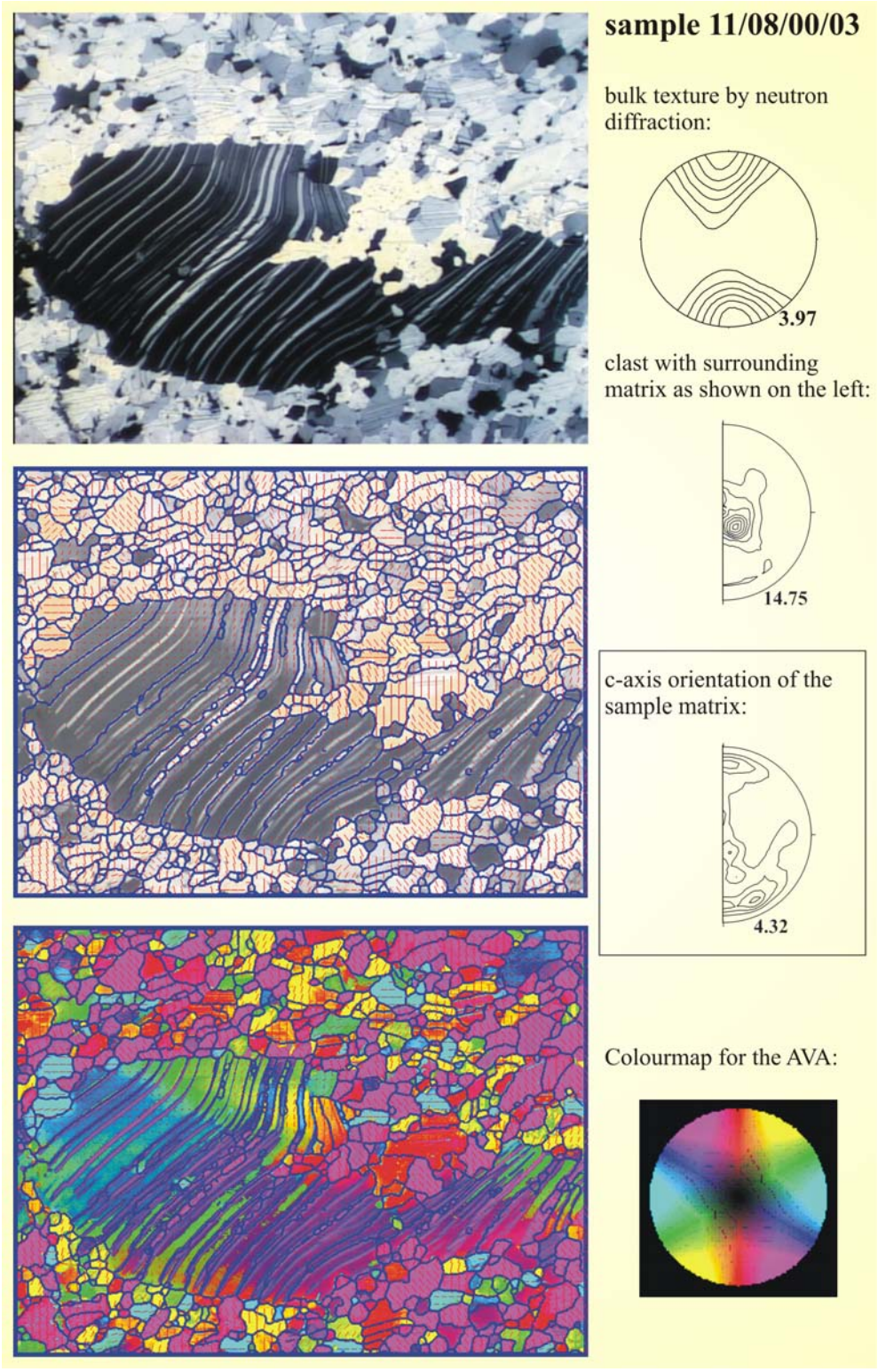

Fig 2.17 *Rotating polarizer stage data showing a homogeneous texture for the mylonitic matrix of this sample. The porphyroclasts show heterogeneities due to the the development of twins, deformation bands, subgrain rotation crystallisation and crystallisation to new grains.*

colour map of orientations (Fig. 2.16, 2.17). This data can be statistically processed and gives an approach on the orientation distribution of the c-axes.

2.4.2.2. SAMPLES AND MEASUREMENTS

Complementary to the bulk textures shown above, two samples are investigated to evaluate the differences in the local textures that may occur between different domains within the mylonitic core zones. As shown in Figure 2.16 the bulk texture for this sample obtained by neutron diffraction shows one single maximum normal to the foliation. However, the investigations by the rotating polarizer stage revealed, that the c-axes orientation shows heterogeneities within the matrix and between coarse-grained domains and the fine-grained matrix.

As shown in Fig. 2.16 the matrix of domain 1 shows maxima, which coincide with the textures of the neutron diffraction data. The matrix of domain 2 however, shows a maximum nearly perpendicular to the maxima of domain 1. For this domain the preferred orientation of the c-axes is parallel to the foliation. Other heterogeneities within the textures of the mylonitic samples are produced by porphyroclasts as shown in the images of Figure 2.16 and 2.17.

The c-axes pole figures of the porphyroclasts and their surrounding matrix show, that there is a distinct deviation to the bulk neutron diffraction textures (Fig 2.16 and 2.17). In Figure 2.16 the texture of the porphyroclast is similar to the texture in the matrix domain 2, whereas they differ completely in Figure 2.17. The AVA shows the existence of pronounced heterogeneities of the texture within a porphyroclast. These result from twinning, subgrain rotation recrystallisation, recrystallisation along twins and the development of partially bent deformation bands (Fig 2.16 and 2.17).

In contrast to the sample in Figure 2.16 the sample of Figure 2.17 shows a uniform texture in the matrix which is similar to the bulk textures measured by neutron diffraction. Even the recrystallised domains of the porphyroclast show textures corresponding to the bulk textures. As described above, the only texture heterogeneities of this sample are resulting from different orientations of c-axes of the porphyroclasts.

2.5. DISCUSSION

From the structural and textural analysis of the investigated samples it is obvious, that in general three different fabric types of graphite-bearing marbles can be distinguished. These occur within crustal dome structures of the northern Central Zone of the Damara Belt. After the formation of the structural domes by the refolding of crustal

scale isoclinal folds, another type of dome structures formed by the intrusion of mainly granitic melts. Subsequently a widespread regional phase of static recrystallisation occurred. During this phase of recrystallisation, a blastic fabric developed during the abnormal grain-coarsening of large domains of the calcite-marble.

As shown above, the peak metamorphism and the intrusion of the granitic magma coincide quite well in the geochronological data. The postulated regional peak metamorphism of upper amphibolite facies to granulite facies cannot be obtained from the investigated samples, as muscovite is the only mineral sensitive to metamorphic changes. Muscovite only occurs in the investigated samples as accessory mineral and is still stable in the marble, allthough it should not be stable in the described metamorphic conditions. This is related due to the absence of quartz in the marble host rock, which is needed for the dissociation reaction of muscovite.

In retrograde metamorphic conditions, this grain-coarsened marble was then deformed along the reactivated rims of the dome structures. Within the distinct shear zones purely ductile deformation occurred in the mylonitic core zones and brittle-ductile deformation occurred in the boundary zones of the shear zones.

Figure 2.18 shows a summarised overview of the different macroscopic and microscopic fabrics observed in the shear zones. It follows the macroscopic setup of the shear zones, showing the different macroscopic fabrics and the equivalent microfabrics. The fabrics of the brittle-ductile boundary zone vary lateral and normal to the mylonitic core zone in a complex pattern of the fabrics shown in Figure 2.18.

Therefore, the brittle-ductile boundary zones show a complex and heterogeneous setup within the shear zones. It is obvious that the different microstructures described above occur in every deformational domain of the brittle-ductile boundary zone. The only significant difference in microstructures between the different deformational domains of this zone is the grain size of the calcite crystals. The above described complex microstructural pattern comprises of brittle and crystal plastic deformational mechanisms. The observed brittle deformational mechanisms are kinking and crystal fracturing, whereas crystal-plastic deformational mechanisms caused polygonisation, the development of deformation bands, subgrain rotation recrystallisation, and ultra fine-grained dynamic recrystallisation.

It is obvious from the macroscopic and microscopic deformational fabrics that a multiple progression of deformation and recovery has occurred in the investigated shear zones. In the brittle-ductile boundary zone brittle deformation and pressure solution prevail

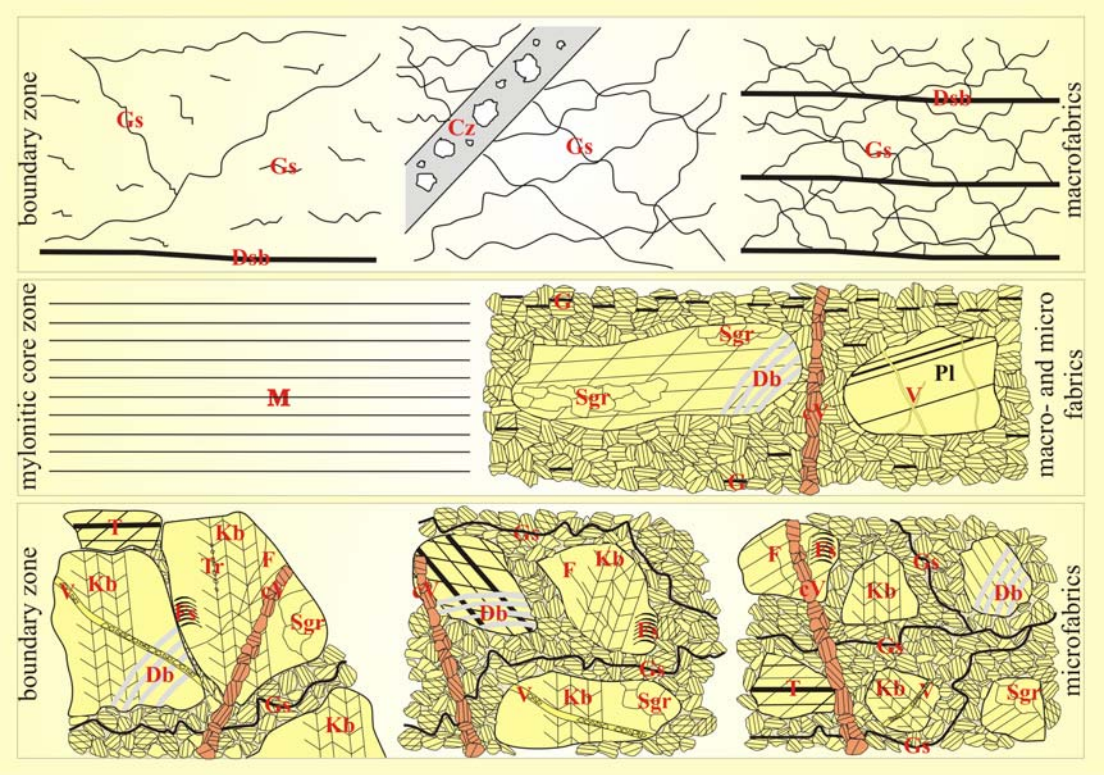

Fig. 2.18 *Fabrics and microfabrics of the investigated shear zones. In the center is the mylonitic core zone, with graphite on the foliation plains. The upper part shows the fabrics of the brittle-ductile domain and in the lower parts the microfabrics of this domains are shown: cV = cretaceous vein; Cz = cataclastic zone; Db = deformation bands; Dsb = ductile shear band; F = fracture; Fs = flexural slip with thickend calcite twins; G = graphite with basal plane parallel to the foliation; Gs = graphite stylolite in fine grained matrix; Kb = kink bands; M = mylonite; Sgr = sub grain rotation; T = twins; Tr = finegrained recrystallisation of twins; V = veins.*

in different intensities. This is observable in the described macroscopic fabrics. These fabrics themselves are overprinted either by cataclastic breccia zones or by mylonitic deformation. This is observable in several cycles of mutual overprinting. In the microstructures brittle and ductile deformational fabrics are preserved next to ultra fine-grained static recrystallisation of the calcite matrix.

Pressure solution is restricted to the shear zone as stylolites are not observed in the undeformed and abnormally grain-coarsened host rock. Therefore, pressure solution was enabled by the deformation of the calcite-marble along the rims of the dome structures. Pressure solution and the resulting formation of graphitic stylolites, is mutually overprinted by the brittle-ductile deformation. The graphitic stylolites are cut by cataclastic breccia zones as shown in Figure 2.18.

Additionally the stylolites oriented parallel and subparallel to the foliation of the mylonitic core zone, develop into ductile shear bands, which themselves partly become overprinted by pressure solution again. These observations imply, that the different domains within the boundary zones do not show a successive deformation but are only related to differences in strain and strain rate within the shear zones. These occur all in the same timeframe of mutual overprinting of brittle, ductile and pressure solution deformation.

The mutual overprinting of brittle, ductile and pressure solution deformation in different domains of the brittle-ductile boundary zones, may be explained by seismic-aseismic deformation within these shear zones. During seismic events, brittle deformation with high strain rates prevailed, where cataclastic breccia zones and brittle deformation fabrics developed in different deformational domains. These are distinguished by differences in deformation intensity. During aseismic deformation ductile deformation has been dominant, which is documented in the mylonitic core zones.

These mylonitic core zones have not been overprinted by the brittle deformation of the brittle-ductile boundary zones. Nevertheless, the ductile deformation in the brittle-ductile boundary zones is clearly related to the deformation in the mylonitic core zones. This is documented by the graphitic stylolites, which have been overprinted by ductile deformation parallel to the foliation of the mylonitic core zone. Therefore, the deformation structures of the brittle-ductile boundary zone are related to brittle seismic deformation and aseismic creep deformation, which mainly has occurred in the mylonitic core zones.

The quantitative calcite-graphite ratios imply that pressure solution has occurred for calcite and graphite. This may only be considered as a first assumption, as the amount of investigated samples, does not give a secure statistical basis for a safe interpretation of the data. Therefore, more investigations in that direction are necessary to confirm this assumption. Nevertheless, thermodynamic conditions for the solution of graphite as described by Holloway (1984) and Luque et al. (1998) may have been existent during the deformation.

These first investigations of the quantitative calcite-graphite ratios showed, that it is not possible to quantify the content of graphite and thus the graphite network intensity by macroscopic optical measurements. The obtained data revealed that the fine-grained to ultra fine-grained domains also occur in dark colours, which are in parts not differentiable anymore from purely graphitic stylolite seams. Also inside the graphitic stylolites ultra fine-grained graphite is present, which is not detectable by macroscopic optical measurements.

The calcite textures prevailing in the mylonitic core zones as well as in the brittle-ductile boundary zones, are of the most common calcite texture type which is characterised by a single maximum normal to the foliation. The textures imply pure shear deformation during ductile deformation. The texture intensities are generally very high and decrease commonly with decreasing grain sizes. This observation applies for the brittle and ductile deformed marble. The host rock for this deformed marble is the abnormally grain-coarsened and blastic graphite-bearing marble described above as type 1. The texture of this marble may only be evaluated in the field, as it is to coarse-grained to measure a statistically relevant texture from the samples.

The grain sizes of the graphite-bearing marbles are continuously reduced by brittle and ductile deformation. This is obvious from the microstructural analysis. In the brittle-ductile boundary zone the texture intensity may be decreased by the reorientation of the grains during cataclastic deformation. This is most drastically observable in the samples 17/08/00/16a, which is the matrix of a cataclastic breccia zone, whereas a clast of several cm in size (sample 17/08/00/16b) still shows high calcite texture intensities (Fig. 2.14, 2.15).

As texture intensities are normally increased during dynamic recrystallisation in ductile deformed material, this implies that the host rock must have preserved strong texture intensities during the period of abnormal grain-coarsening and static recrystallisation. In this case the texture of the grain-coarsened host rock must be related to the prior formation of the dome structures and/or to the widespread intrusion of the granitic melts. From this data it is obvious that the conserved textures are similar to equal to the textures measured in the mylonitic core zones. This may imply that the pre-existing stress field was similar to the retrograde stress field, which led to the reactivation of the rims of the dome structures and thus the formation of the shear zones.

The investigation of the local textures showed that some mylonitic core zones partially show different texture domains. Whether this is related to the different generations of textures, or to differences within the ductile deformation in the shear zones is not clear and needs further investigation. The porphyroclasts often show a different crystallographic orientation than the local textures of the matrix or the overall global textures. This may be the reason for the extensive recrystallisation and subgrain rotation recrystallisation.

From the microstructures it is hard to evaluate the metamorphic temperatures of this deformation. As shown from the microstructures of the brittle-ductile deformed marble, crystal plastic and brittle deformational structures are mutually overprinted. They range from the development of kink bands to fine-grained dynamic recrystallisation along twins

often within one sample of the investigated shear zones. In the cataclastically deformed domains, the ultra fine-grained calcite breccia is only slightly recrystallised along the grain boundaries. As the development of all the observed microstructures are depending on the temperature as well as on the applied strain rate, an estimation of the temperature becomes very difficult (De Bresser & Spiers, 1997).

Some authors postulate temperature estimates from the thickness of the calcite twins (Burkhard, 1993; Passchier & Trouw, 1998). As the development of calcite twins is also strongly dependent on the strain rate (De Bresser & Spiers, 1997), this estimate may only be true at constant strain rates under varying metamorphic temperatures. In the investigated samples however, the multitude of different deformational microstructures imply a complex sequence of deformational mechanisms and different strain rates.

The granulite facies is not directly documented by HP/HT mineral assemblages. However, the regional metamorphic isograds and the intrusion of granitic melts imply these metamorphic grades as described above. Missing fluid inclusions and no differences in cathodoluminescence colours show, that granulite facies conditions may have prevailed during peak metamorphism. This metamorphic event is also connected to a period without strain in this part of the lower crust, because the abnormaly grain-coarsened calcite crystals have been statically recrystallised on a regional scale.

The described twins in host rock are partially recrystallised in the orientation of the host crystal by crystal diffusion annealing. These twins could be either related to the seismic events and have been recrystallised while aseismic creep deformation continued, or have developed due to some post-Damara events, like the cretaceous break-up of Gondwana between Africa and South America.

As compiled by Soula et al. (2001), several models for the formation of dome structures are proposed in the literature. The mode of formation of the dome structures, which host the investigated shear zones is not clear. If their formation had been related to a crustal shear zone, as some of the models imply, this would give some implication about the source of the seismic events. Ritter et al. (2003) and Weckmann et al. (2003) postulated the anomalies of electrical conductivity, to occur at distinct crustal shear zones like the Omaruru Lineament (OmL) and the Autseib Fault further north (see Fig. 4.2).

From the satellite image in Figure 2.2 however, it is observable that there is no distinct shear zone developed which could be a crustal structural lineament of the Damara Orogen. This is also confirmed by own field investigations, which show that the investigated shear zones are only a regional set of (conjugated) shear zones along the rims

of the dome structures. Therefore, the investigated shear zones do not correspond to one single deep crustal shear zone. They rather represent a regional set of shear zones, which are controlled by the crustal dome structures.

Since the dome structures are built up by Damara sediments of the Arandis and Karibib Formation, they have to be allocated to the nCZ according to the definition of the OmL by Miller (1983). Therefore, these shear zones may not be correlated with the OmL, as the OmL is defined to separate the basement level dome structures of the sCZ from the higher stratigraphic levels of the nCZ. The basement level dome structures of the sCZ occur south of the area of the magnetotelluric profile measured by Ritter et al. (2003) and Weckmann et al. (2003). This implies, that the OmL has to be postulated south of the investigated area.

Due to these uncertainties, the source of the seismic events is still a matter of further research and investigation of the structural setting of the various structural domes. Furthermore, the relationship to the Autseib Fault, which is postulated north of the investigated area and the Omaruru Lineament will have to be investigated in more detail, regarding the source of the seismic events in the late Damaran stage of Orogeny.

CHAPTER 3

GRAPHITE CRYSTALLINITY MEASUREMENTS

To obtain implications on the formation of different graphite fabrics, crystallinity measurements of graphite have been conducted. The crystallinity of graphite is either measured by High Resolution Transmission Electron Microscopy (HRTEM), X-ray Diffractometry (XRD) or by Raman spectroscopy. For this work, the determination of graphite crystallinities were focussed on Raman spectroscopy, as the calculation of the graphite crystallinities from the Raman spectra has been generally calibrated with HRTEM and XRD data (Tuinstra & Koenig, 1970; Beny-Bassez & Rouzaud, 1985; Wopenka & Pasteris, 1993). The aim of this work is to investigate the graphite crystallinities of the whole range of microstructural types of graphite-bearing marbles.

3.1. ANALYTICAL TECHNIQUES

Raman spectroscopy is based on the Raman Effect, which originates from the scattering of electromagnetic radiation by the electron sheaths of the investigated molecules. The Raman Effect is virtually independent of the wavelength of the radiation beam. Therefore, a monochromatic laser beam is used for Raman spectroscopy. Approximately 99.99 % of the laser beam radiates through the sample, while a small part is scattered elastically by the molecules (Rayleigh scattering). An even smaller part (about 10^{-6} %) is scattered inelastically, which is referred to as the Raman scattering. This Raman radiation is emitted either in longer (Stokes radiation) or in shorter wavelengths (Anti-stokes radiation) than the original wavelength of the laser beam. This difference in frequency is expressed by wave numbers relative to the original frequency of the laser beam. The original frequency is therefore calibrated to zero. This Raman shift is specifically characteristic for different molecules.

The Raman shift for carbonaceous material (CM) is divided into first and second order regions after Tuinstra & Koenig (1970). The measured first-order region is shown in Figure 3.1. The first-order region lies in the range of 1100 to 1800 wave numbers (Δ cm^{-1}), and the main graphite band - the G band - is at ~1582 Δ cm^{-1}. This band is inherent in graphite lattices. For more poorly crystalline graphite additional bands are recognisable at ~1150 Δ cm^{-1}, at ~1355 Δ cm^{-1}, at ~1500 Δ cm^{-1} and at ~1622 Δ cm^{-1}. The band at ~1355 Δ cm^{-1} is referred to as the main defect band (D1-band) (Fig.3.1). This band occurs when defects are present in the carbon aromatic structure (Beny-Bassez & Rouzaud, 1985). It is also sensitive to graphite intercalations (Dresselhaus & Dresselhaus, 1982). The 1150 Δ

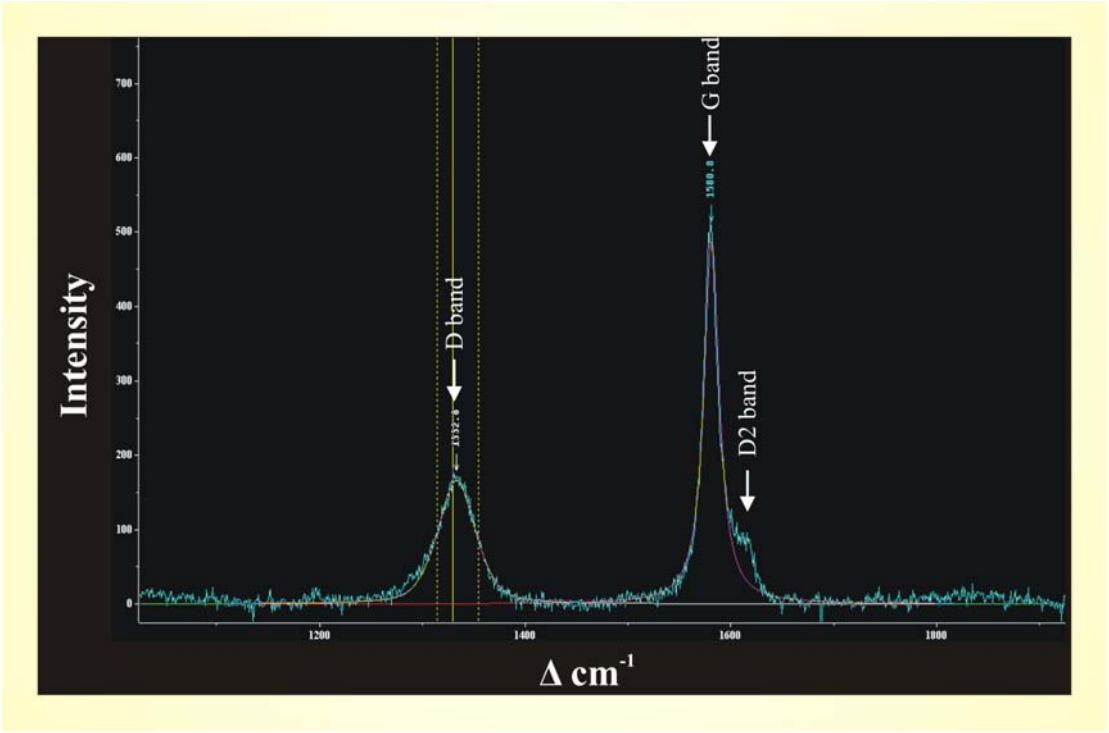

Fig. 3.1 *First-order Raman spectrum measured from sample 17/08/00/20. It shows the Raman graphite band (G band), the first deffect band (D band) and the shoulder peak on the G band. The D band and the shoulder peak are absent in highly crystallised graphite.*

cm^{-1} band appears only in very poorly organised CM (Beyssac et al., 2002). Also the band at 1500 Δ cm^{-1} (D3 band) is attributed to defects outside the plane of aromatic layers like tetrahedral carbons (Beny-Bassez & Rouzaud, 1985). It occurs as a wide band in poorly crystallised CM (Beyssac et al., 2002). The D2 band at ~1622 Δ cm^{-1} appears as a shoulder peak of the G band and is also absent in highly crystalline graphite (Fig. 3.1).

The second order region from 2200 to 3400 Δ cm^{-1} includes several bands at ~2400 Δ cm^{-1}, at ~2700 Δ cm^{-1}, at ~2900 Δ cm^{-1} and at ~3300 Δ cm^{-1}, depending on the degree of graphite crystallinity. The S1 band at ~2700 Δ cm^{-1} splits up into two bands at high crystallinities. It is therefore the most important indicator band for graphite crystallinities in the second order region.

In general, Raman spectra for well crystallised graphite include the existence of D1 and D2 bands in the first order region (Wopenka & Pasteris, 1993). To estimate the degree of graphite crystallinity, it is important to reveal some information about the variation of the G band position, about the full widths at half maximum of the G and D1 bands and about the intensity ratios between D1 and G. This intensity ratio can be used to quantify the crystallinity of graphite according to the linear relationship between the D1/G intensity

ratio and $10^3/L_a$. L_a quantifies after Tuinstra & Koenig (1970), the crystallinity of graphite. It quantifies the mean basal plane diameter of graphite parallel to (001) and is expressed in Å.

The Raman spectroscopic measurements were conducted at the laboratory of the Institut für Mineralogie at the Museum für Naturkunde, Humboldt-Universität Berlin. A Dilor LabRam spectrograph was used equipped with a Jobin Yvon detector and a notch filter to avoid the Rayleigh scattering. This Raman spectograph is equipped with an optical microscope with a 50x objective to focus the laser with an exciting line of 632.8 nm. The grating of 1800 grooves/mm produces an according spectral resolution of about 2.5 Δ cm^{-1}. The confocal pinhole in front of the entrance slit of 100 µm is 1000 µm in diameter. The final laser power is about 20 to 50 mW. Acqusition time for the spectra was generally 5 s.

The measurements, background subtraction peak fits and calculations of the full widths at half maximum were conducted with Labspec V. 2.08 from Dilor. For peak fitting a Gauss-Lorentz function was used for all the samples. The fitted data represent the graphite crystallinities.

3.2. SAMPLES MEASURED

The samples for the crystallinity measurements were selected to cover all microstructurally distinguished types of graphite-bearing marbles from all the main sampling localities shown in Figure 2.1. The sample measurements plotted in Figure 3.2 are distinguished by plot numbers. Plot numbers 1 to 10 represent the type 2 brittle-ductile deformed graphite-bearing marbles with graphitic stylolites and network structures of varying intensity, thickness and orientation to the deformational framework. Samples 11 and 12 are type 3 mylonitic graphite-bearing marbles and samples 13 and 14 are type 1 coarse-grained marble host rock.

The graphite crystallinities were measured on graphite isolated from the marble host-rock as well as on graphite within the marble host-rock. This allows a control whether the processes of graphite isolation has changed the degree of graphite crystallinity. Measuring isolated graphite gives better statistics on the graphite crystallinities within a sample. As the Raman Effect varies with the crystallographic orientation, the measurements were conducted perpendicular to the basal plains of the graphite crystals where possible. This was especially difficult for the ultrafine-grained graphite of the brittle-ductile deformed boundary zone, which has been classified as type 2 of the graphite-bearing marble.

3.3. RESULTS AND QUANTIFICATION

The measurements in general revealed, that next to the inherent G band, only two of the above mentioned defect bands are recognisable in the measured samples. These are the D1 band at ~1355 Δ cm^{-1} and the D2 shoulder band at ~1622 Δ cm^{-1} in the first order region. Figure 3.2 shows the evaluated results of the Raman measurements on the described samples. The plots are distinguished between the measurements of the isolated graphite and of the graphite within the marble host-rock of the same samples. The density variation in the plots represent the statistical means and variations for every sample. The second order region has not been measured due to the setup of the Raman spectroscope.

The measured data shows in general, that the graphite crystallinities of all microstructural types are in the range of well-ordered graphite. In the following, a detailed description of the graphite crystallinities will be presented for the different methods of evaluating graphite crystallinities from Raman spectra.

A first approximation about the degree of graphite crystallinity is the G band position and accordingly also the variation of this G band position within a sample (Beny-Bassez & Rouzaud, 1985; Beyssac et al., 2002). For highly crystalline graphite the G band position should be at ~1582 Δ cm^{-1} with a variation of about 20 Δ cm^{-1}. Both authors state, that a decrease in wave numbers for the G band position occurs for mean wave numbers from ~1590 Δ cm^{-1} to ~1582 Δ cm^{-1} with increasing crystallinities. The G band position of poorly-ordered graphite varies about 50 Δ cm^{-1} (Beyssac et al., 2002).

The G band positions of all measured samples are plotted into Figure 3.2 a. With the exception of sample 5, this plot shows that the mean position of the G band is constant at 1578 Δ cm^{-1} with a standard deviation of 5.5 Δ cm^{-1} for all samples. The variation within the samples is about 20 Δ cm^{-1} with the exception of sample 7, which shows a variation in G band position of 27 Δ cm^{-1}. Graphite crystallinities of sample 14 are very high as no defect bands are recognisable for this sample across all measurements. The variation within the G band position is only 1 Δ cm^{-1} and the mean position is at 1580 Δ cm^{-1}.

A second indicative parameter for the degree of graphite crystallinity is the full width at half maximum (FWHM) of the G band. Similarly to the G band position a decrease in the FWHM from about 60 to 120 Δ cm^{-1} to about 22 Δ cm^{-1} is observable with increasing graphite crystallinities. Also the variability in the FWHM of the G band is representative for the crystallinity of graphite. For poorly ordered CM this variation may be up to 70 Δ cm^{-1}, whereas highly ordered graphite shows a variation of about 5 to 10 Δ cm^{-1} (Beny-Bassez & Rouzaud, 1985; Wopenka & Pasteris, 1993; Beyssac et al., 2002).

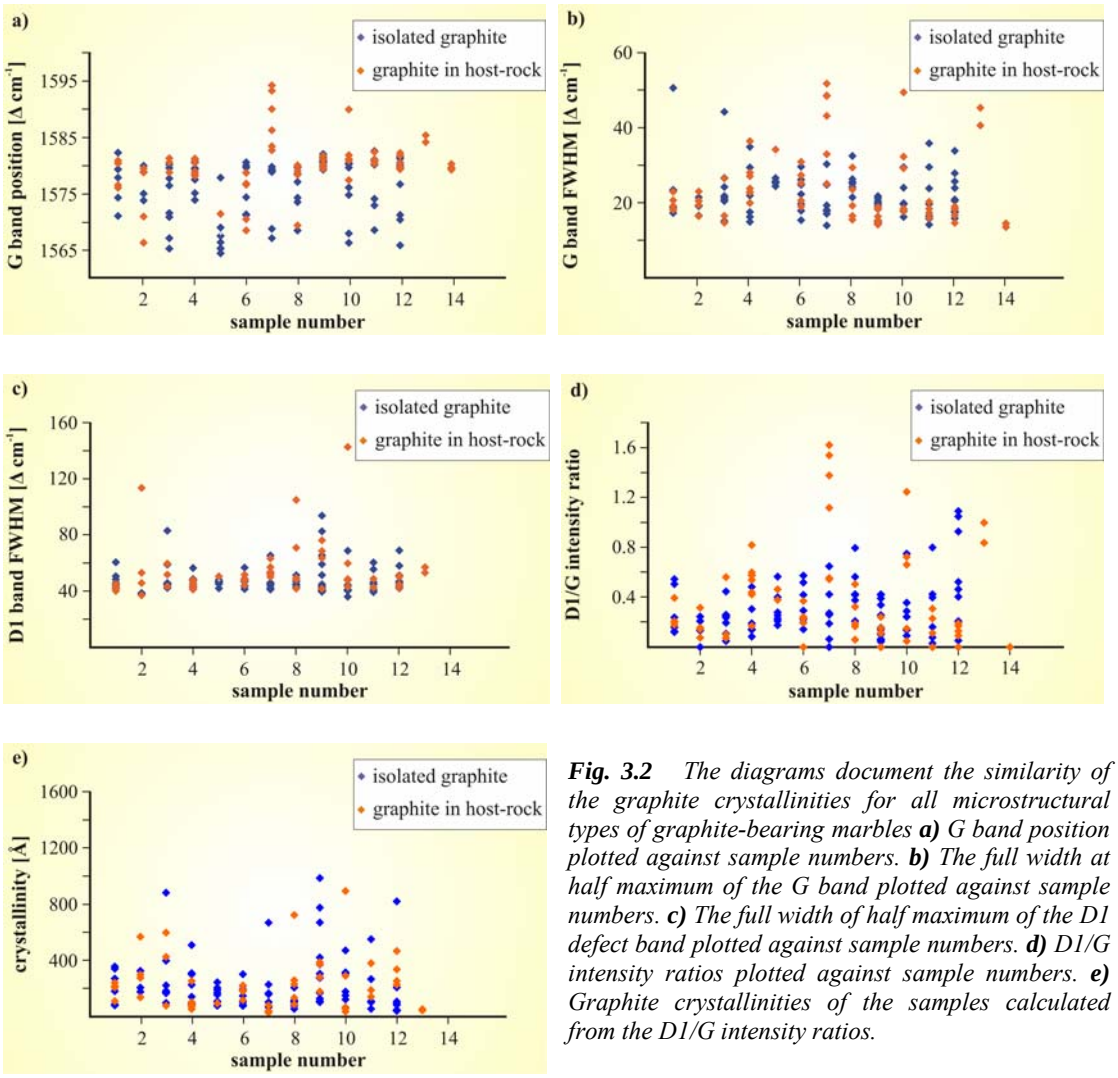

Fig. 3.2 *The diagrams document the similarity of the graphite crystallinities for all microstructural types of graphite-bearing marbles* ***a)*** *G band position plotted against sample numbers.* ***b)*** *The full width at half maximum of the G band plotted against sample numbers.* ***c)*** *The full width of half maximum of the D1 defect band plotted against sample numbers.* ***d)*** *D1/G intensity ratios plotted against sample numbers.* ***e)*** *Graphite crystallinities of the samples calculated from the D1/G intensity ratios.*

Figure 3.2 b shows the plot of the full width at half maximum of the G band for the measured samples. The mean FWHM is at 22 Δ cm^{-1} with a standard deviation of 8 Δ cm^{-1}. In general, the samples show a variation of 10 to 20 Δ cm^{-1}, while sample 7 again shows the highest variation of the FWHM of 30 Δ cm^{-1}. Sample 14 with the highest crystallinities has the lowest mean full width of half maximum of 14 Δ cm^{-1} and a variation of only 1 Δ cm^{-1}.

Thirdly, the full width at half maximum of the D1 band gives a good indication for the degree of graphite crystallinities. After Beny-Bassez & Rouzaud (1985) a decrease from 260 Δ cm^{-1} to about 50 Δ cm^{-1} is observable with increasing graphite crystallinities from poorly to well ordered graphite. Accordingly, the variation of the FWHM for the D1 band has to be considered evaluating the graphite crystallinities. After Beny-Bassez &

Rouzaud (1985) and Wopenka & Pasteris (1993) this variation is from about 120 Δ cm^{-1} for poorly ordered CM to about 25 Δ cm^{-1} for well ordered graphite.

The full width of the half maximum for the D1 band of the measured samples is plotted in Figure 3.2 c. The mean FWHM is nearly constant over all samples with 48 Δ cm^{-1} and a standard deviation of 14 Δ cm^{-1}. The biggest variation of the FWHM is shown by sample 10 with 108 Δ cm^{-1}, whereas the other samples display a variation of 20 to 40 Δ cm^{-1}. As graphite with high crystallinities does not show the existence of the D1 band, these samples cannot be presented in this plot. Therefore, sample 14 does not show any data plot in Figure 3.2 c.

Graphite crystallinities are also characterised by the intensity ratio of the D1 band and the G band. This varies as much as one order of magnitude between the lowest and highest degrees of graphite crystallinity. After Wopenka & Pasteris (1993) and Beyssac et al. (2002) poorly-ordered carbonaceous material shows mean D1/G intensity ratios between 1 and 2.6 with a standard deviation of 0.8 to 1.2. For highly-crystalline graphite mean D1/G intensity ratios of 0.1 to 0.3 are measurable with a standard deviation of up to 0.2. The variation in the measurements of a sample for highly-crystalline graphite is about 0.4 (Wopenka & Pasteris, 1993; Beyssac et al., 2002).

The D1/G intensity ratios of the sample measurements are plotted in Figure 3.2 d. The mean D1/G intensity ratios show a slight variation between the samples. They plot at 0.35 with a standard deviation of 0.3. Again, sample 7 shows the highest variation of 1.5 within the measurements. Sample 14 with the highest graphite crystallinities plots at zero as no defect bands were detectable in the Raman measurements of this sample.

The D1/G intensity ratio is used to calculate the crystallinities of graphite. As described above, there is a linear relationship between this ratio and a factor of the mean basal plane diameter L_a (Tuinstra & Koenig, 1970; Beny-Bassez & Rouzaud, 1985; Wopenka & Pasteris, 1993).

The calculated crystallinities for the measured samples are plotted in Figure 3.2 e. The mean crystallinity for L_a is 226 Å with a standard deviation of 220 Å. The variation in crystallinities of about 890 Å shows that differences may be quite substantial within a sample. As the graphite crystallinities are calculated as factors from the D1/G intensity ratios it is not possible to calculate the crystallinities of highly crystalline graphite due to the missing D1 defect band. Therefore sample 14 shows no values in this plot.

3.4. DISCUSSION

The data plots of the graphite crystallinities indicate in general high graphite crystallinities across all microstructural types of graphite-bearing marbles and sampling localities. Samples 7 and 10 show a broader spectrum of graphite crystallinities but still are clearly in the range of well-ordered graphite. This general pattern of the graphite crystallinities is an important aspect considering the evolution of the complex microfabrics of the graphite-bearing marbles.

Differences in graphite crystallinity within and also between the samples may be related to measurements in different orientations. As described above the Raman Effect varies with the crystallographic orientation of graphite. As shown in Chapter 2, the graphite of the investigated shear zones is mainly ultra fine-grained. This makes a Raman investigation along distinct crystallographic orientations very difficult. Therefore, differences in the described order of magnitude may be attributed to these difficulties.

Pasteris & Wopenka (1991) and Wopenka & Pasteris (1993) studied the correlation of the described parameters indicative for graphite crystallinities and the metamorphic grades of the host rocks. Compared to Pasteris & Wopenka (1991), the graphite crystallinities of the measured samples show metamorphic grades of staurolite, kyanite and and andalusite zones as well as sillimanite zones. Following Wopenka & Pasteris (1993) similar metamorphic grades are indicated by the graphite crystallinities from staurolite and andalusite zones to sillimanite zones and granulite facies.

The obtained metamorphic grades fit very well into the metamorphic isograde postulated by Hartmann et al. (1983) for the central parts of the Damara Belt (Fig. 2.1). South of the Central Zone (CZ), where the sampling sites are located, sillimanite-in due to staurolite breakdown is already observed. In the CZ upper amphibolite- to granulite facies metamorphism dominated. The CZ is characterised therefore by the highest metamorphic grades in the Damara Belt. The the main sampling localities shown in Figure 2.1 are located within the metamorphic isograde of sillimanite, k-feldspar and cordierite-in accompanied with partial melting.

This implies that the measured graphite samples have preserved the crystallinities obtained during peak metamorphism. Therefore, graphite crystallinities were not clearly overprinted by the subsequent retrograde ductile and brittle-ductile deformation. However, graphite crystallinities are not only controlled by temperatures and metamorphic grades, as graphite crystallised in high-strain zones may show clearly higher crystallinities than graphite from outside these zones (Bustin, 1983; Demeny, 1989). This is in agreement with

experimental investigations showing that strain-induced graphitisation increases the crystallinities of graphite (Ross & Bustin 1990; Ross et al., 1991; Wilks et al., 1993; Bustin et al., 1995; Ross & Bustin, 1997).

In addition, fluid-deposited graphite also is reported to be well crystalline (Bartels & Pasteris, 1994). This shows that particularly in high-strain zones graphite crystallinities alone do not give a secure evidence for specific deformational and metamorphic events. It is clearly necessary to discuss the graphite crystallinities together with the microstructural analysis, field relationships and the analysis of stable isotopes to determine the mode of graphite formation.

The data also implies that the method of isolating the graphite from the marble host rock as described in Chapter 2.3.6.1, does not influence the obtained degree of graphite crystallinity. This was also already observed by Hofmann (1989) and Alcántara et al. (2003), who investigated graphite crystallinities of grounded graphite and found no differences even after 40 min of grounding.

CHAPTER 4

CONDUCTIVITY MEASUREMENTS

As described above, a series of follow up magnetotelluric profiles were measured by Ritter et al. (2003) and Weckmann et al. (2003) north-west of Usakos (Fig. 4.1 a). These magnetotelluric profiles revealed surface anomalies of high electrical conductivity in the southern parts of the profile (Figure 4.1 b). Plotting the data on the regional geological map showed, that these anomalies coincide with the graphite-bearing carbonates, which build up the described dome structures (Fig. 4.2). The aim of the conductivity measurements on sample scale is, to understand and quantify the conductivity potentials of the different fabric types of graphite-bearing marbles.

The conductivity measurements were performed at the Mineralogisch-Petrologisches Institut of the Universität Bonn in co-operation with Dr. Georg Nover. These measurements by complex impedance spectroscopy enabled the distinction between electrolytic and electronic conductivities. To exclude the reduction of conductivity potentials by disconnected graphite veins due to microcracks, reference samples were measured under different hydrostatic pressures. Additionally, the samples were drenched in 0.1 M NaCl under vacuum conditions, to fill up the permeable pore space and microcracks with water. Therefore, disconnected graphite veins are able to be connected by electrolytic bridges. In this way upper crustal conditions are simulated in the samples.

4.1. PRINCIPLES OF ELECTRICAL CONDUCTIVITY

An electrical field applied on any kind of material by a potential difference E, enforces the movement of charged material components like electrons and ions along the electric field lines. This causes an electrical current, which is directly proportional to the potential difference or electrode voltage. The degree of mobility of these charged particles characterises the intrinsic resistivity ρ of the material.

In electrically conducting materials, charged components are free to move. In dielectrical or electrically isolating materials however, no free movement of charged material components is possible. In the latter case, the movability of the charged components is restricted to their position within the crystal lattice or the material fabric. An electric field applied on a dielectric material, forces the charged particles to move along the electric field lines until the field forces are balanced by the Coulomb forces within the crystal lattice. Due to these minor shifts around fixed lattice positions, polarisation effects are observable in dielectric materials.

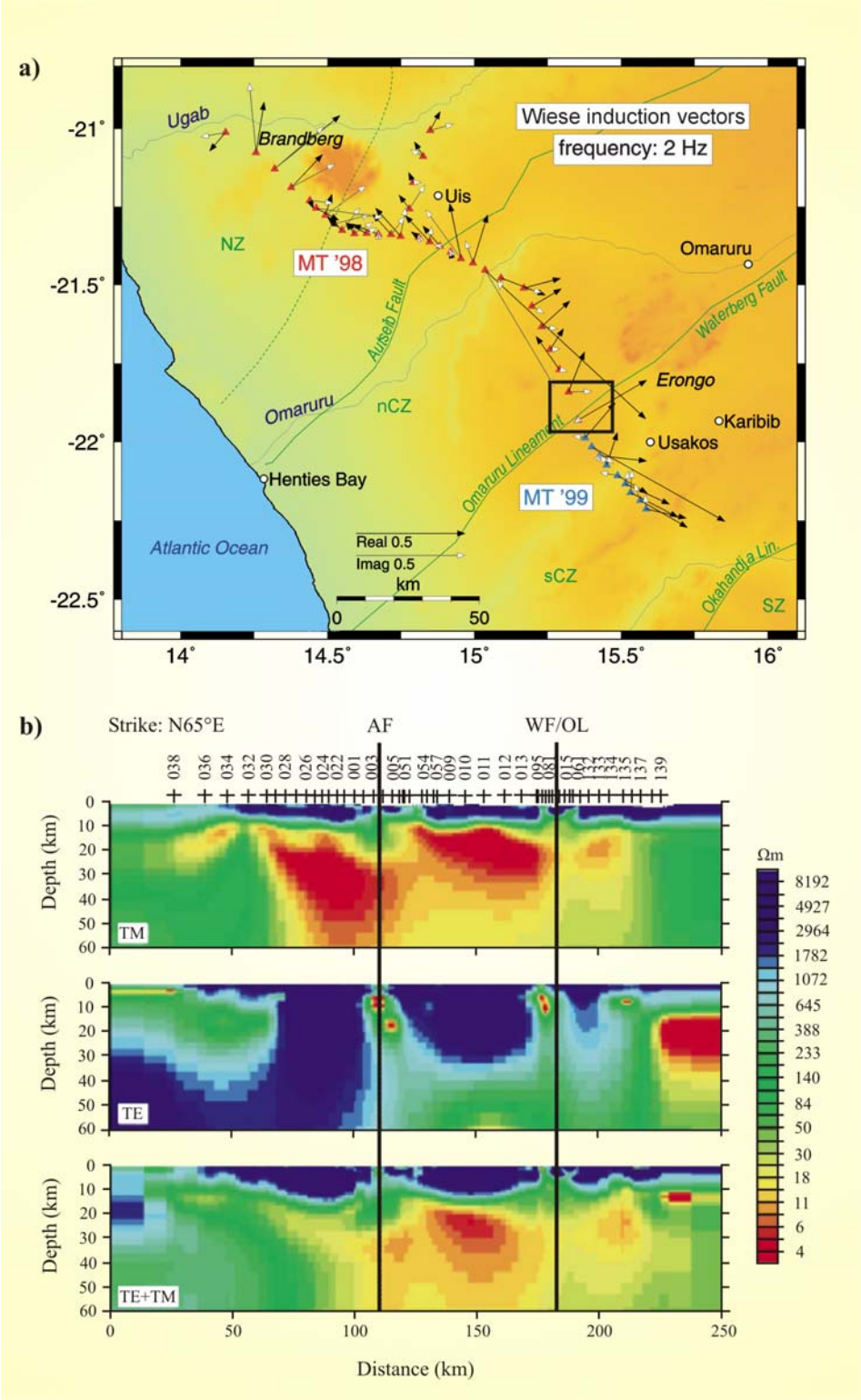

Fig 4.1 ***a)*** *Map of the magnetotelluric profile across the Omaruru Lineament (OL) and the Autseib Fault (AF).* ***b)*** *TE, TM and TE+TM calculations for the surface and upper crustal anomalies of electrical conductivity after Ritter et al. (2003) and Weckmann et al. (2003).*

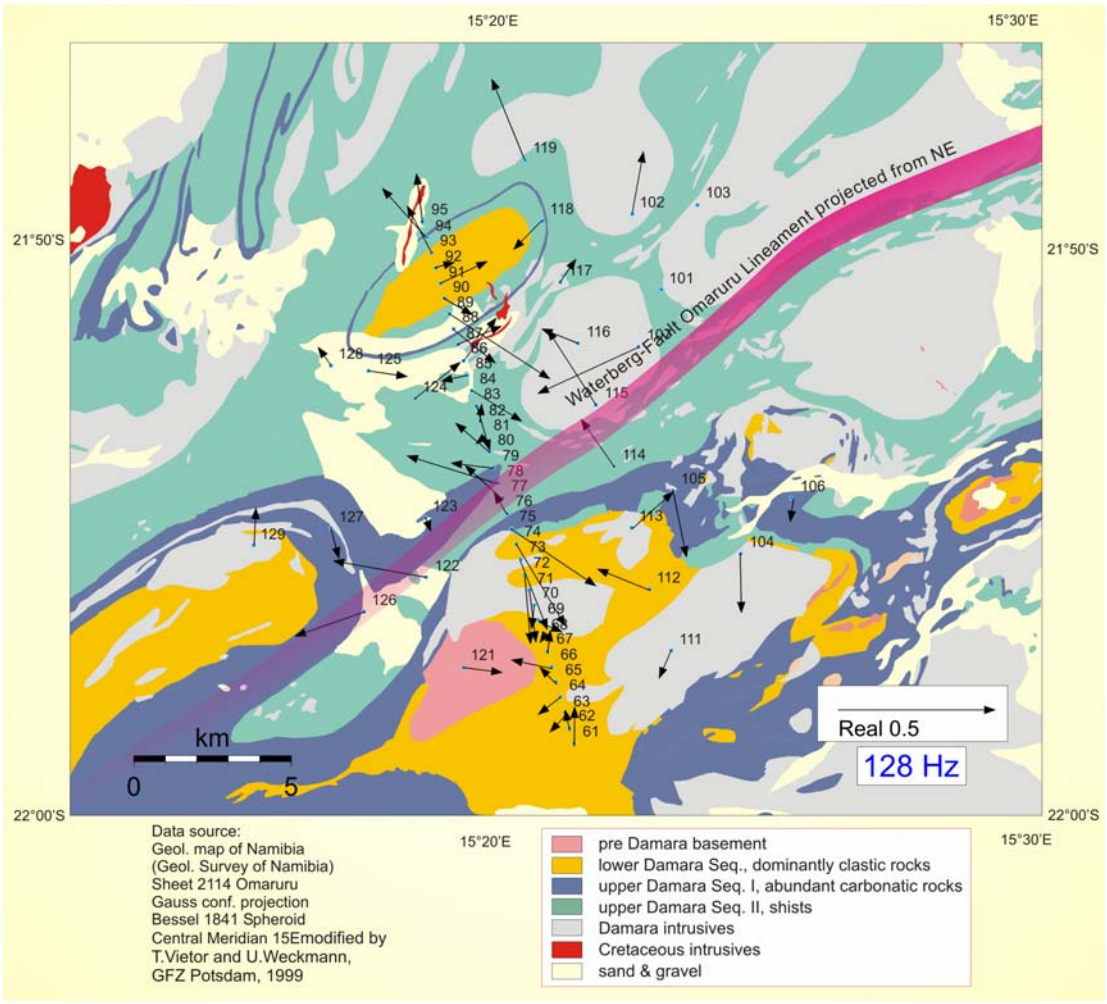

Fig 4.2 *Magnetotelluric profile plotted on a simplified geological map by Weckmann et al. (2003). The anomalies of electrical conductivity coincide with the localities of Proterozoic graphite-bearing carbonates. The Omaruru Lineament is projected into the map by Weckmann et al. (2003).*

In general, the correlation between voltage E, current flow I and electrical resistivity R induced by a potential difference within a electrical conductor, is described by Ohm's Law:

$$E = I \times R \qquad [4.1]$$

Resistivity and conductivity respectively, are material properties. This implies that the intrinsic resistivity ρ for a cylindrical conductor is independent of the applied electrode voltage. The intrinsic resistivity is therefore defined by the geometric properties as:

$$\rho = R\frac{A}{l} \qquad [4.2]$$

The geometric description of the conductor is defined by the cross sectional area A and the length of the conductor l. The intrinsic conductivity σ is the reciprocal value of the intrinsic resistivity. Therefore, it is defined as:

$$\sigma = \frac{1}{\rho} \qquad [4.3]$$

The intrinsic resistivity is expressed in Ω m, whereas conductivity is expressed in S m^{-1}. They both quantify the transport of electrical charge in a conductor between two electrodes of a constant potential difference. This implies that Ohm's Law is only applicable for linear conductors. In linear conductors, a static electrical field strength $\vec{E}$ produces an electric current density $\vec{J}$ by the displacement either of electrons or ions. For linear conductors the electric current density is therefore defined as:

$$\vec{J} = \sigma\vec{E} = \frac{1}{\rho}\vec{E} \qquad [4.4]$$

$\vec{J}$ is expressed in Amp/m^2 and $\vec{E}$ in V/m. When Ohm's Law is expressed in this way it is only applicable for isotropic materials. However, the conductivity σ of crystalline materials is mostly anisotropic. Therefore, Ohm's Law has to be described by a second rank tensor, where the overall conductivity of a crystalline material is calculated according to an ellipsoid of three (positive) vectors. The magnitudes and directions of the vectors defining the ellipsoidal tensor, depend on the material properties in different directions. The tensor is then expressed by:

$$J_i = \sigma_{ij} E_j \qquad [4.5]$$

The different components of the tensor are described by the direction-dependant conductivities. Therefore, this expression enables the determination of the conductivity σ, in dependence of distinct directions of the tensor. However, most geological materials especially silicates and germanates are anisotropic and of dielectric nature. Dielectric materials are isolators, which polarise dipoles, molecules or free electrical charge on grain and material boundaries, according to the electric field lines of a static electrical field. Because of electrical charge culmination due to polarisation effects, conductivity measurements with direct current will produce a linear decrease in the electrical current flow I. This results in a time dependant increase in the electrical resistivity R.

This implies that the linearity of Ohm's Law is not given for dielectric materials. Additionally, it is difficult to distinguish conductivities according to equation [4.5] in the different directions of the tensor ellipsoid. This is also the case for materials developing

semiconductoral properties with increasing temperatures. In these cases, the dependency of the electrical current flow I from the voltage E is following a exponential law:

$$I = I_s \exp(-\frac{eE}{kT}) \qquad [4.6]$$

For this expression e is the elementary charge, k is the Boltzmann constant and T is the absolute temperature. To measure and to distinguish conductivity potentials of materials showing dielectric, semiconducting or ionic conductivity, from linear electronic conductors, impedance spectroscopic measurements were developed (MacDonald & Kenan, 1987).

4.1.1. ELECTRONIC CONDUCTIVITY

Electronic conductivity varies between different materials in many orders of magnitude. The ability for electronic conductivity depends on the amount of electrons in the valence band. If a band is not completely filled with electrons, the electrons are able to move within the valence band. In this way they can react on influences of an applied electric field. If the valence band is filled up completely with electrons, the electrons have to be activated by the application of energy, to overcome the energy gap to the next free band (Fig 4.3 a). Insulators have a large energy gap between the single bands and the valence band is either filled completely by electrons, or the valence band is completely empty (Fig 4.3 b). Metals generally have partially-filled valence bands and therefore are good electronic conductors. Semiconductors have an energy gap of $E_0 < 2.5$ eV and dielectric materials have energy gaps of $E_0 > 2.5$ eV. In Figure 4.4 the electrical conductivity/resistivity ranges of geologic materials are shown.

4.1.2. IONIC OR ELECTROLYTIC CONDUCTIVITY

Ionic or electrolytic conductivity is an important component in upper-crustal conductivity measurements, because most of the minerals are of dielectric nature. Electrical conduction in these materials only occurs through mobile ions as they are electrically charged. The displacement of ions occurs mainly by diffusion, which is controlled by the electrical potential qV between two points of a material, by the number of charge carriers n, by the unit volume and the temperature T.

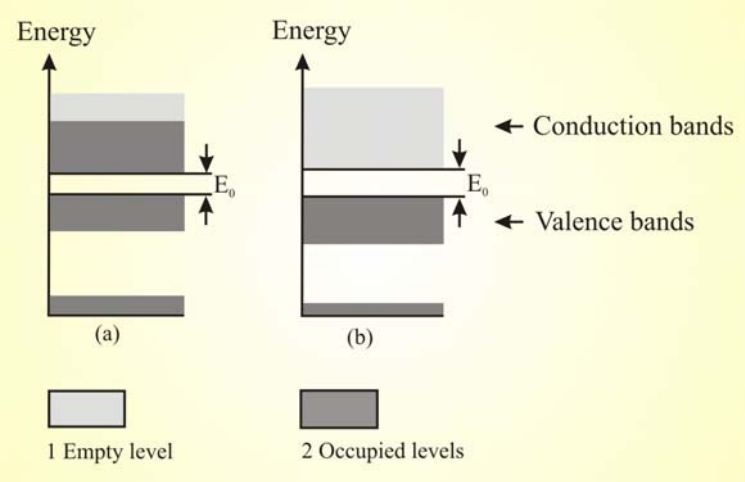

Fig 4.3 ***a)*** *Partial occupation of the conduction band with electrons enables electronic conductivity. If the energy gap E_0 is <2.5 eV between the valence bands, the movement of electrons to higher energy states is enabled.* ***b)*** *The conduction band is completely empty and the valence band is completely occupied by electrons. This prohibits electronic conduction. If E_0 > 2.5 eV electrons are unable to move to empty electron bands. Figure after Guéguen & Palciauskas (1994).*

In a thermodynamic equilibrium the number of charge carriers n follows Boltzmann's Law by applying the Boltzmann constant k. The diffusion follows Fick's Law where D is the diffusion coefficient. The ionic conductivity is thus defined as:

$$\sigma = nq^2 \frac{D}{kT} \qquad [4.7]$$

Diffusional ionic conductivity as described by equation [4.7] depends on the material properties. Therefore, it is referred to as the intrinsic electrolytic conductivity. In the presence of impurities in the dielectric material, extrinsic ionic conductivity also occurs by a different phase of ionic material which causes the impurities. This ionic material becomes mobile in an electrical field or contributes with additional electrons to the conducting charge. At lower temperatures extrinsic electrolytic conductivity dominates because of the lower activation energy, whereas at higher temperatures intrinsic ionic conductivity is dominating. The total sum of the electrolytic conductivity of a material, should always be calculated as the sum of the extrinsic σ_{eo} and intrinsic σ_{io} ionic conductivity:

$$\sigma = \sigma_{\mathrm{io}} \exp(-\frac{E_i}{kT}) + \sigma_{eo} \exp(-\frac{E_e}{kT}) \qquad [4.8]$$

Ionic conduction in solutions occurs, where aquaeous pore fluids contain varying concentrations of salts such as NaCl and KCl. These salts dissociate during solution and the soluted anions and cations move freely in the solution. If an electric field is applied, the anions and cations move along the electric field lines in opposite directions. This diffusion process is controlled by Stoke's Law, where the applied force is balanced by the viscosity of fluid. The conductivity is proportional to the ionic concentration and varies depending on the chemical composition of the salts, because of differences in the mobility of different ions.

4.1.3. ELECTRICAL CONDUCTIVITY OF ROCKS

The total amount of conductivity in rocks is strongly dependent on the composition of the rocks (Fig. 4.4), on the microstructures and on the overall macroscopic fabric. Most igneous rocks, sands and carbonates show conductivities of 1 to 10^{-2} mS/m, whereas sulfides and graphite show conductivities of 10^{5} to 10^{2} mS/m. Other conductive minerals are zeolithes and hydrated minerals, like for example some phyllosilicates.

The microstructures of rocks are of great importance, because an interconnection of conducting minerals is essential for bulk electronic conductivity. If the pore space is interconnected in a permeable network around grain boundaries, the ionic component of conductivity by melts or aqueous fluids will be relatively high.

The ionic conductivity in rocks therefore also depends on the degree of fluid saturation in the rocks, as well as on the volume of interconnected pore space. Bulk conductivities of rocks increase predominantly, when conducting minerals like sulfides and graphite are interconnected and ionic conductivity is prevailing throughout the rock.

For the electrolytic conductivity of clay-bearing rocks, a component of surface conductivity along grain boundaries of clay minerals is measurable. Extrinsic ionic conductivity occurs along charged impurities on the surface of the clay minerals. If for example Al^{3+} is substituted by Si^{4+}, the charge deficit is compensated by cation absorption on the mineral surface. This results in the formation of an electrical double layer. In the combination with electrolytic conductivity, these surface ions are displaced along the grain boundaries.

Rocks with a high concentration of conducting minerals such as sulfides (FeS_2 ρ = 1,2 - 600 x 10^{-3} Ω m, PbS ρ = 6,8 x 10^{-6} – 9 x 10^{-2} Ω m), graphite (parallel to basal plain ρ = 33 - 100 x 10^{-8} Ω m, perpendicular to basal plain ρ = 28 – 200 000 x 10^{-8} Ω m), amorphous carbon (C ρ = 5 x 10^{-5} Ω m) and magnetite (Fe_3O_4 ρ = 52 x 10^{-6} Ω m) may

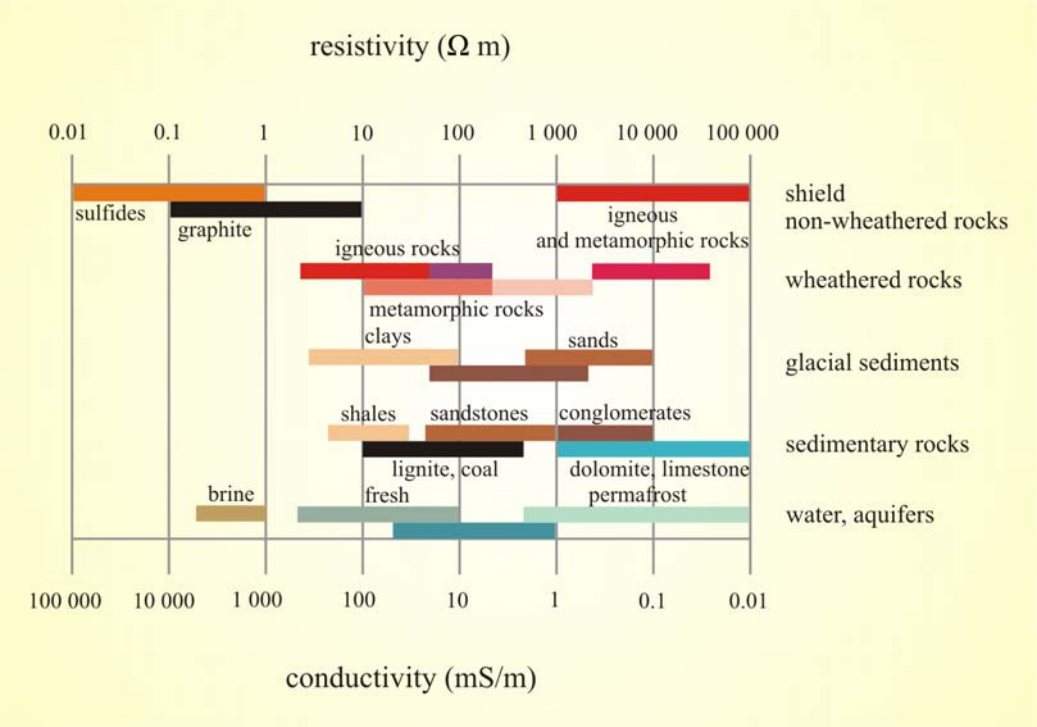

Fig 4.4 *Resistivity ranges of different crustal material after Palacky (1987).*

show higher conductivities, which could purely be electronic conductivity. Silicates have resistivities of about $\rho = 5 - 1 \times 10^5$ Ω m depending on their structure and water content. To obtain electronic conductivities the conducting minerals have to be interconnected. Graphite is known to form films on grain boundaries, whereas dendritic patterns also could result in a strong increase in electrical conductivity. Figure 4.5 a shows, that there can be a decrease of several orders of magnitude in resistivity, when the volume fraction of conductive minerals is increasing by one order of magnitude.

Conductivity variations with increasing pressure are also measurable in crustal rocks. With increasing pressures, the energy gaps between the covalent electron bands decrease. Therefore, a lower activation energy is needed for electrons to reach the next free electron band to perform electronic conductivity. In ionic conductivity components, the effects of pressure are neglectable small, although a decrease in ionic resistivity is measurable with increasing pressure (Fig. 4.5 b). Considering the effects of temperature on the conductivity potentials, the effects of pressure are neglegible in crustal dimensions.

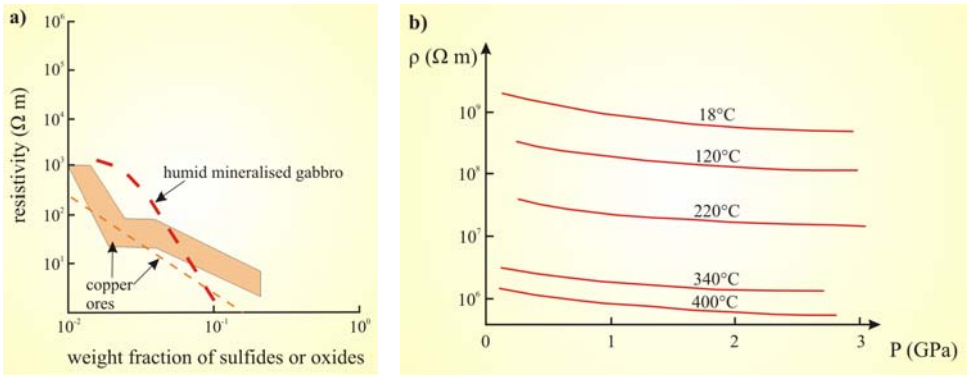

Fig 4.5 ***a)*** *Resistivity variation with the increasing concentration of sulfides and oxides as conducting minerals after Keller (1987).* ***b)*** *Variation of resistivity with increasing pressure and temperature for basalt after Parkhomenko (1967).*

4.1.4. IMPEDANCE SPECTROSCOPY

Impedance spectroscopy is a physical method to determine the conductivity of complex resistors, as they occur in most geological materials. Complex resistors are described by a combination of linear conductors and dielectric materials. As impedance spectroscopic investigations are based on measurements with alternating current, the above mentioned polarisation effects in measurements which occur in direct current are eliminated. Additionally, it is possible to distinguish between electronic and ionic conductivity potentials of the measured materials.

The principle of impedance spectroscopy is the theory of complex impedance. The theory of complex impedance is based on the equivalent-circuit model. This model describes complex resistors like the graphite network structures in a calcite host-rock, by a combination of elementary cells containing resistors and capacitors. Thus, the conductivity of elementary cells includes a component of linear conductivity by a fixed resistor with a constant resistivity, and a frequency-dependant component of a capacitor. Therefore, a combination of pure transport of charge and various effects of polarisation can be measured and distinguished using impedance spectroscopy.

4.1.4.1. POLARISATION EFFECTS AND ELECTRICAL CONDUCTIVITY

The polarisation effects of dielectric materials (permittivity) in alternating current depend directly on the frequency of the applied electrical current. Several different effects of polarisation are described in the measured frequency ranges from 10^{15} to 10^{-5} Hz.

At high frequencies of 10^{15} Hz polarisation effects are induced by the distortion of the electron shells relative to the atomic nucleus by the electrical field. These shifts occur

along electric field lines of the applied field, and produce charge concentrations and thereby charge polarisation on an atomic scale. This kind of polarisation effect is referred to as electron polarisation.

Between 10^{15} and 10^{12} Hz ionic polarisation effects are measurable. Positively and negatively charged ionic components of the molecules are displaced relative to each other around fixed lattice positions. This causes polarisation effects due to concentrations of different charges, relative to the applied field lines on a molecular scale.

Polarisation effects on the same scale are measured between 100 kHz and 10 Hz, either by the reorientation of pre-existing dipoles within the molecules or by the reorientation of charged components in lattice defects. These charged particles and material components are forced into a preferred orientation along the electric field lines. Thereby the materials electrical charge is polarised. These polarisation effects are referred to as dipolar and space-charge polarisation effects.

At frequencies below 10^{-1} Hz the effects of polarisation reach a sample-scale level by free-moving ionic components. Charged particles separate according to the electrical field lines and concentrate either on solid interfaces of the sample or on grain boundaries. These concentrations of charge on specific interfaces are regarded as electrode polarisation. These effects are referred to as the Maxwell-Wagner effect. Polarisation effects on grain-boundary scale commonly overlap with the dipolar polarisation effects at higher frequencies.

If dielectric material is polarised, the electric displacement $\vec{D}$ of two charges of opposite polarity depends on the electric field strength $\vec{E}$ and the Polarisation $\vec{P}$. This is defined as the electrical dipole moment per volume:

$$\vec{D} = \varepsilon_0 \vec{E} + \vec{P} \qquad [4.9]$$

ε is the dielectric permittivity expressed in farads/m. Equation [4.9] shows that the electric displacement $\vec{D}$ is directly related to the electric field strength $\vec{E}$. ε_0 is the permittivity of a vacuum. The permittivity is a parameter which varies with the composition and the material properties of the dielectric material. The permittivity κ of a material is defined as:

$$\kappa = \frac{\varepsilon}{\varepsilon_0} \qquad [4.10]$$

This implies, that the linear approximation between $\vec{E}$ and $\vec{P}$ can be deduced for most dielectric materials. In comparison to a vacuum capacitor, a linear dielectric material shows a higher capacity by the factor ε. This higher capacity depends directly on the susceptibility χ of the polarisation:

$$\vec{P} = \varepsilon_0 \chi \vec{E} \qquad [4.11]$$

The susceptibility χ is here defined as ε-1. The parameters for the permittivity κ and ε and the susceptibility χ are material parameters and therefore second rank tensors. As complex numbers, these parameters contain imaginary parts which represent the dissipation of energy during the redistribution of charge.

Polarisation effects in an oscillating electrical field are not always static, as the redistribution of charge is not always as rapidly as the oscillation of the electric field. These described charge redistributions are additive, so that the overall polarisation is the sum of all polarisation effects. The total polarisation or permittivity κ(ω) decreases, with the increase of frequency ω. At frequencies below 10^{-3} Hz, all different kinds of polarisation effects are induced in dielectric materials by oscillatory electrical fields. Therefore, an electrical current is measurable.

For an ideal dielectric material, the phase difference between the electrical flow I and the electron voltage E is 90°. With increasing frequencies, the polarisation effects vary according to the frequency ranges described above. With every change in polarisation effect, a change in the phase difference is observable. This effect is used in impedance spectroscopic measurements to distinguish between different conductivity components in complex resistors.

4.1.4.2 THEORY OF COMPLEX IMPEDANCE

The theory of complex impedance describes the conductivity potentials of complex resistors with components of linear electrical currents (conductivity by charge transport) and displacement currents (conductivity by polarisation effects). It is based on the combination of elementary cells, which are either parallel or in series. The constant resistor of the elementary cell is equivalent to the electronic conductivity component by charge transport. The capacitor represents the displacement currents of the electrostatic field by the polarisation of dielectric material.

If an oscillatory electrode voltage E is applied, the potential difference E(ω) is defined by the amplitude E_0 and the cyclic frequency ω by:

$$E(\omega) = E_0 \sin(\omega t) = E_0 e^{(i\omega t)} \qquad [4.12]$$

An oscillatory electric potential difference E(ω) always produces an alternating electrical current I(ω) with the amplitude I_0. The electrical current has a phase difference φ to the electrode voltage E. This implies, that I(ω) is defined analogue to equation [4.12] as:

$$I(\omega) = I_0 \sin(\omega t + \varphi) = I_0 e^{(i\omega t + \varphi)} \qquad [4.13]$$

In complex resistors, either a combination or a substitution of charge transport and displacement currents is possible in oscillatory electrical fields. Therefore, the complex oscillatory resistor Z(w) (the impedance) is calculated by integrating equations [4.12] and [4.13] into Ohm's Law [4.1]:

$$Z(w) = \frac{E(\omega)}{I(\omega)} = |Z| e^{i\varphi} = |Z| \cos\varphi + i|Z| \sin\varphi \qquad [4.14]$$

The magnitude of the impedance is described by $|Z|$, where the electrical current by charge transport is the real component of the impedance Z′. This real component of the complex impedance is defined by the term $|Z| \cos\varphi$. The displacement current is defined by the imaginary component of the impedance Z′′ with $i|Z| \sin\varphi$. The unit imaginary number i is the positive square root of –1. It thereby defines the imaginary component of the complex impedance. The complex impedance is described according to equation [4.14] by the phase difference as:

$$\tan\varphi = \frac{Z'}{Z''} \qquad [4.15]$$

Analogue to equations [4.5] and [4.14] the total current density $\vec{J}$ is also defined by a combination of real and imaginary components of the complex electrical conductivity:

$$\vec{J}_T = \sigma \vec{E} + \frac{\delta \vec{D}}{\delta t} = \sigma \vec{E} + \varepsilon \frac{\delta \vec{E}}{\delta t} \qquad [4.16]$$

The electrical current by charge transport is defined by $\sigma \vec{E}$. The displacement currents are either defined by $\frac{\delta \vec{D}}{\delta t}$ where $\vec{D}$ is the electric displacement, or by $\varepsilon \frac{\delta \vec{E}}{\delta t}$ where $\vec{E}$ is the electric field strength and ε is the permittivity.

The complex impedance is described by an elementary cell containing a constant resistor and a capacitor. The constant resistor defines the electrical conductivity by charge

transport and is independent of the cyclic frequency (ω). Therefore, the electrical current is in phase with the electrode voltage. The capacitor represents the displacement currents which depend on the cyclic frequency (ω). This implies, that the phase difference of the electrical current is 90° before the electrode voltage. The imaginary component of the complex impedance is defined by the cyclic frequency (ω) and the capacity C as:

$$Z'' = -\frac{i}{\omega C} \qquad [4.17]$$

If the two components of the complex impedance are connected in series, the electrode voltage of the real component E_R and the imaginary component E_C add to the total electrode voltage E_T by $E_T = E_R + E_C$. The total complex impedance Z_T is therefore defined as:

$$Z_T = R - \frac{i}{\omega C} = R + \frac{1}{i\omega C} \qquad [4.18]$$

The complex impedance of this elementary cell plots in a Cole-Cole diagram as a straight line parallel to the imaginary axis. The resistor R plots at the intersection with the axis of the real component (Fig. 4.6 a). The capacity of the complex resistor cannot be differentiated in this plot. To differentiate the capacity, the complex admittance as the reciprocal value of the complex impedance, is plotted into an Argand diagram. In this case the capacity is distinguished in the maximum of the half-circle. The diameter of the half-circle ranges from 0 to 1/R (Fig. 4.6 b).

Due to this fact, the elementary cell is connected parallel, where the reciprocal components of the complex impedance add to the total admittance Y_T:

$$Y_T = \frac{1}{Z_T} = \frac{1}{R} + i\omega C \qquad [4.19]$$

The real component of the complex admittance is defined by $Y' = \frac{1}{R}$ and the imaginary component is defined by $Y'' = i\omega C$. The complex admittance plots in a Argand diagram as a single line parallel to axis of the imaginary component (Fig 4.6c). The total complex impedance can be calculated as the reciprocal value of the total complex admittance. It is therefore defined by:

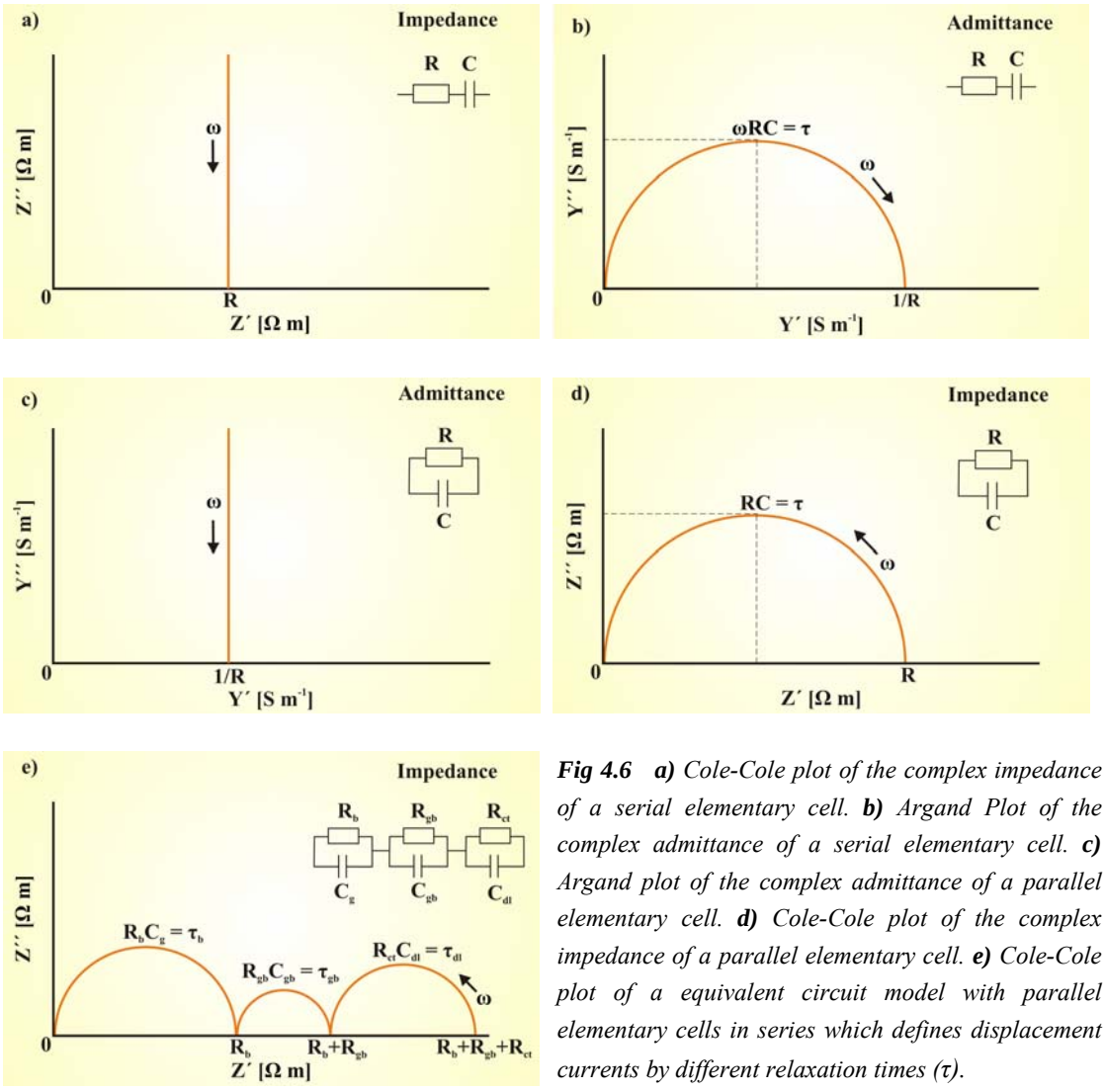

Fig 4.6 ***a)*** *Cole-Cole plot of the complex impedance of a serial elementary cell.* ***b)*** *Argand Plot of the complex admittance of a serial elementary cell.* ***c)*** *Argand plot of the complex admittance of a parallel elementary cell.* ***d)*** *Cole-Cole plot of the complex impedance of a parallel elementary cell.* ***e)*** *Cole-Cole plot of a equivalent circuit model with parallel elementary cells in series which defines displacement currents by different relaxation times (τ).*

$$Z_T = \frac{1}{Y_T} = \left(\frac{1}{R} + i\omega C\right)^{-1} \qquad [4.20]$$

The real component of the complex impedance is accordingly defined as $Z' = \frac{R}{1+(\omega RC)^2}$. The imaginary component is defined by $Z'' = R\frac{\omega RC}{1+(\omega RC)^2}$. Measured in a wide frequency range, the complex impedance plots as a half circle above the axis of the real component from 0 to R (Fig. 4.6 d). The half circle is defined by R and the relaxation moment $\tau = RC$.

The total complex impedance of crustal materials with a fluidal component in the permeable pore space, is described by a set of parallel elementary cells. These are combined in series. The single cells represent different resistivity/conductivity

components, which add up to the total resistivity (Fig. 4.6 e). R_b is the electrolytic bulk resistance which is defined according to equation [4.3] by [4.21]. C_g represents the electrolytic capacity, which is dependent on the permittivity constant ε and is calculated by equation [4.22] as follows:

$$\sigma = \frac{l}{AR_b} \qquad [4.21]$$

$$C_g = \frac{\varepsilon_0 \varepsilon A}{L} \qquad [4.22]$$

The second elementary cell $R_{gb}//C_{gb}$ defines the complex impedance of grain boundary effects within the measured volume. The third elementary cell $R_{ct}//C_{dl}$ represents the complex impedance on the contact between the electrolyte and the electrode. R_{ct} defines the charge transfer whereas C_{dl} represents charge changes in the double layer on the interface to the electrode.

Every half circle is defined by R and the relaxation time τ. If these vary by several orders of magnitude, the three impedance components shown in Figure 4.6 e can be differentiated. If the relaxation times vary less than one order of magnitude between the different impedance components, one big half circle over R will be displayed as shown in Figure 4.6 d. In this case it is very difficult to reconstruct the single components, due to the uncertainty regarding the frequency dependency of the displacement currents of the different materials. A plot of the complex admittance of the described components shows different straight lines and/or curves of different gradients. The different gradients represent at least different relaxation times for the measured conductivities. A further interpretation of these curves is doubtful up to now, due to uncertainties of the correlation of these curves to individual and overlain displacement currents.

For further information on the electrical conductivity of rocks see Guéguen & Palciauskas (1994) and von der Gönna (1997).

4.2. ANALYTICAL TECHNIQUES

For the measurements of the complex impedance a HP 4192A Impedance Spectroscope was used. The measurements were conducted with two different electrode voltages of 0.5 and 1 V in the frequency range of 785 Hz to 1 MHz. For every decade 15 to 20 logarithmic frequency measurements were carried out. The impedance spectroscope was operated and controlled by a graphical software HP-VEE, which was programmed and modified by the group of Dr. Georg Nover. This software shows the measured complex impedance plotted life into a Cole-Cole diagram. Additionally the quality of the

measurements is controlled by a Bode plot, where the impedance and the phase difference is plotted as a function of the applied cyclic frequency.

Reference samples were measured under different hydrostatic pressures, to verify the loss of electronic conductivity by the existence of microcracks. These samples were measured in a autoclave press which enables pressures of up to 4 kbar. The sample and the electrodes were sleeved by a heat shrink tube and thereby separated to the pressure medium glycerine. Abnormal pore pressures are prevented by porous electrodes.

Every measured sample has been evacuated and afterwards saturated with a 0.1 M NaCl pore fluid to simulate upper crustal conditions. The electrical contact between the sample interfaces and the electrodes was established by a moistened filter paper. All the sample measurements have been conducted under room temperature conditions. The analysis of the measured data was carried out by the Least Squares Program IDA by EG&G/Parc.

4.3. SAMPLES MEASURED

For conductivity measurements by complex impedance graphite-bearing marbles ideally should function as complex resistors. Accordingly, the samples had to be restricted to the types where graphite occurs in interconnected graphitic stylolites and/or graphite network structures. The samples for the conductivity measurements were therefore selected according to the classification of the microstructural investigations described above.

Three main types of graphite-bearing marbles had been distinguished and classified. The microstructural investigations had revealed for the graphite-bearing marbles of type 1 that graphite occurs only in single graphite nests. These are disseminated throughout the calcite-marble host rock. As graphite is not interconnected, no electronic conductivity is measurable in this type of marble. Therefore, only a purely dielectric behaviour is measurable in these samples.

Likewise, the finer grained mylonitic graphite-bearing marble of type 3 shows no interconnection of the single graphite grains on the foliation plains. On a microscopic scale the single graphite grains are not interconnected in the graphitic layers parallel to the foliation. Therefore, they are not able to form continuous electronic conductors. Accordingly, this type of graphite bearing marble also shows no electronic component in the conductivity measurements and behaves purely dielectrically.

According to the microstructural investigations, type 2 of the graphite-bearing marbles is the only type to produce electric conductivity by interconnected graphitic

stylolites. The samples of type 2 were selected by the degree of the graphite network intensity and the orientation of the graphite veins. The aim is to distinguish the different conductivity potentials of the samples in relation to the direction of the foliation, the degree of network intensity and the thickness of the graphitic stylolites. These relationships would reveal an estimation of the conductivity potentials of the samples. An upscaling to the results of the magnetotelluric measurements on a crustal scale, these results may give some good indication for the analysis of the magnetotelluric data.

The samples measured, are from all areas of field investigation (Fig. 2.1). Therefore, some of the discussed samples are not from the magnetotelluric profile. However, in mineral composition and in microstructural characterisation the samples of the two localities are identical. This has been investigated by optical methods, Scanning Electron Microscopy (SEM) and energy dispersive x-ray analysis (EDX) and neutron diffraction as described in chapter 2. The samples from the locality on Farm Epako Süd are considered as reference samples for a regional scale investigation. Secondly they derive from ideal outcrops with good sampling opportunities of different microstructural varieties.

4.4. MEASUREMENTS AND RESULTS

Out of a broad range of impedance spectroscopic measurements only the plots of several representative samples have been selected. They show the spectrum of results which will have to be discussed. Generally, measurements have been conducted in different scales and under different hydrostatic pressures. The measured samples were cut into rectangular blocks using foliation and lineation as the external reference system where possible. Due to this structural reference frame, an extrapolation of the measurement results into the crustal framework will later be possible.

The measurements presented here have been conducted in three different scales. Samples were measured either over the complete plains of the rectangular blocks, or over profiles across the blocks. These profiles have been measured either with electrodes of 30 mm in diameter or with point electrodes. For measurements under different hydrostatic pressures, cores have been drilled of 30 mm in length and 20 mm in diameter. These cores have been measured over their complete volume.

The representative plots in Figure 4.7 to 4.10 show, that in nearly all cases only pure ionic conductivities are measurable in the samples. This is obvious, as discussed above, by the form of a half circle in the plots of the measured complex impedance. The different sample plots show, that this result is obtained independent of the sample scale and

sample variety also across the different localities. The sample of Figure 4.7 is from the magnetotelluric profile, whereas the other shown samples are from farm Epako Süd.

Figure 4.7 shows the plots of the complex impedance (Fig. 4.7a) and the plots of the complex admittance (Fig. 4.7 b) across a rectangular block as shown in Figure 4.7 c. The impedance spectroscopic measurements have been conducted with circular electrodes of 30 mm in diameter. The differences in the resistivity of the complex impedance have to be correlated to the different orientations of the measurements. Measurement 1 and 2 had been conducted in a fine-grained brittle-ductile deformed zone with fine-grained graphite parallel to the main foliation. The resistivity of measurement 2 exceeds the resistivity of measurement 1 by nearly 50 000 Ω m. This seems to be related to the orientation of the measurements relative to the lineation on the foliation planes, which is macroscopically not visible. Accordingly, the resistivity of the third measurement orthogonal to the foliation is exceeding the resistivity of the first two measurements by up to 100 000 Ω m.

The curves plotted in this diagram show, that only displacement currents are measurable in this sample due to polarisation effects and ionic conductivities as discussed above. The plots of the complex admittance show by the two gradients of the curves, that the displacement currents had two relaxation phases. These relaxation phases indicate changes in the mode of displacement currents. However, it is not possible to extrapolate from these curves which kinds of polarisation effects or ionic conductivities have been responsible for the displacement currents.

The samples measured in Figures 4.8 and 4.9 are from farm Epako Süd. They have been measured in different scales according to different graphite network densities and thickness of the graphitic stylolites. Different directions have been considered in relationship to the orientation of the foliation planes. Figure 4.8 shows the measurements of a sample with a high graphite network intensity and a distinct difference in thickness of the graphitic stylolites. The measurements were conducted in three different directions as shown in Figure 4.8 c. The circular electrodes had diameters of 30 mm.

The plots of the complex impedance show that there is no clear structural relationship between the resistivities of the conducted measurements (Fig. 4.8 a). Measurement 1 has been conducted perpendicular, whereas measurements 2 and 3 have been performed parallel to the foliation. This implies for this sample, that there is no correlation of the displacement current resistivity with the structural framework. The different gradients in the curves of the complex admittance show the existence of two relaxation phases in the displacement currents (Figure 4.8 b).

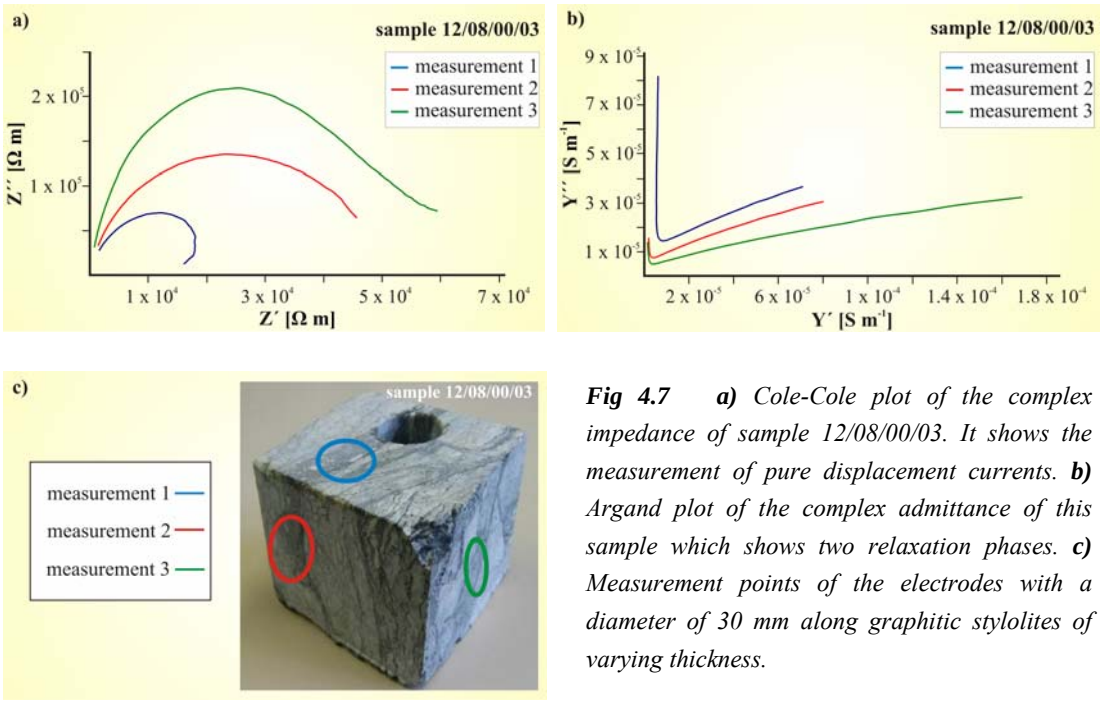

Fig 4.7 ***a)*** *Cole-Cole plot of the complex impedance of sample 12/08/00/03. It shows the measurement of pure displacement currents.* ***b)*** *Argand plot of the complex admittance of this sample which shows two relaxation phases.* ***c)*** *Measurement points of the electrodes with a diameter of 30 mm along graphitic stylolites of varying thickness.*

The measurements plotted in Figure 4.9 had been conducted across the complete plains of the rectangular sample blocks, as well as on single graphitic stylolites (Fig. 4.9 e). The plots in Figure 4.9 a, b represent the impedance spectroscopic measurements of single graphitic stylolites with point electrodes. These measurements show that the conductivity measured even in this scale is purely composed of displacement currents.

The resistivity of these small scale measurements in general is much lower than measured in Figure 4.7 a, 4.8 a and 4.9 c. This is related to geometric factors like the cross sectional area of the conductor, which is calculated into the intrinsic resistivity according to equation [4.2]. The two measurements plotted in Figure 4.9 c, d have been conducted across the plains of the rectangular sample blocks. They show, that measurements on all these sample scales show displacement currents with two relaxation phases (Fig. 4.9 a, b).

The presented representative results apply for nearly all measured samples of the magnetotelluric profile and the locality of farm Epako Süd. Furthermore, these results are obviously representative for samples of varying degrees of graphite network intensity and thickness in different directions of the samples. All the samples presented so far, showed purely displacement currents by polarisation effects and ionic conductivity. Therefore, they show no linear conductivity related to electronic conductivity along or perpendicular to the graphitic stylolites.

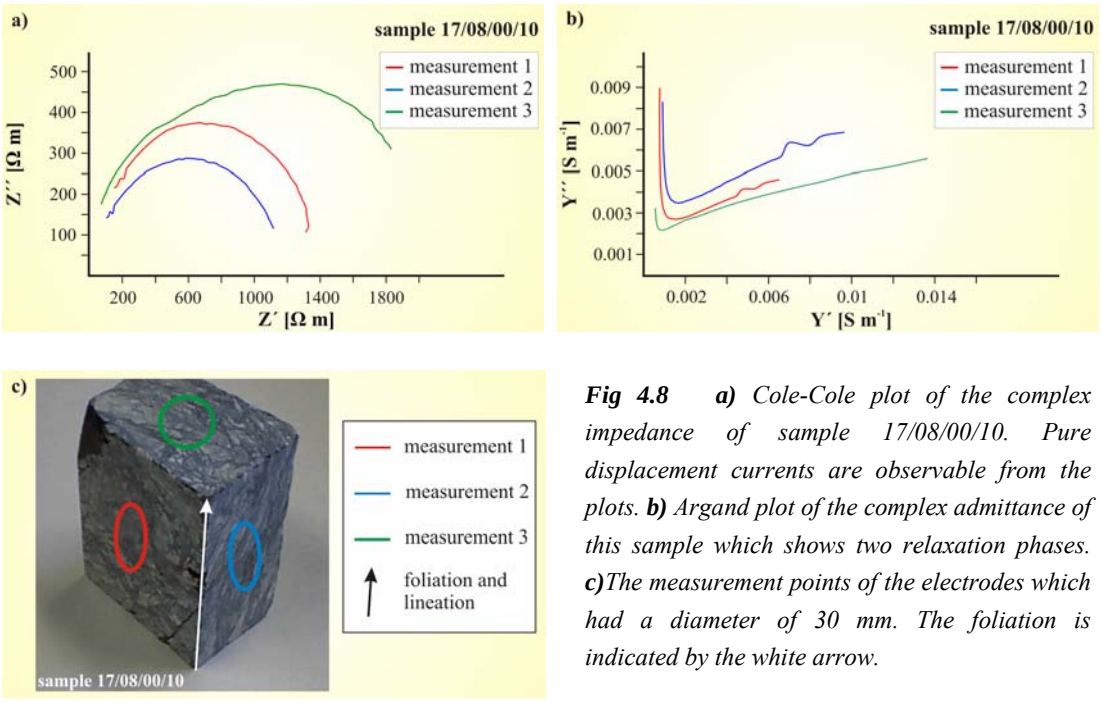

Fig 4.8 ***a)*** *Cole-Cole plot of the complex impedance of sample 17/08/00/10. Pure displacement currents are observable from the plots.* ***b)*** *Argand plot of the complex admittance of this sample which shows two relaxation phases.* ***c)****The measurement points of the electrodes which had a diameter of 30 mm. The foliation is indicated by the white arrow.*

In contrast to the measurements presented so far, the sample of Figure 4.10 shows a definite component of electronic conductivity. The data plot of Figure 4.10 a shows, that this sample reacts as a complex resistor with linear and displacement conductivities. This sample is a core sample (Fig. 4.10 c), which was measured in the autoclave under different hydrostatic pressures. For all samples measured in the autoclave, this core is representative for two cores of one sample, which showed a linear intrinsic electronic conductivity component.

The results of this sample show a half circle plot from the ionic conductivity component, influenced by the linearity of the electronic conductivity component parallel to the axis of real impedance. A pure electronic conductivity would be a point plot on the axis of the real component. This implies that the results show a combination of electronic and ionic conductivity. Opposed to the other measurements presented in Figure 4.7 to 4.9, three relaxation phases are observable in this sample. This may be related to the electronic conductivity component measured in this sample.

The bulk electronic resistivity values of the two impedance measurements are shown in table 4.1. The average electronic resistivity of core 1 is about 519 Ω m. With increasing pressure there is a continuos decrease of the bulk resistivity of about 36 Ω m. The average electronic resistivity of core 2 is about 426 Ω m. For this core there a slight increase measurable for the bulk resistivity up to 75 bars. This is followed by a continuous decrease of the bulk resistivities of about 20 Ω m with a further increase in pressure.

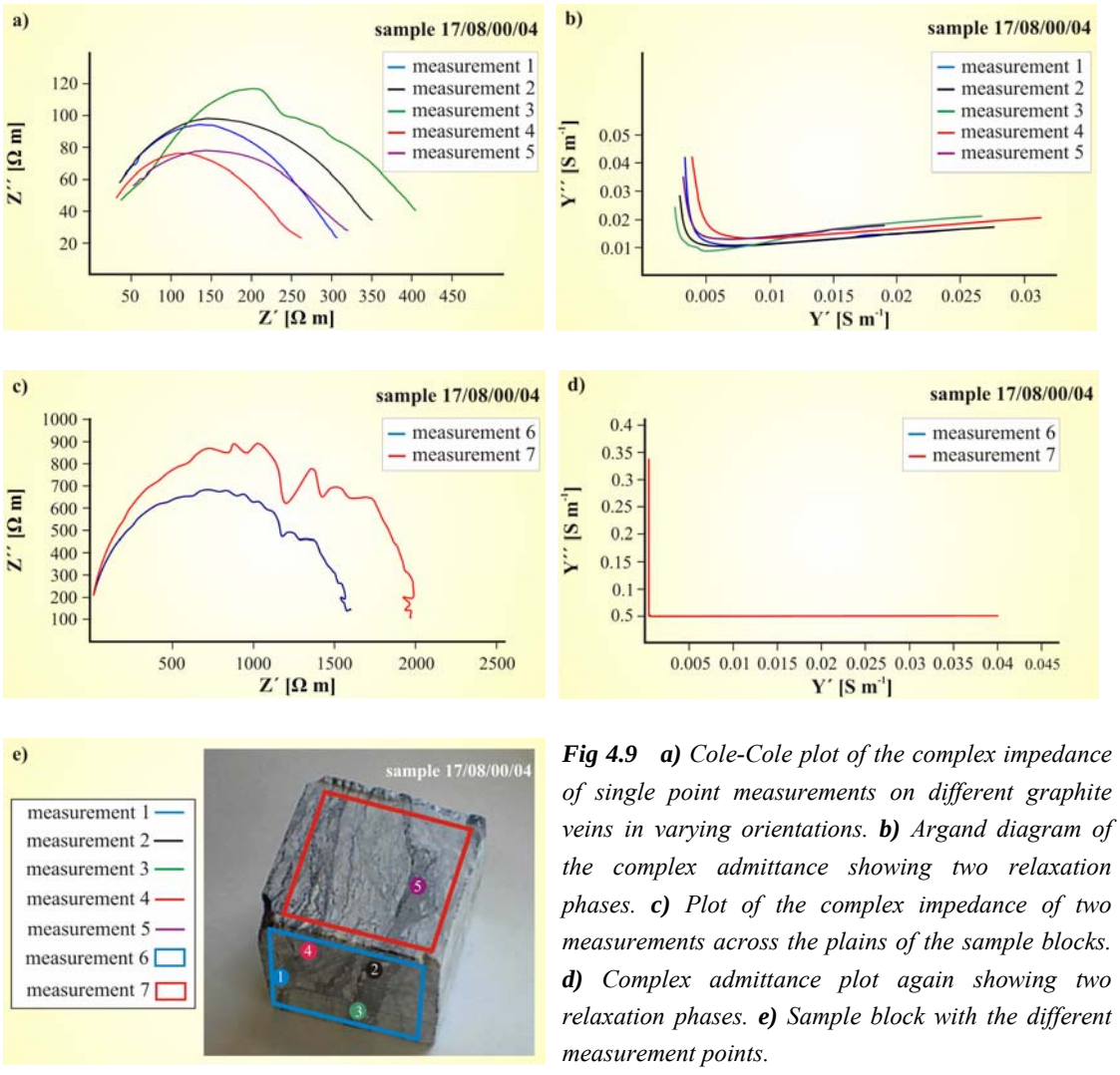

Fig 4.9 ***a)*** *Cole-Cole plot of the complex impedance of single point measurements on different graphite veins in varying orientations.* ***b)*** *Argand diagram of the complex admittance showing two relaxation phases.* ***c)*** *Plot of the complex impedance of two measurements across the plains of the sample blocks.* ***d)*** *Complex admittance plot again showing two relaxation phases.* ***e)*** *Sample block with the different measurement points.*

A decrease in resistivity with increasing pressure is also observable in the plots of the complex impedance in Fig. 4.10 a, b. From 0 to 150 bar, a decrease in resistivity is is obvious with an increase in pressure (Fig. 4.10 a). Accordingly, an increase in conductivity is measureable with increasing pressures accompanied by differing relaxation times τ (Fig. 4.10 b).

All further measurements of this sample of up to 400 bar plot nearly on the same curve. This implies that the resistivity in the displacement currents decreases with increasing pressure up to an equilibrium pressure. Besides the two presented measurements of electronic conductivities, all other measurements under hydrostatic pressures also showed pure ionic conductivities, similar to the measurements shown in Figure 4.7 to 4.9.

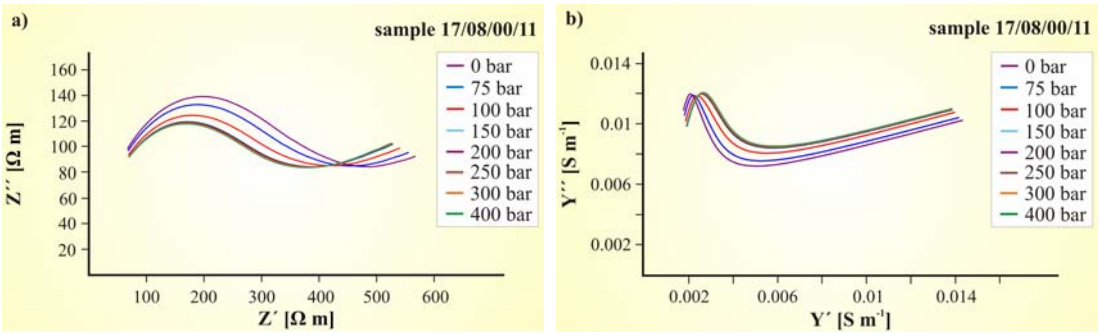

Fig 4.10 ***a)*** *Cole-Cole plot of the complex impedance of sample 17/08/00/04. It shows a combination of displacement currents and linear electrical currents.* ***b)*** *Argand plot of the complex admittance of this sample which shows the existence of three relaxation phases.* ***c)*** *Sample cores drilled parallel to the foliation were measured in the autoclave.*

Both cores of this sample shown in Figure 4.10 c are drilled parallel to the foliation, which is indicated by the preferred orientation of the graphitic stylolites. This is also the direction of the potential difference between the two electrodes. Therefore, a linear conductor parallel to the graphite veins can be assumed for this sample.

In contrast to this measurements and the general microstructural characteristics of the type 2 graphite-bearing marble, hardly no electronic conductivity could be measured along the graphitic stylolites, even on different sample scales (Fig. 4.7 c, 4.8 c, 4.9 e, 4.10 e). This implies, that these interconnected network structures of graphitic stylolites do not generally show electronic conductivity. The reasons for these results have to be discussed, considering other effects on the conductivity potentials of these graphite-bearing marbles.

4.5. DISCUSSION

The data presented in Figure 4.10 and table 4.1 shows the direct relationship between electronic conductivity and the orientation of the graphite fabric elements. Accordingly, interconnected graphite veins have been correlated with crustal anomalies of electrical conductivity (Alabi et al., 1975; Duba & Shankland, 1982; Frost et al., 1989; Mareschal et al., 1992). A combination of conductivity by saline fluids and graphite, as also observed by Leger et al. (1996) is obvious in the presented data (Fig. 4.10 a, b). The type 2 of the graphite-bearing marbles only occurs along the outer rims of dome structures. This shows, that the recognised ring structures in the magnetotelluric data of

pressure [bar]	bulk resistivity core 1 R [Ω m]	bulk resistivity core 2 R [Ω m]	estimated depth [m]
0	542,6910		0
25		400,9720	91
50		425,8540	182
75	537,6420	433,8620	273
100	523,2600	433,0040	364
150	511,3260	432,7180	545
200	511,0200	433,2900	727
250	509,4900	432,4320	909
300	508,8780	431,2880	1091
400	506,4300	430,7160	1455
500		428,7140	1818
600		426,7120	2181
700		424,4240	2545
800		422,9940	2909
		413,8420	

Table 4.1 *Electronic resistivity components of the two cores of sample 17/08/00/11 with increasing pressure. The data was obtained by impedance spectroscopic measurements in an autoclave apparatus. The estimated depth was calculated after a pressure gradient of 2.75 kbar/10 km.*

Weckmann et al. (2003) shown in Fig. 4.1 b, also confirms this correlation between crustal conductivity and the brittle-ductile deformed graphite-bearing marbles.

Other conductivity data of graphite-bearing crustal rocks, obtained by previous authors show quite a strong range. Bulk resistivities on sample scale range mostly between 0.02 and a few times 10^3 Ω m and in exception to 10^4 Ω m (Duba & Shankland, 1982; Mareschal et al., 1992; Duba et al., 1994; Nover et al., 1998; Fowler et al., 2004; Jödicke et al., 2004). This confirms that the data presented above is consistent for crustal conductivity potentials. The range of the published data shows, that quite a strong variation is measurable in the conductivities of graphite-bearing rocks.

Reasons for the relative strong deviation between the above stated data can be manifold. They have to be considered and evaluated individually for every geological setting of the measured samples. Commonly conductivities of graphite-bearing rocks are also scale dependant. A variety of factors described in the following, may influence the conductivity potentials of graphite-bearing rocks to quite some extent.

A first important factor on the conductivity of graphite-bearing rocks is the composition of the conducting minerals. Even if graphite is the main interconnected conducting phase, the total conductivity varies with the volumetric content and the degree of connectivity of other conducting minerals included in the rock. Fowler et al. (2004) presents data which shows, how resistivity data varies with respect to the relative

volumetric content of graphite, pyrite and hematite. The same dataset shows two samples from a locality with a nearly identical content of conducting minerals, but with differences in resistivity by one order of magnitude.

Another influencing factor on conductivities of interconnected graphite in rocks is the degree of the graphite crystallinity. Raab et al. (1998) describes differences in resistivity of 5 orders of magnitude between low grade metamorphic black shale and bituminous black shale. The latter had undergone burial diagenesis to a maximum temperature of 150° C. The molecular structure of these samples lies between the beginning of oil formation and anthracite. In contrast, the low grade metamorphic black shales had been influenced by a thermal metamorphism of 250 – 280° C. Raman investigations showed that the molecular structures of these samples lie between anthracite and graphite (Raab et al., 1998).

Similarly, differences in resistivity within the graphite molecular structures are to be expected with varying degrees of crystallinity. One aim of this work was, to quantify this effect by correlating graphite crystallinities (see chapter 3) with the complex impedance spectroscopic measurements. Unfortunately, this was not possible as only one sample showed electronic conductivity as discussed above. Secondly all the samples were of nearly uniform high crystallinity.

Thirdly, the conductivity of graphite-bearing rocks is also dependant on the thickness of the graphite veins. It can be calculated to the cross sectional area of the conductor. Therefore, this influence can be quantified after equation [4.2] for the intrinsic resistivity and after equation [4.3] for the intrinsic conductivity. Katsube & Mareschal (1993) showed in model calculations, that a pore lining of connected graphite films of 50 to 200 Å thickness will produce bulk resistivities of a few 100 Ω m. Mareschal et al. (1992) shows resistivity data for graphite films of a thickness of 30 to 300 Å in samples of the Kapuskasing gneisses of a few times 10^3 Ω m. Graphite crystallinities in these samples are of disordered graphitic carbon.

A fourth influencing factor are the microstructures of the graphite in the conducting veins. If the basal plains of the graphite are oriented randomly in the graphite veins, the interconnection of the graphite crystals is also randomly. This implies that differences in conductivity can occur due to anisotropic conductivity potentials parallel and perpendicular to the basal plains of graphite. Accordingly, the degree of interconnectivity of the graphite is then more random, which also affects the conductivity. Even for preferred oriented graphite in the graphitic stylolites, the conductivity potentials of the stylolites are still dependent on the degree of interconnectivity between the graphite crystals. Therefore, the

conductivity depends on whether the graphite basal plains are partially or commonly interlocked between the single crystals. The local textures of the fine-grained graphite veins could be determined for example by electron backscatter diffraction (EBSD).

Another important microstructural influence in this respect is the grain-size distribution of graphite within the graphitic stylolites. The degrees of interconnectivity of the graphite crystals may vary to quite some extend within graphitic stylolites or veins, according to the grain-size of the graphite crystals. This applies also to the crustal conductivities of the graphite-bearing rocks. After Frost et al. (1989) graphite-bearing rocks with grain sizes of 1 cm to 0.1 mm are in the range of high crustal conductivities, whereas rocks of the same type with bigger grain sizes range below these conductivities. As this gradient is significantly steep, this influence is also scale dependant. Grain sizes may change for example between shear zones and host rock on a m scale within the crust.

Another influencing factor in conductivity measurements are the microfabrics of the host rock. After Katsube & Mareschal (1993) measurements of the bulk rock resistivity showed, that the resistivity measured parallel to the foliation is lower than the resistivity measured perpendicular to the foliation. One reason may be the interconnection of conductive minerals along the foliation planes, due a shape preferred orientation. Another reason could be that a interconnected fluid network is present parallel to the foliation planes. In combination this could result in additional ionic bridging of electronic conductors.

Additionally, the graphite network intensity is an important factor influencing the conductivity of graphite-bearing carbonates. A higher graphite network intensity of interconnected graphitic stylolites and veins would also produce higher overall conductivities. As shown above, the network densities can vary to a great extend within a crustal shear zone on a cm to m scale. Therefore, this is important for the differentiation of the conductivities on sample scale. Accordingly, caution is necessary for the upscaling of these measurements to crustal dimensions.

The effects of pressure on the conductivity of rocks also have to be considered. The effects of pressure on the resistivity of basalt are shown in Figure 4.5 b. Also Shankland et al. (1997) describes an increase in conductivity with increasing pressure. As discussed below microcracks, permeability, fluid percolation and a reconnection of solid conductors by the closure of microcracks are the main factors for these observations.

For the quantification of conductivity potentials of (sub)surface crustal rocks, microcracks have to be taken into account (Glover & Vine, 1992; Katsube & Mareschal,

1993). As the results shown in table 4.1 and in Figure 4.10 a, b indicate, a reduction of resistivity in linear and displacement currents with increasing hydrostatic pressures is measurable. After equations [4.2] and [4.3], this is only possible for electronic conductivity, due to the reconnection and extension of the graphitic conductors. Therefore, a closure of microcracks had been obtained by increasing the hydrostatic pressures.

Microcracks are either upper crustal tensional microcracks, or originate due to lower crustal hydrofracturing. Therefore, careful investigations on these influences are necessary for the quantification of crustal conductivity potentials. Tensional or tensile microcracks develop, as crustal segments are lifted to upper crustal levels. They develop when σ_3 becomes negative and tensional stresses evolve. As the development of tensile microcracks in dependent on σ_3, they show a preferred orientation orthogonal to σ_3.

Hydrofractures emerge from extensional crustal stresses in combination with fluid overpressures. Therefore, hydrofractures also show a preferred orientation relative to crustal stress field. As microcracks and open hydrofractures are reclosed at conductivity measurements under confining hydrostatic pressures, it is questionable whether these measurements are allways in accordance with deeper crustal conductivities. This matter will be discussed in more detail in the following. The effect of remineralised veins and microveins on the conductivity potentials have to be revealed by microstructural investigations.

The conductivity measurements under hydrostatic pressures of a variety of samples, showed no electronic conductivities with the exception of only one sample (Fig. 4.10 and table 4.1). The investigation of the microstructures by qualitative optical microscopy and cathodoluminescence microscopy (CL) revealed, that the graphite-bearing marbles show microcracks, which very frequently are healed as microveins by a younger generation of calcite. These microveins show a preferred orientation within the different generations.

A first generation of the microcracks originated most likely as hydrofractures, due to extensional stresses during the cretaceous break up of pangaea between Africa and South America. The crustal stresses are documented by widespread intrusions of cretaceous mafic dykes in the vicinity. This is also visible on the satellite image in Figure 2.2. Due to the fluid migration in these microcracks, the vein mineralisation of calcite formed this observed generation of microveins, which show different cathodoluminescence colours as the marble host-rock.

The latest microcracks may have originated due to tensional stresses near (sub)surface crustal levels. It is obvious from table 4.1, that open microcracks still exist up

to estimated depths of 2900 m. Microcracks up to this depth are generally related either to hydrofracturing or to tensional microcracks, resulting from local crustal stress concentrations due to stress inhomogeneities in the crust.

As shown in Chapter 2.3.4, most of the mineralised microcracks cut the graphite veins and network structures on a microscopic scale within 200 µm and several mm. This implies, that the electronic conductivity is cut and disturbed on a µm to mm scale by microcracks and microveins. The increasing hydrostatic pressures could not close the mineralised microveins to reconnect the disturbed graphite veins. Therefore, conductivity measurements even under high pressures did not show any electronic conductivity in the samples, except for the sample of Figure 4.10. In this sample the graphite veins are undisturbed by microveins.

The CL investigations of the microveins also revealed, that the graphitic stylolites themselves often opened due to hydrofracturing or tensional stresses. The remineralisation of the opened graphitic stylolites by calcite disturbed the interconnectivity of graphite along the graphitic stylolites. Therefore, they are not capable of transporting electrical charge over distances greater than on the described scale.

In contrast, the measured magnetotelluric anomalies of high electrical conductivity are crustal phenomena calculated on a kilometer scale. Therefore, the exact localisation to a sample scale of the conducting crustal material is barely possible. Differences in the bulk conductivities of graphite-bearing marbles, which occur on sample scale due to the above mentioned factors, are mostly not measurable in magnetotelluric profiles. This scale incoherence implies that only a mean and thus more general quantification for the conductivity potential of graphite-bearing marble, would be applicable for calculations of magnetotelluric data.

The sample of Figure 4.10 is from farm Epako Süd, where no magnetotelluric measurements have been conducted. This is the reason, why the above described relationship between graphitic stylolite fabrics and electrical conductivity cannot directly be related to the magnetotelluric measurements by Ritter et al. (2003) and Weckmann et al. (2003). Nevertheless, they give a first assumption for the conductivity potentials of this type of graphite-bearing marbles in a general regional context. Compared to the resistivities from the magnetotelluric data by Ritter et al. (2003), this data fits very well into their calculations of the surface anomalies of high electrical conductivity (Fig. 4.1 b and table 4.1).

According to the discussed origin of the described microcracks, it is still debatable whether the conductivity potential of the graphite-bearing marble increases with increasing depth, to the large extends implied by the data in table 4.1. A decrease of resistivity should be related to a decrease of tensile microcracks with an increasing depth. The amount of tensile microcracks decreases rapidly to a depth of about 1000 m.

This an approximate depth related to Mohr criteria, where a maximum normal stress (σ_n) is allowed for tensional microcracks in relationship to the shear stress. The closure of unhealed extensional cracks and microcracks, by greater confining lithostatic pressures in deeper crustal levels, is still a matter of debate. In general, the closure of microcracks in the crust is dependant on the permeability of the microcracks and on the amount of crustal fluids percolating the rocks.

After Weiss et al. (2002) ultrasonic wave velocity measurements show, that dry microcracks of different kind of marbles close completely at approximately 75 MPa confining pressure. Most of the microcracks are already closed between 20 and 50 MPa in these measurements. This is supported by the measurements shown in table 4.1, where the electronic resistivity continuously reduces even to pressures of 800 bar, due to the continuous closure of the microcracks with increasing pressure.

These results only apply for dry rock material, whereas pore fluids and therefore fluid overpressure in the crust are more likely to be expected. As KTB reports by ELEKTB-Group (1997) state, ionic conduction by hydraulic conductors was still measured at depths below 3850 m. Saline fluids were observed to depths of 6000 m. This implies, that the fluid overpressure may still be prevailing in these crustal depths. In contrast, the impedance spectroscopic pressure measurements were conducted with porous electrodes to reduce the fluid overpressure in the sample. This was done, to prevent the sample from cracking completely during the measurement. Therefore, the decrease in resistivity of the impedance spectroscopic measurements may not always be directly applicable to crustal conditions, since the fluid overpressure in the sample was released through the porous electrodes.

Ultrasonic wave velocity measurements show, that the wave velocities are relatively stable with increasing pressure for saturated microcracks, as the lacking compressibility of the pore fluid does not allow further closure of the microcracks (Weiss et al. 2002). Investigations on microscopic scale conductivity by Losito et al. (2001), also shows this correlation between saturated and unsaturated microcracks and electrical conductivity measurements with increasing pressures.

To quantify the conductivity potentials of these Damaran graphite-bearing marbles, a regional investigation of the intensity, distribution and orientation of the healed and unhealed microcracks has to be conducted. The investigations on the cretaceous stress field would help to understand the allocation, orientation and distribution of hydrofractures in the area of the magnetotelluric profile.

In addition, a qualitative and quantitative investigation of the preferred orientation of the microveins would give some indication about the origin of the different microcracks. Tensional microcracks are oriented perpendicular to σ_3 and therefore should be distinguishable from the extensional hydrofractures related to the cretaceous stress field. For further confirmation samples from boreholes can help to verify the origin of the microcracks and the conductivity potential of the graphite-bearing marbles.

A further step would be to correlate conductivity measurements with the degree of graphite network intensity. A quantification of this influence would be helpful for the interpretation of magnetotelluric profiles. Accordingly, EBSD investigations on the microstructures of graphitic stylolites, and the correlation of conductivity measurements with the degree of graphite crystallinity would further enlighten the complex matter of graphite conductivity in geological materials.

CHAPTER 5

STABLE ISOTOPE ANALYSIS

Stable isotopes as $^{13/12}C$ and $^{18/16}O$ are a useful tool to characterise carbonate rocks. Isotopes occur when elements build atoms with different numbers of neutrons in the atomic nucleus. Most elements consist of one stable and several unstable isotopes. The natural occurrence of the different isotopes of an element varies extensively. For carbon two main stable isotopes exist with an occurrence for ^{12}C of 98.89 % and for ^{13}C of 1.11 % respectively (Nier, 1950). ^{14}C isotopes which are well known for radiometric dating, only occur as traces in terrestrial materials. The frequency of occurrence of oxygen isotopes also varies with 99.763 % for ^{16}O isotopes, with 0.0375 % for ^{17}O isotopes and with 0.1995 % for ^{18}O isotopes (Garlick, 1969).

Molecules that consist of heavier isotopes are more stable, as the dissociation energy needed to break-up the molecules is higher than for lighter isotopes (Fig. 5.1). Due to the lower vibrational energies of the heavier isotopes, the bonding energy is higher between heavier isotopes than for molecules with lighter isotopes. Therefore, most inorganic molecules like crustal minerals tend to incorporate heavier isotopes, while the lighter isotopes are enriched in gaseous and fluid phases. Most biological processes are also based on the differences in dissociation energies and lead to a strong fractionation of carbon isotopes. Photosynthesis effects of C_3-plants, which constitute 90% of all plants today, results in a depletion of the heavier ^{13}C isotopes relative to ^{12}C. C_4-plants show a similar depletion effects but to a less great extent.

Isotope fractionation can originate either from kinetic or equilibrated isotope exchange reactions. The described biological depletion of ^{13}C results from kinetic isotopic fractionation, as lighter ^{12}C isotopes are bound in organic molecules, whereas ^{13}C is concentrated in CO_2. Kinetic fractionation is therefore a irreversible process.

After Matthews et al. (1983) and Giletti (1985) there are three main mechanisms for kinetic isotope fractionation between minerals and fluids. One mechanism is controlled by solution and precipitation processes, where mineral grains are dissolved and crystallise to bigger grains with a lower sum of total free energy. Due to the dissociation of the crystal lattices by solution processes atoms are movable and free to form new molecules and crystals. As heavier isotopes are preferably included into molecules with high rates of covalent bonds, isotope fractionation takes place during crystallisation. Lighter isotopes are enriched in the fluid phase and are mostly removed by the mobile fluids.

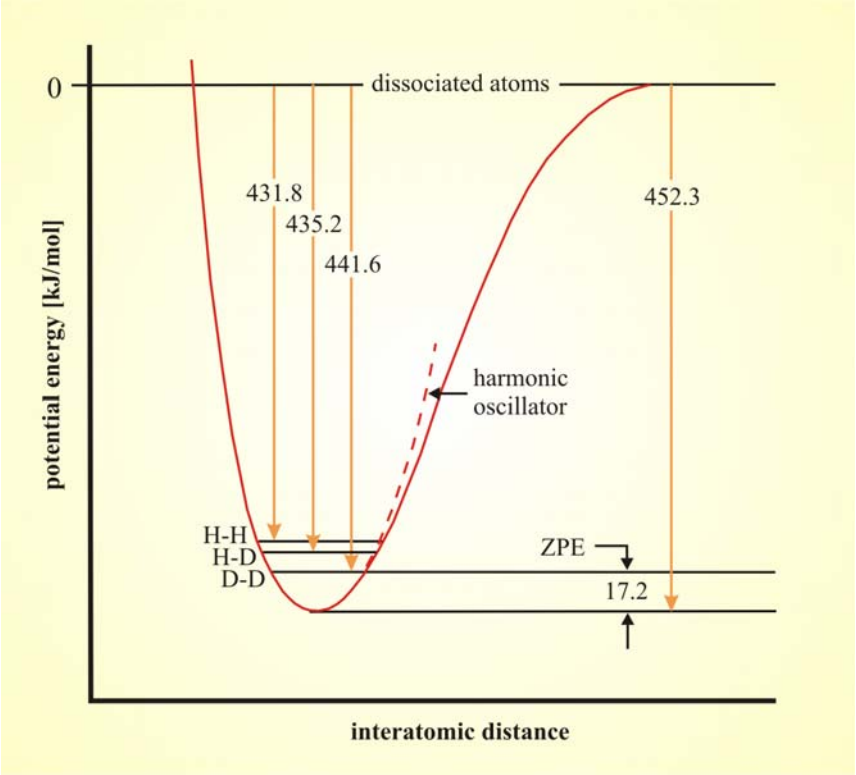

Fig. 5.1 *Potential energy-level diagram for different isotopic species of the hydrogen molecule. The differences of the zero-point energy levels (ZPE) for H_2 is shown for different fundamental vibrational energies. The energy required for the dissociation of of the different species are indicated by the arrows. Figure after O´Neil (1986).*

Further mechanisms of kinetic isotope fractionation are diffusional processes, where the exchange of isotopes occurs between interfaces without a change in phase morphology. A third mechanism is a chemical reaction between two phases with the enrichment of lighter isotopes in the fluid phase.

For kinetic isotope fractionation fluid phases play an important role, whereas equilibrated isotope exchange reactions only occur when fluid phases are absent. Equilibrated isotope fractionation is triggered by thermodynamic factors. Therefore, it is dependent on changes to PT-conditions, where diffusional processes and crystallisation are possible. In these regimes, isotopic fractionation occurs due to isotope exchange reactions between at least two mineral phases. During the isotope exchange reactions, the isotopic composition of the involved phases is approximated constantly between the phases. Equilibrated isotope exchange reactions between solid phases are mainly controlled by temperature. Therefore, several calibrations for geothermometric calculations are discussed in the literature. An overview about the geothermometric calibrations for calcite-graphite thermometry is compiled by Valley (2001).

The isotopic composition of a mineral or a fluid phase is described by the isotopic ratio δ. This ratio is obtained between the concentrations of different isotopes from one element within a phase. The isotopic ratios are calculated to an international standard as for carbon by:

$$\delta = \left[\frac{(^{13}C/^{12}C)_{smp}}{(^{13}C/^{12}C)_{std}} - 1 \right] x10^{3} \qquad [5.1]$$

The isotopic ratio δ is expressed in ‰. Carbon and oxygen isotope ratios are nowadays calculated over the V-PDB standard (Pee Dee Belemnite), whereas older data is also calculated over the SMOW standard (standard mean ocean water). The isotope ratios used in this work are calculated over V-PDB. Cited data calculated to the SMOW standard, is here recalculated to the V-PDB standard for comparison reasons.

Some isotopic ratios are characteristic for different kind of crustal rocks. Figures 5.2 a, b show these for carbon and oxygen isotopes. They vary quite distinctively within the crustal and atmospheric material, depending on the isotopic composition of their base material and the processes of formation. In general, a organic influence in the crustal material shifts isotopic ratios to lighter values. Fluids and gaseous phases are also mostly characterised by lighter isotope ratios, whereas crustal material generally includes heavier isotope ratios.

As isotopic ratios are changed by isotope exchange reactions, the quantification of these isotope fractionations is important for the interpretation of the isotopic ratios. The fractionation factor α between two different phases is calculated as the overall ratio between the isotopic compositions of the two phases A and B:

$$\alpha_{A-B} = \frac{R_A}{R_B} \qquad [5.2]$$

If all isotopes are exchanged in an equilibrated system, the fractionation factor will be identical to the equilibrium constant of the two phases for a specific temperature. Therefore, this fractionation factor α is very important to study the isotopic exchange reactions and rates between two phases at certain temperatures.

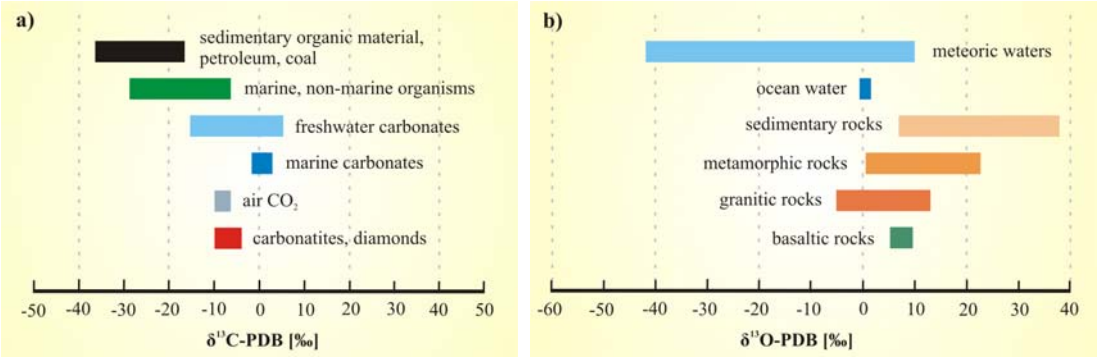

Fig. 5.2 ***a)*** *Carbon isotopic composition of different crustal and atmospheric phases. Organic material generally plots to lighter carbon isotope ratios.* ***b)*** *Oxygen isotope composition of different geological materials. Crustal rocks generally plot to heavier oxygen isotope ratios. Both figures after Hoefs (1997).*

According to equation [5.2] the fractionation factor α for carbon between calcite and graphite will have to be calculated as follows:

$$\alpha_{CaCO_3-C_{graphite}} = \frac{\left(\frac{^{13}C}{^{12}C}\right)_{CaCO_3}}{\left(\frac{^{13}C}{^{12}C}\right)_{C_{graphite}}} \qquad [5.3]$$

Another dimension for the characterisation of isotope fractionation is calculated from the isotopic ratios δ. The quantification of the isotopic fractionation $\Delta_{(A\text{-}B)}$ is calculated for two isotopically equilibrated phases A and B, by the subtraction of the isotopic ratios δ of the two phases. The carbon isotopic fractionation for calcite and graphite is calculated as follows:

$$\Delta_{(cal-gr)} = \delta^{13}C_{calcite} - \delta^{13}C_{graphite} \qquad [5.4]$$

The isotopic fractionation $\Delta_{(A\text{-}B)}$ is expressed in ‰. It is generally used to describe geothermometric correlations and to correlate isotopic fractionations with metamorphic grades. It can also be calculated from the fractionation factor α with some neglectable differences by the following equation:

$$\Delta_{(cal-gr)} \approx 10^3 \ln \alpha \qquad [5.5]$$

5.1. STABLE ISOTOPES OF MARBLES AND GRAPHITE

For carbonates and (in)organic carbon a range of isotope ratios are characteristic. As reported in the literature, carbonates are distinguished as heavy carbonates with carbon isotope ratios of $\delta\ ^{13}C > +20$ ‰ and as light methane with $\delta\ ^{13}C > -80$ ‰ (Hoefs, 1997). For marine carbonate sediments, the mean range of $\delta\ ^{13}C$ ratios vary from –2 to +3 ‰ (Fig. 5.2 a). For graphite the isotopic ratios reported in the literature range mainly between –35 to –2 ‰. Variations in the carbon isotope ratios of carbonates and graphite depend mainly on the origin of the carbon material and on the metamorphic history.

Additionally carbonate rocks are characterised by oxygen isotopes. Oxygen isotope ratios are very good indicators for fluid/rock interactions (Hoefs, 1997). As described above, kinetic isotope fractionation between fluids and rocks are controlled by solution-precipitation processes, by chemical reactions and by diffusion. By these processes, the primary isotopic compositions of the mineral and fluid phases are changed. Therefore, the $\delta\ ^{18}O$ ratios vary quite strongly within different carbonate rocks.

This variation is documented in a database of oxygen isotope ratios from precambrian carbonates and other crustal rocks after Shields & Veizer (2002) (Fig. 5.3). These $\delta\ ^{18}O$ ratios generally range between –25 and 0 ‰. The data shows, that there is a slight positive trend of the mean archean to neoproterozoic oxygen isotope ratios to heavier $\delta\ ^{18}O$ ratios. This may be related to the increasing photosynthetic activity during the proterozoic. As these isotope ratios are gathered from carbonates worldwide, primary oxygen isotopic signatures for seawater are postulated throughout the precambrian (Brasier et al., 1990; Burdett et al., 1990; Kaufman et al., 1991; Veizer et al., 1992; Hall & Veizer, 1996).

Kinetic exchange reactions of oxygen isotopes between associated mineral and fluid phases, mainly occur due to the opening of fluid pathways during deformation. Accordingly, the quantification of isotope fractionation may give some hints on the tectono-(metamorphic) history of the rocks. Kirschner & Kennedy (2001) show the effects of fluid flow on stable isotope ratios in carbonate-hosted fault rocks. The interpretation of the oxygen isotopic ratios becomes difficult, when multiple isotope fractionations have occurred due to a complex deformational path and magmatic intrusions. In general, the interpretation of oxygen isotope fractionations becomes more significant, if several mineral phase have exchanged isotopes with the fluid phase in kinetic isotope fractionation. Additional indications on oxygen isotope exchange reactions may be revealed, by considering primary oxygen signatures for seawater at specific geological times.

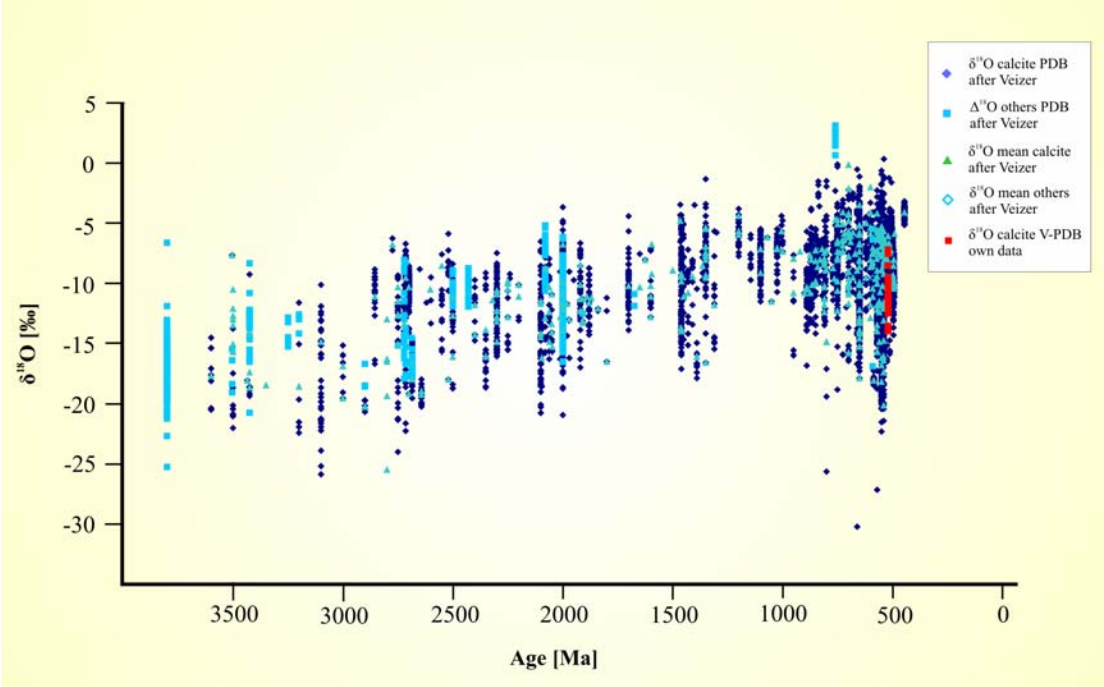

Fig. 5.3 *Precambrian oxygen isotope ratios for carbonates and other crustal rocks. Own measurements are plotted in red signatures into the diagram with a neoproterozoic age of 520 Ma. Database after Shields & Veizer (2002).*

The carbon isotope composition of precambrian rocks and organic material after Shields & Veizer (2002) is shown in Figure 5.4. The precambrian carbon isotope ratios range between –18 and +16 ‰, while the mean precambrian δ ^{13}C ratios for calcite plot within –5 and +6 ‰. This is similar to the present day range for carbonates (Fig 5.2 a). The carbon isotope ratios of organic matter range between –46 to –12 ‰. This shows that there is a significant difference between organic and inorganic carbon isotopes. This allows an estimation about an organic or inorganic formation of carbon bearing mineral phases. This estimate is only possible, when kinetic or equilibrated isotope exchange reactions can be excluded for the measured samples.

Reasons for the variation of carbon isotope ratios in carbonate rocks as documented in Figure 5.4 can be manifold. Differences already occur during the formation and sedimentation of the carbonates. Isotope fractionation already occurs during the precipitation of carbonate. With increasing seawater temperature, δ ^{13}C increases in calcite within the equilibrium between dissolved bicarbonate (HCO_3^-) and solid calcite. In contrast, the carbon isotope ratio between atmospheric CO_2 and dissolved bicarbonate decreases strongly with increasing temperatures. This implies that an increase of δ ^{13}C only occurs with decreasing seawater temperatures (Stosch, 2002).

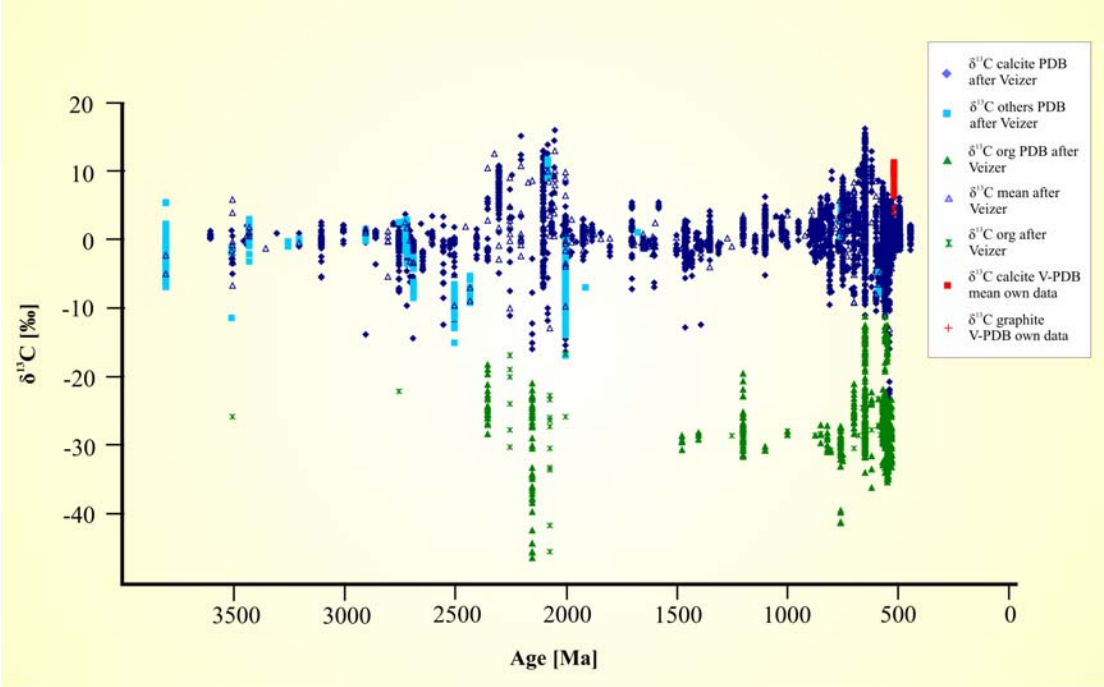

Fig. 5.4 *Precambrian carbon isotope ratios for carbonates, other crustal rocks and organic material. Own measurements for calcite and graphite are plotted into the diagram in red signatures with a neoproterozoic age of 520 Ma. Database after Shields & Veizer (2002).*

Additionally, the carbon isotopic composition of the seawater is changed due to photosynthetic activity of organic material. As organic material concentrates lighter ^{12}C isotopes due to photosynthesis by diffusional processes (Park & Epstein, 1960), dissolved bicarbonate is enriched by ^{13}C isotopes relative to CO_2 in marine environments. In the equilibrium between dissolved bicarbonate and calcite, ^{13}C isotopes will therefore also be enriched in calcite. Additionally, crystallisation processes also fractionate isotopic systems, as chemical bondings are energetically more stable by incorporating heavier isotopes into molecule- and lattice structures (O´Neil, 1986) (Fig 5.1).

The primary isotopic composition of carbonate rocks can change distinctively during deformation and metamorphism. If fluids penetrate the rock pervasively or discrete along shear and fault zones, the isotopic composition of the carbonates can be changed due to isotopic exchanges with the fluid. This kinetic isotope fractionation is irreversible, due to the mobility of the fluids across the crustal segments. Secondly the isotopic composition of carbonates can change, due to the isotopic exchange reactions between carbonates and other carbon bearing mineral phases like graphite. The extent of equilibrated isotope fractionations is temperature dependent (Criss, 1991), and for isotope exchange by diffusion processes also dependent on diffusion rates (Chacko et al. 1991; Hoefs, 1997).

According to the origin of graphite, syngenetic and epigenetic graphite is distinguished. Syngenetic graphite originates from the metamorphism and graphitisation of primarily organic carbon material. Carbon atoms are arranged in a hexagonal crystal structure during graphitisation, which forms the basal plains of the graphite crystals. Therefore, syngenetic graphite commonly has preserved the organic carbon isotope ratios, and in these cases can be related to organic origin. Epigenetic graphite originates from the precipitation of graphite from CO_2- and/or CH_4-bearing fluids. Accordingly, this graphite is characterised by the lighter isotopic ratios of the magmatic or deep crustal fluids. This implies that they can be differentiated from the syngenetic graphite by their different isotopic compositions (Weis et al., 1981).

The primary carbon isotopic ratios of calcite and graphite in graphite-bearing marbles are commonly not detectable, due to isotope exchange reactions between the two phases during metamorphism. The isotope exchange is controlled either by diffusional processes mainly at lower temperatures, or by crystallisation at higher temperatures. Chacko et al. (1991) showed experimental investigations on oxygen isotope exchange rates within calcite under different temperatures. These experiments revealed that at temperatures of 500° C, already 78 % of the oxygen isotopes had been exchanged mainly by diffusion. At temperatures of 800 to 950° C, about 80 to 86 % of the oxygen isotopes had been exchanged due to crystallisation. For equilibrated isotope exchange reactions between calcite and graphite, a minimum temperature of about 600° C is postulated (Valley & O´Neil, 1981; Chacko et al., 1991).

5.2. CHARACTERISATION OF THE GRAPHITE-BEARING MARBLES

The measured samples comprise all types of graphite-bearing calcite-marbles distinguished by the microstructural analysis. The composition of the stable isotopes of calcite and graphite have been measured for all types of graphite-bearing marbles. The main sample localities are pointed out in Figure 2.1. The samples were selected, to characterise the different microstructural types of graphite-bearing marbles in the regional context by their isotopic composition. The samples and their according carbon and oxygen isotope ratios are shown in table 5.1.

As stated above, the interpretation of oxygen isotope ratios of carbonates generally may be difficult, especially in complex deformational regimes. Also the existence of magmatic intrusions indicates the possibility of associated CO_2-bearing fluids percolating the marble host rock. Therefore, this complicates the interpretation of oxygen isotopes furthermore. As field investigations and the microstructural analysis revealed, complex deformational structures, as well as related granitic intrusions have to be considered for the

interpretation of the measured oxygen isotope ratios. Additionally, the investigated marbles are pure graphite-bearing calcite-marbles. Therefore, no additional mineral phase can be considered for the analysis of the oxygen isotope ratios.

The measured data is also plotted into the overall distribution of precambrian $\delta\ ^{18}O$ ratios (Fig. 5.3). It is obvious from this plot, that the measured data fits well into the general distribution for neoproterozoic oxygen isotope ratios. However, uncertainties exist about the initial oxygen isotope ratios, because of the possible overlap of multiple fluid-rock interactions.

As primary oxygen isotope signatures have been postulated for precambrian seawater, it should be possible to characterise, whether the composition of oxygen isotopes have changed after formation and sedimentation. Kumar et al. (2002) and Ray et al. (2003) show the evaluation of primary oxygen isotope ratios of the neoproterozoic formations of the Vindhyan Basin. Following these authors the primary oxygen isotope ratio for neoproterozoic seawater lies within the range of $\delta\ ^{18}O = 7.5 \pm 2$ ‰. This implies, that the oxygen isotope ratios measured in the own samples (table 5.1), would approximately fit into this range. Following this, a fluid rock interaction by kinetic isotope fractionation can be excluded for these samples.

The same general uncertainties regarding the initial carbon isotope ratios exist for calcite and graphite in the measured samples. The own carbon isotopes are also plotted into the database of precambrian carbon isotope ratios of Figure 5.4. They are differentiated between the plots of calcite and graphite. From this plot it is obvious, that both fit quite well into the general pattern of the precambrian carbon isotope ratios. The carbon isotope ratios of graphite and calcite plot explicitly above the range of organic isotope ratios.

This implies that an organic origin of either graphite or calcite cannot be extrapolated from the isotopic data anymore. Secondly, the data shows that the carbon isotope ratios plot clearly above the mean isotopic range for carbonate rocks. Therefore, they may be considered as isotopically heavier than the average neoproterozoic carbonates. As the isotopic ratios of calcite and graphite additionally plot in the same range, it is obvious that are very similar. This indicates, that equilibrated isotope fractionation may have occurred between calcite and graphite.

Therefore, isotope fractionation values $\Delta_{(cal\text{-}gr)}$ between calcite and graphite were calculated for the measured samples. They can reveal indications on the equilibration of the isotope fractionation. Consequently, an equilibrated isotope exchange between these

two minerals would allow geothermometric calculations. In this case, estimations on the metamorphic temperatures during isotope exchange would be possible.

5.3. CALCITE-GRAPHITE THERMOMETRY

Geothermometry by calcite-graphite isotope fractionation is strongly dependent on the equilibration of the isotope exchange between the two phases. After Valley (2001) there are three basic conditions to be fulfilled for stable isotope thermometry. Firstly, the isotope fractionation between the mineral phases have to be equilibrated at one single metamorphic event. Secondly, the analysis of isotope ratio is accurate at the appropriate scale. Thirdly, the isotope fractionation has to be sufficiently sensitive and is accurately calibrated.

The quantification of the equilibration of the isotope exchange $\Delta_{(cal\text{-}gr)}$ is calculated according to equation [5.4], as the difference between the carbon isotopic ratios of calcite and graphite within a sample. A range of thermometer calibrations for equilibrated isotope exchange reactions is shown in Figure 5.5. $\Delta_{(cal\text{-}gr)}$ is also empirically used, to characterise the metamorphic facies of the measured samples during isotope exchange (Fig. 5.6). As $\Delta_{(cal\text{-}gr)}$ is temperature dependent, the variation within different values of the isotope fractionation $\Delta_{(cal\text{-}gr)}$ decrease to a great extend with increasing temperatures. Figure 5.6 shows the variation within $\Delta_{(cal\text{-}gr)}$ from unmetamorphosed to granulite facies metamorphism.

Additionally, the overall value for $\Delta_{(cal\text{-}gr)}$ decreases as equilibrium isotope exchange is reached. Therefore, the histogram for $\Delta_{(cal\text{-}gr)}$ of the amphibolite facies plots mainly between 3 and 8 ‰, and for the granulite facies between 2 and 5 ‰. This implies, that an equilibration of isotope exchange is only reached in amphibolite to granulite facies metamorphism.

The $\Delta_{(cal\text{-}gr)}$ values from the measured samples (table 5.1), plot in an according histogram between 2 and 4.5 ‰, where 90 % of the samples plot between 2 and 3.5 ‰ (Fig. 5.7 a). This implies, that the samples have equilibrated isotopically between calcite and graphite in granulite facies metamorphism. Therefore, the isotope fractionations are appropriate to be used to calculate calcite-graphite temperatures by different geothermometric calibrations as shown in Figure 5.5.

A first approximation of the metamorphic temperatures are shown in Figure 5.7 b. In this figure, the isotopic ratios of calcite are plotted against the isotopic ratios of graphite. All measured samples across all microstructural types and sample localities (Fig. 2.1) are

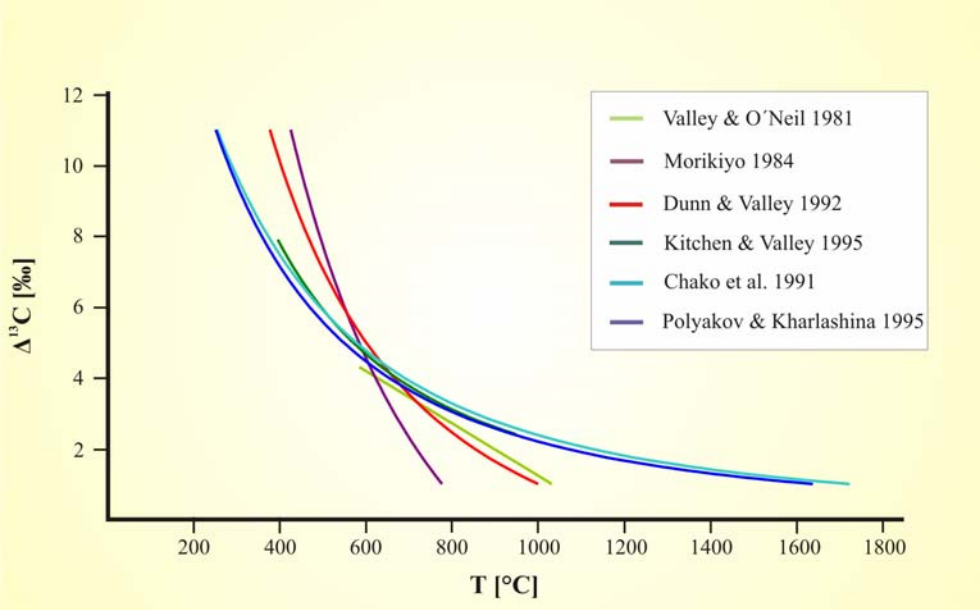

Fig. 5.5 *Different geothermometer calibrations for calcite-graphite carbon isotope fractionations. The geothermometeric calibrations from Valley & O´Neil (1981), Morikiyo (1984), Dunn & Valley (1992), Kitchen & Valley (1995) are empirically derived, whereas the calibration from Chacko et al. (1991) is experimentally derived. The geothermometer after Polyakov & Kharlashina (1995) is theoretically calculated.*

plotted into Figure 5.7 b. It is obvious from this Figure, that they plot all in the same range of metamorphic temperature. The geothermometric calibration for this plot was selected after Valley & O´Neil (1981) as this was the bottom range of temperatures obtained from this data.

The correlation between the between calcite-graphite isotope fractionations and distinct metamorphic temperatures shown in Figure 5.5, is determined either by theoretical calculations (Polyakov & Kharlashina, 1995), experimental calibrations (Chacko et al., 1991) or is empirically derived by the comparison with other geothermometers (Valley & O´Neil, 1981; Morikiyo, 1984; Dunn & Valley, 1992; Kitchen & Valley, 1995). There is still some debate on the correct thermometer calibrations, due to uncertainties in the theoretical calculations as well as in experimental considerations.

After Valley (2001), the geothermometric calibration of Kitchen & Valley (1995) is in excellent agreement with independent petrologic geothermometry at temperatures above 600° C. This applies also to the experimental calibrations of Chacko et al. (1991) and the theoretical calculations of Polyakov & Kharlashina (1995). The empirical calibration of Dunn & Valley (1992) fits data including lower temperatures of the amphibolite facies. For temperatures below 680° C the thermometer calibration of Wada & Suzuki (1983) is more applicable.

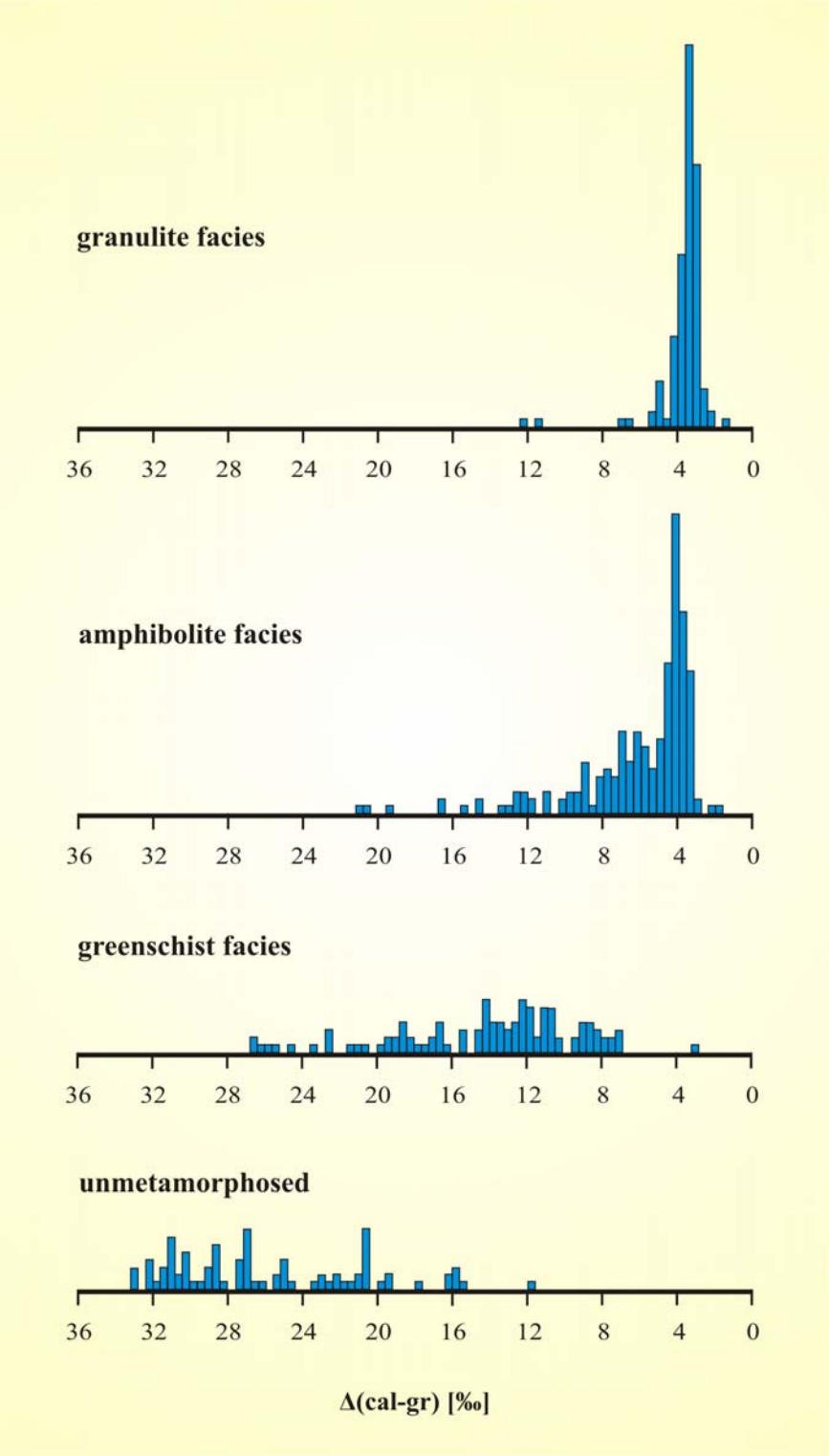

Fig. 5.6 *Histogram of the fractionation between calcite and graphite for several metamorphic grades after Kitchen & Valley (1995).*

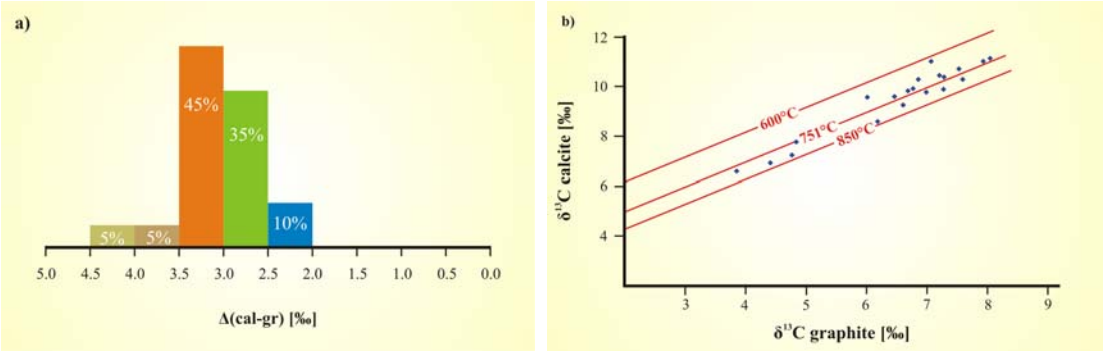

Fig. 5.7 ***a)*** *Histogram of the fractionation between calcite and graphite of the measured samples.* ***b)*** *Plot of the isotopic ratios between calcite and graphite of all measured samples. The metamorphic temperatures were calculated according to the geothermometric calibration of Valley & O´Neil (1981).*

Figure 5.5 shows the plotted thermometer calibrations. It is obvious from this Figure, that the geothermometric calibrations after Kitchen & Valley (1995), Chacko et al. (1991) and Polyakov & Kharlashina (1995) plot with similar gradients. The geothermometric calibrations of Valley & O´Neil (1981) and Morikiyo (1984) however, plot with steeper gradients. This implies that the temperatures gained by the latter are lower with higher fractionations of the carbon isotopes. Therefore the temperature calibrations for the own data were calculated for the most common calibrations used in literature as discussed above (table 5.1).

Because of the different gradients in the geothermometric calibrations, the metamorphic temperatures shown in table 5.1 vary stronger with higher fractionation and temperature values for different calibrations. As these temperatures plot all in the same range across different localities and microstructural types, mean temperatures have been calculated. The standard deviation between the samples show, that this is an appropriate assumption (table 5.1). The implications of these results have to be discussed in detail, regarding the metamorphic and deformational path of the investigated samples.

5.4. DISCUSSION

The investigation of the isotopic composition of the graphite-bearing marbles revealed a mean peak metamorphic temperature of about 788° C across all differentiated microstructural types (Fig. 5.7 b and table 5.1). This is a mean temperature of all geothermometric callibrations calculated for the measured samples. The applicability of the different callibrations will be discussed in the following. Despite the co-existence of brittle and ductile deformational structures within the investigated samples, no differences in metamorphic temperatures are obtained across the distinguished deformational

Sample	calcite		graphite	Δ cal-gr [‰]	Temperature [° C]				
	$\delta^{13}C$ V-PDB [‰]	$\delta^{18}O$ V-PDB [‰]	$\delta^{13}C$ V-PDB [‰]		V-O	D-V	K-V	C et al	P-K
12/08/00/02	9,64	-13,99	6,46	3,19	733	727	782	811	769
15/08/00/01	10,34	-12,20	6,85	3,49	693	702	735	760	721
17/08/00/04	7,80	-11,45	4,84	2,96	759	745	816	849	805
17/08/00/05	10,43	-10,10	7,27	3,16	733	727	782	811	769
17/08/00/10	9,87	-11,20	6,68	3,19	733	727	782	811	769
17/08/00/11	11,20	-10,23	8,03	3,16	733	727	782	811	769
17/08/00/12	9,97	-11,02	6,76	3,20	733	727	782	811	769
17/08/00/13	10,50	-8,49	7,20	3,31	719	718	705	793	752
17/08/00/15	11,07	-10,89	7,92	3,16	733	727	782	811	769
17/08/00/16	6,61	-9,80	3,86	2,75	786	763	854	891	845
17/08/00/17	10,34	-10,34	7,58	2,76	786	763	854	891	845
17/08/00/19	9,82	-12,51	6,98	2,84	786	763	854	891	845
17/08/00/20	10,77	-7,15	7,52	3,25	719	718	705	793	752
17/08/00/21	9,94	-11,65	7,26	2,67	799	773	875	913	866
18/08/00/02	9,61	-11,70	6,01	3,60	679	694	721	745	706
3/10/01/3	9,30	-11,38	6,60	2,70	799	773	875	913	866
3/10/01/4	6,95	-11,68	4,42	2,53	826	793	920	962	913
3/10/01/5	7,26	-9,46	4,77	2,49	826	793	920	962	913
Elim Am	11,08	-7,46	7,06	4,02	626	664	670	688	653
Omaruru Sp	8,63	-7,51	6,18	2,45	826	793	920	962	913
mean isotopic temperatures:					**751**	**741**	**806**	**844**	**800**
standard deviation of temperatures					**53**	**35**	**76**	**76**	**73**

Table 5.1 *Stable isotopes of carbon for calcite and graphite and of oxygen for calcite. The temperatures are calculated by $\Delta_{(cal\text{-}gr)}$ after different geothermometric calibrations: V-O after Valley & O'Neil (1981), D-V after Dunn & Valley (1992), K-V after Kitchen & Valley (1995), C et al. after Chacko et al. (1991) and P-K after Polyakov & Kharlashina (1995).*

structures and the undeformed grain-coarsened marble. This is also applicable on a regional scale as shown by Figure 2.1.

Furthermore, the equilibration of the carbon isotope fractionation and missing fluid inclusions imply, that fluids have not played a role during deformation, metamorphism and the intrusion of the granitic melts. As discussed above, this also may be confirmed by the oxygen isotope ratios which plot within the range of neoproterozoic seawater signatures.

As these results seem to be contradictory, the implications of the isotopic compositions on the microstructural development and the regional correlations have to be discussed in more detail. Field relationships reveal, that the intrusion of syn- to post deformational granitic melts have occurred on a regional scale within the nCZ of the Damara Belt (Fig. 2.1). From the apophysic form of the granitic intrusions observable along the magnetotelluric profile, it is obvious that the intruding granitic melts still had been in a mobile and liquidous phase. Figure 2.1 also includes the metamorphic isograde

which show, that this area of the nCZ was additionally overprinted by high-grade regional metamorphism and partial melting. As discussed in chapter 2, the age of the regional peak metamorphism coincides with the intrusion age of the granites at about 520 Ma.

This implies that the metamorphic regime results from the overlap of high-grade regional metamorphism and a widespread contact metamorphism. The metamorphic temperatures of the upper-amphibolite- and granulite-facies range between 650 to 900° C. As the cotectic line of granite melts lies between 700 and 770° C, it seems that the calcite-graphite geothermometric results shown in table 5.1 are related to this peak metamorphic event. Considering these cotectic melt temperatures, it is obvious, that the geothermometric calibrations of Valley & O´Neil (1981) and Dunn & Valley (1992) seem to be the most appropriate calibrations. The geothermometric calibrations of Kitchen & Valley (1995), Chacko et al. (1991) and Polyakov & Kharlashina (1995) therefore reveal slightly to high temperatures.

In comparison to thermobarometric calculations in the western Central Zone by Masberg (2000) and Jung & Mezger (2003), the obtained temperatures are consistent. Nevertheless, Puhan (1983) measured slightly lower metamorphic temperatures of 580 to 645° C by calcite-dolomite geothermometry. After Rathmell et al. (1999) calcite-graphite geothermometry reveals the peak metamorphic temperatures, whereas calcite-dolomite geothermometry shows lower metamorphic temperatures. This may be the reason for this discrepancy.

From the microstructural analysis and field investigations it is apparent, that the abnormally grain-coarsened calcite-marble (type 1) is the host rock of the mylonitically and cataclastically deformed marble. It shows extreme grain growth of calcite due to recrystallisation processes and graphite is concentrated in disseminated nests of graphite flakes. As discussed above, regional relationships show that this abnormally grain-coarsened type occurs only in conjunction with granite intrusions. The abnormal grain coarsening of calcite and graphite is therefore enhanced by the combination of isochronous regional and contact metamorphism. This interpretation seems to be in accordance with the isotopic analysis, since granulite facies metamorphic temperatures are obtained by this data. Accordingly, during this recrystallisation and abnormal grain growth equilibrated isotope fractionation occurred between calcite and graphite.

Also the mylonitically and brittle-ductile deformed types of graphite-bearing marble show the same equilibrated isotopic fractionation between calcite and graphite. Therefore, they imply the same metamorphic temperatures. In contrast, the microstructural analysis reveals, that the brittle-ductile deformed graphite-bearing marble shows partial

static recrystallisation only within the ultrafine-grained parts. The rate of recrystallisation in the abnormally grain-coarsened graphite-bearing marbles, which is related to temperatures of about 750 to 780° C is exeedingly higher. This implies that this deformation may only have occurred retrograde at much lower temperatures.

The minimum temperature for static recrystallisation of calcite is dependent on several factors and can therefore not be specifically quantified. It depends mainly on the purity of the calcite grain boundaries and on the amount and presence of fluids. Furthermore, it depends on the amount of dislocations, dislocation tangles and subgrain boundaries within the calcite grains. Another main factor influencing static recrystallisation temperatures of calcite are the shape of the grain aggregates, as the decrease in total free surface energy and the total internal free energy is reduced by grain boundary area reduction (GBAR) (Passchier & Trouw, 1998).

Additionally, the mylonitic deformation which is controlled by dynamic recrystallisation processes shows mutual overprinting effects with the cataclastic deformation in the brittle-ductile boundary zone. Temperatures for dynamic recrystallisation depend strongly the strainrate and on the according slip system activated during deformation (Barber et al., 1981). Therefore, no clear temperature for the mylonitic and cataclastic deformation can be deduced from the microstructures.

Furthermore, Rathmell et al. (1999) showed by the comparison of several geothermometers, that calcite-graphite thermometry reveals the peak metamorphic temperature. Also Dunn & Valley (1992) found that calcite-graphite temperatures from contact aureoles are preserved, although being overprinted by a later regional metamorphism. This is mainly related to the inert diffusion rates of graphite (Thrower & Mayer, 1978). Conclusively, this data and the microstructural analysis indicate, that the abnormal grain-coarsening and the equilibrated isotope fractionation of calcite and graphite is related to peak metamorphic granulite facies conditions. Field work and the microstructural analysis also reveal a subsequent deformation with a partial static recrystallisation in the ultra fine-grained domains.

Deduced from the experimental investigations and empirical quantification after Chacko et al. (1991) and Valley & O´Neil (1981), it is obvious that carbon isotope fractionation is not equilibrated below 600° C. This leaves either the possibility that the calcite and graphite isotopic ratios are preserved during the subsequent deformation, or that the deformation occurred below the temperatures where carbon isotopes are exchanged. As the strainrates of the deformation in the shear zone are not clear, it is not possible to

estimate the temperature of deformation from the microstructures. Therefore, it may not be ruled out completely, that the deformation occurred above 600° C.

Likewise, it can also not be precluded that the deformation occurred at temperatures where the isotope exchange rate is minimised. As the isotopic exchange rate has to be calculated over geological time spans, it is not sure whether this possibility of isotopic exchange at lower temperatures is applicable. It seems to be most likely that the equilibrated peak metamorphic isotope ratios were preserved. The already equilibrated mineral phases would in this case not change in isotope composition, as long as no further fluid phase is introduced due to the deformation. This implies that the calcite-graphite thermometry may not be applied to deduce the deformational temperature, as it would not give the retrograde deformational temperature.

Additionally, there are several hints that fluids were not present during metamorphism and retrograde metamorphic deformation. Missing fluid inclusions in the undeformed grain-coarsened host rock as well as in the deformed marble and the equilibrated isotope fractionation imply this assumption.

As the graphite network structures are most probably related to pressure solution, this implies however, that fluids would have to be considered at least for brittle-ductile domains of the boundary zone. In contrast again, the oxygen isotopes of calcite were not changed in composition by either hydrous or CO_2-bearing fluids. Accordingly, the carbon isotopic ratios were not changed by the carbon isotopes of external CO_2- and/or CH_4-bearing fluids.

For the isotopic interpretation of the graphitic stylolites this could only mean, that the fluids just caused the solution of calcite and graphite due to pressure solution effects. No recrystallisation, precipitation or overprinting of calcite and graphite therefore occurred again during pressure solution. The evacuation of calcite and graphite due to pressure solution is confirmed by the calcite-graphite ratios described in chapter 2.3.6.

The carbon isotopic ratios of calcite and graphite are heavier than the mean neoproterozoic isotopic ratios as shown in Figure 5.4. This may be related to the phase of static recrystallisation and abnormal grain growth. As described above, molecules and therefore crystals tend to incorporate heavier isotopes during recrystallisation. This isotopic fractionation must have been prior or at least simultaneously to the equilibrated isotope exchange with graphite, as graphite shows very similar isotopic composition as the the calcite-marble.

Another observation of the stable isotope ratios measured in the samples is the missing influence of possible granitic fluids. There is no implication in the isotopic data, that carbon-bearing fluids have percolated the calcite-marbles.

CHAPTER 6

MOBILISATION AND PRECIPITATION OF GRAPHITE

As graphite is a very important factor in the development of the macro- and microfabrics, it is necessary to know the modes of graphite formation in the investigated graphite-bearing marbles. As described above, graphite occurs in the undeformed host-rock in single nests with graphite flakes of up to 2 mm in size. In the brittle-ductile deformed boundary zones of the investigated shear zones, graphite occurs in graphitic stylolites and is ultra fine-grained. In the mylonitic core zones, graphite occurs in single ultra fine-grained crystals, which show a preferred orientation with the basal planes parallel to the foliation.

Therefore, it is necessary to discuss the mechanisms of graphite formation in the undeformed host-rock, and possible mechanisms of mobilisation and precipitation of graphite in the deformed graphite-bearing marbles.

6.1. THERMODYNAMICS AND MODELS

Graphite is crystallised either from organic matter or from fluids. The origin of the graphitic carbon can be differentiated by the carbon isotopes, if these have not been significantly overprinted. As discussed above, a subsequent metamorphic or deformational event may change the isotopic composition by isotopic exchange reactions. After Weis et al. (1981) syngenetic graphite, crystallised from coal is differentiated by the mode of formation, from epigenetic graphite which originated from carbon bearing fluids.

The conversion of carbonaceous material to syngenetic graphite during metamorphism occurs by many steps of structural ordering of carbon. After Buseck & Huang (1985) the most important factors influencing these processes are temperature, the time of heating, the total and partial pressures of various gaseous species and the presence of catalysts. Additionally, the structural characteristics of the reactants and products are also important (Buseck & Huang, 1985).

After Franklin (1951) aliphatic carbon material must first be aromatised before the polymerisation into graphitic molecules. Otherwise this carbon material will not graphitise even at high metamorphic temperatures. After Ruland (1965), the aromatisation must result in planar hexagonal benzene-ring structures, which then are able to be stacked in graphitic structures. Other aromatic structures are unfavorable for the formation of graphite.

Graphitisation is a complex process of stacking parallel layers of ordered carbon atoms. It includes processes of ordering, removing of foreign atoms like hydrogen and oxygen, and the removal of bonding vacancies. Many of these processes are controlled by diffusion (Buseck & Huang, 1985). After Demeny (1989) the release of volatiles creats bubbles and pores in the carbonaceous matter, which promotes the development of a preferred orientation when shear stresses are prevailing. In general, the occurrence of a crustal stress field enhances the ordered crystallisation of graphite from carbonaceous matter (Ross & Bustin 1990; Ross et al., 1991; Wilks et al., 1993; Bustin et al., 1995; Ross & Bustin, 1997).

From the randomly rotated hexagonal layers, an organised stack of carbon layers develops with increasing temperatures. At temperatures of 500 to 550° C pure graphite develops. Catalising materials for the graphitisation of carbonaceous material are: SiO_2, FeS_2, Fe, Co, Ni, $CaCO_3$ (Demeny, 1989). Graphitisation is also catalysed by mica minerals, as the epitaxial intergrowth between the basal planes favours the structural ordering of the hexagonal carbon ring-structures (Kucha & Wieczorek, 1988).

Carbon is transported in fluids either in CO-, CO_2- or in CH_4-molecules. After Luque et al. (1998) three possible sources of carbon are postulated for the carbon bearing fluids. One source of carbon are the carbon bearing compounds released into fluids during the maturation of organic matter. A second source are devolatised carbonate-rich materials. Thirdly, carbon can be of igneous origin and in this case would be mantle-derived. The according source of carbon can be derived from the carbon isotope ratios, if these are not fractionated by istotopic exchange reactions during metamorphism.

As shown by Holloway (1984) and Luque et al. (1998), the stability of carbon-bearing fluids is strongly dependent on the thermodynamic conditions and the oxygen fugacity of the fluids. The precipitation of epigenetic graphite from saturated C-O-H fluids (containing CO_2-CO-H_2O-CH_4), therefore occures at according changes in temperature and pressure conditions of the fluids. Isobaric cooling and isothermal pressure increase leads to the precipitation of graphite from saturated fluids (Luque et al., 1998). This occurs also by changes and/or chemical reactions of the fluids, that influence the oxygen fugacity of the fluid. Such changes in oxygen fugacity occurs by mixing of CO_2- and CH_4-bearing fluids, by fluid-rock interactions or by redox-reactions through sulfides and oxides. Carbon may also precipitate from C-O-H fluids by the hydratisation of the fluids, which leads to a oversaturation of the fluids (Luque et al., 1998).

Some processes which lead to the precipitation of thin interconnected graphite filmes are described by Glover (1996). Graphite may be precipitated by the isobaric

cooling of C-O-H fluids. After Frost et al. (1989), this leads to a reduction of the CO_2-rich fluid according to:

$$C + O_2 \Leftrightarrow CO_2 \qquad [6.1]$$

Graphite precipitation may also be triggered by titanomagnetite. As described by Fuhrmann et al. (1988) and Frost et al. (1989), oxygen fugacity is changed during interoxide equilibrium by cooling, which leads to the precipitation of graphite according to the following reaction:

$$6Fe_2TiO_4 + CO_2 \Leftrightarrow 2Fe_3O_4 + 6FeTiO_3 + C \qquad [6.2]$$

Walther & Althaus (1993) described a third mechanism for the precipitation of graphite along strike-slip faults by the following chemical reaction:

$$CH_4 + CO_2 \Leftrightarrow 2C + H_2O \qquad [6.3]$$

6.2. IMPLICATIONS OF CARBON ISOTOPES

As described above, the characterisation of graphite by carbon isotopes is a useful tool to evaluate whether it is of syngenetic or epigenetic origin. The carbon isotopes of the investigated samples show carbon isotope ratios that are clearly higher than the isotope ratios of organic carbon. Additionally, the carbon isotopes of graphite and calcite have been fractionated in equilibrium. As discussed above, this applies to all three types of graphite-bearing marble across all sampling sites shown in Figure 2.1.

This implies for all the types of the investigated graphite samples, that it is impossible to find indications about the origin of the carbon of graphite and carbonate from the carbon isotopes. The isotopic equilibration between calcite and graphite during peak metamorphism erased all isotopic signatures of the original carbon material.

The carbon isotopes nevertheless show that graphite of the abnormally grain-coarsened and retrograde undeformed host rock, consists of the same isotopic composition than the deformed graphite bearing marbles in the shear zones. This strongly implies that the graphite has not been soluted by fluids and precipitated again in the interconnected graphitic stylolites. A solution of the carbon material would change the isotopic composition of the graphite, unless the fluids are purely aquaeous fluids, which do not

carry any carbon material. However, for all other compositions of fluids, graphite in the shear zones should show a different isotopic composition, which is not observable.

Additionally, the carbon isotope ratios of graphite are consistent across all sampling localities (Fig. 2.1). This shows that they are even similar to equal on a regional scale, which would not be expected when local fluids overprint the carbon isotope ratios. The carbon isotope ratios therefore strongly imply, that the ultra fine-grained graphite of the shear zones has been grain-size reduced by deformation and concentrated by pressure solution of the calcite-marble as residue in the graphitic stylolites. Likewise, graphite in the mylonitically deformed marble is 'autochtoneous', and was concentrated as single crystals in preferred orientation along the calcite grain-boundaries during dynamic recrystallisation.

6.3. IMPICATIONS OF GRAPHITE CRYSTALLINITIES

As described in chapter 3, the crystallinities of graphite are equally high for all different types of the investigated graphite bearing marbles. Therefore, the graphite crystallinities of the abnormally grain-coarsened and undeformed host rock are similar to the crystallinities of graphite in the shear zones. Even within in different deformational domains of the shear zones, graphite crystallinities do not differ substantially. Again, this also applies on a regional scale across the sampling sites shown in Figure 2.1.

For the investigation of the mechanisms of graphite formation, possible mobilisation and subsequent precipitation, these results give no clear implications. It can not be clearly deduced from the measured graphite crystallinities, whether a concentration of graphite in the shear zones had occurred due to pressure solution or due to solution, fluid mobilisation and finally precipitation.

The microstructural investigation revealed, that graphite grain-sizes are reduced to about 10 to 200 μm in comparison to the grain-sizes of the graphite flakes of up to 2 mm in the undeformed host-rock. As shown by Landis (1971) and Hofmann (1989) it is possible to grind highly crystalline graphite without changing the degree of crystallinity of the graphite. Therefore it is possible, that the deformed graphite from the shear zones remained unchanged in crystallinity and shows the same characteristics as the abnormally grain-coarsened and undeformed host rock. Intensive pressure solution of calcite in the brittle-ductile boundary zone, must have left the deformed graphite as residue in the graphitic stylolites.

On the other hand Bustin et al. (1986), Demeny (1989), Wilks et al. (1993) and Ross & Bustin (1997) showed that graphite formed under shear stress produces highly

crystalline graphite even at 350 to 400° C. This could also imply, that the highly crystalline graphite in the investigated shear zones, could have originated from crustal fluids penetrating the shear zones during deformation.

However, the isotopic composition of the graphite from the shear zones should in this case differ from the isotope ratios of the abnormally grain-coarsened undeformed host rock as discussed above. In the case of solution of graphite by purely aquaeous fluids, the carbon isotope ratios would not have been changed, as long as no mixing with other fluids or rocks had occurred. In this case a mobilisation and subsequent precipitation of graphite would have been possible, with high graphite crystallinities and according isotopic composition.

6.4. IMPLICATIONS OF REGIONAL METAMORPHISM

As discussed in chapter 2, amphibolite- to granulite metamorphic facies occurred in combination with contact metamorphism of granite intrusions. This occurred on a regional scale within the northern Central Zone of the Damara Belt. Calcite-graphite geothermometry revealed temperatures of 750 – 780° C for all localities. Therefore they apply on a regional scale as well.

These metamorphic conditions are well sufficient for the formation of syngenetic graphite as well as for epigenetic graphite. At the described metamorphic facies, the conversion from carbonaceous material to graphite is well possible, as this may occur already at lower metamorphic facies (Weis et al., 1981; Buseck & Huang, 1985; Demeny, 1989).

The thermodynamic conditions for the precipitation of epigenetic graphite are also existent in these metamorphic grades (Holloway, 1984; Luque et al., 1998). Therefore, it is not possible from the evaluation of the regional metamorphism, to preclude on the mode of graphite formation in the investigated samples.

6.5. IMPLICATIONS OF SEM DATA

The SEM and EDX data presented in chapter 2 shows, that graphite in the undeformed host rock, as well as in the brittle-ductile and mylonitically deformed marble shows similar compositions. Additional phases like Fe, Ti, K, Si, Al, Mg, and Cl imply, that propably some mica minerals are epitaxial intergrown with the graphite. This was also observed by qualitative optical microscopy in the abnormally grain-coarsened undeformed host rock as described in chapter 2.

As these additional phases occur in the graphite of all microstructural types, they give an indication, that the graphite in the deformed graphite-bearing marbles is most likely not soluted and precipitated after being mobilized by fluids. The epitaxial intergrowth with mica minerals rather implies, that the graphite of the shear zone is either 'autochtoneous' in the case of pure mylonitic deformation. In the brittle-ductile deformed domains, graphite seems to be a residue of pressure solution in graphitic stylolites.

6.6. DISCUSSION

As the unfractionated carbon isotopic composition is the most reliable characterisation for the origin of graphite and calcite, it is not possible in the measured samples to pinpoint the origin of carbon in this samples. The original carbon isotope ratios have been overprinted during peak metamorphism.

The metamorphic conditions favour both mechanisms of graphite formation, which also do not give implications, whether the investigated graphite is of syngenetic or epigenetic origin. However, the carbon isotopes of graphite and calcite are equilibrated equally within the deformed and undeformed graphite-bearing marble. This gives an first indication, that the graphite of all the investigated types of graphite-bearing marble are genetically related.

From the graphite crystallinities it is obvious, that graphite either had been deformed in the shear zones while keeping the high crystallinities, or it was precipitated under shear stress, obtaining high crystallinities. Regarding the carbon isotope ratios, the latter may only have been possible, when the original graphite had been soluted and mobilised by purely aquaeous fluids.

The investigations by EDX revealed, that it is most likely, that the graphite in all microstructural types is the same, as graphite is epitaxial intergrown with mica minerals. This would not be expected in epigenetic graphite. Considering these implications together with the indications of the carbon isotope ratios, the graphite crystallinities and the thermodynamic crustal conditions, it seems to be the most likely that the graphite in the shear zones is the same as in the undeformed host rock.

CHAPTER 7

REGIONAL IMPLICATIONS

The data gathered in this work implies some new regional proxies for the deformational and metamorphic history. They will be related to the tectono-metamorphic history postulated so far for the northern Central Zone of the Damara Belt.

7.1. REGIONAL METAMORPHISM

The regional metamorphic isograde of the Damara Belt postulated by Hartmann et al. (1983) are in good accordance with the obtained peak metamorphic temperatures of the calcite-graphite geothermometry. The metamorphic isograde increase from east to west in the area of investigation (Fig. 2.1). In the east they are described by partial melting due to the reaction of muscovite, plagioclase, quartz and water to melt and sillimanite. To the west, increasing metamorphic grades are characterised by k-feldspar- and cordierite-in. This already shows, that upper-amphibolite- to granulite-facies metamorphism was prevailing in the region. The metamorphic temperatures implied by these facies are around 650° C for the upper amphibolite-facies and 650 to 900° C for the granulite-facies.

Fieldwork and the geochronological data discussed in chapter 2 shows that the intrusion of the granitic melts occurred during this metamorphic event. The cotectic temperatures of granitic melts are between 700 to 770° C. In the combination of regional and contact metamorphism the obtained calcite-graphite geothermometric temperatures possibly represent peak metamorphism. Thermobarometric calculations of the western part of the Central Zone by Masberg (2000) and Jung & Mezger (2003) show, that the obtained metamorphic temperatures are consistent with this data. Nevertheless, calcite-dolomite geothermometric calculations of the Central Zone by Puhan (1983) show lower temperatures of 580 to 645° C. These temperatures are generally lower as the obtained data. After Rathmell et al. (1999) calcite-graphite geothermometry rather represents peak metamorphic temperatures, while calcite-dolomite may also represent lower metamorphic temperatures. This could be the reason for the discrepancy between these temperatures.

The combination of regional and contact metamorphism as also postulated by Jung et al. (2003) is in accordance with fieldwork, geochronological data, geothermometric data. The geochronological data of the regional widespread intrusions and the metamorphic events in the northern Central Zone are discussed in chapter 2. In general, peak metamorphism is dated to about 520 to 504 Ma and the intrusion ages range mainly from 540 to 510 Ma and a later stage of intrusions at 469 Ma (Miller, 1983; Jacob et al., 2000;

McDermott et al., 2000, Jung et al., 2003). The geothermometric data also shows, that in general temperatures of 700 to 760° C have been present during metamorphism. These temperatures do not directly imply a combination of regional and contact metamorphism. They show however, that the metamorphic temperatures do not exclude the possibility of a combined regional and contact metamorphism in these parts of the northern Central Zone.

Likewise, the apophysic granitic intrusions imply, that mobile melts have intruded the marble in a high-temperature regime. Therefore, this correlation of metamorphic events may also be verified by these field investigations.

7.2. DEFORMATIONAL PATH

As shown on the satellite image in Figure 2.2, the regional structures are dominated by crustal scale dome structures. It is obvious from this image, that two kinds of dome structures are developed in the region. The dominating type of dome structures has developed by by refolding crustal scale isoclinal folds. The second type of dome structures emerged from the widespread intrusion of the granitic melts.

After the emplacement of the granites, a regional phase of static recrystallisation dominated. This is documented by regionally widespread abnormally grain-coarsened calcite-marbles as described in chapter 2. During retrograde metamorphism the rims of the crustal-scale dome structures became reactivated and shear zones developed along the rims of the dome-structures. Based on the investigations of the microstructures, the carbon isotopes and the graphite crystallinities, the reactivation of the dome structures occurred most probably at temperatures below 600° C. The microstructural analysis implies even lower temperatures. As these estimates also depend strongly on the strain rate on geological time scales, it is not possible to estimate an exact temperature.

The shear zones are built up by mylonitic core zones and brittle-ductile boundary zones. The mylonitic core zones are consistent in the shear zones, whereas the boundary zones consist of different domains of brittle-ductile deformation, which vary lateral and perpendicular to the shear zones. The analysis of the macro- and microstructures shows, that the mylonitic core zones are characterised by aseismic creep deformation, whereas the brittle-ductile boundary zones show a mutual overprinting of brittle and ductile deformation, related to seismic events and aseismic creep deformation. The transition between brittle and ductile deformation, is controlled by the differences in strain rates between short-termed seismic deformation with high strain rates and aseismic ductile deformation.

As revealed by fieldwork, this deformation is of Damaran age. The Cretaceous dykes, which occur widespread in the region (Fig. 2.2) are not overprinted by these shear zones. Consequently, the Cretaceous dykes cut the shear zones across the crustal dome structures regardless of the general Damaran strike, whereas the shear zones are oriented parallel to the Damaran strike from north-east to south-west.

7.3. DISCUSSION

The deformational path described above, implies for this part of the Central Zone of the Damara Belt at least two deformational stages during the Damara Orogenesis. This is documented by a regional widespread phase of static recrystallisation. Fieldwork revealed that the abnormally grain-coarsened marbles occur at least from the western sampling locality (Fig. 2.1) to the coast near Swakopmund. This phase of static recrystallisation postdates either a transtensional or a multistage deformation, which led to the formation of the crustal dome structures. After the phase of static recrystallisation a second regional stress field built up, which induced the formation of the investigated shear zones along the rims of the dome structures.

Therefore, a wide range of this crustal segment was free of crustal stresses during the late stage of the Damara Orogenesis. Whether this is purely related to the structural setting of this crustal segment during this stage of orogenesis, or to the widespread magmatic intrusions is not clear. More detailed investigations on a regional scale will reveal more information on this matter.

The models for the formation of dome structures discussed in the literature are related to large-scale buckling, thrust-related antiformal stacking, syn-contractional gravitational collapse or post-contractional extension. A compilation of models is shown by Soula et al. (2001). Which of these models are applicable for the investigated structural domes, is not clear at present. Further investigation and detailed mapping of these dome structures will be necessary on this matter. A thrust-related formation of the dome structures, would reveal some indications about the source of the seismic activity observed in the fabrics of the brittle-ductile boundary zone.

The location of the Omaruru Lineament (OmL) as postulated by Raab (2001), Ritter et al. (2003) and Weckmann et al. (2003) is still a matter of debate. After Miller (1983), the OmL devides the northern and the southern Central Zone of the Damara Belt. Main differences between the two parts of the Central Zone are the stratigraphic levels of the dome structures. In the northern Central Zone, the dome structures are built up by Damaran lithologies, whereas the dome structures of the southern Central zone comprise

mainly basement rocks. After this definition, the OmL is located further south, as the investigated shear zones all are built up by Damaran sediments. Furthermore, there is no distinct shear zone in this area, which strictly divides the crustal segments of different straticgraphic levels. Whether the existing shear zones along the dome structures may be regarded as a conjugated shear zone system, will have to be revealed by further investigations. Nevertheless, the investigated shear zone system would not fulfil the original definition of the OmL by Miller (1983) and may thereby not be defined as such.

CHAPTER 8

CONCLUSIONS

1. The graphite-bearing marbles, that produce high anomalies of electrical conductivity in magnetotelluric profiles occur within crustal scale domestructures in the northern Central Zone of the Damara Belt in north-western Namibia.

2. The undeformed graphite-bearing marbles are abnormally grain-coarsened due to a combination of amphibolite- to granulite facies metamorphism and contact metamorphism of granitic intrusions. Calcite-graphite geothermometry revealed regional peak-metamorphic temperatures of about 750 to 780 ° C.

3. The granitic melts intruded after the formation of the structural domes and themselves formed widespread granitic domes in the Central Zone of the Damara Belt.

4. After the intrusion of the granitic melts, a regional phase of static recrystallisation occurred with the abnormal grain-coarsening of the graphite-bearing marbles.

5. These coarse-grained marbles were subsequently deformed in complex shear zones along the rims of the retrograde reactivated dome structures. The shear zones comprise a mylonitic core zone and a brittle-ductile boundary zone. The brittle-ductile boundary is characterised by brittle and ductile deformation fabrics, which show a mutual overprinting of both deformation mechanisms and pressure solution. This was revealed by detailed investigations of the macro- and microfabrics of the graphite-bearing marbles. The brittle-ductile boundary zone is attributed to a combination of seismic deformation with high strain rates and cataclastic deformation and aseismic creep deformation. Aseismic creep deformation has also dominated the mylonitic core zones of the shear zones.

6. Texture measurements revealed high intensities in preferred-crystallographic orientation, which possibly is related to recrystallisation. The intensities decrease with the decrease in grain size in the mylonitic core zones as well as in the brittle-ductile boundary zones. The mylonitic core zones show a complex pattern of different texture domains in microscopic scales.

7. The graphitic stylolites of the brittle-ductile boundary zone produce the anomalies of high electrical conductivity in magnetotelluric profiles. Electrical conductivity

measurements on sample scale however, showed mainly ionic conductivity as most of the graphitic stylolites are cut by younger microveins. These microveins are either related to hydrofracturing during the Cretaceous break-up of Gondwana, or to tensile fracturing during the exhumation of this crustal segment.

8. The investigations of this work show, that it is not possible to reveal the origin of the graphite. As graphite and calcite are isotopically equilibrated, it is impossible to find any implications on the origin of graphite and on the mode of formation. It is most likely that the graphite in the shear zone is of the same origin as in the undeformed host rock. Several findings imply that graphite from the coarse-grained marble had been deformed in the shear zone, and then formed graphitic stylolites as a residue during pressure solution.

9. Graphite is of uniformly high crystallinity in the abnormally grain-coarsened undeformed marble as well as in the deformed marble. Graphite is epitaxial intergrown with mica minerals, which is observable by qualitative optical microscopy in the undeformed host rock. Within the deformed graphite-bearing marbles it is not possible to observe this directly. EDX data implies this assumption however.

REFERENCES

Alabi, A. O., Camfield, P. A. & Gough, D. I. 1975. The North American Central Plains conductivity anomaly. *The Geophysical Journal of the Royal Astronomical Society* **43**(3), 815-833.

Alcántara, R., Lavela, P., Ortiz, G. F., Tirado, J. L., Menéndez, R., Santamaría, R. & Jiménez-Mateos, J. M. 2003. Electrochemical, textural and microstructural effects of mechanical grinding on graphitized petroleum coke for lithium and sodium batteries. *Carbon* **41**(15), 3003-3013.

Barber, D. J., Heard, H. C. & Wenk, H. R. 1981. Deformation of dolomite single crystals from 20-800 degrees C. *Physics and Chemistry of Minerals* **7**(6), 271-286.

Barnhoorn, A., Bystricky, M., Burlini, L. & Kunze, K. 2004. The role of recrystallisation on the deformation behaviour of calcite rocks: large strain torsion experiments on Carrara marble. *Journal of Structural Geology* **26**, 885-903.

Bartels, K. S. & Pasteris, J. D. 1994. Multiple generations of fluid-deposited graphite in rocks from the KTB. In: *Geological Society of America, 1994 annual meeting.* (edited by Anonymous). *Abstracts with Programs - Geological Society of America* **26; 7**. Geological Society of America (GSA), Boulder, CO, United States, 227.

Beny-Bassez, C. & Rouzaud, J. N. 1985. Characterization of carbonaceous materials by correlated electron and optical microscopy and Raman microspectroscopy. *Scanning Electron Microscopy* **1985**(1), 119-132.

Bestmann, M., Kunze, K. & Matthews, A. 2000. Evolution of a calcite marble shear zone complex on Thassos Island, Greece: microstructural and textural fabrics and their kinematic significance. *Journal of Structural Geology* **22**(11-12), 1789-1807.

Beyssac, O., Rouzaud, J. N., Goffe, B., Brunet, F. & Chopin, C. 2002. Graphitization in a high-pressure, low-temperature metamorphic gradient; a Raman microspectroscopy and HRTEM study. *Contributions to Mineralogy and Petrology* **143**(1), 19-31.

Brasier, M. D., Magaritz, M., Corfield, R., Luo, H., Wu, X., Ouyang, L., Jiang, Z., Hamdi, B., He, T. & Fraser, A. G. 1990. The carbon- and oxygen-isotope record of the Precambrian-Cambrian boundary interval in China and Iran and their correlation. *Geological Magazine* **127**(4), 319-332.

Burdett, J. W., Grotzinger, J. P. & Arthur, M. A. 1990. Did major changes in the stable-isotope composition of Proterozoic seawater occur? *Geology (Boulder)* **18**(3), 227-230.

Burkhard, M. 1993. Calcite twins, their geometry, appearance and significance as stress-strain markers and indicators of tectonic regime: a review. In: *The geometry of naturally deformed rocks.* (edited by Casey, M., Dietrich, D., Ford, M., Watkinson, J. & Hudleston Peter, J.). *Journal of Structural Geology* **15; 3-5**. Pergamon, Oxford-New York, International, 351-368.

Buseck, P. R. & Huang, B. 1985. Conversion of carbonaceous material to graphite during metamorphism. *Geochimica et Cosmochimica Acta* **49**(10), 2003-2016.

Bustin, R. M. 1983. Heating during thrust faulting in the Rocky Mountains: friction or fiction? *Tectonophysics* **95**(3-4), 309-328.

Bustin, R. M., Ross, J. V. & Moffat, I. 1986. Vitrinite anisotropy under differential stress and high confining pressure and temperature: preliminary observations. *International Journal of Coal Geology* **6**(4), 343-351.

Bustin, R. M., Ross, J. V. & Rouzaud, J. N. 1995. The role of strain in the formation of natural graphite: experimental considerations. In: *Geological Association of Canada; Mineralogical Association of Canada; annual meeting; program with abstracts--Association Geologique du Canada; Association Mineralogique du Canada; reunion annuelle; programme et resumes.* (edited by Anonymous). *Program with Abstracts - Geological Association of Canada; Mineralogical Association of Canada; Canadian Geophysical Union, Joint Annual Meeting* **20**. Geological Association of Canada, Waterloo, ON, Canada, 13.

Chacko, T., Mayeda, T. K., Clayton, R. N. & Goldsmith, J. R. 1991. Oxygen and carbon isotope fractionations between CO_2 and calcite. *Geochimica et Cosmochimica Acta* **55**(10), 2867-2882.

Covey, C. S. J. & Rutter, E. H. 1989. Thermally-induced grain growth of calcite marbles on Naxos Islands, Greece. *Contributions to Mineralogy and Petrology* **101**(1), 69-86.

Criss, R. E. 1991. Temperature dependence of isotopic fractionation factors. In: *Stable isotope geochemistry; a tribute to Samuel Epstein.* (edited by Taylor Hugh, P. J., O´Neil, J. R. & Kaplan Isaac, R.). *Special Publication - Geochemical Society* **3**. Geochemical Society, University Park, PA, United States, 11-16.

De Bresser, J. H. P. & Spiers, C. J. 1997. Strength characteristics of the r, f, and c slip systems in calcite. *Tectonophysics* **272**(1-2), 1-23.

Demeny, A. 1989. Structural ordering of carbonaceous matter in Penninic terranes. *Acta Mineralogica-Petrographica (Szeged)* **30**, 103-113.

Dresselhaus, M. S. & Dresselhaus, G. 1982. Light scattering in graphite intercalation compounds. In: *Light scattering in solids* (edited by Cardona, M. & Guntherodth, G.). Springer, New York, 3-57.

Duba, A., Heikamp, S., Meurer, W., Nover, G. & Will, G. 1994. Evidence from borehole samples for the role of accessory minerals in lower-crustal conductivity. *Nature (London)* **367**(6458), 59-61.

Duba, A. G. & Shankland, T. J. 1982. Free carbon and electrical conductivity in the Earth's mantle. *Geophysical Research Letters* **9**(11), 1171-1174.

Dunn, S. R. & Valley, J. W. 1992. Calcite-graphite isotope thermometry: a test for polymetamorphsim in marble, Tudor gabbro aureole, Ontario, Canada. *Journal of Metamorphic Geology* **10**(4), 487-501.

ELEKTB-Group. 1997. KTB and the electrical conductivity of the crust. *The KTB deep drill hole.* **102**(8), 18,289-18,305.

Fowler, C. M. R., Stead, D., Pandit, B. I., Janser, B. W., Nisbet, E. G. & Nover, G. 2004. A data base for physical properties of rocks from the Trans-Hudson Orogen, Canada. *Canadian Journal of Earth Sciences = Journal Canadien des Sciences de la Terre* **in print**.

Franklin, R. E. 1951. The structure of graphitic carbons. *Acta Crystallographica* **4**, 253-261.

Frost, B. R., Fyfe, W. S., Tazaki, K. & Chan, T. 1989. Grain-boundary graphite in rocks and implications for high electrical conductivity in the lower crust. *Nature (London)* **340**(6229), 134-136.

Fueten, F. & Goodchild, J. S. 2001. Quartz c-axes orientation determination using the rotating stage polarizer microscope. *Journal of Structural Geology* **23**(6-7), 895-902.

Fuhrmann, M. L., Frost, B. R. & Lindsley, D. H. 1988. Crystallisation conditions of the Sybille Monzosyenite, Laramie anorthosite complex, Wyoming. *Journal of Petrology* **29**, 699-729.

Garlick, G. D. 1969. The stable isotopes of oxygen. In: *Handbook of Geochemistry* (edited by Wedepohl, K. H.) **8B**. Springer, Berlin Heidelberg New York.

Giletti, B. J. 1985. The nature of oxygen transport within minerals in the presence of hydrothermal water and the role of diffusion. *Chemical Geology* **53**(3-4), 197-206.

Glover, P. W. J. 1996. Graphite and electrical conductivity in the lower continental crust: a review. In: *Geophysical studies of the continental lithosphere; density inhomogeneities in the crust and mantle and their relation to tectonics.* (edited by Goetze, H. J. & Jacoby, W. R.). *Physics and Chemistry of the Earth* **21; 4**. Pergamon, Oxford-New York-Toronto, International, 279-287.

Glover, P. W. J. & Vine, F. J. 1992. Electrical conductivity of carbon-bearing granulite at raised temperatures and pressures. *Nature (London)* **360**(6406), 723-726.

Gross, C. J., Weber, K., Siegesmund, S. & Vollbrecht, A. 1999. Fabric Development and Spathization Processes in Metacarbonates: Two Case Studies from the Damara Orogen, Namibia. In: *Sonderforschungsbereich 486 Wechselwirkungen an geologischen Grenzflächen Arbeits- und Ergebnisbericht für die Jahre 1997-1999*. Georg-August Universität Göttingen, Göttingen, B3-1 - B3-33.

Guéguen, Y. & Palciauskas, V. 1994. *Introduction to the Physics of Rocks*. Princeton University Press, Princeton, New Jersey 08540.

Haack, U. & Gohn, E. 1988. Rb-Sr data on some pegmatites in the Damara Orogen (Namibia). *Communications of the Geological Survey of Namibia* **4**, 13-17.

Haack, U., Hoefs, J. & Gohn, E. 1983. Genesis of Damaran granites in the light of Rb/Sr and delta ^{18}O data. In: *Intercontinental fold belts* (edited by Martin, H. & Eder, F. W.). Springer, Berlin, 847-872.

Haack, U. & Martin, H. 1983. Geochronology of the Damara Orogen - a review. In: *Intercontinental fold belts* (edited by Martin, H. & Eder, F. W.). Springer, Berlin, 839-845.

Hall, S. M. & Veizer, J. 1996. Geochemistry of Precambrian carbonates: VII, Belt Supergroup, Montana and Idaho, USA. *Geochimica et Cosmochimica Acta* **60**(4), 667-677.

Hartmann, O., Hoffer, E. & Haak, U. 1983. Regional metamorphism in the Damara Orogen: Interaction of crustal motion and heat transfer. In: *Evolution of the Damara Orogen of South-West Africa/Namibia* (edited by Miller, R. M. G.). *Special Publication - Geological Society of South Africa* **11**, 233-241.

Hawkesworth, C. J., Kramers, K. D. & Miller, R. M. G. 1981. Old model Nd ages in Namibian Pan-African rocks. *Nature* **289**, 278-282.

Heilbronner, R. 2000. Automatic grain boundary detection and grain size analysis using polarization micrographs or orientation images. *Journal of Structural Geology* **22**(7), 969-981.

Hoefs, J. 1997. *Stable isotope geochemistry. 4 ed*. Springer, Berlin, Federal Republic of Germany.

Hofmann, K. H. 1989. Das Auftreten von Graphit in metamorphen Gesteinen in Bayern Translated Title: The occurrence of graphite in metamorphic rocks in Bavaria. *Geologische Blaetter fuer Nordost-Bayern und Angrenzende Gebiete* **39**(1-2), 59-98.

Holloway, J. R. 1984. Graphite-CH_4-H_2O-CO_2 equilibria at low-grade metamorphic conditions. *Geology (Boulder)* **12**(8), 455-458.

Jacob, R. E., Moore, J. M. & Armstrong, R. A. 2000. Zircon and titanite age determinations from igneous rocks in the Karibib District, Namibia: implications for Navachab vein-style gold mineralization. In: *Henno Martin commemorative volume.* (edited by Miller, R. M.). *Communications of the Geological Survey of South West Africa/Namibia* **12**. Geological Survey of South West Africa/Namibia, Windhoek, Namibia, 157-166.

Jödicke, H., Kruhl, J. H., Ballhaus, C., Giese, P. & Untiedt, J. 2004. Syngenetic, thin graphite-rich horizons in lower crustal rocks from the Serre San Bruno, Calabria (Italy), and implications for the nature of high-conducting deep crustal layers. *Physics of the Earth and Planetary Interiors* **141**(1), 37-89.

Jung, S., Hoernes, S. & Mezger, K. 2000a. Geochronology and petrogenesis of Pan-African, syn-tectonic, S-type and post-tectonic A-type granite (Namibia): products of melting of crustal sources, fractional crystallization and wall rock entrainment. *Lithos* **50**(4), 259-287.

Jung, S., Hoernes, S. & Mezger, K. 2000b. Geochronology and petrology of migmatites from the Proterozoic Damara Belt - importance of episodic fluid-present disequilibrium melting and consequences for granite petrology. *Lithos* **51**(3), 153-179.

Jung, S. & Mezger, K. 2003. Petrology of basement-dominated terranes: I. Regional metamorphic T-t path form U-Pb monazite and Sm-Nd garnet geochronology (Central Damara orogen, Namiba). *Chemical Geology* **198**(3-4), 223-247.

Jung, S., Mezger, K. & Hoernes, S. 1998. Petrology and geochemistry of syn- to post-collisional metaluminous A-type granites - a major and trace element and Nd-Sr-Pb-O-isotope study from the Proterozoic Damara Belt, Namibia. *Lithos* **45**, 147-175.

Jung, S., Mezger, K. & Hoernes, S. 2003. Petrology of basement-dominated terranes: II. Contrasting isotopic (Sr, Nd, Pb and O) signatures of basement-derived granites and constraints on the source region of granite (Damara orogen, Namibia). *Chemical Geology* **199**(1-2), 1-28.

Kasch, K. W. 1983. Continental collision, suture propagation and thermal relaxation: a plate tectonic model for the Damara Orogen in central Namibia. In: *Evolution of the Damara Orogen of South-West Africa/Namibia* (edited by Miller, R. M. G.). *Special Publication - Geological Society of South Africa* **11**, 423-429.

Katsube, T. J. & Mareschal, M. 1993. Petrophysical model of deep electrical conductors; graphite lining as a source and its disconnection due to uplift. *Journal of Geophysical Research, B, Solid Earth and Planets* **98**(5), 8019-8030.

Kaufman, A. J., Hayes, J. M., Knoll, A. H. & Germs, G. J. B. 1991. Isotopic compositions of carbonates and organic carbon from upper Proterozoic successions in Namibia:

stratigraphic variation and the effects of diagenesis and metamorphism. *Precambrian Research* **49**(3-4), 301-327.

Keller, G. V. 1987. Resistivity Characteristics of Geologic Targets. In: *Electromagnetic Methods in Applied Geophysics* (edited by Nabighian, M. N.). *Investigations in Geophysics, Vol 3* **1**. Soc. of Epl. Geophys., Tusla, Okla.

Kirschner, D. L. & Kennedy, L. A. 2001. Limited syntectonic fluid flow in carbonate-hosted thrust faults of the Front Ranges, Canadian Rockies, inferred from stable isotope data and structures. *Journal of Geophysical Research, B, Solid Earth and Planets* **106**(5), 8827-8840.

Kitchen, N. E. & Valley, J. W. 1995. Carbon isotope thermometry in marbles of the Adirondack Mountains, New York. *Journal of Metamorphic Geology* **13**(5), 577-594.

Klein, J. 1980. Evolution of the first generation folds in a marble unit (Damara Orogenic Belt, Namibia). *Geologische Rundschau* **69**(3), 770-800.

Kröner, A. 1982. Rb-Sr geochronology and tectonic evolution of the Pan-African Damara Belt of Namibia, South-western Africa. *American Journal of Science* **282**, 1471-1507.

Kucha, H. & Wieczorek, A. 1988. Graphite in Kupferschiefer (Poland) and its genetic meaning. *Mineralium Deposita* **23**(3), 174-178.

Kukla, P. A. 1992. *Tectonics and sedimentation of a late Proterozoic Damaran convergent continental margin, Khomas Hochland, central Namibia*. Ministry of Mines and Energy, Geological Survey of Namibia, Windhoek, Namibia.

Kumar, B., Das Sharma, S., Sreenivas, B., Dayal, A. M., Rao, M. N., Dubey, N. & Chawla, B. R. 2002. Carbon, oxygen and strontium isotope geochemistry of Proterozoic carbonate rocks of the Vindhyan Basin, central India. *Precambrian Research* **113**(1-2), 43-63.

Landis, C. A. 1971. Graphitization of dispersed carbonaceous material in metamorphic rocks. *Contributions to Mineralogy and Petrology* **30**, 34-45.

Leger, A., Mathez, E. A., Duba, A., Pineau, F. & Ginsberg, S. 1996. Carbonaceous material in metamorphosed carbonate rocks from the Waits River Formation, NE Vermont, and its effect on electrical conductivity. *Journal of Geophysical Research, B, Solid Earth and Planets* **101**(10), 22,203-22,214.

Leiss, B. & Molli, G. 2003. 'High-temperature' texture in naturally deformed Carrara Marble from the Alpi Apuane, Italy. *Journal of Structural Geology* **25**(4), 649-658.

Leiss, B. & Ullemeyer, K. 1999. Texture characterisation of carbonate rocks and some implications for the modeling of physical anisotropies, derived from idealized texture types. *Zeitschrift der Deutschen Geologischen Gesellschaft* **150**(2), 259-274.

Leiss, B. & Weiss, T. 2000. Fabric anisotropy and its influence on physical weathering of different types of Carrara marbles. *Journal of Structural Geology* **22**, 1737-1745.

Losito, G., Schnegg, P. A., Lambelet, C., Viti, C. & Trova, A. 2001. Microscopic scale conductivity as explanation of magnetotelluric results from the Alps of western Switzerland. *Geophysical Journal International* **147**(3), 602-609.

Luque, F. J., Pasteris, J. D., Wopenka, B., Rodas, M. & Barrenechea, J. F. 1998. Natural fluid-deposited graphite; mineralogical characteristics and mechanisms of formation. *American Journal of Science* **298**(6), 471-498.

MacDonald, J. R. & Kenan, W. R. 1987. *Impedance Spectroscopy : Emphasizing Solid Materials and Systems*. John Wiley & Sons, New York.

Mareschal, M., Fyfe, W. S., Percival, J. & Chan, T. 1992. Grain-boundary graphite in Kapuskasing gneisses and implications for lower-crustal conductivity. *Nature (London)* **357**(6380), 674-676.

Marlow, A. G. 1983. Geology and Rb-Sr geochronology of mineralized and radioactive granites and alaskites, Namibia. In: *Evolution of the Damara Orogen of South-West Africa/Namibia* (edited by Miller, R. M. G.). *Special Publication - Geological Society of South Africa* **11**, 289-298.

Masberg, P. 2000. Garnet growth in medium-pressure granulite facies metapelites from the central Damara Orogen:

igneous versus metamorphic history. In: *Henno Martin commemorative volume.* (edited by Miller, R. M.). *Communications of the Geological Survey of South West Africa/Namibia* **12**. Geological Survey of South West Africa/Namibia, Windhoek, Namibia, 115-124.

Matthews, A., Goldsmith, J. R. & Clayton, R. N. 1983. Oxygen isotope fractionation between zoisite and water. *Geochimica et Cosmochimica Acta* **47**(3), 645-654.

McDermott, F., Harris, N. B. W. & Hawkesworth, C. J. 2000. Geochemical constraints on the petrogenesis of Pan-Africa A-type granites in the Damara Belt, Namibia. In: *Henno Martin commemorative volume.* (edited by Miller, R. M.). *Communications of the Geological Survey of South West Africa/Namibia* **12**. Geological Survey of South West Africa/Namibia, Windhoek, Namibia, 139-148.

Miller, R. M. G. 1983. The Pan-African Damara Orogen of South West Africa/Namibia. In: *Evolution of the Damara Orogen of South-West Africa/Namibia* (edited by Miller, R. M. G.). *Special Publication - Geological Society of South Africa* **11**, 431-515.

Morikiyo, T. 1984. Carbon isotopic study on coexisting calcite and graphite in the Ryoke metamorphic rocks, northern Kiso District, central Japan. *Contributions to Mineralogy and Petrology* **87**(3), 251-259.

Nier, A. O. 1950. A redetermination of the relative abundances of the isotopes of carbon, nitrogen, oxygen, argon and potassium. *Physical Reviews* **77**, 789.

Nover, G., Heikamp, S., Meurer, H. J. & Freund, D. 1998. In-situ electrical conductivity and permeability of mid-crustal rocks from the KTB drilling; consequences for high conductive layers in the Earth crust. *Surveys in Geophysics* **19**(1), 73-85.

O´Neil, J. R. 1986. Theoretical and experimental aspects of isotopic fractionation. In: *Stable isotopes in high temperature geological processes.* (edited by Valley John, W., Taylor Hugh, P., Jr. & O´Neil, J. R.). *Reviews in Mineralogy* **16**. Mineralogical Society of America, Washington, DC, United States, 1-40.

Palacky, G. J. 1987. Resistivity Characteristics of Geologic Targets. In: *Electromagnetic Methods in Applied Geophysics* (edited by Nabighian, M. N.). *Investigations in Geophysics, Vol 3* **1**. Soc. of Epl. Geophys., Tusla, Okla.

Park, R. & Epstein, S. 1960. Carbon isotope fractionation during photosynthesis. *Geochimica et Cosmochimica Acta* **21**, 110-126.

Parkhomenko, E. I. 1967. *Electrical Properties of Rocks*. Plenum Press, New York.

Passchier, C. W. & Trouw, R. A. J. 1998. *Microtectonics*. Springer Berlin Heidelberg.

Pasteris, J. D. & Wopenka, B. 1991. Raman spectra of graphite as indicators of degree of metamorphism. *The Canadian Mineralogist* **29 Part 1**, 1-9.

Polyakov, V. B. & Kharlashina, N. N. 1995. The use of heat capacity data to calculate carbon isotope fractionation between graphite, diamond, and carbon dioxide: a new approach. *Geochimica et Cosmochimica Acta* **59**(12), 2561-2572.

Porada, H. 1985. Stratigraphy and facies in the upper Proterozoic Damara Orogen, Namibia, based on a geodynamic model. In: *Stratigraphic methods as applied to the Proterozoic record.* (edited by Young, G. M., Chen, J. B. & Zhang, H.). *Precambrian Research* **29; 1-3**. Elsevier, Amsterdam, International, 235-264.

Pieri, M., Burlini, L., Kunze, K., Stretton, I. & Olgaard, D. L. 2001a. Rheological and microstructural evolution of Carrara Marble with high shear strain: results from high temperature torsion experiments. *Journal of Structural Geology* **23**(9), 1393-1413.

Pieri, M., Kunze, K., Burlini, L., Stretton, I., Olgaard, D. L., Burg, J. P. & Wenk, H. R. 2001b. Texture development of calcite by deformation and dynamic recrystallization at 1000 K during torsion experiments of marble to large strains. *Tectonophysics* **330**(1-2), 119-140.

Puhan, D. 1983. Temperature and pressure of metamorphism in the Central Damara orogen. In: *Evolution of the Damara Orogen of South-West Africa/Namibia* (edited by Miller, R. M. G.). *Special Publication - Geological Society of South Africa* **11**, 219-223.

Raab, M. J. 2001. The Geomorphic Response of the Passive Continental Margin of Northern Namibia to Gondwana Break-Up and Global Scale Tectonics. *Doctoral thesis Georg-August-Universität Göttingen*, 253.

Raab, M. J., Brown, R. W., Gallagher, K., Carter, A. & Weber, K. 2002. Late Cretaceous reactivation of major crustal shear zones in northern Namibia: constraints from apatite fission track analysis. *Tectonophysics* **349**(1-4), 75-92.

Raab, S., Hoth, P., Huenges, E. & Mueller, H. J. 1998. Role of sulfur and carbon in the electrical conductivity of the middle crust. *Journal of Geophysical Research, B, Solid Earth and Planets* **103**(5), 9681-9689.

Rathmell, M. A., Streepey, M. M., Essene, E. J. & van, d. P. B. A. 1999. Comparison of garnet-biotite, calcite-graphite, and calcite-dolomite thermometry in the Grenville Orogen; Ontario, Canada. *Contributions to Mineralogy and Petrology* **134**(2-3), 217-231.

Ray, J. S., Veizer, J. & Davis, W. J. 2003. C, O, Sr and Pb isotope systematics of carbonate sequences of the Vindhyan Supergroup, India: age, diagenesis, correlations and implications for global events. *Precambrian Research* **121**(1-2), 103-140.

Ritter, O., Weckmann, U., Vietor, T. & Haak, V. 2003. A magnetotelluric study of the Damara Belt in Namibia : 1. Regional scale conductivity anomalies. *Physics of the Earth and Planetary Interiors* **138**(2), 71-91.

Ross, J. V. & Bustin, R. M. 1990. The role of strain energy in creep graphitization of anthracite. *Nature (London)* **343**(6253), 58-60.

Ross, J. V. & Bustin, R. M. 1997. Vitrinite anisotropy resulting from simple shear experiments at high temperature and high confining pressure. *International Journal of Coal Geology* **33**(2), 153-168.

Ross, J. V., Bustin, R. M. & Rouzaud, J. N. 1991. Graphitization of high rank coals-the role of shear strain: experimental considerations. *Organic Geochemistry* **17**(5), 585-596.

Ruland, W. 1965. X-ray studies on the carbonization and graphitization of acenaphthylene and bifluorenyl. *Carbon* **2**, 365-378.

Shankland, T. J., Duba, A. G., Mathez, E. A. & Peach, C. L. 1997. Increase of electrical conductivity with pressure as an indicator of conduction through a solid phase in midcrustal rocks. *Journal of Geophysical Research, B, Solid Earth and Planets* **102**(7), 14,741-14,750.

Shields, G. & Veizer, J. 2002. Precambrian marine carbonate isotope database: version 1.1. *Geochemics Geophysics Geosystems 3* **3**(5), 1030.

Soula, J. C., Debat, P., Brusset, S., Bessiere, G., Christophoul, F. & Deramond, J. 2001. Thrust-related, diapiric, and extensional doming in a frontal orogenic wedge: example of the Montagne Noire, southern French Hercynian Belt. *Journal of Structural Geology* **23**(11), 1677-1699.

Steven, N. M., Armstrong, R. A. & Moore, J. M. 1993. New Rb-Sr data from the Central Zone of the Damara Orogen, Namibia. *Communications of the Geological Survey of Namibia* **8**, 5-14.

Stosch, H.-G. 2002. *Einführung in die Isotopengeochemie*. Online in Internet http://129.13.109.66/WWW_only/html/ftp-Inhalte.html.

Tack, L. & Bowden, P. 1999. Post-collisional granite magmatism in the central Damaran (Pan-African) orogenic belt, western Namibia. *Journal of African Earth Sciences (1994)* **28**(3), 653-674.

Thrower, P. A. & Mayer, R. M. 1978. Point defects and self-diffusion in graphite. *Physica Status Solidi* **47**, 11-37.

Tuinstra, F. & Koenig, J. L. 1970. Raman Spectrum of Graphite. *Journal of Chemical Physics* **53**(3), 1126-1130.

Ullemeyer, K., Spalthoff, P., Heinitz, J., Isakov, N. N., Nikitin, A. & Weber, K. 1998. The SKAT texture diffractometer at the pulsed reactor IBR-2 at Dubna: experimental layout and first measurements. *Nuclear Instruments and Methods in Physics Research A* **412**(1), 80-88.

Valley, J. W. 2001. Stable Isotope Thermometry at High Temperatures. In: *Stable Isotope Geochemistry* (edited by Valley, J. W. & Cole, D. R.). *Reviews in Mineralogy and Geochemistry* **43**. Geochemical Society, 365-413.

Valley, J. W. & O´Neil, J. R. 1981. $^{13}C/^{12}C$ exchange between calcite and graphite: a possible thermometer in Grenville marbles. *Geochimica et Cosmochimica Acta* **45**(3), 411-419.

Veizer, J., Clayton, R. N. & Hinton, R. W. 1992. Geochemistry of Precambrian carbonates: IV, Early Paleoproterozoic (2.25 + or - 0.25 Ga) seawater. In: *The Taylor Colloquium; Origin and evolution of planetary crusts.* (edited by McLennan Scott, M. & Rudnick Roberta, L.). *Geochimica et Cosmochimica Acta* **56; 3**. Pergamon, Oxford, International, 875-885.

von der Gönna, J. 1997. In-situ Untersuchungen zur Phasentransformation Olivin-Spinell im Modellsystem Mg_2GeO_4 mitttels Impedanzspektroskopie und energiedispersiver Röntgenbeugung. *Doctoral thesis Rheinische-Friedrich-Wilhelms-Universität Bonn*, 4-26.

Wada, H. & Suzuki, K. 1983. Carbon isotopic thermometry calibrated by dolomite-calcite solvus temperatures. *Geochimica et Cosmochimica Acta* **47**(4), 697-706.

Walther, J. & Althaus, E. 1993. Graphite deposition in tectonically mobilized fault planes if the KTB-pilot drill hole. *KTB Report* **93-2**, 493-497.

Weckmann, U., Ritter, O. & Haak, V. 2003. A magnetotelluric study of the Damara Belt in Namibia : 2. MT phases over 90° reveal the internal structure of the Waterberg Fault/Omaruru Lineament. *Physics of the Earth and Planetary Interiors* **138**(2), 91-112.

Weis, P. L., Friedman, I. & Gleason, J. P. 1981. The origin of epigenetic graphite: evidence from isotopes. *Geochimica et Cosmochimica Acta* **45**(12), 2325-2332.

Weiss, T., Leiss, B., Oppermann, H. & Siegesmund, S. 1999. Microfabric of fresh and weathered marbles: Implications and consequences for the reconstruction of the Marmorpalais Potsdam. *Zeitschrift der Deutschen Geologischen Gesellschaft* **150**(2), 313-332.

Weiss, T., Rasolofosaon, P. N. J. & Siegesmund, S. 2002. Ultrasonic wave velocities as a diagnostic tool for the quality assessment of marble. In: *Natural Stone, Weathering Phenomena, Conservation strategies and Case Studies* (edited by Siegesmund, S., Weiss, T. & Vollbrecht, A.) **205**. Geological Society of London, Special Publications, London, 149-164.

Wenk, H. R., Takeshita, T., Bechler, E., Erskine, B. G. & Matthies, S. 1987. Pure shear and simple shear on calcite textures. Comparison of experimental, theoretical and natural data. *Journal of Structural Geology* **9**(5-6), 731-745.

Wilks, K. R., Mastalerz, M., Ross, J. V. & Bustin, R. M. 1993. The effect of experimental deformation on the graphitization of Pennsylvania anthracite. In: *Advances in organic petrology and geochemistry.* (edited by Goodarzi, F. & Bustin, R. M.). *International Journal of Coal Geology* **24; 1-4**. Elsevier, Amsterdam, International, 347-369.

Wopenka, B. & Pasteris, J. D. 1993. Structural characterization of kerogens to granulite-facies graphite; applicability of Raman microprobe spectroscopy. *American Mineralogist* **78**(5-6), 533-557.

APPENDICES

I. STRUCTURAL AND TEXTURAL ANALYSIS

I.1 SAMPLE LOCALITIES:

sample	geographical coordinates
Elim Sp	S 21°29´06.3´´ E 015°08´14.6´´
Radial 01	S 21°30´42.69´´ E 015°02´19.97´´
Omaruru Sp	S 21°30´42.69´´ E 015°02´19.97´´
13.8.97/3A	S 21°29´06.3´´ E 015°08´14.6´´
11/08/00/03	S 21°51´41.98´´ E 015°19´22.4´´
11/08/00/06	S 21°51´32.33´´ E 015°19´33.82´´
12/08/00/02	S 21°49´58.55´´ E 015°18´45.25´´
12/08/00/03	S 21°49´50.52´´ E 015°18´59.98´´
12/08/00/04	S 21°49´50.52´´ E 015°18´59.98´´
15/08/00/01	S 21°28´23.19´´ E 015°01´45.98´´
16/08/00/02	S 21°25´50.88´´ E 015°09´09.50´´
17/08/00/01	S 21°16´31.62´´ E 015°59´59.24´´
17/08/00/02	S 21°16´31.62´´ E 015°59´59.24´´
17/08/00/04	S 21°16´31.62´´ E 015°59´59.24´´
17/08/00/05	S 21°16´31.62´´ E 015°59´59.24´´
17/08/00/07	S 21°16´31.62´´ E 015°59´59.24´´
17/08/00/08a	S 21°16´31.62´´ E 015°59´59.24´´
17/08/00/08b	S 21°16´31.62´´ E 015°59´59.24´´
17/08/00/10	S 21°16´31.62´´ E 015°59´59.24´´
17/08/00/11	S 21°16´31.62´´ E 015°59´59.24´´
17/08/00/12	S 21°16´31.62´´ E 015°59´59.24´´
17/08/00/13	S 21°16´31.62´´ E 015°59´59.24´´
17/08/00/15	S 21°16´31.62´´ E 015°59´59.24´´
17/08/00/16a	S 21°16´31.62´´ E 015°59´59.24´´
17/08/00/16b	S 21°16´31.62´´ E 015°59´59.24´´
17/08/00/17	S 21°16´31.62´´ E 015°59´59.24´´
17/08/00/19	S 21°16´31.62´´ E 015°59´59.24´´
17/08/00/20	S 21°16´31.62´´ E 015°59´59.24´´
17/08/00/21	S 21°16´31.62´´ E 015°59´59.24´´
18/08/00/02	S 21°49´50.52´´ E 015°18´52.68´´
3.10.01/3	S 21°29´53.60´´ E 015°09´58.00´´
3.10.01/4	S 21°30´11.80´´ E 015°09´17.60´´
4.10.01/1	S 21°28´48.10´´ E 015°08´43.60´´

II. GRAPHITE CRYSTALLINITY MEASUREMENTS

II.1 RAMAN MEASUREMENTS AND CALCULATIONS:

sample	lab number	G band (G (ordered peak (O) measurement wave number (F	G band (G (ordered peak (O) measurement intensity (I	G band (G (ordered peak (O) measurement f. width at half max. (W)
12/08/00/02	12-02-2i	1582,49	397,11	22,77
	12-02-3i	1579,86	528	17,53
	12-02-4i	1580,74	449,5	21,91
	12-02-5i	1570,22	633,67	28,09
	12-02-6i	1573,73	629,1	22,8
	12-02-7i	1578,99	517,54	18,41
	12-02-1g	1580,74	697,32	17,52
	12-02-2g	1577,24	555,52	18,41
	12-02-3g	1576,36	702,4	19,29
	12-02-4g	1581,62	479,52	21,9
12/08/00/03	12-03-2i	1580,74	449,53	15,77
	12-03-3i	1579,86	306,45	20,16
	12-03-4i	1575,48	652,63	21,05
	12-03-5i	1574,6	618,06	22,8
	12-03-1g	1571,97	413,22	19,31
	12-03-2g	1564,95	418,01	21,08
	12-03-3g	1578,11	524,78	17,53
	12-03-4g	1579,86	505,1	20,15
15/08/00/01	15-01-1i	1579,86	446,55	19,28
	15-01-2i	1562,66	556,11	25,43
	15-01-3i	1570,55	643,54	26,28
	15-01-4i	1573,18	908,48	30,66
	15-01-5i	1580,18	481,25	15,74
	15-01-6i	1580,18	739,49	24,5
	15-01-7i	1578,43	924,37	36,77
	15-01-8i	1568,79	687,86	26,3
	15-01-1g	1577,55	470,64	17,49
	15-01-2g	1579,3	469,41	24,49
	15-01-3g	1581,05	507,22	14,86
17/08/00/11	17-11-1i	1578,43	152,7	18,36
	17-11-2i	1574,05	821,56	32,4
	17-11-3i	1579,3	499,62	16,62
	17-11-4i	1579,3	556,36	14,87
	17-11-5i	1580,18	567,05	16,62
	17-11-6i	1574,93	504,51	22,76
	17-11-7i	1577,55	449,47	26,25
	17-11-1g	1576,67	717,06	33,24
	17-11-2g	1576,67	777,14	27,11
	17-11-3g	1579,3	675	21,86

sample	lab number	G band (G (ordered peak (O) measurement wave number (F	G band (G (ordered peak (O) measurement intensity (I	G band (G (ordered peak (O) measurement f. width at half max. (W)
	17-11-4g	1578,43	596,57	21
	17-11-5g	1579,3	539,54	26,61
	17-11-6g	1580,18	296,35	20,98
	17-11-7g	1578,43	827,44	23,62
17/08/00/12	17-12-1i	1564,41	731,54	27,18
	17-12-2i	1574,93	437,36	22,75
	17-12-3i	1566,16	643,55	25,43
	17-12-4i	1566,16	605,89	31,56
	17-12-5i	1562,66	840,53	23,68
	17-12-6i	1568,79	399,86	27,17
	17-12-7i	1564,41	621,73	25,43
	17-12-2g	1568,79	522,08	30,68
	17-12-3g	1568,79	427,22	32,41
17/08/00/15	17-15-1i	1580,18	510	20,11
	17-15-2i	1580,18	563,5	20,12
	17-15-3i	1579,3	479,78	26,23
	17-15-4i	1580,18	504,99	18,36
	17-15-5i	1573,18	323,5	22,78
	17-15-6i	1574,93	289,27	22,76
	17-15-7i	1573,18	518,72	31,54
	17-15-1g	1578,43	663,36	19,25
	17-15-2g	1578,43	335,45	17,49
	17-15-3g	1566,16	405,01	25,42
	17-15-4g	1577,55	222	23,62
	17-15-5g	1568,79	366,95	26,28
17/08/00/16	17-16-1i	1567,92	897,73	19,29
	17-16-2i	1579,3	359,09	16,62
	17-16-3i	1580,18	507,71	16,62
	17-16-4i	1563,53	516,27	32,42
	17-16-5i	1579,3	509	22,74
	17-16-6i	1580,18	403,51	16,62
	17-16-7i	1579,3	549,93	16,62
	17-16-1g	1587,17	344	50,57
	17-16-2g	1581,62	122,66	51,52
	17-16-3g	1579,86	442,42	48,1
	17-16-4g	1586	501,35	54,18
	17-16-5g	1581,62	169,53	19,27
	17-16-6g	1582,49	168,96	20,15
17/08/00/19	17-19-1i	1572,3	476,66	27,15
	17-19-2i	1570,55	583,4	27,17
	17-19-3i	1576,67	579,43	22,74
	17-19-4i	1575,8	658,61	20,12
	17-19-5i	1575,8	596,03	33,27
	17-19-6i	1576,67	627,39	28
	17-19-1g	1581,05	627,95	16,62
	17-19-2g	1579,3	533,18	19,25

sample	lab number	G band (G (ordered peak (O) measurement wave number (F	G band (G (ordered peak (O) measurement intensity (I	G band (G (ordered peak (O) measurement f. width at half max. (W)
	17-19-3g	1579,3	377,45	28,86
	17-19-4g	1579,3	499	19,24
	17-19-5g	1567,92	398,14	28,05
17/08/00/20	17-2010i	1580,18	550,69	14,87
	17-2011i	1581,92	483,49	19,23
	17-2012i	1581,92	418,37	14,86
	17-2013i	1580,18	822,29	23,61
	17-2014i	1580,18	606,06	17,49
	17-2015i	1578,43	573,36	19,24
	17-20-1i	1582,8	775,5	14,86
	17-20-2i	1579,3	775,25	14,87
	17-20-3i	1581,05	903,48	14,87
	17-20-4i	1582,8	533,7	15,73
	17-20-5i	1580,18	513,22	21,86
	17-20-6i	1579,3	510,96	17,48
	17-20-7i	1581,05	599	18,36
	17-20-8i	1581,05	514,26	14,87
	17-20-9i	1580,18	514,68	15,74
	17-20-1g	1581,05	457,9	18,36
	17-20-2g	1581,05	516,81	14,87
	17-20-3g	1581,05	476,97	14,87
	17-20-4g	1579,3	487,48	14,87
	17-20-5g	1582,8	224,38	17,48
	17-20-6g	1581,05	252,85	23,6
18/08/00/02	18-02-1i	1579,86	554,29	22,78
	18-02-2i	1571,1	630,7	25,47
	18-02-3i	1565,83	755,07	17,57
	18-02-4i	1576,36	610,36	28,94
	18-02-5i	1579,86	442,42	15,77
	18-02-6i	1578,99	745,52	28,92
	18-02-7i	1575,48	649,66	19,29
	18-02-1g	1579,86	498,65	29,79
	18-02-2g	1581,62	546,91	20,15
	18-02-3g	1581,62	419,25	17,52
	18-02-5g	1586,87	191,15	42,83
	18-02-6g	1574,6	430,54	23,67
3.10.01/3	3-013-1i	1581,62	712,84	19,27
	3-013-2i	1579,86	488,13	16,65
	3-013-3i	1574,6	318,55	14,91
	3-013-4i	1581,62	404,48	40,26
	3-013-5i	1571,97	375,72	17,54
	3-013-6i	1564,95	377,88	34,25
	3-013-7i	1579,86	422,76	26,28
	3-013-1g	1579,86	476,51	28,04
	3-013-2g	1580,74	707,54	19,27
	3-013-3g	1580,74	731,55	21,02

sample	lab number	G band (G (ordered peak (O) measurement wave number (F	G band (G (ordered peak (O) measurement intensity (I	G band (G (ordered peak (O) measurement f. width at half max. (W)
	3-013-4g	1580,74	480,65	18,4
3.10.01/4	3-01410i	1569,67	520,42	21,02
	3-014-1i	1580,18	186,79	22,74
	3-014-2i	1580,18	265,44	17,49
	3-014-3i	1572,3	202,25	20,15
	3-014-4i	1565,29	267,7	21,92
	3-014-5i	1580,18	311,78	20,11
	3-014-6i	1579,3	198,15	21,85
	3-014-7i	1581,05	445	27,11
	3-014-8i	1577,55	169,98	22,74
	3-014-9i	1576,67	448,55	18,38
	3-014-1g	1580,74	512	21,02
	3-014-2g	1581,62	428,43	17,51
	3-014-3g	1580,18	467,73	22,74
	3-014-4g	1579,86	390,9	21,02
	3-014-5g	1580,74	427,83	22,78
Elim Spatkristall	Elim 01	1580,18	118,97	46,26
	Elim 02	1581,92	108,65	24,49
Omaruru Spatkristall	Rad 01	1579,3	464,73	14,87
	Rad 02	1580,18	459,53	15,74
	Rad 03	1579,3	477,09	13,99
	Rad 04	1580,18	514,62	16,61

sample	lab number	G band (G (ordered peak (O) function of meas. wave number (F	G band (G (ordered peak (O) function of meas. Intensity (I	G band (G (ordered peak (O) function of meas. f. width at half max. (W)
12/08/00/02	12-02-2i	1582,51	376,82	22,7186
	12-02-3i	1579,53	505,003	17,6463
	12-02-4i	1579,53	444,274	16,7984
	12-02-5i	1571,18	524,488	50,643
	12-02-6i	1574,46	618,807	23,0683
	12-02-7i	1578,04	515,438	18,25
	12-02-1g	1580,61	682,731	17,6251
	12-02-2g	1576,7	543,339	18,6876
	12-02-3g	1576,21	654,683	20,2408
	12-02-4g	1581,09	463,953	22,5514
12/08/00/03	12-03-2i	1580,17	443,64	16,0985
	12-03-3i	1579,05	287,076	18,6463
	12-03-4i	1575,18	649,911	20,0762
	12-03-5i	1573,94	605,779	21,0218
	12-03-1g	1571,07	413,225	18,9978
	12-03-2g	1566,39	388,051	22,6218
	12-03-3g	1578,97	518,289	15,9374
	12-03-4g	1579,68	489,659	20,1115
15/08/00/01	15-01-1i	1579,76	440,623	20,0054
	15-01-2i	1565,32	540,429	23,8225
	15-01-3i	1570,98	636,002	21,4134
	15-01-4i	1571,69	896,341	26,2946
	15-01-5i	1580,39	474,05	14,6029
	15-01-6i	1577,89	717,593	20,3826
	15-01-7i	1576,61	699,493	44,161
	15-01-8i	1567,19	665,791	20,9289
	15-01-1g	1578,96	470,398	16,0457
	15-01-2g	1580,79	448,116	26,1242
	15-01-3g	1581,5	499,717	14,1854
17/08/00/11	17-11-1i	1580,87	121,579	29,1035
	17-11-2i	1574,04	789,533	34,6974
	17-11-3i	1579,6	476,836	17,0527
	17-11-4i	1579,72	540,656	14,4205
	17-11-5i	1579,64	553,606	15,7714
	17-11-6i	1575,26	495,817	19,5114
	17-11-7i	1577,69	438,791	21,5306
	17-11-1g	1579,11	650,848	36,2335
	17-11-2g	1578,36	728,443	27,7066
	17-11-3g	1581,46	621,383	26,7658
	17-11-4g	1578,41	584,374	19,5215
	17-11-5g	1580,64	516,118	22,4875
	17-11-6g	1581,26	279,409	22,357
	17-11-7g	1578,77	790,566	23,4237
17/08/00/12	17-12-1i	1566,46	731,538	25,4083
	17-12-2i	1578,03	402,193	25,0189
	17-12-3i	1565,34	629,65	24,9894

sample	lab number	G band (G (ordered peak (O) function of meas. wave number (F	G band (G (ordered peak (O) function of meas. Intensity (I	G band (G (ordered peak (O) function of meas. f. width at half max. (W)
	17-12-4i	1567,59	605,888	25,0486
	17-12-5i	1564,47	839,506	24,0268
	17-12-6i	1569,1	388,083	26,2521
	17-12-7i	1565,38	598,649	24,9041
	17-12-2g	1568,01	511,148	32,2915
	17-12-3g	1571,55	411,942	33,9613
17/08/00/15	17-15-1i	1580,21	503,688	17,3981
	17-15-2i	1578,93	541,596	19,2132
	17-15-3i	1580,78	465,561	21,885
	17-15-4i	1579,83	495,903	14,8532
	17-15-5i	1571,46	305,607	25,8086
	17-15-6i	1574,53	270,41	24,4327
	17-15-7i	1571,34	503,172	29,3287
	17-15-1g	1576,76	645,69	20,1826
	17-15-2g	1578,89	315,39	18,5458
	17-15-3g	1568,59	405,011	24,8774
	17-15-4g	1576,98	199,76	27,0177
	17-15-5g	1570,59	301,114	30,6547
17/08/00/16	17-16-1i	1567,19	879,676	16,5687
	17-16-2i	1579,33	337,19	18,8498
	17-16-3i	1579,99	488,244	17,6551
	17-16-4i	1568,87	495,667	30,0261
	17-16-5i	1579,05	478,145	24,43
	17-16-6i	1579,52	379,945	17,3173
	17-16-7i	1579,47	541,672	13,435
	17-16-1g	1593,6	322,803	43,0641
	17-16-2g	1594,57	115,486	48,4573
	17-16-3g	1586,54	395,684	48,6091
	17-16-4g	1590,32	480,845	51,7922
	17-16-5g	1582,94	147,219	24,6986
	17-16-6g	1583,66	136,845	32,7022
17/08/00/19	17-19-1i	1573,66	465,982	24,7576
	17-19-2i	1568,56	573,285	25,1858
	17-19-3i	1579,84	556,082	23,7654
	17-19-4i	1577,28	634,145	21,0438
	17-19-5i	1574,44	584,054	25,9746
	17-19-6i	1578,7	564,548	32,2254
	17-19-1g	1580,07	620,789	16,027
	17-19-2g	1578,55	517,039	18,7833
	17-19-3g	1579,22	363,881	23,1723
	17-19-4g	1580,25	483,038	14,9974
	17-19-5g	1569,49	379,902	29,1222
17/08/00/20	17-2010i	1580,17	536,754	14,7645
	17-2011i	1581,42	474,423	14,668
	17-2012i	1580,93	422,76	20,8158
	17-2013i	1580,53	807,982	18,8048

sample	lab number	G band (G (ordered peak (O) function of meas. wave number (F	G band (G (ordered peak (O) function of meas. Intensity (I	G band (G (ordered peak (O) function of meas. f. width at half max. (W)
	17-2014i	1579,99	572,242	19,4036
	17-2015i	1580,01	559,823	19,5359
	17-20-1i	1581,65	768,895	14,6654
	17-20-2i	1580,09	770,899	13,9147
	17-20-3i	1580,91	900,805	14,4525
	17-20-4i	1581,93	533,7	13,9119
	17-20-5i	1580,75	491,547	17,8184
	17-20-6i	1581,1	472,94	20,0949
	17-20-7i	1582,26	533,853	21,3611
	17-20-8i	1580,84	514,256	13,8199
	17-20-9i	1579,45	514,679	14,4007
	17-20-1g	1580,62	452,776	13,9929
	17-20-2g	1579,62	521,401	13,6727
	17-20-3g	1580,09	480,675	15,8578
	17-20-4g	1580,15	487,484	14,6909
	17-20-5g	1581,95	211,757	17,9347
	17-20-6g	1581,41	234,852	18,3847
18/08/00/02	18-02-1i	1580,45	538,406	19,4269
	18-02-2i	1568,03	624,69	23,6295
	18-02-3i	1566,36	733,16	17,4281
	18-02-4i	1576,25	590,288	29,2048
	18-02-5i	1580,63	436,15	15,7241
	18-02-6i	1579,83	727,495	29,173
	18-02-7i	1574,94	628,937	19,1773
	18-02-1g	1582,08	466,898	32,0512
	18-02-2g	1581,11	546,913	17,1895
	18-02-3g	1581,37	419,245	18,0022
	18-02-5g	1590,25	161,268	49,4372
	18-02-6g	1577,59	381,023	28,9114
3.10.01/3	3-013-1i	1581,29	712,836	19,2287
	3-013-2i	1580,34	485,443	15,2394
	3-013-3i	1574,25	307,747	16,0103
	3-013-4i	1582,81	382,145	29,2093
	3-013-5i	1573,06	370,921	13,64
	3-013-6i	1568,63	360,802	35,6522
	3-013-7i	1581,13	390,469	23,4603
	3-013-1g	1580,54	466,589	16,8247
	3-013-2g	1581,23	699,92	17,9541
	3-013-3g	1582,63	715,139	19,839
	3-013-4g	1580,9	467,438	15,4609
3.10.01/4	3-01410i	1570,51	514,422	20,4356
	3-014-1i	1579,82	171,891	17,205
	3-014-2i	1580,26	243,459	20,0774
	3-014-3i	1571,35	198,997	17,0248
	3-014-4i	1565,91	247,854	17,9389
	3-014-5i	1579,76	282,444	23,5544

sample	lab number	G band (G (ordered peak (O) function of meas. wave number (F	G band (G (ordered peak (O) function of meas. Intensity (I	G band (G (ordered peak (O) function of meas. f. width at half max. (W)
	3-014-6i	1581,77	161,818	33,6083
	3-014-7i	1580,75	415,185	25,3214
	3-014-8i	1581,45	156,678	27,5599
	3-014-9i	1576,85	443,49	15,3604
	3-014-1g	1582,02	511,654	16,2126
	3-014-2g	1582,46	425,59	14,1091
	3-014-3g	1579,55	447,737	18,5711
	3-014-4g	1580,66	388,84	16,2443
	3-014-5g	1579,91	421,448	17,8496
Elim Spatkristall	Elim 01	1585,64	92,033	40,4928
	Elim 02	1584,4	86,7425	45,2778
Omaruru Spatkristall	Rad 01	1579,85	457,607	13,9269
	Rad 02	1579,65	417,175	13,9287
	Rad 03	1579,46	451,104	13,9798
	Rad 04	1580,48	497,532	12,9713

sample	lab number	shoulder peak (D2) wave number (F	shoulder peak (D2) intensitiy (I
12/08/00/02	12-02-2i	1620,89	86,35
	12-02-3i	1611,32	56
	12-02-4i		
	12-02-5i		
	12-02-6i	1613,06	112,5
	12-02-7i	1612,19	62,76
	12-02-1g	1619,5	83,5
	12-02-2g	1616,54	69,27
	12-02-3g	1610,44	99,7
	12-02-4g	1615,67	99,62
12/08/00/03	12-03-2i	1620,02	50,36
	12-03-3i	1619,15	41,96
	12-03-4i	1611,32	83,78
	12-03-5i		
	12-03-1g	1606,96	61,51
	12-03-2g	1601,73	80,66
	12-03-3g	1616,54	44,64
	12-03-4g	1619,15	111,53
15/08/00/01	15-01-1i		
	15-01-2i		
	15-01-3i		
	15-01-4i		
	15-01-5i		
	15-01-6i		
	15-01-7i		
	15-01-8i	1603,73	124,73
	15-01-1g	1617,64	39,81
	15-01-2g	1615,04	116,18
	15-01-3g		
17/08/00/11	17-11-1i	1616,78	44,64
	17-11-2i		
	17-11-3i		
	17-11-4i		
	17-11-5i		
	17-11-6i		
	17-11-7i		
	17-11-1g		
	17-11-2g		
	17-11-3g	1611,56	221
	17-11-4g		
	17-11-5g		
	17-11-6g	1612,43	67,66
	17-11-7g	1614,17	212,05
17/08/00/12	17-12-1i	1596,76	174,5
	17-12-2i	1608,96	125,71
	17-12-3i	1595,89	147,8

sample	lab number	shoulder peak (D2) wave number (F	shoulder peak (D2) intensitiy (I
	17-12-4i	1601,99	133,38
	17-12-5i		
	17-12-6i	1600,25	106,85
	17-12-7i		
	17-12-2g		
	17-12-3g		
17/08/00/15	17-15-1i	1604,6	97,63
	17-15-2i	1615,04	64,13
	17-15-3i		
	17-15-4i		
	17-15-5i	1606,34	78,74
	17-15-6i	1608,09	76,49
	17-15-7i	1608,09	84,89
	17-15-1g	1619,38	82,99
	17-15-2g	1613,3	58,91
	17-15-3g	1604,6	89,12
	17-15-4g	1616,78	79
	17-15-5g	1609,82	183,57
17/08/00/16	17-16-1i		
	17-16-2i	1615,04	57,93
	17-16-3i		
	17-16-4i	1609,82	82,96
	17-16-5i	1613,3	111,68
	17-16-6i	1612,43	67,74
	17-16-7i		
	17-16-1g		
	17-16-2g	1604,34	111,52
	17-16-3g	1610,44	278,31
	17-16-4g	1602,6	443,46
	17-16-5g	1620,02	47,03
	17-16-6g	1611,32	63,8
17/08/00/19	17-19-1i		
	17-19-2i		
	17-19-3i	1615,91	163,49
	17-19-4i	1612,43	126,48
	17-19-5i		
	17-19-6i		
	17-19-1g	1619,38	65,53
	17-19-2g	1615,91	71,31
	17-19-3g	1610,69	95,59
	17-19-4g		
	17-19-5g	1600,25	112
17/08/00/20	17-2010i	1612,43	61,34
	17-2011i	1608,96	44,36
	17-2012i	1620,25	80,64
	17-2013i	1617,64	127,76

sample	lab number	shoulder peak (D2) wave number (F	shoulder peak (D2) intensitiy (I
	17-2014i	1617,64	82,26
	17-2015i		
	17-20-1i	1615,04	75,05
	17-20-2i		
	17-20-3i		
	17-20-4i		
	17-20-5i	1614,17	88,57
	17-20-6i	1615,91	104,85
	17-20-7i	1612,43	137
	17-20-8i		
	17-20-9i		
	17-20-1g	1617,64	36,69
	17-20-2g		
	17-20-3g	1617,64	45,82
	17-20-4g		
	17-20-5g		
	17-20-6g	1619,38	37,8
18/08/00/02	18-02-1i	1617,41	99,11
	18-02-2i	1603,47	77,18
	18-02-3i		
	18-02-4i		
	18-02-5i		
	18-02-6i	1613,93	206,17
	18-02-7i	1612,19	81,55
	18-02-1g	1610,44	177,1
	18-02-2g	1618,28	70,43
	18-02-3g		
	18-02-5g	1613,06	135,99
	18-02-6g	1606,08	157,11
3.10.01/3	3-013-1i	1619,15	89,97
	3-013-2i	1615,67	45,58
	3-013-3i	1613,06	33,14
	3-013-4i	1618,28	153,61
	3-013-5i		
	3-013-6i		
	3-013-7i	1617,41	87,42
	3-013-1g		
	3-013-2g	1611,32	102,02
	3-013-3g	1614,8	123,31
	3-013-4g		
3.10.01/4	3-01410i	1601,99	80,8
	3-014-1i	1601,12	48,45
	3-014-2i	1618,51	47,97
	3-014-3i		
	3-014-4i		
	3-014-5i	1610,69	74,55

sample	lab number	shoulder peak (D2) wave number (F	shoulder peak (D2) intensitiy (I
	3-014-6i	1610,69	75,59
	3-014-7i	1615,91	135
	3-014-8i	1618,51	59,94
	3-014-9i		
	3-014-1g		
	3-014-2g		
	3-014-3g		
	3-014-4g		
	3-014-5g		
Elim Spatkristall	Elim 01	1603,73	60,33
	Elim 02	1620,25	45,49
Omaruru Spatkristall	Rad 01		
	Rad 02		
	Rad 03		
	Rad 04		

sample	lab number	dissorderd peak (D1) measurement wave number (F	dissorderd peak (D1) measurement intensity (I	dissorderd peak (D1) measurement f. width at half max. (W)
12/08/00/02	12-02-2i	1339,81	224,18	41,19
	12-02-3i	1332,47	74,01	43,98
	12-02-4i	1339,81	59,52	30,2
	12-02-5i	1324,22	312,13	45,87
	12-02-6i	1329,73	161,51	38,54
	12-02-7i	1335,23	90,36	44
	12-02-1g	1340,72	155,92	41,21
	12-02-2g	1338,89	115,33	41,23
	12-02-3g	1334,31	158,47	33,94
	12-02-4g	1339,81	190,98	48,55
12/08/00/03	12-03-2i	1335,23	71	32,06
	12-03-3i	1342,55	43,67	47,62
	12-03-4i	1334,31	171,82	41,25
	12-03-5i	1333,39	137	43,11
	12-03-1g	1337,97	80,63	40,33
	12-03-2g	1328,81	77,9	44,04
	12-03-3g	1341,64	43,59	32,98
	12-03-4g	1336,14	168,87	45,79
15/08/00/01	15-01-1i	1331,56	128,34	45,83
	15-01-2i	1330,46	127,37	36,67
	15-01-3i	1329,54	179,72	45,81
	15-01-4i	1327,71	233	45,82
	15-01-5i			
	15-01-6i	1335,04	186,04	46,7
	15-01-7i	1336,87	359,99	75,91
	15-01-8i	1323,13	79,16	36,69
	15-01-1g	1338,7	57,34	33,84
	15-01-2g	1335,04	263,26	45,77
	15-01-3g	1337,78	46,85	
17/08/00/11	17-11-1i	1339,61	69,44	31,09
	17-11-2i	1333,21	472,09	51,32
	17-11-3i	1337,78	100,44	43,04
	17-11-4i	1321,38	56,78	22,89
	17-11-5i	1328,63	89,07	36,61
	17-11-6i	1326,8	164,51	43,97
	17-11-7i	1331,38	76,13	37,54
	17-11-1g	1328,63	565,09	49,49
	17-11-2g	1331,38	420,72	43,07
	17-11-3g	1330,46	376,3	44,85
	17-11-4g	1331,38	114,5	37,54
	17-11-5g	1331,38	228,53	46,7
	17-11-6g	1330,46	132,32	43,94
	17-11-7g	1327,71	511	43,04
17/08/00/12	17-12-1i	1323,13	188,37	43,09

sample	lab number	dissorderd peak (D1) measurement wave number (F	dissorderd peak (D1) measurement intensity (I	dissorderd peak (D1) measurement f. width at half max. (W)
	17-12-2i	1334,12	243,06	50,37
	17-12-3i	1327,71	152,53	43,99
	17-12-4i	1324,05	180,78	47,67
	17-12-5i	1316,71	167,92	42,17
	17-12-6i	1323,13	172,89	46,76
	17-12-7i	1329,54	160,42	43,09
	17-12-2g	1325,88	202,5	48,58
	17-12-3g	1329,54	210,74	41,22
17/08/00/15	17-15-1i	1326,8	124,51	42,11
	17-15-2i	1333,21	113,72	41,22
	17-15-3i	1330,46	252,93	43,94
	17-15-4i	1333,21	76,92	48,52
	17-15-5i	1326,8	138,79	43,97
	17-15-6i	1331,38	173,24	40,3
	17-15-7i	1334,12	157,06	48,57
	17-15-1g	1333,21	141,78	36,62
	17-15-2g	1335,04	83,25	39,34
	17-15-3g	1330,46	117,06	31,14
	17-15-4g	1341,44	102,87	15,56
	17-15-5g	1327,71	149,23	
17/08/00/16	17-16-1i	1322,21	72,55	33,93
	17-16-2i	1335,95	80,96	42,13
	17-16-3i	1333,21	144,05	43,95
	17-16-4i	1329,54	149,49	42,16
	17-16-5i	1330,46	213,06	46,71
	17-16-6i	1341,44	252,2	43,88
	17-16-7i			
	17-16-1g	1332,29	536,38	54,04
	17-16-2g	1331,56	170,9	47,67
	17-16-3g	1330,64	458,2	53,19
	17-16-4g	1331,56	768,59	54,12
	17-16-5g	1331,56	94,46	44,93
	17-16-6g	1333,39	90,88	39,42
17/08/00/19	17-19-1i	1324,96	218,39	44,9
	17-19-2i	1325,88	135,98	34,83
	17-19-3i	1335,95	327,45	49,46
	17-19-4i	1331,38	269,31	45,79
	17-19-5i	1333,21	262,7	46,73
	17-19-6i	1323,13	461,78	54,99
	17-19-1g	1332,29	115,2	43,02
	17-19-2g	1337,78	113,59	40,28
	17-19-3g	1335,95	195,92	47,61
	17-19-4g	1332,29	43,7	35,68
	17-19-5g	1328,63	143,6	40,33

sample	lab number	dissorderd peak (D1) measurement wave number (F	dissorderd peak (D1) measurement intensity (I	dissorderd peak (D1) measurement f. width at half max. (W)
17/08/00/20	17-2010i	1337,78	73,11	38,44
	17-2011i	1329,54	20,33	
	17-2012i	1337,78	186,86	42,08
	17-2013i	1335,04	219,79	40,25
	17-2014i	1338,7	105,81	35,68
	17-2015i	1337,78	115,82	36,62
	17-20-1i	1331,38	144,6	37,52
	17-20-2i	1346,92	75,01	19,18
	17-20-3i	1336,87	102,39	40,25
	17-20-4i	1346,01	39,21	13,7
	17-20-5i	1329,54	180,27	39,35
	17-20-6i	1334,12	200,1	40,27
	17-20-7i	1335,95	216,49	41,18
	17-20-8i			
	17-20-9i	1346,92	46,01	
	17-20-1g	1346,01	40,75	
	17-20-2g			
	17-20-3g	1345,09	62,44	34,75
	17-20-4g			
	17-20-5g	1348,74	55,76	14,6
	17-20-6g	1344,18	49	26,49
18/08/00/02	18-02-1i	1337,97	169	40,3
	18-02-2i	1326,98	96,88	36,7
	18-02-3i	1321,47	71,94	36,71
	18-02-4i	1333,39	228,89	44,92
	18-02-5i	1332,47	74,01	45,83
	18-02-6i	1334,31	572,55	46,74
	18-02-7i	1332,47	174,71	39,42
	18-02-1g	1336,14	359,12	50,39
	18-02-2g	1344,38	89,04	41,21
	18-02-3g	1340,72	36,58	
	18-02-5g	1334,31	230,09	44,9
	18-02-6g	1328,81	283,93	44,04
3.10.01/3	3-013-1i	1338,89	132	37,55
	3-013-2i	1338,89	23	
	3-013-3i	1320,55	34,71	
	3-013-4i	1333,39	313,83	48,57
	3-013-5i			
	3-013-6i	1326,06	161,03	50,49
	3-013-7i	1337,97	170,04	46,74
	3-013-1g	1336,14	70,56	
	3-013-2g	1337,06	169,77	42,15
	3-013-3g	1333,39	236,9	43,97
	3-013-4g			

sample	lab number	dissorderd peak (D1) measurement wave number (F	dissorderd peak (D1) measurement intensity (I	dissorderd peak (D1) measurement f. width at half max. (W)
3.10.01/4	3-01410i	1328,63	127,56	38,48
	3-014-1i	1335,04	87,09	41,18
	3-014-2i	1339,61	116,53	36,61
	3-014-3i			
	3-014-4i			
	3-014-5i	1336,87	157,6	50,34
	3-014-6i	1330,46	175,57	50,34
	3-014-7i	1335,04	392,39	46,69
	3-014-8i	1330,46	183,17	46,68
	3-014-9i	1330,46	38,48	
	3-014-1g	1337,97	61,68	29,31
	3-014-2g			
	3-014-3g	1337,78	90,98	41,2
	3-014-4g	1332,47	60,54	35,76
	3-014-5g	1341,64	77	42,15
Elim Spatkristall	Elim 01	1336,87	105,46	44,87
	Elim 02	1329,54	96,4	28,36
Omaruru Spatkristall	Rad 01			
	Rad 02	1332,29	53,74	
	Rad 03	1324,96	178,1	2,75
	Rad 04			

sample	lab number	dissorderd peak (D1) function of meas. wave number (F	dissorderd peak (D1) function of meas. Intensity (I	dissorderd peak (D1) function of meas. F. width at half max. (W)
12/08/00/02	12-02-2i	1339,87	205,35	41,0948
	12-02-3i	1332,7	63,6505	49,9216
	12-02-4i	1335,48	53,6588	43,3199
	12-02-5i	1326,53	265,075	60,0061
	12-02-6i	1329,78	147,265	47,6603
	12-02-7i	1331,91	81,9594	45,1889
	12-02-1g	1337,24	141,97	40,794
	12-02-2g	1335,01	97,35	39,3494
	12-02-3g	1331,53	130,263	41,9071
	12-02-4g	1336,42	183,071	44,438
12/08/00/03	12-03-2i	1335,69	58,6312	37,8724
	12-03-3i			
	12-03-4i	1330,94	159,339	37,7999
	12-03-5i	1328,26	126,468	37,251
	12-03-1g	1331,56	64,3954	52,3581
	12-03-2g	1323,22	55,8303	113,451
	12-03-3g	1334,04	39,1355	36,2262
	12-03-4g	1337,33	154,6	45,0413
15/08/00/01	15-01-1i	1332,01	113,009	45,0875
	15-01-2i	1324,93	104,916	44,7885
	15-01-3i	1326,6	164,809	43,437
	15-01-4i	1327,35	211,992	41,4662
	15-01-5i	133,23	23,0564	58,2942
	15-01-6i	1332,01	179,115	44,2934
	15-01-7i	1334,95	312,083	82,658
	15-01-8i	1322,32	71,9885	44,57
	15-01-1g	1335,36	47,5938	51,1475
	15-01-2g	1333,58	251,2	42,6133
	15-01-3g	1332,39	35,889	58,9871
17/08/00/11	17-11-1i	1333,66	58,6302	55,8544
	17-11-2i	1326,47	453,967	46,6628
	17-11-3i	1332,05	90,8531	46,933
	17-11-4i	1329,87	45,6286	42,25
	17-11-5i	1329,14	77,0558	47,9653
	17-11-6i	1327,42	151,572	44,6187
	17-11-7i	1329,2	62,6733	40,7432
	17-11-1g	1325,65	532,274	47,3183
	17-11-2g	1327,21	392,237	42,7238
	17-11-3g	1330,8	356,305	44,8143
	17-11-4g	1329,52	99,4069	40,404
	17-11-5g	1331,17	217,712	43,144
	17-11-6g	1331,4	122,866	43,42
	17-11-7g	1328,08	473,295	43,1196
17/08/00/12	17-12-1i	1322,71	166,924	45,7517

sample	lab number	dissorderd peak (D1) function of meas. wave number (F	dissorderd peak (D1) function of meas. Intensity (I	dissorderd peak (D1) function of meas. F. width at half max. (W)
	17-12-2i	1329,69	227,06	47,317
	17-12-3i	1322,21	132,304	44,3789
	17-12-4i	1324,07	168,714	41,2751
	17-12-5i	1321,83	147,911	45,6466
	17-12-6i	1324,89	155,087	44,5394
	17-12-7i	1324,23	151,9	46,1856
	17-12-2g	1324,35	193,224	47,1725
	17-12-3g	1326,62	190,801	49,87
17/08/00/15	17-15-1i	1331,08	112,607	40,791
	17-15-2i	1330,13	106,684	47,434
	17-15-3i	1331,75	241,326	42,6803
	17-15-4i	1332,02	70,7673	56,1229
	17-15-5i	1325,97	128,099	48,124
	17-15-6i	1326,78	155,17	46,6375
	17-15-7i	1325,37	147,449	45,9974
	17-15-1g	1333,14	125,548	46,9232
	17-15-2g	1335,96	72,7349	51,0356
	17-15-3g	1325,68	97,593	43,5395
	17-15-4g	1335,69	73,8345	47,8316
	17-15-5g			
17/08/00/16	17-16-1i	1321,58	56,5026	41,6044
	17-16-2i	1329,34	63,6368	64,8709
	17-16-3i	1330,36	126,936	44,5031
	17-16-4i	1325,7	134,896	43,5138
	17-16-5i	1329,41	202,204	45,2838
	17-16-6i	1339,55	246,109	40,4072
	17-16-7i			
	17-16-1g	1329,87	522,875	49,4426
	17-16-2g	1331,26	158,95	56,4573
	17-16-3g	1328,73	441,88	53,0644
	17-16-4g	1327,88	739,196	51,187
	17-16-5g	1330,07	81,4696	52,1528
	17-16-6g	1330,79	74,4376	62,7218
17/08/00/19	17-19-1i	1325,94	194,989	44,1855
	17-19-2i	1325,21	119,789	42,0041
	17-19-3i	1329,83	313,258	46,1914
	17-19-4i	1329,4	238,52	43,6325
	17-19-5i	1326,98	247,321	43,7256
	17-19-6i	1325,39	448,75	50,7063
	17-19-1g	1333,01	103,198	47,5681
	17-19-2g	1332,68	96,7854	41,0647
	17-19-3g	1332,01	183,506	48,7009
	17-19-4g	1324,61	28,6701	104,759
	17-19-5g	1321,9	122,856	70,4486

sample	lab number	dissorderd peak (D1) function of meas. wave number (F	dissorderd peak (D1) function of meas. Intensity (I	dissorderd peak (D1) function of meas. F. width at half max. (W)
17/08/00/20	17-2010i	1334,02	62,153	50,7895
	17-2011i			
	17-2012i	1336,62	178,59	42,8265
	17-2013i	1336,42	207,194	41,7477
	17-2014i	1335,22	80,6838	64,8443
	17-2015i	1332,84	87,7097	82,2106
	17-20-1i	1333,47	117,696	40,2888
	17-20-2i	1342,83	49,3757	44,1207
	17-20-3i	1333,39	91,9725	58,521
	17-20-4i	1340,74	23,2153	39,5124
	17-20-5i	1332,76	166,114	39,4883
	17-20-6i	1334,39	197,989	40,0849
	17-20-7i	1333,5	208,294	38,7959
	17-20-8i			
	17-20-9i	1338,75	28,4746	93,5214
	17-20-1g	1331,54	50,2055	62,9814
	17-20-2g			
	17-20-3g	1337,78	55,3621	40,9091
	17-20-4g			
	17-20-5g	1330,03	51,1333	68,082
	17-20-6g	1338,1	36,0354	75,7599
18/08/00/02	18-02-1i	1335,64	154,881	39,4901
	18-02-2i	1324,86	85,3399	35,2597
	18-02-3i	1323,91	66,8553	40,1324
	18-02-4i	1330,54	210,327	43,5993
	18-02-5i	1332,37	61,2759	68,2714
	18-02-6i	1332,32	544,528	43,5378
	18-02-7i	1329,8	152,677	40,3124
	18-02-1g	1334,29	338,249	47,8929
	18-02-2g	1335,85	81,1213	42,3511
	18-02-3g	1329,74	20,1215	142,871
	18-02-5g	1331,87	200,768	59,1313
	18-02-6g	1327,93	251,836	47,0394
3.10.01/3	3-013-1i	1336,14	115,056	38,5804
	3-013-2i	1339,53	14,0829	59,809
	3-013-3i	1327,14	23,998	40,0794
	3-013-4i	1332,93	305,292	45,646
	3-013-5i			
	3-013-6i	1322,35	143,295	54,902
	3-013-7i	1335,12	165,442	44,1698
	3-013-1g	1333,63	52,7411	48,0881
	3-013-2g	1333,46	160,311	41,9454
	3-013-3g	1335,34	220,21	41,7939
	3-013-4g			

sample	lab number	dissorderd peak (D1) function of meas. wave number (F	dissorderd peak (D1) function of meas. Intensity (I	dissorderd peak (D1) function of meas. F. width at half max. (W)
3.10.01/4	3-01410i	1326,24	106,783	44,4356
	3-014-1i	1332,94	79,6503	46,088
	3-014-2i	1333,89	98,358	41,2725
	3-014-3i			
	3-014-4i			
	3-014-5i	1332,61	147,585	57,4559
	3-014-6i	1331,56	169,465	50,6634
	3-014-7i	1333,15	384,729	42,577
	3-014-8i	1332,2	170,752	45,7596
	3-014-9i	1326,31	23,1992	68,4843
	3-014-1g	1333,31	47,0691	49,487
	3-014-2g			
	3-014-3g	1332,98	84,7304	44,0079
	3-014-4g	1330,75	49,7358	41,5414
	3-014-5g	1334,24	71,6761	50,2227
Elim Spatkristall	Elim 01	1331,06	91,7932	56,3895
	Elim 02	1332,39	72,5575	52,4464
Omaruru Spatkristall	Rad 01			
	Rad 02			
	Rad 03			
	Rad 04			

sample	lab number	D1/G intensity ratio	graphite crystallinity own calculation based on Tuinstra & Koenig L_a [Å]	graphite crystallinity after Zheng & Chen L_a [Å]
12/08/00/02	12-02-2i	0,544955151	79,18072888	80,74058924
	12-02-3i	0,126039845	342,3516266	349,0959537
	12-02-4i	0,120778619	357,2647755	364,3028916
	12-02-5i	0,505397645	85,3782096	87,06016033
	12-02-6i	0,237982117	181,3159181	184,8878416
	12-02-7i	0,159009231	271,3675539	276,7134947
	12-02-1g	0,207944271	207,5072609	211,5951539
	12-02-2g	0,17916991	240,832548	245,5769492
	12-02-3g	0,198971105	216,8653888	221,1376369
	12-02-4g	0,394589538	109,3540043	111,5082782
12/08/00/03	12-03-2i	0,132159409	326,4992371	332,9312721
	12-03-3i	0		
	12-03-4i	0,245170493	175,9997527	179,4669478
	12-03-5i	0,208769205	206,6873136	210,7590537
	12-03-1g	0,155836167	276,8930151	282,3478075
	12-03-2g	0,143873615	299,9156322	305,8239701
	12-03-3g	0,075509031	571,4541119	582,7117579
	12-03-4g	0,315729926	136,6672667	139,3596119
15/08/00/01	15-01-1i	0,25647549	168,2419868	171,5563539
	15-01-2i	0,19413466	222,2681212	226,6468032
	15-01-3i	0,259132833	166,5167072	169,7970863
	15-01-4i	0,236508204	182,4458744	186,0400581
	15-01-5i	0,048637064	887,1823845	904,6598775
	15-01-6i	0,249605278	172,8727312	176,278324
	15-01-7i	0,446156002	96,71492911	98,62021321
	15-01-8i	0,108124772	399,0754876	406,9372747
	15-01-1g	0,101177726	426,4767329	434,8783245
	15-01-2g	0,560569138	76,97524375	78,49165605
	15-01-3g	0,071818649	600,8181224	612,6542395
17/08/00/11	17-11-1i	0,482239531	89,47824316	91,24096455
	17-11-2i	0,574981666	75,04577726	76,52417907
	17-11-3i	0,190533223	226,469407	230,9308543
	17-11-4i	0,084394883	511,2862818	521,3586216
	17-11-5i	0,139188882	310,0100063	316,1172034
	17-11-6i	0,305701499	141,1505872	143,9312538
	17-11-7i	0,142831781	302,1032558	308,05469
	17-11-1g	0,817816141	52,7624045	53,80182387
	17-11-2g	0,538459426	80,13592843	81,71460622
	17-11-3g	0,573406418	75,25194127	76,73440451
	17-11-4g	0,170108355	253,6615324	258,6586645
	17-11-5g	0,421826017	102,2932308	104,3084074
	17-11-6g	0,439735298	98,12709195	100,0601957
	17-11-7g	0,598678668	72,07530242	73,49518588

sample	lab number	D1/G intensity ratio	graphite crystallinity own calculation based on Tuinstra & Koenig L_a [Å]	graphite crystallinity after Zheng & Chen L_a [Å]
17/08/00/12	17-12-1i	0,228182268	189,1029765	192,8283051
	17-12-2i	0,564554828	76,4318077	77,93751431
	17-12-3i	0,210123084	205,3555715	209,4010763
	17-12-4i	0,278457405	154,9606702	158,0133955
	17-12-5i	0,176188139	244,9083477	249,7330422
	17-12-6i	0,399623276	107,9765584	110,1036966
	17-12-7i	0,253738	170,0570906	173,4072153
	17-12-2g	0,378019673	114,1473556	116,3960585
	17-12-3g	0,463174427	93,16133082	94,99660903
17/08/00/15	17-15-1i	0,223564985	193,0085166	196,8107844
	17-15-2i	0,196980775	219,0566363	223,372052
	17-15-3i	0,518355275	83,24396061	84,88386664
	17-15-4i	0,142703916	302,3739453	308,3307121
	17-15-5i	0,419162519	102,9432358	104,9712176
	17-15-6i	0,573832329	75,19608761	76,67745054
	17-15-7i	0,293038961	147,2498604	150,1506826
	17-15-1g	0,194440056	221,9190164	226,290821
	17-15-2g	0,230618916	187,1049728	190,7909408
	17-15-3g	0,240963826	179,0722983	182,6000225
	17-15-4g	0,369616039	116,7426234	119,0424531
	17-15-5g	0		
17/08/00/16	17-16-1i	0,064231149	671,7915981	685,0258926
	17-16-2i	0,188726831	228,6370514	233,1412013
	17-16-3i	0,259984762	165,9710584	169,2406882
	17-16-4i	0,272150456	158,5518052	161,6752758
	17-16-5i	0,422892637	102,0352266	104,0453206
	17-16-6i	0,647749016	66,61522438	67,9275443
	17-16-7i	0		
	17-16-1g	1,619795975	26,63912415	27,16391489
	17-16-2g	1,376357307	31,35083153	31,96844291
	17-16-3g	1,11674973	38,6388686	39,40005431
	17-16-4g	1,537285404	28,06892328	28,62188107
	17-16-5g	0,553390527	77,9737707	79,50985398
	17-16-6g	0,54395557	79,32623256	80,88895934
17/08/00/19	17-19-1i	0,418447494	103,1191409	105,150588
	17-19-2i	0,208951917	206,506581	210,5747606
	17-19-3i	0,563330588	76,59791069	78,10688953
	17-19-4i	0,376128488	114,7212919	116,9813014
	17-19-5i	0,423455708	101,89955	103,9069711
	17-19-6i	0,794883695	54,28460334	55,35401003
	17-19-1g	0,166236837	259,5690989	264,6826101
	17-19-2g	0,187191682	230,5120913	235,0531795
	17-19-3g	0,504302231	85,56366289	87,24926705

sample	lab number	D1/G intensity ratio	graphite crystallinity own calculation based on Tuinstra & Koenig L_a [Å]	graphite crystallinity after Zheng & Chen L_a [Å]
	17-19-4g	0,059353715	726,996545	741,318377
	17-19-5g	0,323388663	133,4306083	136,0591912
17/08/00/20	17-2010i	0,1157942	372,6434146	379,9844899
	17-2011i	0		
	17-2012i	0,422438263	102,1449756	104,1572316
	17-2013i	0,25643393	168,2692535	171,5841578
	17-2014i	0,140995942	306,0367934	312,0657183
	17-2015i	0,156673984	275,4123233	280,8379461
	17-20-1i	0,153071616	281,8938433	287,447152
	17-20-2i	0,064049506	673,6967834	686,9686101
	17-20-3i	0,102100344	422,6229271	430,9485988
	17-20-4i	0,043498782	991,9805565	1011,522573
	17-20-5i	0,337941235	127,6847619	130,2001517
	17-20-6i	0,418634499	103,0730772	105,1036169
	17-20-7i	0,390171077	110,592375	112,7710448
	17-20-8i	0		
	17-20-9i	0,05532497	779,9361919	795,3009349
	17-20-1g	0,110883748	389,1458103	396,8119828
	17-20-2g	0		
	17-20-3g	0,115175742	374,6443925	382,0248871
	17-20-4g	0		
	17-20-5g	0,241471592	178,6957448	182,216051
	17-20-6g	0,153438761	281,2193325	286,7593533
18/08/00/02	18-02-1i	0,287665814	150,0002574	152,9552624
	18-02-2i	0,136611599	315,858582	322,0809961
	18-02-3i	0,091187872	473,1983022	482,5203088
	18-02-4i	0,356312512	121,1014057	123,4871034
	18-02-5i	0,14049272	307,132967	313,1834865
	18-02-6i	0,748497241	57,64877107	58,78445186
	18-02-7i	0,242754044	177,7517087	181,2534173
	18-02-1g	0,72446016	59,56151686	60,73487874
	18-02-2g	0,148325785	290,9133169	296,6443092
	18-02-3g	0,047994609	899,0581784	916,7696245
	18-02-5g	1,244933899	34,66043145	35,34324195
	18-02-6g	0,660946977	65,2850343	66,57114948
3.10.01/3	3-013-1i	0,16140599	267,3379481	272,6045056
	3-013-2i	0,029010409	1487,3953	1516,696987
	3-013-3i	0,077979639	553,3488812	564,2498542
	3-013-4i	0,798890474	54,01234273	55,07638589
	3-013-5i	0		
	3-013-6i	0,397156889	108,6471045	110,7874525
	3-013-7i	0,423700729	101,8406226	103,8468829
	3-013-1g	0,113035455	381,7381546	389,2583962

sample	lab number	D1/G intensity ratio	graphite crystallinity own calculation based on Tuinstra & Koenig L_a [Å]	graphite crystallinity after Zheng & Chen L_a [Å]
	3-013-2g	0,229041891	188,3932497	192,1045967
	3-013-3g	0,307926151	140,1308264	142,8914037
	3-013-4g	0		
3.10.01/4	3-01410i	0,207578603	207,8728033	211,9678975
	3-014-1i	0,463376791	93,12064586	94,95512258
	3-014-2i	0,404002317	106,8061847	108,9102666
	3-014-3i	0		
	3-014-4i	0		
	3-014-5i	0,52252836	82,5791467	84,20595589
	3-014-6i	1,047256795	41,20283228	42,01452807
	3-014-7i	0,926644749	46,56579139	47,48313748
	3-014-8i	1,089827544	39,59337079	40,37336019
	3-014-9i	0,052310537	824,8805812	841,1307286
	3-014-1g	0,091994004	469,051724	478,292043
	3-014-2g	0		
	3-014-3g	0,189241452	228,0152979	232,5071993
	3-014-4g	0,127908137	337,3510636	343,9968795
	3-014-5g	0,170071041	253,717187	258,7154156
Elim Spatkristall	Elim 01	0,997394413	43,26267072	44,11494533
	Elim 02	0,836470012	51,58576572	52,60200531
Omaruru Spatkristall	Rad 01	0		
	Rad 02	0		
	Rad 03	0		
	Rad 04	0		

II..2 STATISTICAL ANALYSIS OF SAMPLE MEASUREMENTS:

sample	G band postion of sample [Δ cm^{-1}]		G band FWHM of sample [cm^{-1}]	
12/08/00/02	**G band position 1:**		**G band FWHM 1:**	
	sum of raman shift:	15779,86	sum of wavenumbers:	228,2295
	mean raman shift:	1577,986	mean wavenumbers:	22,82295
	standard deviation:	3,420848498	standard deviation:	10,04927333
	maximum raman shift:	1582,51	maximum wavenumbers:	50,643
	minimum raman shift:	1571,18	minimum wavenumbers:	16,7984
	variation of raman shift:	11,33	variation of wavenumbers:	33,8446
12/08/00/03	**G band position 2:**		**G band FWHM 2:**	
	sum of raman shift:	12604,45	sum of wavenumbers:	153,5113
	mean raman shift:	1575,55625	mean wavenumbers:	19,1889125
	standard deviation:	4,914299652	standard deviation:	2,306406458
	maximum raman shift:	1580,17	maximum wavenumbers:	22,6218
	minimum raman shift:	1566,39	minimum wavenumbers:	15,9374
	variation of raman shift:	13,78	variation of wavenumbers:	6,6844
15/08/00/01	**G band position 3:**		**G band FWHM 3:**	
	sum of raman shift:	17331,08	sum of wavenumbers:	247,9666
	mean raman shift:	1575,552727	mean wavenumbers:	22,54241818
	standard deviation:	5,766836379	standard deviation:	8,282343669
	maximum raman shift:	1581,5	maximum wavenumbers:	44,161
	minimum raman shift:	1565,32	minimum wavenumbers:	14,1854
	variation of raman shift:	16,18	variation of wavenumbers:	29,9756
17/08/00/11	**G band position 4:**		**G band FWHM 4:**	
	sum of raman shift:	22104,83	sum of wavenumbers:	330,5831
	mean raman shift:	1578,916429	mean wavenumbers:	23,61307857
	standard deviation:	2,142319401	standard deviation:	6,614637212
	maximum raman shift:	1581,46	maximum wavenumbers:	36,2335
	minimum raman shift:	1574,04	minimum wavenumbers:	14,4205
	variation of raman shift:	7,42	variation of wavenumbers:	21,813
17/08/00/12	**G band position 5:**		**G band FWHM 5:**	
	sum of raman shift:	14115,93	sum of wavenumbers:	241,901
	mean raman shift:	1568,436667	mean wavenumbers:	26,87788889
	standard deviation:	4,207701273	standard deviation:	3,612933014
	maximum raman shift:	1571,55	maximum wavenumbers:	33,9613
	minimum raman shift:	1564,47	minimum wavenumbers:	24,0268
	variation of raman shift:	7,08	variation of wavenumbers:	9,9345
17/08/00/15	**G band position 6:**		**G band FWHM 6:**	
	sum of raman shift:	18908,89	sum of wavenumbers:	274,1977
	mean raman shift:	1575,740833	mean wavenumbers:	22,84980833
	standard deviation:	4,280767685	standard deviation:	4,946035567
	maximum raman shift:	1580,78	maximum wavenumbers:	30,6547
	minimum raman shift:	1570,59	minimum wavenumbers:	14,8532
	variation of raman shift:	10,19	variation of wavenumbers:	15,8015
17/08/00/16	**G band position 7:**		**G band FWHM 7:**	
	sum of raman shift:	20565,05	sum of wavenumbers:	387,6055

sample	G band postion of sample [Δ cm^{-1}]		G band FWHM of sample [cm^{-1}]	
	mean raman shift:	1581,926923	mean wavenumbers:	29,81580769
	standard deviation:	8,216469624	standard deviation:	13,81697602
	maximum raman shift:	1594,57	maximum wavenumbers:	51,7922
	minimum raman shift:	1567,19	minimum wavenumbers:	13,435
	variation of raman shift:	27,38	variation of wavenumbers:	38,3572
17/08/00/19	**G band position 8:**		**G band FWHM 8:**	
	sum of raman shift:	17340,06	sum of wavenumbers:	255,0548
	mean raman shift:	1576,369091	mean wavenumbers:	23,1868
	standard deviation:	4,234580155	standard deviation:	5,232664364
	maximum raman shift:	1580,25	maximum wavenumbers:	32,2254
	minimum raman shift:	1568,56	minimum wavenumbers:	14,9974
	variation of raman shift:	11,69	variation of wavenumbers:	17,228
17/08/00/20	**G band position 9:**		**G band FWHM 9:**	
	sum of raman shift:	33195,87	sum of wavenumbers:	346,9658
	mean raman shift:	1580,755714	mean wavenumbers:	16,52218095
	standard deviation:	0,797493395	standard deviation:	2,667774257
	maximum raman shift:	1582,26	maximum wavenumbers:	21,3611
	minimum raman shift:	1579,45	minimum wavenumbers:	13,6727
	variation of raman shift:	2,81	variation of wavenumbers:	7,6884
18/08/00/02	**G band position 10:**		**G band FWHM 10:**	
	sum of raman shift:	18938,89	sum of wavenumbers:	299,3552
	mean raman shift:	1578,240833	mean wavenumbers:	24,94626667
	standard deviation:	6,401668047	standard deviation:	9,617434428
	maximum raman shift:	1590,25	maximum wavenumbers:	49,4372
	minimum raman shift:	1566,36	minimum wavenumbers:	15,7241
	variation of raman shift:	23,89	variation of wavenumbers:	33,7131
3.10.01/3	**G band position 11:**		**G band FWHM 11:**	
	sum of raman shift:	17366,81	sum of wavenumbers:	222,5189
	mean raman shift:	1578,800909	mean wavenumbers:	20,22899091
	standard deviation:	4,638653801	standard deviation:	6,750722562
	maximum raman shift:	1582,81	maximum wavenumbers:	35,6522
	minimum raman shift:	1573,06	minimum wavenumbers:	13,64
	variation of raman shift:	9,75	variation of wavenumbers:	22,0122
3.10.01/4	**G band position 12:**		**G band FWHM 12:**	
	sum of raman shift:	23673,03	sum of wavenumbers:	301,0728
	mean raman shift:	1578,202	mean wavenumbers:	20,07152
	standard deviation:	4,9394537	standard deviation:	5,316176167
	maximum raman shift:	1582,46	maximum wavenumbers:	33,6083
	minimum raman shift:	1565,91	minimum wavenumbers:	14,1091
	variation of raman shift:	16,55	variation of wavenumbers:	19,4992
Elim Spatkristall	**G band position 13:**		**G band FWHM 13:**	
	sum of raman shift:	3170,04	sum of wavenumbers:	85,7706
	mean raman shift:	1585,02	mean wavenumbers:	42,8853
	standard deviation:	0,876812409	standard deviation:	3,383505948
	maximum raman shift:	1585,64	maximum wavenumbers:	45,2778
	minimum raman shift:	1584,4	minimum wavenumbers:	40,4928

sample	G band postion of sample [Δ cm^{-1}]		G band FWHM of sample [cm^{-1}]	
	variation of raman shift:	1,24	variation of wavenumbers:	4,785
Omaruru Spatkristall	**G band position 14:**		**G band FWHM 14:**	
	sum of raman shift:	6319,44	sum of wavenumbers:	54,8067
	mean raman shift:	1579,86	mean wavenumbers:	13,701675
	standard deviation:	0,442944691	standard deviation:	0,487533865
	maximum raman shift:	1580,48	maximum wavenumbers:	13,9798
	minimum raman shift:	1579,46	minimum wavenumbers:	12,9713
	variation of raman shift:	1,02	variation of wavenumbers:	1,0085

sample	D1 band postion of sample [Δ cm^{-1}]		D1 band FWHM of sample [cm^{-1}]	
12/08/00/02	**D1 band FWHM 1:**		**D1/G intensity ratio 1:**	
	sum of wavenumbers:	453,6801	sum of intensity ratios:	2,67483743
	mean wavenumbers:	45,36801	mean intensity ratios:	0,26748374
	standard deviation:	6,080375201	standard deviation:	0,15633062
	maximum wavenumbers:	60,0061	maximum intensity ratios:	0,54495515
	minimum wavenumbers:	41,0948	minimum intensity ratios:	0,12077861
	variation of wavenumbers:	18,9113	variation of intensity ratios:	0,42417653
12/08/00/03	**D1 band FWHM 2:**		**D1/G intensity ratio 2:**	
	sum of wavenumbers:	359,9999	sum of intensity ratios:	1,27704784
	mean wavenumbers:	44,9999875	mean intensity ratios:	0,15963098
	standard deviation:	27,95850796	standard deviation:	0,09832481
	maximum wavenumbers:	113,451	maximum intensity ratios:	0,31572992
	minimum wavenumbers:	36,2262	minimum intensity ratios:	0,07550903
	variation of wavenumbers:	77,2248	variation of intensity ratios:	0,24022089
15/08/00/01	**D1 band FWHM 3:**		**D1/G intensity ratio 3:**	
	sum of wavenumbers:	557,3427	sum of intensity ratios:	2,53233981
	mean wavenumbers:	50,66751818	mean intensity ratios:	0,23021271
	standard deviation:	12,23244323	standard deviation:	0,15767821
	maximum wavenumbers:	82,658	maximum intensity ratios:	0,56056913
	minimum wavenumbers:	41,4662	minimum intensity ratios:	0,07181864
	variation of wavenumbers:	41,1918	variation of intensity ratios:	0,48875048
17/08/00/11	**D1 band FWHM 4:**		**D1/G intensity ratio 4:**	
	sum of wavenumbers:	629,9714	sum of intensity ratios:	5,47990179
	mean wavenumbers:	44,99795714	mean intensity ratios:	0,39142155
	standard deviation:	3,923606228	standard deviation:	0,22206625
	maximum wavenumbers:	55,8544	maximum intensity ratios:	0,81781614
	minimum wavenumbers:	40,404	minimum intensity ratios:	0,08439488
	variation of wavenumbers:	15,4504	variation of intensity ratios:	0,73342125
17/08/00/12	**D1 band FWHM 5:**		**D1/G intensity ratio 5:**	
	sum of wavenumbers:	412,1368	sum of intensity ratios:	2,95206110
	mean wavenumbers:	45,79297778	mean intensity ratios:	0,32800678
	standard deviation:	2,37190353	standard deviation:	0,13073679
	maximum wavenumbers:	49,87	maximum intensity ratios:	0,56455482
	minimum wavenumbers:	41,2751	minimum intensity ratios:	0,17618813
	variation of wavenumbers:	8,5949	variation of intensity ratios:	0,38836668
17/08/00/15	**D1 band FWHM 6:**		**D1/G intensity ratio 6:**	
	sum of wavenumbers:	517,117	sum of intensity ratios:	3,40327759
	mean wavenumbers:	43,09308333	mean intensity ratios:	0,28360646
	standard deviation:	4,147101138	standard deviation:	0,16213686
	maximum wavenumbers:	56,1229	maximum intensity ratios:	0,57383232
	minimum wavenumbers:	40,791	minimum intensity ratios:	0,14270391
	variation of wavenumbers:	15,3319	variation of intensity ratios:	0,43112841
17/08/00/16	**D1 band FWHM 7:**		**D1/G intensity ratio 7:**	
	sum of wavenumbers:	605,2091	sum of intensity ratios:	8,60326936
	mean wavenumbers:	46,55454615	mean intensity ratios:	0,66178995
	standard deviation:	7,949872904	standard deviation:	0,56397877
	maximum wavenumbers:	64,8709	maximum intensity ratios:	1,61979597
	minimum wavenumbers:	40,4072	minimum intensity ratios:	0,06423114

sample	D1 band postion of sample [Δ cm^{-1}]		D1 band FWHM of sample [cm^{-1}]	
	variation of wavenumbers:	24,4637	variation of intensity ratios:	1,55556482
17/08/00/19	**D1 band FWHM 8:**		**D1/G intensity ratio 8:**	
	sum of wavenumbers:	582,9867	sum of intensity ratios:	4,02567101
	mean wavenumbers:	52,99879091	mean intensity ratios:	0,36597009
	standard deviation:	18,96806464	standard deviation:	0,20989332
	maximum wavenumbers:	104,759	maximum intensity ratios:	0,79488369
	minimum wavenumbers:	41,0647	minimum intensity ratios:	0,05935371
	variation of wavenumbers:	63,6943	variation of intensity ratios:	0,73552997
17/08/00/20	**D1 band FWHM 9:**		**D1/G intensity ratio 9:**	
	sum of wavenumbers:	924,4844	sum of intensity ratios:	3,27809819
	mean wavenumbers:	44,02306667	mean intensity ratios:	0,15609991
	standard deviation:	17,38052537	standard deviation:	0,13826649
	maximum wavenumbers:	93,5214	maximum intensity ratios:	0,42243826
	minimum wavenumbers:	38,7959	minimum intensity ratios:	0,04349878
	variation of wavenumbers:	54,7255	variation of intensity ratios:	0,37893948
18/08/00/02	**D1 band FWHM 10:**		**D1/G intensity ratio 10:**	
	sum of wavenumbers:	649,8888	sum of intensity ratios:	4,83018323
	mean wavenumbers:	54,1574	mean intensity ratios:	0,40251526
	standard deviation:	29,40042191	standard deviation:	0,36521965
	maximum wavenumbers:	142,871	maximum intensity ratios:	1,24493389
	minimum wavenumbers:	35,2597	minimum intensity ratios:	0,04799460
	variation of wavenumbers:	107,6113	variation of intensity ratios:	1,19693928
3.10.01/3	**D1 band FWHM 11:**		**D1/G intensity ratio 11:**	
	sum of wavenumbers:	415,014	sum of intensity ratios:	2,53814762
	mean wavenumbers:	37,72854545	mean intensity ratios:	0,23074069
	standard deviation:	7,087753325	standard deviation:	0,24142451
	maximum wavenumbers:	59,809	maximum intensity ratios:	0,79889047
	minimum wavenumbers:	40,0794	minimum intensity ratios:	0,02901040
	variation of wavenumbers:	19,7296	variation of intensity ratios:	0,76988006
3.10.01/4	**D1 band FWHM 12:**		**D1/G intensity ratio 12:**	
	sum of wavenumbers:	581,9953	sum of intensity ratios:	5,29274032
	mean wavenumbers:	38,79968667	mean intensity ratios:	0,35284935
	standard deviation:	7,827510915	standard deviation:	0,38377432
	maximum wavenumbers:	68,4843	maximum intensity ratios:	1,08982754
	minimum wavenumbers:	41,2725	minimum intensity ratios:	0,05231053
	variation of wavenumbers:	27,2118	variation of intensity ratios:	1,03751700
Elim Spatkristall	**D1 band FWHM 13:**		**D1/G intensity ratio 13:**	
	sum of wavenumbers:	108,8359	sum of intensity ratios:	1,83386442
	mean wavenumbers:	54,41795	mean intensity ratios:	0,91693221
	standard deviation:	2,788192749	standard deviation:	0,11379073
	maximum wavenumbers:	56,3895	maximum intensity ratios:	0,99739441
	minimum wavenumbers:	52,4464	minimum intensity ratios:	0,83647001
	variation of wavenumbers:	3,9431	variation of intensity ratios:	0,16092440
Omaruru Spatkristall	**D1 band FWHM 14:**		**D1/G intensity ratio 14:**	
	sum of wavenumbers:	0	sum of intensity ratios:	0
	mean wavenumbers:	0	mean intensity ratios:	0
	standard deviation:	#DIV/0!	standard deviation:	0
	maximum wavenumbers:		maximum intensity ratios:	0

sample	D1 band postion of sample [Δ cm^{-1}]		D1 band FWHM of sample [cm^{-1}]	
	minimum wavenumbers:		minimum intensity ratios:	0
	variation of wavenumbers:	0	variation of intensity ratios:	0

sample	Crystallinities of samples L_a [Å]	
12/08/00/02	**Crystallinities 1:**	
	sum of crystallinities:	2091,418015
	mean crystallinities:	209,1418015
	standard deviation:	98,63689724
	maximum crystallinity:	357,2647755
	minimum crystallinity:	79,18072888
	variation of crystallinity:	278,0840466
12/08/00/03	**Crystallinities 2:**	
	sum of crystallinities:	1994,116329
	mean crystallinities:	249,2645412
	standard deviation:	143,8070253
	maximum crystallinity:	571,4541119
	minimum crystallinity:	136,6672667
	variation of crystallinity:	434,7868451
15/08/00/01	**Crystallinities 3:**	
	sum of crystallinities:	3399,588321
	mean crystallinities:	309,0534837
	standard deviation:	249,4896342
	maximum crystallinity:	600,8181224
	minimum crystallinity:	76,97524375
	variation of crystallinity:	523,8428787
17/08/00/11	**Crystallinities 4:**	
	sum of crystallinities:	2389,85099
	mean crystallinities:	170,7036422
	standard deviation:	133,0645958
	maximum crystallinity:	511,2862818
	minimum crystallinity:	52,7624045
	variation of crystallinity:	458,5238773
17/08/00/12	**Crystallinities 5:**	
	sum of crystallinities:	1356,101709
	mean crystallinities:	150,6779677
	standard deviation:	56,69868814
	maximum crystallinity:	244,9083477
	minimum crystallinity:	76,4318077
	variation of crystallinity:	168,47654
17/08/00/15	**Crystallinities 6:**	
	sum of crystallinities:	1827,911154
	mean crystallinities:	152,3259295
	standard deviation:	69,08918422
	maximum crystallinity:	302,3739453
	minimum crystallinity:	75,19608761
	variation of crystallinity:	227,1778577
17/08/00/16	**Crystallinities 7:**	
	sum of crystallinities:	1675,599715
	mean crystallinities:	128,8922858
	standard deviation:	179,2634085

sample	Crystallinities of samples L_a [Å]	
	maximum crystallinity:	671,7915981
	minimum crystallinity:	26,63912415
	variation of crystallinity:	645,152474
17/08/00/19	**Crystallinities 8:**	
	sum of crystallinities:	2093,201084
	mean crystallinities:	190,2910077
	standard deviation:	190,1264101
	maximum crystallinity:	726,996545
	minimum crystallinity:	54,28460334
	variation of crystallinity:	672,7119417
17/08/00/20	**Crystallinities 9:**	
	sum of crystallinities:	5939,692557
	mean crystallinities:	282,8425027
	standard deviation:	252,2481041
	maximum crystallinity:	991,9805565
	minimum crystallinity:	102,1449756
	variation of crystallinity:	889,8355809
18/08/00/02	**Crystallinities 10:**	
	sum of crystallinities:	2952,170472
	mean crystallinities:	246,014206
	standard deviation:	246,0173612
	maximum crystallinity:	899,0581784
	minimum crystallinity:	34,66043145
	variation of crystallinity:	864,397747
3.10.01/3	**Crystallinities 11:**	
	sum of crystallinities:	3282,844429
	mean crystallinities:	298,4404027
	standard deviation:	449,792051
	maximum crystallinity:	1487,3953
	minimum crystallinity:	54,01234273
	variation of crystallinity:	1433,382957
3.10.01/4	**Crystallinities 12:**	
	sum of crystallinities:	2730,756629
	mean crystallinities:	182,0504419
	standard deviation:	230,5586932
	maximum crystallinity:	824,8805812
	minimum crystallinity:	39,59337079
	variation of crystallinity:	785,2872104
Elim Spatkristall	**Crystallinities 13:**	
	sum of crystallinities:	94,84843644
	mean crystallinities:	47,42421822
	standard deviation:	5,885316916
	maximum crystallinity:	51,58576572
	minimum crystallinity:	43,26267072
	variation of crystallinity:	8,323095001
Omaruru Spatkristall	**Crystallinities 14:**	

sample	Crystallinities of samples L_a [Å]	
	sum of crystallinities:	0
	mean crystallinities:	0
	standard deviation:	#DIV/0!
	maximum crystallinity:	0
	minimum crystallinity:	0
	variation of crystallinity:	0

II.3 SAMPLES AND ACCORDING PLOT NUMBERS:

sample	type of marble	sample locality	plot number for sample
12/08/00/02	cataclasite with graphite network structures	MT-Station 94	1
12/08/00/03	cataclasite with graphite network structures	MT-Station 94	2
15/08/00/01	cataclasite with graphite network structures	Omaruru River near Farm Elim	3
17/08/00/11	cataclasite with graphite network structures	Farm Epako Süd	4
17/08/00/12	cataclasite with graphite network structures	Farm Epako Süd	5
17/08/00/15	cataclasite with graphite network structures	Farm Epako Süd	6
17/08/00/16	cataclasite with graphite network structures	Farm Epako Süd	7
17/08/00/19	cataclasite with graphite network structures	Farm Epako Süd	8
17/08/00/20	cataclasite with graphite network structures	Farm Epako Süd	9
18/08/00/02	cataclasite with graphite network structures	MT-Station 94	10
3.10.01/3	mylonite	Farm Elim	11
3.10.01/4	mylonite	Farm Elim	12
Elim Spatkristall	grain coarsened marble	Farm Elim	13
Omaruru Spatkristall	grain coarsened marble	Omaruru River near Farm Elim	14

III. CONDUCTIVITY MEASUREMENTS

III.1 COMPLEX IMPEDANCE DATA FOR SAMPLE 12/08/00/03:

frequency [Hz]	measurement 1	phase difference [°]	real impedance Z´ [Ω m]	imaginary impedance Z´´ [Ω m]
785,412918011400	159120,000000000000	4,4000000000	158651,033934348000	12207,53175553940
881,247788255900	160004,000000000000	4,6000000000	159488,607668513000	12832,14868831470
988,776281235900	161772,000000000000	4,8000000000	161204,642826511000	13536,73207155530
1109,425234722800	163540,000000000000	5,0000000000	162917,680925924000	14253,45016895200
1244,795587027200	164424,000000000000	5,3000000000	163721,037774302000	15187,94147031340
1396,683620478200	166192,000000000000	5,5000000000	165426,884999038000	15928,79730284110
1567,104796997800	167076,000000000000	5,8000000000	166220,689308279000	16884,08190813790
1758,320502056700	168844,000000000000	6,1000000000	167887,995839227000	17942,05086069500
1972,868051885100	172380,000000000000	6,5000000000	171271,916481530000	19513,96998931180
2213,594362117900	175916,000000000000	7,0000000000	174604,748812135000	21438,76741445990
2483,693724635000	177684,000000000000	7,5000000000	176163,888748344000	23192,41593842760
2786,750193874500	178568,000000000000	8,0000000000	176830,188499045000	24851,86229223700
3126,785145056700	179452,000000000000	8,5000000000	177480,874712023000	26524,69444603090
3508,310635390900	180336,000000000000	9,0000000000	178115,764589565000	28210,76568749510
3936,389276332400	180336,000000000000	9,6000000000	177810,581341147000	30074,40870779500
4416,701411361400	181220,000000000000	10,300000000	178299,646574316000	32402,53742338490
4955,620490689000	181220,000000000000	11,000000000	177890,478184386000	34578,40614213740
5560,297643070000	181220,000000000000	11,700000000	177454,757740876000	36749,11366450720
6238,756566936200	182104,000000000000	12,400000000	177855,928573765000	39104,16201843090
7000,000000000000	183872,000000000000	13,500000000	178791,602003362000	42924,06594291300
7854,129180113700	182988,000000000000	14,300000000	177318,250658680000	45197,85534010930
8812,477882559200	182104,000000000000	15,300000000	175649,764130839000	48052,33789089430
9887,762812359300	180336,000000000000	16,200000000	173175,522100237000	50312,14009869040
11094,252347227800	179452,000000000000	17,200000000	171426,612639579000	53065,40099650430
12447,955870272400	176800,000000000000	18,100000000	168051,181351792000	54927,59275871340
13966,836204782100	175032,000000000000	19,100000000	165396,297992757000	57273,60329411050
15671,047969978300	173264,000000000000	20,100000000	162711,226494938000	59543,85332268220
17583,205020567000	170612,000000000000	21,200000000	159065,628372981000	61697,49115084590
19728,680518851200	167076,000000000000	22,200000000	154690,753827715000	63128,12729848220
22135,943621178600	163540,000000000000	23,200000000	150315,393381801000	64425,25989450410
24836,937246350300	160004,000000000000	24,200000000	145942,867068028000	65589,32510678700
27867,501938744800	156468,000000000000	25,300000000	141459,988380323000	66867,83016846720
31267,851450567400	152932,000000000000	26,400000000	136982,990916934000	67998,94722310930
35083,106353909100	148512,000000000000	27,500000000	131731,752856964000	68575,21004876130
39363,892763324500	144976,000000000000	28,500000000	127407,389725281000	69176,56842739700
44167,014113613600	140556,000000000000	29,700000000	122091,371143374000	69639,68860018550
49556,204906889700	136136,000000000000	30,800000000	116935,364528553000	69707,46745202010
55602,976430699800	130832,000000000000	32,000000000	110951,828516338000	69330,39717815870
62387,565669362300	126412,000000000000	33,100000000	105897,698405423000	69033,84109575600
70000,000000000100	121992,000000000000	34,200000000	100897,213416902000	68569,67543093710

frequency [Hz]	measurement 1	phase difference [°]	real impedance Z´ [Ω m]	imaginary impedance Z´´ [Ω m]
78541,291801137600	117572,000000000000	35,500000000	95717,189724189200	68274,40790884660
88124,778825591900	112268,000000000000	36,600000000	90130,712304756000	66936,97426263980
98877,628123593000	107848,000000000000	37,700000000	85331,875583477900	65951,96822996150
110942,523472278000	103428,000000000000	38,900000000	80492,132365749300	64948,96312655570
124479,558702724000	98124,000000000000	40,200000000	74946,721513745600	63334,89015022490
139668,362047821000	93942,680000000000	41,430000000	70434,905732656800	62162,29709409190
156710,479699784000	89337,040000000000	42,760000000	65591,614364967200	60653,49817577740
175832,050205670000	84713,720000000000	44,040000000	60896,852561569800	58889,62306156180
197286,805188511000	80134,600000000000	45,300000000	56366,253151838600	56959,63151902270
221359,436211786000	75767,640000000000	46,560000000	52097,419219758500	55014,49065301200
248369,372463502000	71542,120000000000	47,880000000	47982,267998859200	53065,77891428760
278675,019387447000	67325,440000000000	49,090000000	44089,594358757300	50880,47307635650
312678,514505673000	63259,040000000000	50,330000000	40382,349055193700	48692,62805092880
350831,063539090000	59325,240000000000	51,560000000	36882,190257027200	46467,06514190500
393638,927633243000	55603,600000000000	52,860000000	33571,488611337400	44325,11122804810
441670,141136134000	51996,880000000000	54,130000000	30467,475099205100	42135,59648104820
495562,049068895000	48513,920000000000	55,370000000	27569,231412155200	39919,14218904790
556029,764306995000	45154,720000000000	56,620000000	24843,643322244900	37705,99587274520
623875,656693619000	41945,800000000000	57,840000000	22327,136595155200	35509,84524186610
699999,999999997000	38878,320000000000	58,790000000	20145,823646590000	33251,60982002070
785412,918011371000	36058,360000000000	60,290000000	17870,893379747600	31318,30927268100
881247,788255913000	33291,440000000000	61,300000000	15987,331751720100	29201,45888023480
988776,281235923000	30736,680000000000	62,590000000	14149,776046779200	27286,02820581250

frequency [Hz]	measurement 1	phase difference [°]	real admittance Y´ [S m-1]	imaginary admittance Y´´ [S m-1]
785,412918011400	159120,000000000000	4,4000000000	0,000006303142	0,000081916641
881,247788255900	160004,000000000000	4,6000000000	0,000006270040	0,000077929272
988,776281235900	161772,000000000000	4,8000000000	0,000006203295	0,000073873073
1109,425234722800	163540,000000000000	5,0000000000	0,000006138069	0,000070158452
1244,795587027200	164424,000000000000	5,3000000000	0,000006107951	0,000065841708
1396,683620478200	166192,000000000000	5,5000000000	0,000006044967	0,000062779379
1567,104796997800	167076,000000000000	5,8000000000	0,000006016098	0,000059227384
1758,320502056700	168844,000000000000	6,1000000000	0,000005956352	0,000055734989
1972,868051885100	172380,000000000000	6,5000000000	0,000005838669	0,000051245339
2213,594362117900	175916,000000000000	7,0000000000	0,000005727221	0,000046644473
2483,693724635000	177684,000000000000	7,5000000000	0,000005676532	0,000043117543
2786,750193874500	178568,000000000000	8,0000000000	0,000005655143	0,000040238433
3126,785145056700	179452,000000000000	8,5000000000	0,000005634410	0,000037700717
3508,310635390900	180336,000000000000	9,0000000000	0,000005614326	0,000035447460
3936,389276332400	180336,000000000000	9,6000000000	0,000005623962	0,000033250862
4416,701411361400	181220,000000000000	10,3000000000	0,000005608536	0,000030861781
4955,620490689000	181220,000000000000	11,0000000000	0,000005621436	0,000028919783
5560,297643070000	181220,000000000000	11,7000000000	0,000005635239	0,000027211541
6238,756566936200	182104,000000000000	12,4000000000	0,000005622528	0,000025572725
7000,000000000000	183872,000000000000	13,5000000000	0,000005593104	0,000023296954
7854,129180113700	182988,000000000000	14,3000000000	0,000005639577	0,000022124944
8812,477882559200	182104,000000000000	15,3000000000	0,000005693147	0,000020810642
9887,762812359300	180336,000000000000	16,2000000000	0,000005774488	0,000019875919
11094,252347227800	179452,000000000000	17,2000000000	0,000005833400	0,000018844671
12447,955870272400	176800,000000000000	18,1000000000	0,000005950568	0,000018205786
13966,836204782100	175032,000000000000	19,1000000000	0,000006046085	0,000017460050
15671,047969978300	173264,000000000000	20,1000000000	0,000006145857	0,000016794345
17583,205020567000	170612,000000000000	21,2000000000	0,000006286713	0,000016208114
19728,680518851200	167076,000000000000	22,2000000000	0,000006464510	0,000015840799
22135,943621178600	163540,000000000000	23,2000000000	0,000006652679	0,000015521862
24836,937246350300	160004,000000000000	24,2000000000	0,000006851996	0,000015246383
27867,501938744800	156468,000000000000	25,3000000000	0,000007069137	0,000014954874
31267,851450567400	152932,000000000000	26,4000000000	0,000007300176	0,000014706110
35083,106353909100	148512,000000000000	27,5000000000	0,000007591184	0,000014582529
39363,892763324500	144976,000000000000	28,5000000000	0,000007848838	0,000014455762
44167,014113613600	140556,000000000000	29,7000000000	0,000008190587	0,000014359628
49556,204906889700	136136,000000000000	30,8000000000	0,000008551733	0,000014345665
55602,976430699800	130832,000000000000	32,0000000000	0,000009012920	0,000014423688
62387,565669362300	126412,000000000000	33,1000000000	0,000009443076	0,000014485649
70000,000000000100	121992,000000000000	34,2000000000	0,000009911076	0,000014583706
78541,291801137600	117572,000000000000	35,5000000000	0,000010447444	0,000014646777
88124,778825591900	112268,000000000000	36,6000000000	0,000011094997	0,000014939426
98877,628123593000	107848,000000000000	37,7000000000	0,000011718950	0,000015162550
110942,523472278000	103428,000000000000	38,9000000000	0,000012423574	0,000015396705
124479,558702724000	98124,000000000000	40,2000000000	0,000013342812	0,000015789086
139668,362047821000	93942,680000000000	41,4300000000	0,000014197506	0,000016086922
156710,479699784000	89337,040000000000	42,7600000000	0,000015245851	0,000016487095

frequency [Hz]	measurement 1	phase difference [°]	real admittance Y´ [S m-1]	imaginary admittance Y´´ [S m-1]
175832,050205670000	84713,720000000000	44,0400000000	0,000016421210	0,000016980920
197286,805188511000	80134,600000000000	45,3000000000	0,000017741112	0,000017556293
221359,436211786000	75767,640000000000	46,5600000000	0,000019194809	0,000018177029
248369,372463502000	71542,120000000000	47,8800000000	0,000020841032	0,000018844536
278675,019387447000	67325,440000000000	49,0900000000	0,000022681089	0,000019653905
312678,514505673000	63259,040000000000	50,3300000000	0,000024763294	0,000020536990
350831,063539090000	59325,240000000000	51,5600000000	0,000027113357	0,000021520619
393638,927633243000	55603,600000000000	52,8600000000	0,000029787181	0,000022560575
441670,141136134000	51996,880000000000	54,1300000000	0,000032821886	0,000023732902
495562,049068895000	48513,920000000000	55,3700000000	0,000036272321	0,000025050638
556029,764306995000	45154,720000000000	56,6200000000	0,000040251745	0,000026520981
623875,656693619000	41945,800000000000	57,8400000000	0,000044788547	0,000028161204
699999,999999997000	38878,320000000000	58,7900000000	0,000049638080	0,000030073732
785412,918011371000	36058,360000000000	60,2900000000	0,000055956912	0,000031930204
881247,788255913000	33291,440000000000	61,3000000000	0,000062549525	0,000034244864
988776,281235923000	30736,680000000000	62,5900000000	0,000070672497	0,000036648793

frequency [Hz]	measurement 2	phase difference [°]	real impedance Z´ [Ω m]	imaginary impedance Z´´ [Ω m]
785,412918011400	10156,6664206088	8,0000000000	454794,474322529000	63917,19503932350
881,247788255900	10676,3477086778	8,1900000000	452932,987605396000	65187,94933766660
988,776281235900	11262,5610835340	8,6000000000	449164,338730985000	67929,71953686080
1109,425234722800	11858,8705405681	8,9000000000	446336,556317832000	69894,43948082850
1244,795587027200	12636,3673033007	9,3000000000	442553,472311200000	72470,91036616010
1396,683620478200	13252,7593559638	9,6900000000	439589,540837530000	75061,45409096340
1567,104796997800	14047,5561475707	10,200000000	435628,596781778000	78381,95609921520
1758,320502056700	14927,7863160982	10,700000000	431657,871070424000	81562,60147242250
1972,868051885100	16235,6230311074	11,200000000	428481,211856527000	84841,56461288380
2213,594362117900	17837,0544888306	11,700000000	423650,956787401000	87733,89546304160
2483,693724635000	19296,0900607718	12,300000000	417831,585816092000	91102,01862972120
2786,750193874500	20676,7494271412	12,900000000	411988,667292085000	94358,00103272470
3126,785145056700	22068,5457790977	13,400000000	405484,114865779000	96599,94210927660
3508,310635390900	23471,3570519959	14,100000000	397818,223741436000	99925,03107434360
3936,389276332400	25021,9080448854	14,800000000	390936,970828990000	103290,0031128530
4416,701411361400	26958,9111362562	15,500000000	383231,976719256000	106279,6332128180
4955,620490689000	28769,2339102583	16,200000000	376312,207193595000	109328,8027058050
5560,297643070000	30575,2625688700	17,000000000	367588,247316095000	112383,0053481440
6238,756566936200	32534,6627993345	17,800000000	359645,931261703000	115469,6761531040
7000,000000000000	35712,8228645036	18,600000000	350113,232804821000	117826,1205291810
7854,129180113700	37604,6156429709	19,500000000	341160,808456081000	120811,3784938860
8812,477882559200	39979,5451252241	20,300000000	331637,527278767000	122676,4463963030
9887,762812359300	41859,7005621104	21,300000000	321694,347060738000	125423,3848577100
11094,252347227800	44150,4136290915	22,200000000	311211,027931014000	127002,8679917180
12447,955870272400	45699,7571752495	23,200000000	301299,917290580000	129137,3094991900
13966,836204782100	47651,6379406999	24,200000000	290652,547738992000	130624,4342718200
15671,047969978300	49540,4859644716	25,300000000	279817,165450210000	132268,9681497900
17583,205020567000	51332,3126375038	26,300000000	269261,492338527000	133077,3183064240
19728,680518851200	52522,6019123372	27,400000000	258531,840151720000	134010,1773290580
22135,943621178600	53601,8162322274	28,500000000	247137,433154347000	134184,6779251660
24836,937246350300	54570,3184888468	29,700000000	236323,364344112000	134796,4671683950
27867,501938744800	55634,0347001647	30,900000000	224881,650492053000	134588,8913394050
31267,851450567400	56575,1240896269	32,000000000	213789,532848650000	133590,5268361340
35083,106353909100	57054,5747605694	33,200000000	202590,681460176000	132571,6271662280
39363,892763324500	57554,9049315943	34,400000000	191531,946128344000	131144,6605710240
44167,014113613600	57940,2209153543	35,700000000	181075,136492227000	130115,6851433420
49556,204906889700	57996,6129200807	36,900000000	170326,434780482000	127884,7046326110
55602,976430699800	57682,8904522280	38,200000000	159535,236169752000	125541,8515247460
62387,565669362300	57436,1557916690	39,500000000	149584,055237210000	123307,5794701660
70000,000000000100	57049,9699585397	40,700000000	139399,676665335000	119902,6377091020
78541,291801137600	56804,3073801604	42,000000000	129842,263907410000	116910,4995430200
88124,778825591900	55691,5625865163	43,300000000	120495,879939789000	113549,5730574800
98877,628123593000	54872,0375673279	44,700000000	111771,795667580000	110607,4102275460
110942,523472278000	54037,5373212943	46,000000000	102876,126031496000	106531,3470709530
124479,558702724000	52694,6286049871	47,400000000	94611,015538363600	102888,7064492480
139668,362047821000	51719,0311822845	48,800000000	86588,681669361300	98909,45426379630
156710,479699784000	50463,7104822468	50,200000000	79353,119225751000	95242,57185284190

frequency [Hz]	measurement 2	phase difference [°]	real impedance Z´ [Ω m]	imaginary impedance Z´´ [Ω m]
175832,050205670000	48996,1663872194	51,600000000	71834,498493626000	90632,58095281870
197286,805188511000	47390,4134238269	53,000000000	65092,312904125600	86380,41676671520
221359,436211786000	45772,0562233060	54,200000000	58888,859056313000	81651,41678529350
248369,372463502000	44150,7280566873	55,500000000	53251,248770725100	77481,04774948740
278675,019387447000	42332,5535995286	56,780000000	47664,636205540600	72783,73596079740
312678,514505673000	40512,2665383728	58,020000000	42760,337184282400	68484,02693829320
350831,063539090000	38660,5981980650	59,250000000	38255,848576116500	64302,30026382290
393638,927633243000	36878,4925417360	60,450000000	34118,787646768700	60182,15199006020
441670,141136134000	35056,8162722321	61,630000000	30357,857793125200	56216,01701588960
495562,049068895000	33212,7263012879	62,760000000	26954,580888031400	52358,00014355180
556029,764306995000	31371,3885661240	63,880000000	23856,479077356000	48654,13744192030
623875,656693619000	29544,1912412326	64,970000000	21075,028140770300	45133,82980704540
699999,999999997000	27665,3393702572	65,740000000	18801,776312341400	41718,95022050140
785412,918011371000	26056,8333148706	67,060000000	16334,291564378200	38593,49650595920
881247,788255913000	24295,6137883554	67,890000000	14430,095985142700	35519,25552053660
988776,281235923000	22701,9754672360	69,060000000	12533,242292735200	32752,68799765290

frequency [Hz]	measurement 2	phase difference [°]	real admittance Y´ [S m-1]	imaginary admittance Y´´ [S m-1]
785,412918011400	10156,6664206088	8,0000000000	0,000002198795	0,000015645242
881,247788255900	10676,3477086778	8,1900000000	0,000002207832	0,000015340259
988,776281235900	11262,5610835340	8,6000000000	0,000002226357	0,000014721097
1109,425234722800	11858,8705405681	8,9000000000	0,000002240462	0,000014307290
1244,795587027200	12636,3673033007	9,3000000000	0,000002259614	0,000013798640
1396,683620478200	13252,7593559638	9,6900000000	0,000002274849	0,000013322417
1567,104796997800	14047,5561475707	10,2000000000	0,000002295533	0,000012758038
1758,320502056700	14927,7863160982	10,7000000000	0,000002316650	0,000012260521
1972,868051885100	16235,6230311074	11,2000000000	0,000002333825	0,000011786676
2213,594362117900	17837,0544888306	11,7000000000	0,000002360434	0,000011398103
2483,693724635000	19296,0900607718	12,3000000000	0,000002393309	0,000010976705
2786,750193874500	20676,7494271412	12,9000000000	0,000002427251	0,000010597935
3126,785145056700	22068,5457790977	13,4000000000	0,000002466188	0,000010351973
3508,310635390900	23471,3570519959	14,1000000000	0,000002513711	0,000010007503
3936,389276332400	25021,9080448854	14,8000000000	0,000002557957	0,000009681479
4416,701411361400	26958,9111362562	15,5000000000	0,000002609386	0,000009409140
4955,620490689000	28769,2339102583	16,2000000000	0,000002657368	0,000009146720
5560,297643070000	30575,2625688700	17,0000000000	0,000002720435	0,000008898143
6238,756566936200	32534,6627993345	17,8000000000	0,000002780512	0,000008660282
7000,000000000000	35712,8228645036	18,6000000000	0,000002856219	0,000008487082
7854,129180113700	37604,6156429709	19,5000000000	0,000002931169	0,000008277366
8812,477882559200	39979,5451252241	20,3000000000	0,000003015340	0,000008151524
9887,762812359300	41859,7005621104	21,3000000000	0,000003108541	0,000007972995
11094,252347227800	44150,4136290915	22,2000000000	0,000003213254	0,000007873838
12447,955870272400	45699,7571752495	23,2000000000	0,000003318952	0,000007743695
13966,836204782100	47651,6379406999	24,2000000000	0,000003440534	0,000007655536
15671,047969978300	49540,4859644716	25,3000000000	0,000003573762	0,000007560352
17583,205020567000	51332,3126375038	26,3000000000	0,000003713862	0,000007514429
19728,680518851200	52522,6019123372	27,4000000000	0,000003867996	0,000007462120
22135,943621178600	53601,8162322274	28,5000000000	0,000004046332	0,000007452416
24836,937246350300	54570,3184888468	29,7000000000	0,000004231490	0,000007418592
27867,501938744800	55634,0347001647	30,9000000000	0,000004446783	0,000007430034
31267,851450567400	56575,1240896269	32,0000000000	0,000004677497	0,000007485561
35083,106353909100	57054,5747605694	33,2000000000	0,000004936061	0,000007543092
39363,892763324500	57554,9049315943	34,4000000000	0,000005221061	0,000007625167
44167,014113613600	57940,2209153543	35,7000000000	0,000005522569	0,000007685469
49556,204906889700	57996,6129200807	36,9000000000	0,000005871079	0,000007819543
55602,976430699800	57682,8904522280	38,2000000000	0,000006268208	0,000007965471
62387,565669362300	57436,1557916690	39,5000000000	0,000006685205	0,000008109802
70000,000000000100	57049,9699585397	40,7000000000	0,000007173618	0,000008340100
78541,291801137600	56804,3073801604	42,0000000000	0,000007701653	0,000008553552
88124,778825591900	55691,5625865163	43,3000000000	0,000008299039	0,000008806726
98877,628123593000	54872,0375673279	44,7000000000	0,000008946801	0,000009040986
110942,523472278000	54037,5373212943	46,0000000000	0,000009720428	0,000009386908
124479,558702724000	52694,6286049871	47,4000000000	0,000010569594	0,000009719240
139668,362047821000	51719,0311822845	48,8000000000	0,000011548854	0,000010110257
156710,479699784000	50463,7104822468	50,2000000000	0,000012601899	0,000010499506

frequency [Hz]	measurement 2	phase difference [°]	real admittance Y´ [S m-1]	imaginary admittance Y´´ [S m-1]
175832,050205670000	48996,1663872194	51,6000000000	0,000013920888	0,000011033560
197286,805188511000	47390,4134238269	53,0000000000	0,000015362797	0,000011576698
221359,436211786000	45772,0562233060	54,2000000000	0,000016981141	0,000012247185
248369,372463502000	44150,7280566873	55,5000000000	0,000018778902	0,000012906382
278675,019387447000	42332,5535995286	56,7800000000	0,000020979915	0,000013739333
312678,514505673000	40512,2665383728	58,0200000000	0,000023386158	0,000014601945
350831,063539090000	38660,5981980650	59,2500000000	0,000026139794	0,000015551543
393638,927633243000	36878,4925417360	60,4500000000	0,000029309365	0,000016616222
441670,141136134000	35056,8162722321	61,6300000000	0,000032940401	0,000017788525
495562,049068895000	33212,7263012879	62,7600000000	0,000037099445	0,000019099278
556029,764306995000	31371,3885661240	63,8800000000	0,000041917334	0,000020553237
623875,656693619000	29544,1912412326	64,9700000000	0,000047449521	0,000022156329
699999,999999997000	27665,3393702572	65,7400000000	0,000053186464	0,000023969922
785412,918011371000	26056,8333148706	67,0600000000	0,000061220898	0,000025911101
881247,788255913000	24295,6137883554	67,8900000000	0,000069299608	0,000028153743
988776,281235923000	22701,9754672360	69,0600000000	0,000079787814	0,000030531845

frequency [Hz]	measurement 3	phase difference [°]	real impedance Z´ [Ω m]	imaginary impedance Z´´ [Ω m]
785,412918011400	596980,000000000000	6,9000000000	592656,277985040000	71719,2900475076
881,247788255900	590696,000000000000	7,1000000000	586166,506381207000	73010,8979047021
988,776281235900	584412,000000000000	7,3000000000	579675,014982924000	74258,0820419324
1109,425234722800	579699,000000000000	7,5000000000	574739,594693537000	75665,9031037717
1244,795587027200	574986,000000000000	7,8000000000	569666,137801313000	78034,5541317109
1396,683620478200	568702,000000000000	8,0000000000	563167,431229469000	79148,0208621911
1567,104796997800	563989,000000000000	8,3000000000	558081,660251219000	81415,3094463379
1758,320502056700	559276,000000000000	8,6000000000	552987,713766445000	83631,5287398241
1972,868051885100	554563,000000000000	9,0000000000	547735,409225461000	86752,7662361056
2213,594362117900	548279,000000000000	9,3000000000	541072,265335808000	88603,9814307297
2483,693724635000	543566,000000000000	9,6900000000	535810,868333123000	91491,5828483977
2786,750193874500	538853,000000000000	10,1000000000	530502,492038765000	94496,8864548455
3126,785145056700	532569,000000000000	10,6000000000	523480,895961229000	97966,7868444658
3508,310635390900	526285,000000000000	11,1000000000	516439,609669159000	101321,423153087
3936,389276332400	521572,000000000000	11,6000000000	510919,022084029000	104876,613487943
4416,701411361400	515288,000000000000	12,1000000000	503839,968502869000	108013,930041585
4955,620490689000	509004,000000000000	12,7000000000	496550,985006617000	111902,597400412
5560,297643070000	502720,000000000000	13,3000000000	489236,482922498000	115650,603879204
6238,756566936200	494865,000000000000	14,0000000000	480165,394583571000	119718,678865930
7000,000000000000	488581,000000000000	14,7000000000	472588,645918991000	123981,310323189
7854,129180113700	482297,000000000000	15,5000000000	464756,076691159000	128888,267067415
8812,477882559200	474442,000000000000	16,4000000000	455138,840708734000	133954,645467448
9887,762812359300	468158,000000000000	17,3000000000	446978,906373631000	139218,426298508
11094,252347227800	460303,000000000000	18,4000000000	436770,474787997000	145294,198653862
12447,955870272400	452448,000000000000	19,5000000000	426496,257361674000	151030,245846601
13966,836204782100	444593,000000000000	20,7000000000	415891,867998743000	157152,441220351
15671,047969978300	435167,000000000000	22,0000000000	403479,816440265000	163016,427437022
17583,205020567000	425741,000000000000	23,4000000000	390725,772093324000	169082,140106742
19728,680518851200	416315,000000000000	25,0000000000	377309,526360163000	175942,321636579
22135,943621178600	406889,000000000000	26,6000000000	363821,523273334000	182188,247491629
24836,937246350300	395892,000000000000	28,4000000000	348245,832809311000	188295,819377249
27867,501938744800	383324,000000000000	30,3000000000	330960,236040790000	193397,546871268
31267,851450567400	372327,000000000000	32,4000000000	314366,083518389000	199502,783094145
35083,106353909100	358188,000000000000	34,6000000000	294837,569572615000	203394,815353080
39363,892763324500	344049,000000000000	36,9000000000	275130,707067825000	206573,978103145
44167,014113613600	329910,000000000000	39,3000000000	255297,623590872000	208958,683688555
49556,204906889700	312629,000000000000	41,7000000000	233420,748289700000	207970,300545238
55602,976430699800	296919,000000000000	44,1000000000	213225,342205548000	206629,731651393
62387,565669362300	279638,000000000000	46,5000000000	192490,096837850000	202842,238361134
70000,000000000100	262357,000000000000	48,8000000000	172811,790688357000	197401,318253156
78541,291801137600	245076,000000000000	51,1000000000	153898,674316469000	190728,717868163
88124,778825591900	227795,000000000000	53,3000000000	136136,020355289000	182640,482880506
98877,628123593000	212085,000000000000	55,4000000000	120431,140669587000	174574,876720627
110942,523472278000	196375,000000000000	57,6000000000	105222,986864000000	165804,896370458
124479,558702724000	182236,000000000000	59,8000000000	91668,342994107500	157501,982808835
139668,362047821000	166651,680000000000	61,9100000000	78469,262386722200	147021,621904080
156710,479699784000	152088,510000000000	63,9500000000	66790,479120010200	136638,013645323

frequency [Hz]	measurement 3	phase difference [°]	real impedance Z´ [Ω m]	imaginary impedance Z´´ [Ω m]
175832,050205670000	138248,000000000000	65,5300000000	57264,634658460800	125830,326715911
197286,805188511000	125507,190000000000	67,0100000000	49019,401450476800	115538,534797413
221359,436211786000	114038,890000000000	68,1700000000	42405,810407352100	105861,303960077
248369,372463502000	103670,290000000000	69,2800000000	36678,688951235600	96964,9565848539
278675,019387447000	94244,290000000000	70,3400000000	31707,351570227600	88750,3805851338
312678,514505673000	85603,790000000000	71,3400000000	27389,072571475800	81103,9306448124
350831,063539090000	77717,370000000000	72,3300000000	23589,880264289200	74050,7066059021
393638,927633243000	70475,060000000000	73,2400000000	20322,427315965300	67481,3532021321
441670,141136134000	63876,860000000000	74,0800000000	17521,097759169200	61426,9027118675
495562,049068895000	57844,220000000000	74,9100000000	15058,932737218000	55849,6403947630
556029,764306995000	52345,720000000000	75,7000000000	12929,341160261100	50723,8261518192
623875,656693619000	47318,520000000000	76,4500000000	11086,437171507100	46001,4483014679
699999,999999997000	42731,200000000000	76,8100000000	9750,445599535300	41603,8972219010
785412,918011371000	38662,310000000000	77,7700000000	8190,090026344900	37784,8731623710
881247,788255913000	34939,040000000000	78,2600000000	7109,076948542000	34208,1502139667
988776,281235923000	31482,840000000000	79,1100000000	5947,865826699100	30915,8876077202

frequency [Hz]	measurement 3	phase difference [°]	real admittance Y´ [S m-1]	imaginary admittance Y´´ [S m-1]
785,412918011400	596980,000000000000	6,9000000000	1,68732E-06	1,39433E-05
881,247788255900	590696,000000000000	7,1000000000	1,706E-06	1,36966E-05
988,776281235900	584412,000000000000	7,3000000000	1,7251E-06	1,34665E-05
1109,425234722800	579699,000000000000	7,5000000000	1,73992E-06	1,3216E-05
1244,795587027200	574986,000000000000	7,8000000000	1,75541E-06	1,28148E-05
1396,683620478200	568702,000000000000	8,0000000000	1,77567E-06	1,26346E-05
1567,104796997800	563989,000000000000	8,3000000000	1,79185E-06	1,22827E-05
1758,320502056700	559276,000000000000	8,6000000000	1,80836E-06	1,19572E-05
1972,868051885100	554563,000000000000	9,0000000000	1,8257E-06	1,1527E-05
2213,594362117900	548279,000000000000	9,3000000000	1,84818E-06	1,12862E-05
2483,693724635000	543566,000000000000	9,6900000000	1,86633E-06	1,093E-05
2786,750193874500	538853,000000000000	10,1000000000	1,88501E-06	1,05824E-05
3126,785145056700	532569,000000000000	10,6000000000	1,91029E-06	1,02075E-05
3508,310635390900	526285,000000000000	11,1000000000	1,93633E-06	9,86958E-06
3936,389276332400	521572,000000000000	11,6000000000	1,95726E-06	9,53501E-06
4416,701411361400	515288,000000000000	12,1000000000	1,98476E-06	9,25807E-06
4955,620490689000	509004,000000000000	12,7000000000	2,01389E-06	8,93634E-06
5560,297643070000	502720,000000000000	13,3000000000	2,044E-06	8,64673E-06
6238,756566936200	494865,000000000000	14,0000000000	2,08262E-06	8,35292E-06
7000,000000000000	488581,000000000000	14,7000000000	2,11601E-06	8,06573E-06
7854,129180113700	482297,000000000000	15,5000000000	2,15167E-06	7,75866E-06
8812,477882559200	474442,000000000000	16,4000000000	2,19713E-06	7,46521E-06
9887,762812359300	468158,000000000000	17,3000000000	2,23724E-06	7,18296E-06
11094,252347227800	460303,000000000000	18,4000000000	2,28953E-06	6,88259E-06
12447,955870272400	452448,000000000000	19,5000000000	2,34469E-06	6,62119E-06
13966,836204782100	444593,000000000000	20,7000000000	2,40447E-06	6,36325E-06
15671,047969978300	435167,000000000000	22,0000000000	2,47844E-06	6,13435E-06
17583,205020567000	425741,000000000000	23,4000000000	2,55934E-06	5,91429E-06
19728,680518851200	416315,000000000000	25,0000000000	2,65034E-06	5,68368E-06
22135,943621178600	406889,000000000000	26,6000000000	2,7486E-06	5,48883E-06
24836,937246350300	395892,000000000000	28,4000000000	2,87153E-06	5,31079E-06
27867,501938744800	383324,000000000000	30,3000000000	3,02151E-06	5,1707E-06
31267,851450567400	372327,000000000000	32,4000000000	3,181E-06	5,01246E-06
35083,106353909100	358188,000000000000	34,6000000000	3,3917E-06	4,91655E-06
39363,892763324500	344049,000000000000	36,9000000000	3,63464E-06	4,84088E-06
44167,014113613600	329910,000000000000	39,3000000000	3,917E-06	4,78564E-06
49556,204906889700	312629,000000000000	41,7000000000	4,28411E-06	4,80838E-06
55602,976430699800	296919,000000000000	44,1000000000	4,68987E-06	4,83957E-06
62387,565669362300	279638,000000000000	46,5000000000	5,19507E-06	4,92994E-06
70000,000000000100	262357,000000000000	48,8000000000	5,78664E-06	5,06582E-06
78541,291801137600	245076,000000000000	51,1000000000	6,49778E-06	5,24305E-06
88124,778825591900	227795,000000000000	53,3000000000	7,34559E-06	5,47524E-06
98877,628123593000	212085,000000000000	55,4000000000	8,3035E-06	5,7282E-06
110942,523472278000	196375,000000000000	57,6000000000	9,50363E-06	6,03118E-06
124479,558702724000	182236,000000000000	59,8000000000	1,09089E-05	6,34913E-06
139668,362047821000	166651,680000000000	61,9100000000	1,27438E-05	6,80172E-06
156710,479699784000	152088,510000000000	63,9500000000	1,49722E-05	7,31861E-06

frequency [Hz]	measurement 3	phase difference [°]	real admittance Y´ [S m-1]	imaginary admittance Y´´ [S m-1]
175832,050205670000	138248,000000000000	65,5300000000	1,74628E-05	7,94721E-06
197286,805188511000	125507,190000000000	67,0100000000	2,04001E-05	8,65512E-06
221359,436211786000	114038,890000000000	68,1700000000	2,35817E-05	9,44632E-06
248369,372463502000	103670,290000000000	69,2800000000	2,72638E-05	1,0313E-05
278675,019387447000	94244,290000000000	70,3400000000	3,15384E-05	1,12676E-05
312678,514505673000	85603,790000000000	71,3400000000	3,65109E-05	1,23299E-05
350831,063539090000	77717,370000000000	72,3300000000	4,23911E-05	1,35043E-05
393638,927633243000	70475,060000000000	73,2400000000	4,92067E-05	1,48189E-05
441670,141136134000	63876,860000000000	74,0800000000	5,7074E-05	1,62795E-05
495562,049068895000	57844,220000000000	74,9100000000	6,64058E-05	1,79052E-05
556029,764306995000	52345,720000000000	75,7000000000	7,73435E-05	1,97146E-05
623875,656693619000	47318,520000000000	76,4500000000	9,02003E-05	2,17384E-05
699999,999999997000	42731,200000000000	76,8100000000	0,000102559	2,40362E-05
785412,918011371000	38662,310000000000	77,7700000000	0,000122099	2,64656E-05
881247,788255913000	34939,040000000000	78,2600000000	0,000140665	2,92328E-05
988776,281235923000	31482,840000000000	79,1100000000	0,000168128	3,23458E-05

III.2 COMPLEX IMPEDANCE DATA FOR SAMPLE 17/08/00/04:

frequency [Hz]	measurement 1	phase difference [°]	real impedance Z´ [Ω m]	imaginary impedance Z´´ [Ω m]
785,412918011374	306,987179487180	4,42000000000	306,074172444177	23,658599538134
881,247788255917	306,282051282051	4,47000000000	305,350426478213	23,870734951281
988,776281235928	305,384615384615	4,54000000000	304,426414967027	24,172736376606
1109,425234722780	304,487179487180	4,65000000000	303,484963637118	24,684394224594
1244,795587027250	303,782051282051	4,75000000000	302,738712585698	25,155647141047
1396,683620478220	302,948717948718	4,86000000000	301,859522074125	25,666215925862
1567,104796997840	302,243589743590	5,00000000000	301,093461634781	26,342264554821
1758,320502056710	301,666666666667	5,10000000000	300,472388065582	26,816446221377
1972,868051885120	301,217948717949	5,26000000000	299,949502574478	27,614281362582
2213,594362117870	300,256410256410	5,41000000000	298,918925415394	28,308795957656
2483,693724635030	299,102564102564	5,58000000000	297,685237352220	29,083385553969
2786,750193874480	297,500000000000	5,75000000000	296,003134179646	29,805948329593
3126,785145056740	296,346153846154	5,96000000000	294,744292536345	30,770845237952
3508,310635390910	294,935897435897	6,17000000000	293,227444685051	31,699357718940
3936,389276332440	293,397435897436	6,43000000000	291,551795251694	32,857359551619
4416,701411361350	291,858974358974	6,71000000000	289,859819632121	34,101992268881
4955,620490688970	290,384615384615	6,99000000000	288,226304648591	35,338677970304
5560,297643069970	288,717948717949	7,28000000000	286,390517133484	36,585866231590
6238,756566936220	286,923076923077	7,61000000000	284,395985298729	37,997047477018
7000,000000000000	285,128205128205	7,96000000000	282,380991611366	39,485046995203
7854,129180113750	283,205128205128	8,33000000000	280,217333558834	41,029143481921
8812,477882559180	281,089743589744	8,73000000000	277,833192794121	42,663344139585
9887,762812359290	278,782051282051	9,16000000000	275,226922935844	44,379871657039
11094,252347227800	276,474358974359	9,61000000000	272,594570909531	46,154859775883
12447,955870272500	274,102564102564	10,0700000000	269,879977597513	47,927167030466
13966,836204782200	271,474358974359	10,6200000000	266,824295890425	50,031217285992
15671,047969978400	268,717948717949	11,1700000000	263,627549843490	52,056228510143
17583,205020567100	265,897435897436	11,6900000000	260,382241474718	53,875177414395
19728,680518851200	262,564102564103	12,3900000000	256,448916832677	56,337030545099
22135,943621178700	258,974358974359	13,0500000000	252,285928420397	58,476738343024
24836,937246350300	256,217948717949	13,8000000000	248,822033128129	61,116553201384
27867,501938744900	252,692307692308	14,5300000000	244,610300276494	63,397187362747
31267,851450567500	249,230769230769	15,3600000000	240,328386325920	66,016990671647
35083,106353909100	245,384615384615	16,2100000000	235,629344581230	68,501251373062
39363,892763324500	241,282051282051	17,0900000000	230,628078225908	70,906401718737
44167,014113613600	237,179487179487	18,0500000000	225,507051165268	73,489312239738
49556,204906889700	232,692307692308	19,0100000000	220,001673844574	75,795603861684
55602,976430699800	227,948717948718	20,0300000000	214,160877454386	78,075198254195
62387,565669362300	223,076923076923	21,0800000000	208,148423666982	80,234327656048
70000,000000000200	218,076923076923	22,1900000000	201,925386453581	82,363114828606
78541,291801137600	212,756410256410	23,3300000000	195,361264951993	84,257143682605
88124,778825591900	207,500000000000	24,5900000000	188,681565604794	86,345334563739
98877,628123593100	201,987179487179	25,8100000000	181,837503123370	87,942840157937
110942,523472278000	196,410256410256	27,1300000000	174,800052932269	89,565229403037
124479,558702725000	190,641025641026	28,5200000000	167,506832365850	91,024511908722

frequency [Hz]	measurement 1	phase difference [°]	real impedance Z´ [Ω m]	imaginary impedance Z´´ [Ω m]
139668,362047822000	184,743589743590	30,0000000000	159,992641904279	92,371794871795
156710,479699784000	178,461538461538	31,6000000000	152,000499016298	93,511330911583
175832,050205671000	171,474358974359	33,1400000000	143,581870146241	93,742745591194
197286,805188512000	164,743589743590	34,8000000000	135,279068427796	94,021401855704
221359,436211787000	157,628205128205	36,3300000000	126,988150003823	93,384478424126
248369,372463503000	150,705128205128	37,9100000000	118,902858810643	92,596683709410
278675,019387448000	143,782051282051	39,4800000000	110,977683046069	91,417898338349
312678,514505674000	136,858974358974	41,0700000000	103,179005824182	89,913689834884
350831,063539090000	129,871794871795	42,6600000000	95,506141406560	88,007159122720
393638,927633244000	123,012820512821	44,2400000000	88,129302470171	85,821792434326
441670,141136134000	116,282051282051	45,8400000000	81,009569554549	83,420411716488
495562,049068895000	110,576923076923	47,2100000000	75,116367209447	81,146702301544
556029,764306995000	103,141025641026	49,0400000000	67,612241012745	77,888741391277
623875,656693620000	96,730769230769	50,6100000000	61,384924028940	74,757827803766
699999,999999997000	89,743589743590	50,9000000000	56,599110923321	69,645190377767
785412,918011371000	84,807692307692	53,6100000000	50,314571753820	68,269968095685
881247,788255913000	79,807692307692	54,4000000000	46,457890887553	64,891695352792
988776,281235923000	73,333333333333	56,6400000000	40,325836629822	61,250344308279

frequency [Hz]	measurement 1	phase difference [°]	real admittance Y´ [S m^{-1}]	imaginary admittance Y´´ [S m^{-1}]
785,412918011374	306,987179487180	4,42000000000	0,003267181912	0,042267928767
881,247788255917	306,282051282051	4,47000000000	0,003274925834	0,041892300427
988,776281235928	305,384615384615	4,54000000000	0,003284866066	0,041368920110
1109,425234722780	304,487179487180	4,65000000000	0,003295056164	0,040511425596
1244,795587027250	303,782051282051	4,75000000000	0,003303178478	0,039752505447
1396,683620478220	302,948717948718	4,86000000000	0,003312799256	0,038961723181
1567,104796997840	302,243589743590	5,00000000000	0,003321227882	0,037961808406
1758,320502056710	301,666666666667	5,10000000000	0,003328092829	0,037290548932
1972,868051885120	301,217948717949	5,26000000000	0,003333894510	0,036213145903
2213,594362117870	300,256410256410	5,41000000000	0,003345388716	0,035324709730
2483,693724635030	299,102564102564	5,58000000000	0,003359252911	0,034383892417
2786,750193874480	297,500000000000	5,75000000000	0,003378342607	0,033550350049
3126,785145056740	296,346153846154	5,96000000000	0,003392771380	0,032498294807
3508,310635390910	294,935897435897	6,17000000000	0,003410321981	0,031546380493
3936,389276332440	293,397435897436	6,43000000000	0,003429922286	0,030434581891
4416,701411361350	291,858974358974	6,71000000000	0,003449943498	0,029323799974
4955,620490688970	290,384615384615	6,99000000000	0,003469495962	0,028297606403
5560,297643069970	288,717948717949	7,28000000000	0,003491735725	0,027332959501
6238,756566936220	286,923076923077	7,61000000000	0,003516224039	0,026317834316
7000,000000000000	285,128205128205	7,96000000000	0,003541314854	0,025326043049
7854,129180113750	283,205128205128	8,33000000000	0,003568658610	0,024372919226
8812,477882559180	281,089743589744	8,73000000000	0,003599281965	0,023439325261
9887,762812359290	278,782051282051	9,16000000000	0,003633365477	0,022532737538
11094,252347227800	276,474358974359	9,61000000000	0,003668451637	0,021666190838
12447,955870272500	274,102564102564	10,0700000000	0,003705350834	0,020864992904
13966,836204782200	271,474358974359	10,6200000000	0,003747784649	0,019987520877
15671,047969978400	268,717948717949	11,1700000000	0,003793230262	0,019209997125
17583,205020567100	265,897435897436	11,6900000000	0,003840507687	0,018561423795
19728,680518851200	262,564102564103	12,3900000000	0,003899412064	0,017750314319
22135,943621178700	258,974358974359	13,0500000000	0,003963756545	0,017100816980
24836,937246350300	256,217948717949	13,8000000000	0,004018936697	0,016362179273
27867,501938744900	252,692307692308	14,5300000000	0,004088135286	0,015773570431
31267,851450567500	249,230769230769	15,3600000000	0,004160973305	0,015147615634
35083,106353909100	245,384615384615	16,2100000000	0,004243953578	0,014598273462
39363,892763324500	241,282051282051	17,0900000000	0,004335985487	0,014103098955
44167,014113613600	237,179487179487	18,0500000000	0,004434451139	0,013607420855
49556,204906889700	232,692307692308	19,0100000000	0,004545419962	0,013193377308
55602,976430699800	227,948717948718	20,0300000000	0,004669386920	0,012808164723
62387,565669362300	223,076923076923	21,0800000000	0,004804264103	0,012463493236
70000,000000000200	218,076923076923	22,1900000000	0,004952324309	0,012141357234
78541,291801137600	212,756410256410	23,3300000000	0,005118721975	0,011868429860
88124,778825591900	207,500000000000	24,5900000000	0,005299934823	0,011581401648
98877,628123593100	201,987179487179	25,8100000000	0,005499415593	0,011371022339
110942,523472278000	196,410256410256	27,1300000000	0,005720822066	0,011165047046
124479,558702725000	190,641025641026	28,5200000000	0,005969905740	0,010986051768
139668,362047822000	184,743589743590	30,0000000000	0,006250287439	0,010825815406
156710,479699784000	178,461538461538	31,6000000000	0,006578925770	0,010693891214

frequency [Hz]	measurement 1	phase difference [°]	real admittance Y´ [S m^{-1}]	imaginary admittance Y´´ [S m^{-1}]
175832,050205671000	171,474358974359	33,1400000000	0,006964667607	0,010667492121
197286,805188512000	164,743589743590	34,8000000000	0,007392126599	0,010635876303
221359,436211787000	157,628205128205	36,3300000000	0,007874750518	0,010708417682
248369,372463503000	150,705128205128	37,9100000000	0,008410226718	0,010799522833
278675,019387448000	143,782051282051	39,4800000000	0,009010820667	0,010938776959
312678,514505674000	136,858974358974	41,0700000000	0,009691894121	0,011121776916
350831,063539090000	129,871794871795	42,6600000000	0,010470530850	0,011362711965
393638,927633244000	123,012820512821	44,2400000000	0,011346963745	0,011652052138
441670,141136134000	116,282051282051	45,8400000000	0,012344220633	0,011987473802
495562,049068895000	110,576923076923	47,2100000000	0,013312677878	0,012323359689
556029,764306995000	103,141025641026	49,0400000000	0,014790221194	0,012838826025
623875,656693620000	96,730769230769	50,6100000000	0,016290644907	0,013376525635
699999,999999997000	89,743589743590	50,9000000000	0,017668122055	0,014358493308
785412,918011371000	84,807692307692	53,6100000000	0,019874957992	0,014647729124
881247,788255913000	79,807692307692	54,4000000000	0,021524868669	0,015410292404
988776,281235923000	73,333333333333	56,6400000000	0,024797997601	0,016326438835

frequency [Hz]	measurement 2	phase difference [°]	real impedance Z´ [Ω m]	imaginary impedance Z´´ [Ω m]
785,412918011374	351,217948717949	5,700000000000	349,481376142151	34,882878772141
881,247788255917	349,871794871795	5,780000000000	348,093019908048	35,235242841604
988,776281235928	348,333333333333	5,910000000000	346,481893347588	35,866540025237
1109,425234722780	346,923076923077	6,060000000000	344,984431958917	36,624622970869
1244,795587027250	345,576923076923	6,210000000000	343,549112038215	37,382046239708
1396,683620478220	343,910256410256	6,370000000000	341,787005362097	38,156355037900
1567,104796997840	342,435897435897	6,560000000000	340,193889068752	39,121115692244
1758,320502056710	341,025641025641	6,710000000000	338,689707982184	39,846826020305
1972,868051885120	339,551282051282	6,930000000000	337,070623046443	40,969113021303
2213,594362117870	338,012820512821	7,130000000000	335,398995859464	41,954504019181
2483,693724635030	336,153846153846	7,380000000000	333,369167898705	43,178769998102
2786,750193874480	334,679487179487	7,650000000000	331,700755192164	44,552981310714
3126,785145056740	332,371794871795	7,920000000000	329,201441810073	45,797606230760
3508,310635390910	330,384615384615	8,190000000000	327,015058795921	47,065331227353
3936,389276332440	328,269230769231	8,560000000000	324,612487309646	48,861241822810
4416,701411361350	326,089743589744	8,900000000000	322,163579305698	50,449470199064
4955,620490688970	323,397435897436	9,250000000000	319,192094185665	51,983733555853
5560,297643069970	321,153846153846	9,630000000000	316,628333066895	53,724217990471
6238,756566936220	318,397435897436	10,04000000000	313,521587903890	55,508027386002
7000,000000000000	315,512820512821	10,47000000000	310,259592337944	57,335200969806
7854,129180113750	312,371794871795	10,92000000000	306,715568237367	59,175150462469
8812,477882559180	308,974358974359	11,39000000000	302,889312095637	61,018186812194
9887,762812359290	305,576923076923	11,90000000000	299,009764870524	63,011240499086
11094,252347227800	302,179487179487	12,44000000000	295,084955495262	65,094635050955
12447,955870272500	298,269230769231	13,00000000000	290,624609708058	67,095977939872
13966,836204782200	294,487179487180	13,58000000000	286,254207725035	69,146420312457
15671,047969978400	290,512820512821	14,20000000000	281,636302931075	71,264940564278
17583,205020567100	286,217948717949	14,86000000000	276,645491419986	73,402903520941
19728,680518851200	281,602564102564	15,54000000000	271,308202436679	75,444439157016
22135,943621178700	276,858974358974	16,26000000000	265,784892350847	77,519563215694
24836,937246350300	272,115384615385	17,00000000000	260,225236478403	79,558838881283
27867,501938744900	267,115384615385	17,77000000000	254,371129020376	81,522741729681
31267,851450567500	261,858974358974	18,58000000000	248,210803457044	83,435720764807
35083,106353909100	256,410256410256	19,43000000000	241,807335768890	85,296142707186
39363,892763324500	250,897435897436	20,33000000000	235,268319802076	87,168463548557
44167,014113613600	245,064102564103	21,23000000000	228,432662374537	88,740819953558
49556,204906889700	239,038461538462	22,18000000000	221,350193789715	90,241220093316
55602,976430699800	232,948717948718	23,16000000000	214,175413051393	91,618762479181
62387,565669362300	226,794871794872	24,19000000000	206,880387712128	92,932335882254
70000,000000000200	220,448717948718	25,25000000000	199,385977257537	94,036531828277
78541,291801137600	214,102564102564	26,36000000000	191,840598239371	95,063625127872
88124,778825591900	207,628205128205	27,52000000000	184,134990348862	95,936316866892
98877,628123593100	201,025641025641	28,67000000000	176,379392437792	96,444897599849
110942,523472278000	194,551282051282	29,92000000000	168,622010732158	97,040294952363
124479,558702725000	187,948717948718	31,23000000000	160,713615149168	97,446675080537
139668,362047822000	181,217948717949	32,62000000000	152,633404955677	97,688221547828
156710,479699784000	174,358974358974	34,14000000000	144,311471395954	97,853212328713

frequency [Hz]	measurement 2	phase difference [°]	real impedance Z´ [Ω m]	imaginary impedance Z´´ [Ω m]
175832,050205671000	166,923076923077	35,57000000000	135,776140241174	97,098678418795
197286,805188512000	159,679487179487	37,12000000000	127,324162976500	96,364392532915
221359,436211787000	152,307692307692	38,57000000000	119,081316552160	94,959323840785
248369,372463503000	145,000000000000	40,06000000000	110,978780152054	93,320471258787
278675,019387448000	137,820512820513	41,54000000000	103,157681143343	91,394674764110
312678,514505674000	130,705128205128	43,05000000000	95,513853023823	89,224068611908
350831,063539090000	123,717948717949	44,58000000000	88,120719455178	86,838180759841
393638,927633244000	116,858974358974	46,11000000000	81,015529064719	84,217005044083
441670,141136134000	110,128205128205	47,64000000000	74,202918172355	81,376584466705
495562,049068895000	103,525641025641	49,19000000000	67,659463722878	78,356590778967
556029,764306995000	97,051282051282	50,72000000000	61,444206362919	75,123637107295
623875,656693620000	90,833333333333	52,24000000000	55,622270546665	71,811262791278
699999,999999997000	84,487179487180	53,10000000000	50,727811344841	67,563101274743
785412,918011371000	79,038461538462	55,23000000000	45,074333385544	64,925979948058
881247,788255913000	73,589743589744	56,42000000000	40,702543929948	61,308672137267
988776,281235923000	68,358974358974	58,17000000000	36,052572706620	58,078923687038

frequency [Hz]	measurement 2	phase difference [°]	real admittance Y´ [S m^{-1}]	imaginary admittance Y´´ [S m^{-1}]
785,412918011374	351,217948717949	5,700000000000	0,002861382804	0,028667358750
881,247788255917	349,871794871795	5,780000000000	0,002872795324	0,028380675692
988,776281235928	348,333333333333	5,910000000000	0,002886153704	0,027881139338
1109,425234722780	346,923076923077	6,060000000000	0,002898681527	0,027304035342
1244,795587027250	345,576923076923	6,210000000000	0,002910791980	0,026750809562
1396,683620478220	343,910256410256	6,370000000000	0,002925798770	0,026207954062
1567,104796997840	342,435897435897	6,560000000000	0,002939500185	0,025561643177
1758,320502056710	341,025641025641	6,710000000000	0,002952555027	0,025096101744
1972,868051885120	339,551282051282	6,930000000000	0,002966737329	0,024408631924
2213,594362117870	338,012820512821	7,130000000000	0,002981523536	0,023835343150
2483,693724635030	336,153846153846	7,380000000000	0,002999677524	0,023159529557
2786,750193874480	334,679487179487	7,650000000000	0,003014765521	0,022445187069
3126,785145056740	332,371794871795	7,920000000000	0,003037653768	0,021835202368
3508,310635390910	330,384615384615	8,190000000000	0,003057963152	0,021247061774
3936,389276332440	328,269230769231	8,560000000000	0,003080596216	0,020466119212
4416,701411361350	326,089743589744	8,900000000000	0,003104013192	0,019821813709
4955,620490688970	323,397435897436	9,250000000000	0,003132909675	0,019236786810
5560,297643069970	321,153846153846	9,630000000000	0,003158277057	0,018613579451
6238,756566936220	318,397435897436	10,040000000000	0,003189573026	0,018015412312
7000,000000000000	315,512820512821	10,470000000000	0,003223107439	0,017441292314
7854,129180113750	312,371794871795	10,920000000000	0,003260349665	0,016898985337
8812,477882559180	308,974358974359	11,390000000000	0,003301536106	0,016388556466
9887,762812359290	305,576923076923	11,900000000000	0,003344372383	0,015870184305
11094,252347227800	302,179487179487	12,440000000000	0,003388854570	0,015362249120
12447,955870272500	298,269230769231	13,000000000000	0,003440864836	0,014904023023
13966,836204782200	294,487179487180	13,580000000000	0,003493398431	0,014462064637
15671,047969978400	290,512820512821	14,200000000000	0,003550678622	0,014032145289
17583,205020567100	286,217948717949	14,860000000000	0,003614734492	0,013623439292
19728,680518851200	281,602564102564	15,540000000000	0,003685845069	0,013254787380
22135,943621178700	276,858974358974	16,260000000000	0,003762441090	0,012899969485
24836,937246350300	272,115384615385	17,000000000000	0,003842824829	0,012569313656
27867,501938744900	267,115384615385	17,770000000000	0,003931263756	0,012266515806
31267,851450567500	261,858974358974	18,580000000000	0,004028833500	0,011985274303
35083,106353909100	256,410256410256	19,430000000000	0,004135523833	0,011723859582
39363,892763324500	250,897435897436	20,330000000000	0,004250466025	0,011472038846
44167,014113613600	245,064102564103	21,230000000000	0,004377657685	0,011268771243
49556,204906889700	239,038461538462	22,180000000000	0,004517728143	0,011081410457
55602,976430699800	232,948717948718	23,160000000000	0,004669070020	0,010914794884
62387,565669362300	226,794871794872	24,190000000000	0,004833710972	0,010760517214
70000,000000000200	220,448717948718	25,250000000000	0,005015397842	0,010634165048
78541,291801137600	214,102564102564	26,360000000000	0,005212660976	0,010519270632
88124,778825591900	207,628205128205	27,520000000000	0,005430798340	0,010423581316
98877,628123593100	201,025641025641	28,670000000000	0,005669596579	0,010368614876
110942,523472278000	194,551282051282	29,920000000000	0,005930423885	0,010304997532
124479,558702725000	187,948717948718	31,230000000000	0,006222248184	0,010262022785
139668,362047822000	181,217948717949	32,620000000000	0,006551645757	0,010236648637
156710,479699784000	174,358974358974	34,140000000000	0,006929456060	0,010219388574

frequency [Hz]	measurement 2	phase difference [°]	real admittance Y´ [S m^{-1}]	imaginary admittance Y´´ [S m^{-1}]
175832,050205671000	166,923076923077	35,570000000000	0,007365064276	0,010298801346
197286,805188512000	159,679487179487	37,120000000000	0,007853968772	0,010377277060
221359,436211787000	152,307692307692	38,570000000000	0,008397622977	0,010530824774
248369,372463503000	145,000000000000	40,060000000000	0,009010731589	0,010715762431
278675,019387448000	137,820512820513	41,540000000000	0,009693897623	0,010941556525
312678,514505674000	130,705128205128	43,050000000000	0,010469685479	0,011207738176
350831,063539090000	123,717948717949	44,580000000000	0,011348068947	0,011515671923
393638,927633244000	116,858974358974	46,110000000000	0,012343312591	0,011874086468
441670,141136134000	110,128205128205	47,640000000000	0,013476558936	0,012288547210
495562,049068895000	103,525641025641	49,190000000000	0,014779898406	0,012762168314
556029,764306995000	97,051282051282	50,720000000000	0,016274927437	0,013311389577
623875,656693620000	90,833333333333	52,240000000000	0,017978410269	0,013925392217
699999,999999997000	84,487179487180	53,100000000000	0,019713052337	0,014800978361
785412,918011371000	79,038461538462	55,230000000000	0,022185574913	0,015402154897
881247,788255913000	73,589743589744	56,420000000000	0,024568488931	0,016310906192
988776,281235923000	68,358974358974	58,170000000000	0,027737271571	0,017217949929

frequency [Hz]	measurement 3	phase difference [°]	real impedance Z´ [Ω m]	imaginary impedance Z´´ [Ω m]
785,412918011374	405,256410256410	5,770000000000	403,203172738621	40,742601137157
881,247788255917	403,397435897436	5,950000000000	401,224226995073	41,816395837422
988,776281235928	401,474358974359	6,130000000000	399,178796076143	42,871315317747
1109,425234722780	399,423076923077	6,370000000000	396,957097933127	44,315423716897
1244,795587027250	397,179487179487	6,620000000000	394,531326489454	45,788398690410
1396,683620478220	395,192307692308	6,850000000000	392,371347175458	47,134763974035
1567,104796997840	392,435897435897	7,160000000000	389,375666075978	48,913436438333
1758,320502056710	389,807692307692	7,390000000000	386,569803964202	50,138045886601
1972,868051885120	386,987179487180	7,720000000000	383,479670622107	51,984798806984
2213,594362117870	383,717948717949	8,020000000000	379,964967629560	53,535852870557
2483,693724635030	380,641025641026	8,410000000000	376,547924784937	55,670914679117
2786,750193874480	377,179487179487	8,770000000000	372,769636317125	57,507945442166
3126,785145056740	373,525641025641	9,190000000000	368,731123633023	59,655368307844
3508,310635390910	369,807692307692	9,610000000000	364,618149681680	61,736004184343
3936,389276332440	365,961538461538	10,09000000000	360,301493958901	64,114593378733
4416,701411361350	361,858974358974	10,59000000000	355,695589574663	66,502367486142
4955,620490688970	357,564102564103	11,09000000000	350,887040071227	68,777703891049
5560,297643069970	353,076923076923	11,64000000000	345,815766229704	71,237415986476
6238,756566936220	348,141025641026	12,17000000000	340,317046865422	73,392651860954
7000,000000000000	343,076923076923	12,73000000000	334,643851818843	75,599388805580
7854,129180113750	337,820512820513	13,31000000000	328,746216943343	77,772898414259
8812,477882559180	332,307692307692	13,89000000000	322,590481863316	79,773324978076
9887,762812359290	326,602564102564	14,48000000000	316,228027285894	81,664371896446
11094,252347227800	320,641025641026	15,06000000000	309,628372995236	83,312291772894
12447,955870272500	314,615384615385	15,65000000000	302,951813089597	84,870720407054
13966,836204782200	308,269230769231	16,54000000000	295,513426430672	87,759520499242
15671,047969978400	301,858974358974	17,67000000000	287,617431555069	91,624524373758
17583,205020567100	294,871794871795	18,45000000000	279,715442004956	93,320131348416
19728,680518851200	287,435897435897	19,24000000000	271,381610302595	94,717562913909
22135,943621178700	280,000000000000	20,13000000000	262,895971402012	96,362379695565
24836,937246350300	273,012820512821	21,07000000000	254,759702280901	98,150365552617
27867,501938744900	265,192307692308	21,90000000000	246,055037332041	98,913490802316
31267,851450567500	257,179487179487	23,15000000000	236,471078129545	101,107456867209
35083,106353909100	249,230769230769	25,98000000000	224,045255282396	109,177378228308
39363,892763324500	242,307692307692	28,37000000000	213,205929912658	115,135785929302
44167,014113613600	233,589743589744	29,90000000000	202,498189302650	116,441623311728
49556,204906889700	224,294871794872	31,13000000000	191,995627695841	115,956321341952
55602,976430699800	214,743589743590	32,41000000000	181,293924186076	115,097012946368
62387,565669362300	205,064102564103	33,51000000000	170,980291072481	113,212305979476
70000,000000000200	195,384615384615	34,48000000000	161,060198674591	110,610850877730
78541,291801137600	185,833333333333	35,50000000000	151,289800494549	107,913965936283
88124,778825591900	176,538461538462	36,40000000000	142,094712687063	104,761257288884
98877,628123593100	167,564102564103	37,16000000000	133,540515447592	101,215903899064
110942,523472278000	158,910256410256	37,84000000000	125,495708942081	97,484853333726
124479,558702725000	150,769230769231	38,47000000000	118,042356540247	93,794258935026
139668,362047822000	143,076923076923	38,96000000000	111,254486478761	89,963576826996
156710,479699784000	135,641025641026	39,45000000000	104,739202060217	86,186932818951

frequency [Hz]	measurement 3	phase difference [°]	real impedance Z´ [Ω m]	imaginary impedance Z´´ [Ω m]
175832,050205671000	128,333333333333	39,73000000000	98,696673915251	82,026891947160
197286,805188512000	121,730769230769	40,07000000000	93,155512973625	78,360899561807
221359,436211787000	115,512820512821	40,22000000000	88,202202315047	74,589430951058
248369,372463503000	110,000000000000	40,48000000000	83,669588134454	71,410083471530
278675,019387448000	104,935897435897	40,72000000000	79,531616036113	68,456297163676
312678,514505674000	100,128205128205	41,06000000000	75,498883817923	65,769111324722
350831,063539090000	95,641025641026	41,53000000000	71,597701107166	63,411158180846
393638,927633244000	91,410256410256	42,13000000000	67,792104419221	61,319373410059
441670,141136134000	87,307692307692	42,88000000000	63,977371852956	59,409839478686
495562,049068895000	83,333333333333	43,78000000000	60,166815638908	57,657599154995
556029,764306995000	79,423076923077	44,82000000000	56,336752560259	55,983885707345
623875,656693620000	75,576923076923	45,98000000000	52,519116165609	54,347159437808
699999,999999997000	71,679487179487	47,13000000000	48,766222830835	52,533840456678
785412,918011371000	67,846153846154	48,61000000000	44,858583515721	50,899981106864
881247,788255913000	63,910256410256	49,93000000000	41,140503877368	48,907870687048
988776,281235923000	60,275641025641	51,67000000000	37,382341053567	47,283331930044

frequency [Hz]	measurement 3	phase difference [°]	real admittance Y´ [S m^{-1}]	imaginary admittance Y´´ [S m^{-1}]
785,412918011374	405,256410256410	5,770000000000	0,002480139214	0,024544333746
881,247788255917	403,397435897436	5,950000000000	0,002492371928	0,023914064806
988,776281235928	401,474358974359	6,130000000000	0,002505143083	0,023325619767
1109,425234722780	399,423076923077	6,370000000000	0,002519163923	0,022565506908
1244,795587027250	397,179487179487	6,620000000000	0,002534652974	0,021839593185
1396,683620478220	395,192307692308	6,850000000000	0,002548606077	0,021215763392
1567,104796997840	392,435897435897	7,160000000000	0,002568213905	0,020444280198
1758,320502056710	389,807692307692	7,390000000000	0,002586854922	0,019944933679
1972,868051885120	386,987179487180	7,720000000000	0,002607700164	0,019236392618
2213,594362117870	383,717948717949	8,020000000000	0,002631821576	0,018679071059
2483,693724635030	380,641025641026	8,410000000000	0,002655704451	0,017962701094
2786,750193874480	377,179487179487	8,770000000000	0,002682621927	0,017388901522
3126,785145056740	373,525641025641	9,190000000000	0,002712003235	0,016762950735
3508,310635390910	369,807692307692	9,610000000000	0,002742595235	0,016198003308
3936,389276332440	365,961538461538	10,09000000000	0,002775453382	0,015597073105
4416,701411361350	361,858974358974	10,59000000000	0,002811392745	0,015037058646
4955,620490688970	357,564102564103	11,09000000000	0,002849920019	0,014539595587
5560,297643069970	353,076923076923	11,64000000000	0,002891713154	0,014037567003
6238,756566936220	348,141025641026	12,17000000000	0,002938436406	0,013625342247
7000,000000000000	343,076923076923	12,73000000000	0,002988251523	0,013227620167
7854,129180113750	337,820512820513	13,31000000000	0,003041860099	0,012857949496
8812,477882559180	332,307692307692	13,89000000000	0,003099905472	0,012535518612
9887,762812359290	326,602564102564	14,48000000000	0,003162275047	0,012245242041
11094,252347227800	320,641025641026	15,06000000000	0,003229678179	0,012003030750
12447,955870272500	314,615384615385	15,65000000000	0,003300854977	0,011782626508
13966,836204782200	308,269230769231	16,54000000000	0,003383941001	0,011394775112
15671,047969978400	301,858974358974	17,67000000000	0,003476840728	0,010914108497
17583,205020567100	294,871794871795	18,45000000000	0,003575061830	0,010715801463
19728,680518851200	287,435897435897	19,24000000000	0,003684848059	0,010557704076
22135,943621178700	280,000000000000	20,13000000000	0,003803785941	0,010377493822
24836,937246350300	273,012820512821	21,07000000000	0,003925267580	0,010188449064
27867,501938744900	265,192307692308	21,90000000000	0,004064131386	0,010109844389
31267,851450567500	257,179487179487	23,15000000000	0,004228846961	0,009890467340
35083,106353909100	249,230769230769	25,98000000000	0,004463383966	0,009159406612
39363,892763324500	242,307692307692	28,37000000000	0,004690301064	0,008685396916
44167,014113613600	233,589743589744	29,90000000000	0,004938315762	0,008587994323
49556,204906889700	224,294871794872	31,13000000000	0,005208451942	0,008623936914
55602,976430699800	214,743589743590	32,41000000000	0,005515904653	0,008688322784
62387,565669362300	205,064102564103	33,51000000000	0,005848627311	0,008832962030
70000,000000000200	195,384615384615	34,48000000000	0,006208858602	0,009040704344
78541,291801137600	185,833333333333	35,50000000000	0,006609830912	0,009266641174
88124,778825591900	176,538461538462	36,40000000000	0,007037559534	0,009545513541
98877,628123593100	167,564102564103	37,16000000000	0,007488364087	0,009879870272
110942,523472278000	158,910256410256	37,84000000000	0,007968399943	0,010258003842
124479,558702725000	150,769230769231	38,47000000000	0,008471535382	0,010661633360
139668,362047822000	143,076923076923	38,96000000000	0,008988401562	0,011115609620
156710,479699784000	135,641025641026	39,45000000000	0,009547523566	0,011602686942

frequency [Hz]	measurement 3	phase difference [°]	real admittance Y´ [S m^{-1}]	imaginary admittance Y´´ [S m^{-1}]
175832,050205671000	128,333333333333	39,73000000000	0,010132053699	0,012191123865
197286,805188512000	121,730769230769	40,07000000000	0,010734737731	0,012761466568
221359,436211787000	115,512820512821	40,22000000000	0,011337585386	0,013406725152
248369,372463503000	110,000000000000	40,48000000000	0,011951773904	0,014003624578
278675,019387448000	104,935897435897	40,72000000000	0,012573616001	0,014607859926
312678,514505674000	100,128205128205	41,06000000000	0,013245228928	0,015204705976
350831,063539090000	95,641025641026	41,53000000000	0,013966928889	0,015770095180
393638,927633244000	91,410256410256	42,13000000000	0,014750980347	0,016308059662
441670,141136134000	87,307692307692	42,88000000000	0,015630526404	0,016832228614
495562,049068895000	83,333333333333	43,78000000000	0,016620457463	0,017343767598
556029,764306995000	79,423076923077	44,82000000000	0,017750401906	0,017862282822
623875,656693620000	75,576923076923	45,98000000000	0,019040686002	0,018400225704
699999,999999997000	71,679487179487	47,13000000000	0,020505996609	0,019035349240
785412,918011371000	67,846153846154	48,61000000000	0,022292277679	0,019646372715
881247,788255913000	63,910256410256	49,93000000000	0,024306945850	0,020446606772
988776,281235923000	60,275641025641	51,67000000000	0,026750598593	0,021149101791

frequency [Hz]	measurement 4	phase difference [°]	real impedance Z´ [Ω m]	imaginary impedance Z´´ [Ω m]
785,412918011374	262,820512820513	5,150000000000	261,759535648509	23,591681930588
881,247788255917	261,602564102564	5,230000000000	260,513462137979	23,846123163315
988,776281235928	260,705128205128	5,290000000000	259,594734155580	24,036178380642
1109,425234722780	259,679487179487	5,380000000000	258,535535143734	24,347754100628
1244,795587027250	258,589743589744	5,510000000000	257,394918034404	24,829652834296
1396,683620478220	257,371794871795	5,630000000000	256,130276899613	25,249199014163
1567,104796997840	256,025641025641	5,750000000000	254,737452685522	25,650712697348
1758,320502056710	254,679487179487	5,870000000000	253,344076003960	26,046503483313
1972,868051885120	253,205128205128	6,010000000000	251,813420796267	26,511093079271
2213,594362117870	251,602564102564	6,170000000000	250,145125057341	27,041942848694
2483,693724635030	250,256410256410	6,300000000000	248,745100647245	27,461714775605
2786,750193874480	248,653846153846	6,490000000000	247,060372406425	28,105294759156
3126,785145056740	247,179487179487	6,660000000000	245,511485158158	28,667220614318
3508,310635390910	245,641025641026	6,860000000000	243,882474495767	29,340281385778
3936,389276332440	243,974358974359	7,090000000000	242,108807891439	30,113335556455
4416,701411361350	242,307692307692	7,340000000000	240,322100238377	30,956516091038
4955,620490688970	240,641025641026	7,600000000000	238,527124237454	31,826313399054
5560,297643069970	239,038461538462	7,870000000000	236,787028368250	32,730555925739
6238,756566936220	237,243589743590	8,160000000000	234,841632078817	33,673858065007
7000,000000000000	235,705128205128	8,480000000000	233,128257925558	34,758061205859
7854,129180113750	234,743589743590	8,820000000000	231,967727806529	35,993418592612
8812,477882559180	232,948717948718	9,210000000000	229,945623562292	37,284251346916
9887,762812359290	231,025641025641	9,610000000000	227,783638664027	38,567612945115
11094,252347227800	228,974358974359	10,08000000000	225,439987367841	40,075792734595
12447,955870272500	226,730769230769	10,56000000000	222,890750784286	41,551834265094
13966,836204782200	224,358974358974	11,06000000000	220,191917107031	43,040318494885
15671,047969978400	221,794871794872	11,61000000000	217,256979760795	44,635970917198
17583,205020567100	219,294871794872	12,20000000000	214,342293227739	46,342444145762
19728,680518851200	216,410256410256	12,79000000000	211,040686634498	47,908534358637
22135,943621178700	213,333333333333	13,44000000000	207,490954795721	49,584420830247
24836,937246350300	210,833333333333	14,18000000000	204,409435477880	51,647624650692
27867,501938744900	207,692307692308	14,91000000000	200,699554111807	53,439532687686
31267,851450567500	204,358974358974	15,70000000000	196,734697923565	55,299629600709
35083,106353909100	200,897435897436	16,53000000000	192,594524344587	57,158804594276
39363,892763324500	197,371794871795	17,41000000000	188,329822189434	59,055088561530
44167,014113613600	193,653846153846	18,34000000000	183,817400090498	60,934190354409
49556,204906889700	189,807692307692	19,29000000000	179,151627068218	62,702907253027
55602,976430699800	185,833333333333	20,33000000000	174,257245556009	64,563458310492
62387,565669362300	181,666666666667	21,37000000000	169,176490602997	66,197377629569
70000,000000000200	177,307692307692	22,47000000000	163,846453022576	67,766935768117
78541,291801137600	172,820512820513	23,62000000000	158,342115853460	69,243801156454
88124,778825591900	168,333333333333	24,86000000000	152,735184831951	70,767749896835
98877,628123593100	163,589743589744	26,10000000000	146,908100855198	71,969535991814
110942,523472278000	158,846153846154	27,39000000000	141,038815631743	73,076351009825
124479,558702725000	154,102564102564	28,79000000000	135,054061511094	74,215906194982
139668,362047822000	149,102564102564	30,27000000000	128,773861213000	75,158946841040
156710,479699784000	143,910256410256	31,87000000000	122,215534982995	75,983714761033

frequency [Hz]	measurement 4	phase difference [°]	real impedance Z´ [Ω m]	imaginary impedance Z´´ [Ω m]
175832,050205671000	138,012820512821	33,39000000000	115,232966412786	75,953288787345
197286,805188512000	132,435897435897	35,03000000000	108,445347584934	76,018902365362
221359,436211787000	126,538461538462	36,54000000000	101,666238706496	75,338955101557
248369,372463503000	120,897435897436	38,15000000000	95,073291071348	74,681050685146
278675,019387448000	115,192307692308	39,69000000000	88,641751264751	73,565669195605
312678,514505674000	109,423076923077	41,28000000000	82,230837392051	72,190713704158
350831,063539090000	103,782051282051	42,87000000000	76,061784742766	70,606791954142
393638,927633244000	98,205128205128	44,43000000000	70,128894737634	68,747256881009
441670,141136134000	92,756410256410	46,02000000000	64,410722020717	66,745865283367
495562,049068895000	87,371794871795	47,64000000000	58,869951960955	64,561283252689
556029,764306995000	82,051282051282	49,21000000000	53,603156798128	62,121771284585
623875,656693620000	76,923076923077	50,75000000000	48,669640658655	59,568664929399
699999,999999997000	71,884615384615	52,24000000000	44,018923211736	56,830734011390
785412,918011371000	67,083333333333	53,76000000000	39,657579584915	54,105914580360
881247,788255913000	62,371794871795	55,10000000000	35,685765055288	51,154344565717
988776,281235923000	58,051282051282	56,78000000000	31,803701148839	48,564142543988

frequency [Hz]	measurement 4	phase difference [°]	real admittance Y´ [S m^{-1}]	imaginary admittance Y´´ [S m^{-1}]
785,412918011374	262,820512820513	5,150000000000	0,003820300176	0,042387821392
881,247788255917	261,602564102564	5,230000000000	0,003838573223	0,041935537829
988,776281235928	260,705128205128	5,290000000000	0,003852158262	0,041603951517
1109,425234722780	259,679487179487	5,380000000000	0,003867940241	0,041071550003
1244,795587027250	258,589743589744	5,510000000000	0,003885080590	0,040274425368
1396,683620478220	257,371794871795	5,630000000000	0,003904263143	0,039605216761
1567,104796997840	256,025641025641	5,750000000000	0,003925610425	0,038985271552
1758,320502056710	254,679487179487	5,870000000000	0,003947201039	0,038392869148
1972,868051885120	253,205128205128	6,010000000000	0,003971194215	0,037720059185
2213,594362117870	251,602564102564	6,170000000000	0,003997679346	0,036979591503
2483,693724635030	250,256410256410	6,300000000000	0,004020179684	0,036414332032
2786,750193874480	248,653846153846	6,490000000000	0,004047593672	0,035580484338
3126,785145056740	247,179487179487	6,660000000000	0,004073129204	0,034883046859
3508,310635390910	245,641025641026	6,860000000000	0,004100335631	0,034082836045
3936,389276332440	243,974358974359	7,090000000000	0,004130374309	0,033207878886
4416,701411361350	242,307692307692	7,340000000000	0,004161082144	0,032303376680
4955,620490688970	240,641025641026	7,600000000000	0,004192395323	0,031420541470
5560,297643069970	239,038461538462	7,870000000000	0,004223204315	0,030552490531
6238,756566936220	237,243589743590	8,160000000000	0,004258188768	0,029696626923
7000,000000000000	235,705128205128	8,480000000000	0,004289484290	0,028770304364
7854,129180113750	234,743589743590	8,820000000000	0,004310944498	0,027782856953
8812,477882559180	232,948717948718	9,210000000000	0,004348854240	0,026820975717
9887,762812359290	231,025641025641	9,610000000000	0,004390130941	0,025928490867
11094,252347227800	228,974358974359	10,08000000000	0,004435770298	0,024952719130
12447,955870272500	226,730769230769	10,56000000000	0,004486502901	0,024066326257
13966,836204782200	224,358974358974	11,06000000000	0,004541492772	0,023234028812
15671,047969978400	221,794871794872	11,61000000000	0,004602844066	0,022403455766
17583,205020567100	219,294871794872	12,20000000000	0,004665434828	0,021578490700
19728,680518851200	216,410256410256	12,79000000000	0,004738422794	0,020873107754
22135,943621178700	213,333333333333	13,44000000000	0,004819487196	0,020167624896
24836,937246350300	210,833333333333	14,18000000000	0,004892142076	0,019361974665
27867,501938744900	207,692307692308	14,91000000000	0,004982572106	0,018712738486
31267,851450567500	204,358974358974	15,70000000000	0,005082987447	0,018083303762
35083,106353909100	200,897435897436	16,53000000000	0,005192255613	0,017495117456
39363,892763324500	197,371794871795	17,41000000000	0,005309833506	0,016933341806
44167,014113613600	193,653846153846	18,34000000000	0,005440181395	0,016411147735
49556,204906889700	189,807692307692	19,29000000000	0,005581863901	0,015948223835
55602,976430699800	185,833333333333	20,33000000000	0,005738642298	0,015488637476
62387,565669362300	181,666666666667	21,37000000000	0,005910986783	0,015106338586
70000,000000000200	177,307692307692	22,47000000000	0,006103275241	0,014756458864
78541,291801137600	172,820512820513	23,62000000000	0,006315439165	0,014441725949
88124,778825591900	168,333333333333	24,86000000000	0,006547279863	0,014130730473
98877,628123593100	163,589743589744	26,10000000000	0,006806976567	0,013894767921
110942,523472278000	158,846153846154	27,39000000000	0,007090246721	0,013684317651
124479,558702725000	154,102564102564	28,79000000000	0,007404442257	0,013474200495
139668,362047822000	149,102564102564	30,27000000000	0,007765551103	0,013305135876
156710,479699784000	143,910256410256	31,87000000000	0,008182265864	0,013160714808

frequency [Hz]	measurement 4	phase difference [°]	real admittance Y´ [S m^{-1}]	imaginary admittance Y´´ [S m^{-1}]
175832,050205671000	138,012820512821	33,39000000000	0,008678072180	0,013165986832
197286,805188512000	132,435897435897	35,03000000000	0,009221234680	0,013154622980
221359,436211787000	126,538461538462	36,54000000000	0,009836106978	0,013273345757
248369,372463503000	120,897435897436	38,15000000000	0,010518201155	0,013390277598
278675,019387448000	115,192307692308	39,69000000000	0,011281365561	0,013593297131
312678,514505674000	109,423076923077	41,28000000000	0,012160887955	0,013852197169
350831,063539090000	103,782051282051	42,87000000000	0,013147206621	0,014162943427
393638,927633244000	98,205128205128	44,43000000000	0,014259457585	0,014546034931
441670,141136134000	92,756410256410	46,02000000000	0,015525365477	0,014982201456
495562,049068895000	87,371794871795	47,64000000000	0,016986594463	0,015489159286
556029,764306995000	82,051282051282	49,21000000000	0,018655617686	0,016097416080
623875,656693620000	76,923076923077	50,75000000000	0,020546689609	0,016787349543
699999,999999997000	71,884615384615	52,24000000000	0,022717502543	0,017596112691
785412,918011371000	67,083333333333	53,76000000000	0,025215860637	0,018482267748
881247,788255913000	62,371794871795	55,10000000000	0,028022378067	0,019548681710
988776,281235923000	58,051282051282	56,78000000000	0,031442881296	0,020591324125

frequency [Hz]	measurement 5	phase difference [°]	real impedance Z´ [Ω m]	imaginary impedance Z´´ [Ω m]
785,412918011374	320,576923076923	5,050000000000	319,332527146526	28,218800748451
881,247788255917	318,910256410256	5,160000000000	317,617850080201	28,681927307741
988,776281235928	317,307692307692	5,270000000000	315,966409470802	29,144462317264
1109,425234722780	315,576923076923	5,390000000000	314,181560087362	29,643577378066
1244,795587027250	314,166666666667	5,580000000000	312,677957193149	30,548151007287
1396,683620478220	312,435897435897	5,730000000000	310,874789561411	31,193833071987
1567,104796997840	310,641025641026	5,890000000000	309,001071722896	31,877648680694
1758,320502056710	308,846153846154	6,050000000000	307,125972929450	32,551244180541
1972,868051885120	307,115384615385	6,250000000000	305,289994642509	33,434692142036
2213,594362117870	304,871794871795	6,480000000000	302,924063643151	34,406728619120
2483,693724635030	302,884615384615	6,690000000000	300,822273219631	35,285268479353
2786,750193874480	300,897435897436	6,920000000000	298,705502121314	36,253136858836
3126,785145056740	298,782051282051	7,180000000000	296,439119087062	37,343846122178
3508,310635390910	296,538461538462	7,460000000000	294,028484154325	38,500775024761
3936,389276332440	294,294871794872	7,700000000000	291,641273710950	39,431447259960
4416,701411361350	291,987179487180	8,020000000000	289,131377806990	40,737689579918
4955,620490688970	289,679487179487	8,350000000000	286,608721743480	42,067159556349
5560,297643069970	287,179487179487	8,690000000000	283,882744706645	43,389458564209
6238,756566936220	284,615384615385	9,020000000000	281,095738125005	44,621779073921
7000,000000000000	282,051282051282	9,380000000000	278,280006235367	45,969161798057
7854,129180113750	279,358974358974	9,770000000000	275,307398996051	47,405407000967
8812,477882559180	276,474358974359	10,200000000000	272,104849818676	48,959390063998
9887,762812359290	273,461538461538	10,650000000000	268,751012253533	50,538168055966
11094,25234722780	270,384615384615	11,120000000000	265,308252753927	52,147591098195
12447,95587027250	267,307692307692	11,620000000000	261,829221283782	53,841073993672
13966,83620478220	263,910256410256	12,120000000000	258,027698512456	55,410560716280
15671,04796997840	260,384615384615	12,680000000000	254,034153668199	57,155898200238
17583,20502056710	256,858974358974	13,280000000000	249,990338319524	59,003080052096
19728,68051885120	252,948717948718	13,900000000000	245,541489506894	60,765375359954
22135,94362117870	248,717948717949	14,550000000000	240,741259171865	62,484111154829
24836,93724635030	244,871794871795	15,210000000000	236,294111992138	64,243976850606
27867,50193874490	240,448717948718	15,870000000000	231,283924275647	65,752051943944
31267,85145056750	236,153846153846	16,590000000000	226,323333478340	67,426906917836
35083,10635390910	231,538461538462	17,320000000000	221,039798703998	68,930882487414
39363,89276332450	226,666666666667	18,070000000000	215,487074788078	70,307171590493
44167,01411361360	221,666666666667	18,830000000000	209,803153656499	71,545424919407
49556,20490688970	216,538461538462	19,610000000000	203,978990648758	72,673768991003
55602,97643069980	211,346153846154	20,420000000000	198,065216022180	73,738503833813
62387,56566936230	206,025641025641	21,220000000000	192,056590308043	74,570978800568
70000,00000000020	200,769230769231	22,060000000000	186,071128028505	75,404372140271
78541,29180113760	195,256410256410	22,890000000000	179,880613559392	75,947551716407
88124,77882559190	189,935897435897	23,770000000000	173,823794468761	76,556734591163
98877,62812359310	184,423076923077	24,630000000000	167,643900283684	76,859573245298
110942,5234722780	179,038461538462	25,540000000000	161,543630715036	77,190841979235
124479,5587027250	173,589743589744	26,500000000000	155,351426360146	77,455363968036
139668,3620478220	168,141025641026	27,510000000000	149,129358431998	77,664914583592
156710,4796997840	162,628205128205	28,610000000000	142,771206073926	77,873717128555

frequency [Hz]	measurement 5	phase difference [°]	real impedance Z´ [Ω m]	imaginary impedance Z´´ [Ω m]
175832,0502056710	156,602564102564	29,640000000000	136,111099980220	77,447605164216
197286,8051885120	150,961538461538	30,770000000000	129,710363286549	77,230873041460
221359,4362117870	145,064102564103	31,810000000000	123,275577195829	76,463886376274
248369,3724635030	139,423076923077	32,900000000000	117,062384959125	75,731053118122
278675,0193874480	133,782051282051	33,980000000000	110,936453895815	74,771254117175
312678,5145056740	128,205128205128	35,080000000000	104,916715676116	73,682003703960
350831,0635390900	122,692307692308	36,210000000000	98,995174265500	72,480051317637
393638,9276332440	117,243589743590	37,330000000000	93,226952878976	71,097078652111
441670,1411361340	111,858974358974	38,490000000000	87,553897816400	69,618568800264
495562,0490688950	106,538461538462	39,670000000000	82,006266310878	68,010411502443
556029,7643069950	101,346153846154	40,870000000000	76,637575108578	66,315344988059
623875,6566936200	96,217948717949	42,060000000000	71,436410448956	64,457217731284
699999,9999999970	90,448717948718	42,410000000000	66,781693078904	61,001442999996
785412,9180113710	86,282051282051	44,470000000000	61,572368495032	60,443658156589
881247,7882559130	81,346153846154	45,350000000000	57,167973758891	57,870713853078
988776,2812359230	76,923076923077	46,990000000000	52,471230382717	56,248819947066

frequency [Hz]	measurement 5	phase difference [°]	real admittance Y´ [S m^{-1}]	imaginary admittance Y´´ [S m^{-1}]
785,412918011374	320,576923076923	5,050000000000	0,003131532	0,035437367
881,247788255917	318,910256410256	5,160000000000	0,003148438	0,034865161
988,776281235928	317,307692307692	5,270000000000	0,003164893	0,034311836
1109,425234722780	315,576923076923	5,390000000000	0,003182873	0,03373412
1244,795587027250	314,166666666667	5,580000000000	0,003198179	0,032735205
1396,683620478220	312,435897435897	5,730000000000	0,003216729	0,032057618
1567,104796997840	310,641025641026	5,890000000000	0,003236235	0,031369942
1758,320502056710	308,846153846154	6,050000000000	0,003255993	0,030720792
1972,868051885120	307,115384615385	6,250000000000	0,003275574	0,029909054
2213,594362117870	304,871794871795	6,480000000000	0,003301157	0,029064083
2483,693724635030	302,884615384615	6,690000000000	0,003324222	0,028340439
2786,750193874480	300,897435897436	6,920000000000	0,003347779	0,02758382
3126,785145056740	298,782051282051	7,180000000000	0,003373374	0,026778174
3508,310635390910	296,538461538462	7,460000000000	0,003401031	0,025973503
3936,389276332440	294,294871794872	7,700000000000	0,00342887	0,025360469
4416,701411361350	291,987179487180	8,020000000000	0,003458635	0,024547293
4955,620490688970	289,679487179487	8,350000000000	0,003489077	0,023771512
5560,297643069970	287,179487179487	8,690000000000	0,003522581	0,023047073
6238,756566936220	284,615384615385	9,020000000000	0,003557507	0,022410581
7000,000000000000	282,051282051282	9,380000000000	0,003593503	0,021753714
7854,129180113750	279,358974358974	9,770000000000	0,003632303	0,02109464
8812,477882559180	276,474358974359	10,200000000000	0,003675054	0,020425091
9887,762812359290	273,461538461538	10,650000000000	0,003720916	0,019787025
11094,252347227800	270,384615384615	11,120000000000	0,003769201	0,019176341
12447,955870272500	267,307692307692	11,620000000000	0,003819283	0,018573181
13966,836204782200	263,910256410256	12,120000000000	0,003875553	0,018047101
15671,047969978400	260,384615384615	12,680000000000	0,003936479	0,017496007
17583,205020567100	256,858974358974	13,280000000000	0,004000155	0,016948268
19728,680518851200	252,948717948718	13,900000000000	0,004072631	0,01645674
22135,943621178700	248,717948717949	14,550000000000	0,004153837	0,016004069
24836,937246350300	244,871794871795	15,210000000000	0,004232014	0,015565662
27867,501938744900	240,448717948718	15,870000000000	0,00432369	0,015208651
31267,851450567500	236,153846153846	16,590000000000	0,004418457	0,014830875
35083,106353909100	231,538461538462	17,320000000000	0,004524072	0,014507286
39363,892763324500	226,666666666667	18,070000000000	0,00464065	0,0142233
44167,014113613600	221,666666666667	18,830000000000	0,004766373	0,013977134
49556,204906889700	216,538461538462	19,610000000000	0,004902466	0,013760123
55602,976430699800	211,346153846154	20,420000000000	0,005048842	0,013561436
62387,565669362300	206,025641025641	21,220000000000	0,005206799	0,013410043
70000,000000000200	200,769230769231	22,060000000000	0,005374289	0,01326183
78541,291801137600	195,256410256410	22,890000000000	0,005559243	0,013166981
88124,778825591900	189,935897435897	23,770000000000	0,005752952	0,013062208
98877,628123593100	184,423076923077	24,630000000000	0,005965025	0,013010741
110942,523472278000	179,038461538462	25,540000000000	0,006190278	0,012954905
124479,558702725000	173,589743589744	26,500000000000	0,006437018	0,012910662
139668,362047822000	168,141025641026	27,510000000000	0,006705588	0,012875827

frequency [Hz]	measurement 5	phase difference [°]	real admittance Y´ [S m^{-1}]	imaginary admittance Y´´ [S m^{-1}]
156710,479699784000	162,628205128205	28,610000000000	0,007004213	0,012841303
175832,050205671000	156,602564102564	29,640000000000	0,007346939	0,012911955
197286,805188512000	150,961538461538	30,770000000000	0,007709484	0,01294819
221359,436211787000	145,064102564103	31,810000000000	0,008111907	0,013078069
248369,372463503000	139,423076923077	32,900000000000	0,008542454	0,013204623
278675,019387448000	133,782051282051	33,980000000000	0,00901417	0,013374124
312678,514505674000	128,205128205128	35,080000000000	0,00953137	0,013571835
350831,063539090000	122,692307692308	36,210000000000	0,010101502	0,0137969
393638,927633244000	117,243589743590	37,330000000000	0,010726512	0,014065276
441670,141136134000	111,858974358974	38,490000000000	0,011421536	0,014363984
495562,049068895000	106,538461538462	39,670000000000	0,01219419	0,014703631
556029,764306995000	101,346153846154	40,870000000000	0,01304843	0,015079466
623875,656693620000	96,217948717949	42,060000000000	0,013998464	0,015514166
699999,999999997000	90,448717948718	42,410000000000	0,014974164	0,016393055
785412,918011371000	86,282051282051	44,470000000000	0,016241051	0,016544333
881247,788255913000	81,346153846154	45,350000000000	0,017492311	0,017279897
988776,281235923000	76,923076923077	46,990000000000	0,019058063	0,017778151

frequency [Hz]	measurement 6	phase difference [°]	real impedance Z´ [Ω m]	imaginary impedance Z´´ [Ω m]
785,4129180114	1598,3000000000	1,2800000000	1597,9011726658	35,7033947042
881,2477882559	1597,2000000000	1,5200000000	1596,6379877966	42,3671562042
988,7762812359	1577,4000000000	1,2000000000	1577,0540501132	33,0345731240
1109,4252347228	1567,5000000000	1,8100000000	1566,7179161439	49,5098094685
1244,7955870272	1562,0000000000	2,5600000000	1560,4411172602	69,7676111371
1396,6836204782	1548,8000000000	2,8700000000	1546,8573567045	77,5484236400
1567,1047969978	1542,2000000000	3,5800000000	1539,1905287905	96,2982662450
1758,3205020567	1566,4000000000	3,1900000000	1563,9728501446	87,1658419938
1972,8680518851	1568,6000000000	3,9400000000	1564,8926955916	107,7813123136
2213,5943621179	1562,0000000000	4,9700000000	1556,1271864232	135,3225024693
2483,6937246350	1549,9000000000	5,8600000000	1541,8007455934	158,2418114397
2786,7501938745	1532,3000000000	5,9800000000	1523,9617169457	159,6370110088
3126,7851450567	1523,5000000000	6,8000000000	1512,7829516003	180,3884457150
3508,3106353909	1518,0000000000	7,6500000000	1504,4894165016	202,0781918833
3936,3892763324	1503,7000000000	8,2300000000	1488,2140175848	215,2503841209
4416,7014113614	1497,1000000000	8,6000000000	1480,2671780655	223,8693626696
4955,6204906890	1480,6000000000	9,2600000000	1461,3052600309	238,2504921421
5560,2976430700	1469,6000000000	9,8900000000	1447,7607423785	252,4143276990
6238,7565669362	1459,7000000000	10,7800000000	1433,9400891996	273,0199820276
7000,0000000000	1445,4000000000	11,7500000000	1415,1123259292	294,3437870980
7854,1291801137	1436,6000000000	13,1200000000	1399,1001309724	326,0956661978
8812,4778825592	1425,6000000000	14,2100000000	1381,9802338153	349,9514156904
9887,7628123593	1397,0000000000	14,7500000000	1350,9631766628	355,6789216431
11094,2523472278	1369,5000000000	15,1600000000	1321,8404439055	358,1453487842
12447,9558702724	1331,0000000000	15,5500000000	1282,2812430707	356,8134157640
13966,8362047821	1310,1000000000	16,9800000000	1252,9884893027	382,5988181828
15671,0479699783	1272,7000000000	17,7100000000	1212,3847144529	387,1544835862
17583,2050205670	1234,2000000000	17,4500000000	1177,4008853551	370,1037627004
19728,6805188512	1236,4000000000	20,5000000000	1158,1014947867	432,9964061892
22135,9436211786	1223,9700000000	23,0100000000	1126,5868391394	478,4398131196
24836,9372463503	1190,0900000000	24,4900000000	1083,0219282504	493,3332656824
27867,5019387448	1166,1100000000	26,7600000000	1041,2200537411	525,0460282559
31267,8514505674	1126,0700000000	27,8400000000	995,7332084447	525,8792851030
35083,1063539091	1101,3200000000	30,5200000000	948,7342545711	559,2933546926
39363,8927633245	1055,0100000000	31,6200000000	898,3874108274	553,1240007149
44167,0141136136	1022,2300000000	34,3000000000	844,4624595824	576,0532330055
49556,2049068897	978,8900000000	35,7000000000	794,9404436391	571,2226563844
55602,9764306998	938,3000000000	38,1900000000	737,4707848184	580,1238932671
62387,5656693623	891,7700000000	40,1500000000	681,6324306226	575,0051846927
70000,0000000001	842,6000000000	41,0500000000	635,4356452805	553,3500706668
78541,2918011376	800,2500000000	43,4000000000	581,4413804445	549,8417805212
88124,7788255919	754,6000000000	45,7500000000	526,5526809965	540,5214465082
98877,6281235930	709,7200000000	47,6100000000	478,4744111279	524,1800418709
110942,5234722780	667,0400000000	50,4900000000	424,3794424667	514,6304017561
124479,5587027240	623,5900000000	52,6800000000	378,0614373694	495,9173698049
139668,3620478210	579,7000000000	54,6800000000	335,1491927196	472,9980006506
156710,4796997840	536,6900000000	56,5800000000	295,5938909189	447,9513452948

frequency [Hz]	measurement 6	phase difference [°]	real impedance Z´ [Ω m]	imaginary impedance Z´´ [Ω m]
175832,0502056700	492,6900000000	57,7000000000	263,2700590209	416,4520526101
197286,8051885110	454,7400000000	59,7500000000	229,0861783217	392,8205576366
221359,4362117860	417,4500000000	61,3600000000	200,0857424165	366,3743961873
248369,3724635020	385,0000000000	63,3900000000	172,4473290435	344,2192886893
278675,0193874470	352,0000000000	64,9800000000	148,8729781740	318,9683939979
312678,5145056730	321,3100000000	66,3700000000	128,7902966061	294,3691145486
350831,0635390900	292,7100000000	67,7000000000	111,0706124557	270,8181366687
393638,9276332430	265,9800000000	68,9300000000	95,6220084487	248,1970827795
441670,1411361340	241,2300000000	70,0800000000	82,1889310014	226,7970293475
495562,0490688950	218,4600000000	71,1400000000	70,6186908250	206,7311590113
556029,7643069950	197,4500000000	72,1100000000	60,6547698650	187,9029041623
623875,6566936190	177,8700000000	72,9900000000	52,0338420156	170,0888479151
785412,9180113710	143,5500000000	74,5100000000	38,3379253104	138,3358448953
988776,2812359230	114,6310000000	75,5900000000	28,5269483520	111,0246791426

frequency [Hz]	measurement 6	phase difference [°]	real admittance Y´ [S m^{-1}]	imaginary admittance Y´´ [S m^{-1}]
785,4129180114	1598,3000000000	1,2800000000	0,0006258209	0,0280085412
881,2477882559	1597,2000000000	1,5200000000	0,0006263161	0,0236031891
988,7762812359	1577,4000000000	1,2000000000	0,0006340937	0,0302713159
1109,4252347228	1567,5000000000	1,8100000000	0,0006382770	0,0201980175
1244,7955870272	1562,0000000000	2,5600000000	0,0006408444	0,0143332986
1396,6836204782	1548,8000000000	2,8700000000	0,0006464720	0,0128951686
1567,1047969978	1542,2000000000	3,5800000000	0,0006496921	0,0103844029
1758,3205020567	1566,4000000000	3,1900000000	0,0006393973	0,0114723839
1972,8680518851	1568,6000000000	3,9400000000	0,0006390215	0,0092780462
2213,5943621179	1562,0000000000	4,9700000000	0,0006426210	0,0073897540
2483,6937246350	1549,9000000000	5,8600000000	0,0006485922	0,0063194423
2786,7501938745	1532,3000000000	5,9800000000	0,0006561845	0,0062642115
3126,7851450567	1523,5000000000	6,8000000000	0,0006610334	0,0055435923
3508,3106353909	1518,0000000000	7,6500000000	0,0006646773	0,0049485795
3936,3892763324	1503,7000000000	8,2300000000	0,0006719464	0,0046457525
4416,7014113614	1497,1000000000	8,6000000000	0,0006755537	0,0044668908
4955,6204906890	1480,6000000000	9,2600000000	0,0006843197	0,0041972631
5560,2976430700	1469,6000000000	9,8900000000	0,0006907219	0,0039617402
6238,7565669362	1459,7000000000	10,7800000000	0,0006973792	0,0036627356
7000,0000000000	1445,4000000000	11,7500000000	0,0007066577	0,0033973878
7854,1291801137	1436,6000000000	13,1200000000	0,0007147451	0,0030665848
8812,4778825592	1425,6000000000	14,2100000000	0,0007235994	0,0028575395
9887,7628123593	1397,0000000000	14,7500000000	0,0007402126	0,0028115245
11094,2523472278	1369,5000000000	15,1600000000	0,0007565210	0,0027921625
12447,9558702724	1331,0000000000	15,5500000000	0,0007798601	0,0028025852
13966,8362047821	1310,1000000000	16,9800000000	0,0007980919	0,0026137038
15671,0479699783	1272,7000000000	17,7100000000	0,0008248207	0,0025829483
17583,2050205670	1234,2000000000	17,4500000000	0,0008493284	0,0027019450
19728,6805188512	1236,4000000000	20,5000000000	0,0008634822	0,0023094880
22135,9436211786	1223,9700000000	23,0100000000	0,0008876369	0,0020901271
24836,9372463503	1190,0900000000	24,4900000000	0,0009233423	0,0020270273
27867,5019387448	1166,1100000000	26,7600000000	0,0009604118	0,0019045949
31267,8514505674	1126,0700000000	27,8400000000	0,0010042851	0,0019015771
35083,1063539091	1101,3200000000	30,5200000000	0,0010540359	0,0017879705
39363,8927633245	1055,0100000000	31,6200000000	0,0011131055	0,0018079129
44167,0141136136	1022,2300000000	34,3000000000	0,0011841853	0,0017359507
49556,2049068897	978,8900000000	35,7000000000	0,0012579559	0,0017506308
55602,9764306998	938,3000000000	38,1900000000	0,0013559859	0,0017237697
62387,5656693623	891,7700000000	40,1500000000	0,0014670663	0,0017391148
70000,0000000001	842,6000000000	41,0500000000	0,0015737235	0,0018071743
78541,2918011376	800,2500000000	43,4000000000	0,0017198638	0,0018187050
88124,7788255919	754,6000000000	45,7500000000	0,0018991452	0,0018500654
98877,6281235930	709,7200000000	47,6100000000	0,0020899759	0,0019077415
110942,5234722780	667,0400000000	50,4900000000	0,0023563818	0,0019431421
124479,5587027240	623,5900000000	52,6800000000	0,0026450727	0,0020164650
139668,3620478210	579,7000000000	54,6800000000	0,0029837458	0,0021141738
156710,4796997840	536,6900000000	56,5800000000	0,0033830198	0,0022323853

frequency [Hz]	measurement 6	phase difference [°]	real admittance Y´ [S m^{-1}]	imaginary admittance Y´´ [S m^{-1}]
175832,0502056700	492,6900000000	57,7000000000	0,0037983810	0,0024012368
197286,8051885110	454,7400000000	59,7500000000	0,0043651695	0,0025456916
221359,4362117860	417,4500000000	61,3600000000	0,0049978574	0,0027294484
248369,3724635020	385,0000000000	63,3900000000	0,0057988721	0,0029051248
278675,0193874470	352,0000000000	64,9800000000	0,0067171357	0,0031351069
312678,5145056730	321,3100000000	66,3700000000	0,0077645601	0,0033970955
350831,0635390900	292,7100000000	67,7000000000	0,0090032816	0,0036925149
393638,9276332430	265,9800000000	68,9300000000	0,0104578435	0,0040290562
441670,1411361340	241,2300000000	70,0800000000	0,0121670885	0,0044092288
495562,0490688950	218,4600000000	71,1400000000	0,0141605570	0,0048372002
556029,7643069950	197,4500000000	72,1100000000	0,0164867496	0,0053218975
623875,6566936190	177,8700000000	72,9900000000	0,0192182618	0,0058792802
785412,9180113710	143,5500000000	74,5100000000	0,0260838319	0,0072287844
988776,2812359230	114,6310000000	75,5900000000	0,0350545732	0,0090070064

frequency [Hz]	measurement 7	phase difference [°]	real impedance Z´ [Ω m]	imaginary impedance Z´´ [Ω m]
785,4129180114	1962,0000000000	0,200000	1961,9880468200	6,8486580800
881,2477882559	1969,0000000000	0,010000	1968,9999700100	0,3436553300
988,7762812359	1964,0000000000	0,330000	1963,9674243600	11,3117654100
1109,4252347228	1969,0000000000	1,010000	1968,6940841700	34,7073907400
1244,7955870272	1933,0000000000	1,130000	1932,6240765600	38,1205809400
1396,6836204782	1962,0000000000	1,920000	1960,8984973200	65,7349466900
1567,1047969978	1923,0000000000	2,860000	1920,6047772300	95,9494121800
1758,3205020567	1983,0000000000	2,690000	1980,8148953700	93,0663757600
1972,8680518851	1987,0000000000	4,200000	1981,6638662500	145,5242976900
2213,5943621179	1984,0000000000	5,010000	1976,4200712000	173,2619466200
2483,6937246350	1962,0000000000	5,970000	1951,3590734100	204,0631437300
2786,7501938745	1943,0000000000	6,420000	1930,8153471700	217,2581302000
3126,7851450567	1936,0000000000	7,470000	1919,5693012400	251,6936585500
3508,3106353909	1931,0000000000	8,000000	1912,2076407400	268,7432579500
3936,3892763324	1921,0000000000	8,930000	1897,7150291400	298,1923341800
4416,7014113614	1912,0000000000	9,830000	1883,9292433600	326,4270301500
4955,6204906890	1894,0000000000	10,540000	1862,0433781100	346,4541211200
5560,2976430700	1883,0000000000	11,470000	1845,3945299800	374,4436255600
6238,7565669362	1869,0000000000	12,640000	1823,7033485100	408,9830028500
7000,0000000000	1849,0000000000	13,970000	1794,3107647900	446,3741472800
7854,1291801137	1834,0000000000	15,650000	1766,0090776700	494,7402728500
8812,4778825592	1817,0000000000	17,120000	1736,4893062300	534,8774526400
9887,7628123593	1781,0000000000	17,850000	1695,2666864000	545,9229450900
11094,2523472278	1738,0000000000	18,200000	1651,0514255500	542,8380883700
12447,9558702724	1679,0000000000	18,930000	1588,1923367000	544,6889953400
13966,8362047821	1647,0000000000	20,890000	1538,7372921500	587,2789335000
15671,0479699783	1589,0000000000	21,680000	1476,5966520400	587,0122036200
17583,2050205670	1523,0000000000	21,170000	1420,2173288300	550,0106716100
19728,6805188512	1533,0000000000	25,660000	1381,8148545400	663,8348497700
22135,9436211786	1509,0000000000	26,450000	1351,0430133700	672,1337486200
24836,9372463503	1312,0000000000	23,290000	1205,0922088200	518,7453790000
27867,5019387448	1337,0000000000	30,060000	1157,1752785500	669,7121581100
31267,8514505674	1333,0000000000	33,450000	1112,2114247700	734,7616937500
35083,1063539091	1300,0000000000	37,380000	1033,0145621900	789,2280496200
39363,8927633245	1218,0000000000	37,830000	962,0177957900	747,0246050700
44167,0141136136	1185,0000000000	41,680000	885,0413600000	787,9890805600
49556,2049068897	1132,0000000000	41,400000	849,1257308200	748,6050315500
55602,9764306998	1061,0000000000	46,360000	732,2225644900	767,8353443600
62387,5656693623	994,6000000000	48,350000	660,9898126100	743,1834414400
70000,0000000001	928,9000000000	49,210000	606,8396630100	703,2786314100
78541,2918011376	868,0000000000	51,800000	536,7784871700	682,1237832800
88124,7788255919	807,5000000000	54,040000	474,1803992700	653,6124225800
98877,6281235930	749,9000000000	55,720000	422,3719151700	619,6385844000
110942,5234722780	694,2000000000	58,490000	362,8218046300	591,8394867600
124479,5587027240	640,8000000000	60,520000	315,3503157200	557,8340419700
139668,3620478210	588,9000000000	62,250000	274,2003910200	521,1692197000
156710,4796997840	539,1000000000	63,850000	237,5935963200	483,9195108500

frequency [Hz]	measurement 7	phase difference [°]	real impedance Z´ [Ω m]	imaginary impedance Z´´ [Ω m]
175832,0502056700	490,8000000000	64,620000	210,3665898800	443,4304205400
197286,8051885110	447,8000000000	66,340000	179,7059130200	410,1592676400
221359,4362117860	407,0000000000	67,590000	155,1613158500	376,2631606500
248369,3724635020	371,7000000000	69,240000	131,7506426700	347,5667679100
278675,0193874470	337,3000000000	70,410000	113,0923538700	317,7757220000
312678,5145056730	305,6000000000	71,420000	97,3728562400	289,6720332800
350831,0635390900	276,6000000000	72,330000	83,9575616200	263,5501619200
393638,9276332430	249,8000000000	73,160000	72,3670753700	239,0879470000
441670,1411361340	225,5000000000	73,910000	62,4966398100	216,6666102800
495562,0490688950	203,2000000000	74,580000	54,0293832500	195,8853382600
556029,7643069950	182,9000000000	75,170000	46,8136117400	176,8075104600
623875,6566936190	164,2000000000	75,630000	40,7516000200	159,0627143500
785412,9180113710	131,8000000000	76,200000	31,4387097100	127,9954980900
881247,7882559130	118,0000000000	76,220000	28,1069454800	114,6036631900
988776,2812359230	105,1000000000	76,250000	24,9807872800	102,0880515400

frequency [Hz]	measurement 7	phase difference [°]	real admittance Y´ [S m^{-1}]	imaginary admittance Y´´ [S m^{-1}]
785,4129180114	1962,0000000000	0,200000	0,0005096871	0,1460140057
881,2477882559	1969,0000000000	0,010000	0,0005078720	2,9098923040
988,7762812359	1964,0000000000	0,330000	0,0005091734	0,0884035306
1109,4252347228	1969,0000000000	1,010000	0,0005079509	0,0288123071
1244,7955870272	1933,0000000000	1,130000	0,0005174312	0,0262325488
1396,6836204782	1962,0000000000	1,920000	0,0005099703	0,0152126084
1567,1047969978	1923,0000000000	2,860000	0,0005206693	0,0104221587
1758,3205020567	1983,0000000000	2,690000	0,0005048427	0,0107450193
1972,8680518851	1987,0000000000	4,200000	0,0005046264	0,0068717047
2213,5943621179	1984,0000000000	5,010000	0,0005059653	0,0057716078
2483,6937246350	1962,0000000000	5,970000	0,0005124633	0,0049004440
2786,7501938745	1943,0000000000	6,420000	0,0005179159	0,0046028197
3126,7851450567	1936,0000000000	7,470000	0,0005209502	0,0039730838
3508,3106353909	1931,0000000000	8,000000	0,0005229558	0,0037210236
3936,3892763324	1921,0000000000	8,930000	0,0005269495	0,0033535403
4416,7014113614	1912,0000000000	9,830000	0,0005308055	0,0030634718
4955,6204906890	1894,0000000000	10,540000	0,0005370444	0,0028863851
5560,2976430700	1883,0000000000	11,470000	0,0005418895	0,0026706290
6238,7565669362	1869,0000000000	12,640000	0,0005483348	0,0024450894
7000,0000000000	1849,0000000000	13,970000	0,0005573171	0,0022402731
7854,1291801137	1834,0000000000	15,650000	0,0005662485	0,0020212626
8812,4778825592	1817,0000000000	17,120000	0,0005758746	0,0018695871
9887,7628123593	1781,0000000000	17,850000	0,0005898777	0,0018317603
11094,2523472278	1738,0000000000	18,200000	0,0006056747	0,0018421699
12447,9558702724	1679,0000000000	18,930000	0,0006296467	0,0018359100
13966,8362047821	1647,0000000000	20,890000	0,0006498835	0,0017027684
15671,0479699783	1589,0000000000	21,680000	0,0006772330	0,0017035421
17583,2050205670	1523,0000000000	21,170000	0,0007041176	0,0018181465
19728,6805188512	1533,0000000000	25,660000	0,0007236860	0,0015063988
22135,9436211786	1509,0000000000	26,450000	0,0007401689	0,0014877991
24836,9372463503	1312,0000000000	23,290000	0,0008298120	0,0019277280
27867,5019387448	1337,0000000000	30,060000	0,0008641733	0,0014931788
31267,8514505674	1333,0000000000	33,450000	0,0008991096	0,0013609855
35083,1063539091	1300,0000000000	37,380000	0,0009680406	0,0012670609
39363,8927633245	1218,0000000000	37,830000	0,0010394818	0,0013386440
44167,0141136136	1185,0000000000	41,680000	0,0011298907	0,0012690531
49556,2049068897	1132,0000000000	41,400000	0,0011776819	0,0013358179
55602,9764306998	1061,0000000000	46,360000	0,0013657050	0,0013023626
62387,5656693623	994,6000000000	48,350000	0,0015128826	0,0013455628
70000,0000000001	928,9000000000	49,210000	0,0016478817	0,0014219115
78541,2918011376	868,0000000000	51,800000	0,0018629659	0,0014660096
88124,7788255919	807,5000000000	54,040000	0,0021089020	0,0015299587
98877,6281235930	749,9000000000	55,720000	0,0023675817	0,0016138440
110942,5234722780	694,2000000000	58,490000	0,0027561739	0,0016896473
124479,5587027240	640,8000000000	60,520000	0,0031710766	0,0017926479
139668,3620478210	588,9000000000	62,250000	0,0036469678	0,0019187626
156710,4796997840	539,1000000000	63,850000	0,0042088676	0,0020664594

frequency [Hz]	measurement 7	phase difference [°]	real admittance Y´ [S m^{-1}]	imaginary admittance Y´´ [S m^{-1}]
175832,0502056700	490,8000000000	64,620000	0,0047536066	0,0022551452
197286,8051885110	447,8000000000	66,340000	0,0055646472	0,0024380773
221359,4362117860	407,0000000000	67,590000	0,0064449054	0,0026577143
248369,3724635020	371,7000000000	69,240000	0,0075900958	0,0028771450
278675,0193874470	337,3000000000	70,410000	0,0088423308	0,0031468735
312678,5145056730	305,6000000000	71,420000	0,0102698025	0,0034521800
350831,0635390900	276,6000000000	72,330000	0,0119107795	0,0037943441
393638,9276332430	249,8000000000	73,160000	0,0138184388	0,0041825613
441670,1411361340	225,5000000000	73,910000	0,0160008603	0,0046153858
495562,0490688950	203,2000000000	74,580000	0,0185084474	0,0051050273
556029,7643069950	182,9000000000	75,170000	0,0213613084	0,0056558683
623875,6566936190	164,2000000000	75,630000	0,0245389138	0,0062868285
785412,9180113710	131,8000000000	76,200000	0,0318079212	0,0078127748
881247,7882559130	118,0000000000	76,220000	0,0355783947	0,0087257246
988776,2812359230	105,1000000000	76,250000	0,0400307640	0,0097954656

III.3 COMPLEX IMPEDANCE DATA FOR SAMPLE 17/08/00/10:

frequency [Hz]	measurement 1	phase difference [°]	real impedance Z´ [Ω m]	imaginary impedance Z´´ [Ω m]
785,412918011374	1313,496143958870	4,85000000000	1308,793114703990	111,052704146510
881,247788255917	1319,151670951160	5,02000000000	1314,091687845160	115,430355234186
988,776281235928	1329,177377892030	5,28000000000	1323,537520023870	122,314900927837
1109,425234722780	1332,005141388170	5,53000000000	1325,805825895310	128,361243008038
1244,795587027250	1329,434447300770	5,77000000000	1322,698848268760	133,655177447041
1396,683620478220	1327,892030848330	6,03000000000	1320,544841513560	139,493968122016
1567,104796997840	1326,221079691520	6,36000000000	1318,058848043810	146,912304833781
1758,320502056710	1323,264781491000	6,59000000000	1314,521720701390	151,862858325157
1972,868051885120	1321,593830334190	6,96000000000	1311,854992987280	160,145963894662
2213,594362117870	1323,007712082260	7,29000000000	1312,313317417000	167,878417788331
2483,693724635030	1317,737789203090	7,63000000000	1306,070743194690	174,963124299702
2786,750193874480	1311,182519280210	8,00000000000	1298,422181135320	182,481337132858
3126,785145056740	1303,727506426740	8,30000000000	1290,071989527840	188,201149968236
3508,310635390910	1296,015424164520	8,80000000000	1280,759224951870	198,272003502821
3936,389276332440	1285,861182519280	9,26000000000	1269,104221048900	206,914129110959
4416,701411361350	1278,663239074550	9,72000000000	1260,307510609540	215,881119280498
4955,620490688970	1271,593830334190	10,2200000000	1251,418384091280	225,616704395646
5560,297643069970	1258,997429305910	10,7100000000	1237,066168276490	233,969703817852
6238,756566936220	1245,758354755780	11,2000000000	1222,033080417010	241,969065812849
7000,000000000000	1233,933161953730	11,7600000000	1208,032800472020	251,491155217956
7854,129180113750	1220,565552699230	12,3300000000	1192,411863235790	260,641932256750
8812,477882559180	1206,683804627250	12,8900000000	1176,275546320480	269,187004660625
9887,762812359290	1191,259640102830	13,4900000000	1158,393560343210	277,891866547603
11094,252347227800	1174,935732647820	14,1300000000	1139,387259939250	286,828603421639
12447,955870272500	1158,097686375320	14,7700000000	1119,830672809890	295,244839788984
13966,836204782200	1139,588688946020	15,4100000000	1098,619383014100	302,816497634172
15671,047969978400	1120,694087403600	16,0900000000	1076,793743161450	310,596961076140
17583,205020567100	1102,185089974290	16,8100000000	1055,087660101460	318,750689510248
19728,680518851200	1079,948586118250	17,5000000000	1029,965272517560	324,746803012198
22135,943621178700	1058,354755784060	18,2500000000	1005,118586779720	331,438403931515
24836,937246350300	1039,845758354760	19,1000000000	982,601118168953	340,256144311178
27867,501938744900	1016,580976863750	19,8600000000	956,120359615868	345,355961942572
31267,851450567500	994,087403598972	20,6800000000	930,035727629119	351,060267372315
35083,106353909100	971,336760925450	21,5600000000	903,375493064975	356,942322588339
39363,892763324500	949,485861182519	22,4700000000	877,400684229042	362,893152181077
44167,014113613600	924,550128534704	23,3300000000	848,958122598449	366,146208839659
49556,204906889700	898,843187660668	24,1800000000	819,981518389530	368,170321323694
55602,976430699800	874,935732647815	24,9600000000	793,219018238046	369,210137143389
62387,565669362300	849,228791773779	26,0100000000	763,216795703499	372,410611467551
70000,000000000200	824,293059125964	27,0000000000	734,450493524422	374,221217844436
78541,291801137600	799,357326478149	27,7700000000	707,291389103750	372,439292091989
88124,778825591900	773,778920308483	29,0400000000	676,500233809390	375,607842263181
98877,628123593100	748,200514138818	30,0800000000	647,437678424819	375,004615856221
110942,523472278000	722,750642673522	31,1300000000	618,672028465200	373,648782521425

frequency [Hz]	measurement 1	phase difference [°]	real impedance Z´ [Ω m]	imaginary impedance Z´´ [Ω m]
124479,558702725000	697,172236503856	32,2200000000	589,812665956604	371,712451269731
139668,362047822000	671,593830334190	33,4000000000	560,678674235385	369,699468758882
156710,479699784000	645,886889460154	34,6800000000	531,140373081416	367,504800049534
175832,050205671000	618,251928020566	35,8300000000	501,252340979030	361,913715081632
197286,805188512000	591,902313624679	37,1800000000	471,592790590857	357,699019759596
221359,436211787000	564,524421593830	38,3300000000	442,842168986345	350,112319039644
248369,372463503000	538,046272493573	39,5400000000	414,930701446245	342,529275159884
278675,019387448000	512,210796915167	40,7300000000	388,149651097768	334,215123579337
312678,514505674000	486,760925449871	41,9400000000	362,074743776247	325,327647863166
350831,063539090000	462,210796915167	43,1400000000	337,268324007121	316,052050153738
393638,927633244000	437,660668380463	44,3900000000	312,750030366311	306,160544736100
441670,141136134000	414,010282776350	45,6400000000	289,461240196483	296,001190315964
495562,049068895000	390,874035989717	46,9300000000	266,924505138061	285,541276469255
556029,764306995000	368,380462724936	48,2100000000	245,489606050799	274,661643915676
623875,656693620000	346,658097686375	49,4900000000	225,182428584645	263,561587770786
699999,999999997000	321,208226221080	49,0300000000	210,604597864926	242,529231125333
785412,918011371000	305,269922879177	52,1200000000	187,438699985341	240,949080850009
881247,788255913000	284,575835475578	52,7400000000	172,291575442357	226,492867808710
988776,281235923000	266,838046272494	54,8600000000	153,585652204136	218,206302327755

frequency [Hz]	measurement 1	phase difference [°]	real admittance Y´ [S m-1]	imaginary admittance Y´´ [S m-1]
785,412918011374	1313,496143958870	4,850000000000	0,000764062699	0,009004733452
881,247788255917	1319,151670951160	5,020000000000	0,000760981908	0,008663232457
988,776281235928	1329,177377892030	5,280000000000	0,000755550927	0,008175618771
1109,425234722780	1332,005141388170	5,530000000000	0,000754258264	0,007790513527
1244,795587027250	1329,434447300770	5,770000000000	0,000756029992	0,007481939863
1396,683620478220	1327,892030848330	6,030000000000	0,000757263191	0,007168768754
1567,104796997840	1326,221079691520	6,360000000000	0,000758691466	0,006806781781
1758,320502056710	1323,264781491000	6,590000000000	0,000760732960	0,006584888570
1972,868051885120	1321,593830334190	6,960000000000	0,000762279372	0,006244303482
2213,594362117870	1323,007712082260	7,290000000000	0,000762013146	0,005956691832
2483,693724635030	1317,737789203090	7,630000000000	0,000765655310	0,005715490073
2786,750193874480	1311,182519280210	8,000000000000	0,000770165524	0,005480012453
3126,785145056740	1303,727506426740	8,300000000000	0,000775150541	0,005313463813
3508,310635390910	1296,015424164520	8,800000000000	0,000780786881	0,005043576412
3936,389276332440	1285,861182519280	9,260000000000	0,000787957351	0,004832922741
4416,701411361350	1278,663239074550	9,720000000000	0,000793457146	0,004632179059
4955,620490688970	1271,593830334190	10,220000000000	0,000799093263	0,004432295927
5560,297643069970	1258,997429305910	10,710000000000	0,000808364197	0,004274057639
6238,756566936220	1245,758354755780	11,200000000000	0,000818308453	0,004132759684
7000,000000000000	1233,933161953730	11,760000000000	0,000827792093	0,003976282980
7854,129180113750	1220,565552699230	12,330000000000	0,000838636406	0,003836681195
8812,477882559180	1206,683804627250	12,890000000000	0,000850140941	0,003714889585
9887,762812359290	1191,259640102830	13,490000000000	0,000863264467	0,003598522017
11094,252347227800	1174,935732647820	14,130000000000	0,000877664720	0,003486402639
12447,955870272500	1158,097686375320	14,770000000000	0,000892992150	0,003387019400
13966,836204782200	1139,588688946020	15,410000000000	0,000910233349	0,003302329985
15671,047969978400	1120,694087403600	16,090000000000	0,000928682959	0,003219606517
17583,205020567100	1102,185089974290	16,810000000000	0,000947788547	0,003137248116
19728,680518851200	1079,948586118250	17,500000000000	0,000970906521	0,003079322077
22135,943621178700	1058,354755784060	18,250000000000	0,000994907480	0,003017151869
24836,937246350300	1039,845758354760	19,100000000000	0,001017706963	0,002938962357
27867,501938744900	1016,580976863750	19,860000000000	0,001045893427	0,002895563159
31267,851450567500	994,087403598972	20,680000000000	0,001075227510	0,002848513754
35083,106353909100	971,336760925450	21,560000000000	0,001106959407	0,002801573074
39363,892763324500	949,485861182519	22,470000000000	0,001139730135	0,002755632048
44167,014113613600	924,550128534704	23,330000000000	0,001177914403	0,002731149404
49556,204906889700	898,843187660668	24,180000000000	0,001219539682	0,002716134197
55602,976430699800	874,935732647815	24,960000000000	0,001260685860	0,002708484680
62387,565669362300	849,228791773779	26,010000000000	0,001310243702	0,002685208126
70000,000000000200	824,293059125964	27,000000000000	0,001361562159	0,002672216198
78541,291801137600	799,357326478149	27,770000000000	0,001413844443	0,002685001344
88124,778825591900	773,778920308483	29,040000000000	0,001478196089	0,002662351228
98877,628123593100	748,200514138818	30,080000000000	0,001544550207	0,002666633843
110942,523472278000	722,750642673522	31,130000000000	0,001616365302	0,002676310072
124479,558702725000	697,172236503856	32,220000000000	0,001695453587	0,002690251555
139668,362047822000	671,593830334190	33,400000000000	0,001783552766	0,002704899748
156710,479699784000	645,886889460154	34,680000000000	0,001882741457	0,002721052895

frequency [Hz]	measurement 1	phase difference [°]	real admittance Y´ [S m-1]	imaginary admittance Y´´ [S m-1]
175832,050205671000	618,251928020566	35,830000000000	0,001995003152	0,002763089539
197286,805188512000	591,902313624679	37,180000000000	0,002120473468	0,002795646465
221359,436211787000	564,524421593830	38,330000000000	0,002258140868	0,002856226261
248369,372463503000	538,046272493573	39,540000000000	0,002410040994	0,002919458489
278675,019387448000	512,210796915167	40,730000000000	0,002576325902	0,002992084826
312678,514505674000	486,760925449871	41,940000000000	0,002761860685	0,003073824209
350831,063539090000	462,210796915167	43,140000000000	0,002964998278	0,003164035796
393638,927633244000	437,660668380463	44,390000000000	0,003197441736	0,003266260193
441670,141136134000	414,010282776350	45,640000000000	0,003454693966	0,003378364793
495562,049068895000	390,874035989717	46,930000000000	0,003746377649	0,003502120647
556029,764306995000	368,380462724936	48,210000000000	0,004073492219	0,003640843278
623875,656693620000	346,658097686375	49,490000000000	0,004440843836	0,003794179601
699999,999999997000	321,208226221080	49,030000000000	0,004748234417	0,004123214325
785412,918011371000	305,269922879177	52,120000000000	0,005335077548	0,004150254471
881247,788255913000	284,575835475578	52,740000000000	0,005804114319	0,004415150065
988776,281235923000	266,838046272494	54,860000000000	0,006511024862	0,004582819054

frequency [Hz]	measurement 2	phase difference [°]	real impedance Z´ [Ω m]	imaginary impedance Z´´ [Ω m]
785,412918011374	1120,000000000000	6,150000000000	1113,554212549080	119,987564831539
881,247788255917	1115,566037735850	6,460000000000	1108,482912149740	125,511824230595
988,776281235928	1109,905660377360	6,730000000000	1102,257771898030	130,070670130143
1109,425234722780	1104,056603773580	7,110000000000	1095,566795180010	136,654241189414
1244,795587027250	1096,132075471700	7,490000000000	1086,779468175390	142,884269359171
1396,683620478220	1090,943396226420	7,850000000000	1080,720197361480	149,001170414865
1567,104796997840	1085,566037735850	8,200000000000	1074,467461231690	154,833126429181
1758,320502056710	1078,207547169810	8,600000000000	1066,084592357190	161,230135869637
1972,868051885120	1070,849056603770	9,000000000000	1057,665127744850	167,517699308647
2213,594362117870	1061,037735849060	9,440000000000	1046,669054777060	174,025764379269
2483,693724635030	1050,377358490570	9,900000000000	1034,736531830880	180,590434199147
2786,750193874480	1041,226415094340	10,360000000000	1024,251568705240	187,246285664298
3126,785145056740	1030,849056603770	10,830000000000	1012,488607619700	193,692015687784
3508,310635390910	1018,679245283020	11,320000000000	998,862063692241	199,954951143651
3936,389276332440	1006,981132075470	11,870000000000	985,448672490227	207,127772747271
4416,701411361350	995,188679245283	12,400000000000	971,973194730862	213,702166630693
4955,620490688970	984,433962264151	12,990000000000	959,241619200057	221,282041868626
5560,297643069970	972,169811320755	13,640000000000	944,751320732405	229,257680390010
6238,756566936220	957,830188679245	14,160000000000	928,727831098483	234,314502514092
7000,000000000000	943,018867924528	14,780000000000	911,816728388951	240,571900045971
7854,129180113750	927,547169811321	15,370000000000	894,372811703016	245,847566413486
8812,477882559180	912,264150943396	16,010000000000	876,880684507625	251,607126755014
9887,762812359290	895,660377358491	16,610000000000	858,286886162258	256,029554176565
11094,252347227800	879,339622641509	17,300000000000	839,559001147695	261,493509554627
12447,955870272500	862,169811320755	17,970000000000	820,111604671752	265,995750784838
13966,836204782200	843,867924528302	18,620000000000	799,697357963757	269,438693794137
15671,047969978400	827,641509433962	19,310000000000	781,081089243232	273,683759409895
17583,205020567100	810,377358490566	20,100000000000	761,020719386184	278,494035517966
19728,680518851200	789,433962264151	20,720000000000	738,373837649655	279,302804587778
22135,943621178700	768,113207547170	21,380000000000	715,254057081823	280,017023476062
24836,937246350300	752,075471698113	22,290000000000	695,877332924980	285,258221005383
27867,501938744900	732,830188679245	23,060000000000	674,273521521137	287,045821455638
31267,851450567500	711,792452830189	23,830000000000	651,110898180718	287,581456593285
35083,106353909100	692,735849056604	24,670000000000	629,507664380235	289,141932370099
39363,892763324500	672,735849056604	25,500000000000	607,201477613100	289,620248239618
44167,014113613600	653,113207547170	26,320000000000	585,406081244990	289,580009520576
49556,204906889700	632,924528301887	26,980000000000	564,040150859467	287,144853244135
55602,976430699800	611,886792452830	28,060000000000	539,962852740507	287,829054194580
62387,565669362300	591,415094339623	28,830000000000	518,111744937934	285,187716373118
70000,000000000200	570,660377358491	29,540000000000	496,481209234013	281,353292435806
78541,291801137600	550,377358490566	30,500000000000	474,221181322251	279,337623538938
88124,778825591900	530,849056603774	31,500000000000	452,623226869857	277,367870156287
98877,628123593100	511,415094339623	32,400000000000	431,802045674191	274,029910903881
110942,523472278000	492,075471698113	33,320000000000	411,185972678059	270,304209585642
124479,558702725000	473,113207547170	34,350000000000	390,605202540951	266,952585496965
139668,362047822000	454,150943396226	35,410000000000	370,145135468149	263,145697431951
156710,479699784000	434,716981132075	36,550000000000	349,224441437292	258,884420518880

frequency [Hz]	measurement 2	phase difference [°]	real impedance Z´ [Ω m]	imaginary impedance Z´´ [Ω m]
175832,050205671000	413,962264150943	37,530000000000	328,286350884117	252,176184371494
197286,805188512000	394,811320754717	38,700000000000	308,122759878388	246,852878940087
221359,436211787000	376,320754716981	39,550000000000	290,169345798018	239,622747647022
248369,372463503000	358,018867924528	40,680000000000	271,507874388745	233,368772407248
278675,019387448000	343,396226415094	41,250000000000	258,178952756932	226,416864807948
312678,514505674000	324,150943396226	42,560000000000	238,759684127059	219,243351872321
350831,063539090000	306,226415094340	43,830000000000	220,911038834624	212,068220680371
393638,927633244000	290,754716981132	44,780000000000	206,382541226660	204,803691674745
441670,141136134000	275,188679245283	45,860000000000	191,645241629227	197,486481931393
495562,049068895000	261,037735849057	46,930000000000	178,260416523810	190,693270562860
556029,764306995000	246,037735849057	48,070000000000	164,407873324019	183,042668934879
623875,656693620000	232,169811320755	49,180000000000	151,765877909497	175,698433661415
699999,999999997000	212,924528301887	47,680000000000	143,355836094424	157,435570981432
785412,918011371000	204,433962264151	51,850000000000	126,283431772419	160,766102729403
881247,788255913000	190,283018867925	52,010000000000	117,123751990654	149,965509331722
988776,281235923000	179,056603773585	54,550000000000	103,851448743970	145,863442811107

frequency [Hz]	measurement 2	phase difference [°]	real admittance Y´ [S m-1]	imaginary admittance Y´´ [S m-1]
785,412918011374	1120,000000000000	6,150000000000	0,000898025430	0,008334196976
881,247788255917	1115,566037735850	6,460000000000	0,000902133889	0,007967376828
988,776281235928	1109,905660377360	6,730000000000	0,000907228804	0,007688128300
1109,425234722780	1104,056603773580	7,110000000000	0,000912769540	0,007317738486
1244,795587027250	1096,132075471700	7,490000000000	0,000920149883	0,006998671054
1396,683620478220	1090,943396226420	7,850000000000	0,000925308884	0,006711356677
1567,104796997840	1085,566037735850	8,200000000000	0,000930693610	0,006458566219
1758,320502056710	1078,207547169810	8,600000000000	0,000938011868	0,006202314441
1972,868051885120	1070,849056603770	9,000000000000	0,000945478842	0,005969518470
2213,594362117870	1061,037735849060	9,440000000000	0,000955411833	0,005746275579
2483,693724635030	1050,377358490570	9,900000000000	0,000966429588	0,005537391858
2786,750193874480	1041,226415094340	10,360000000000	0,000976322644	0,005340559875
3126,785145056740	1030,849056603770	10,830000000000	0,000987665434	0,005162835424
3508,310635390910	1018,679245283020	11,320000000000	0,001001139233	0,005001126475
3936,389276332440	1006,981132075470	11,870000000000	0,001014766195	0,004827937783
4416,701411361350	995,188679245283	12,400000000000	0,001028834957	0,004679409740
4955,620490688970	984,433962264151	12,990000000000	0,001042490213	0,004519119543
5560,297643069970	972,169811320755	13,640000000000	0,001058479600	0,004361904030
6238,756566936220	957,830188679245	14,160000000000	0,001076741718	0,004267768274
7000,000000000000	943,018867924528	14,780000000000	0,001096711619	0,004156761450
7854,129180113750	927,547169811321	15,370000000000	0,001118101967	0,004067561109
8812,477882559180	912,264150943396	16,010000000000	0,001140406007	0,003974450219
9887,762812359290	895,660377358491	16,610000000000	0,001165111592	0,003905799091
11094,252347227800	879,339622641509	17,300000000000	0,001191101517	0,003824186695
12447,955870272500	862,169811320755	17,970000000000	0,001219346238	0,003759458552
13966,836204782200	843,867924528302	18,620000000000	0,001250473057	0,003711419418
15671,047969978400	827,641509433962	19,310000000000	0,001280276803	0,003653852177
17583,205020567100	810,377358490566	20,100000000000	0,001314024670	0,003590741174
19728,680518851200	789,433962264151	20,720000000000	0,001354327509	0,003580343568
22135,943621178700	768,113207547170	21,380000000000	0,001398104618	0,003571211448
24836,937246350300	752,075471698113	22,290000000000	0,001437034881	0,003505595725
27867,501938744900	732,830188679245	23,060000000000	0,001483077665	0,003483764351
31267,851450567500	711,792452830189	23,830000000000	0,001535836680	0,003477275663
35083,106353909100	692,735849056604	24,670000000000	0,001588543010	0,003458509085
39363,892763324500	672,735849056604	25,500000000000	0,001646899813	0,003452797262
44167,014113613600	653,113207547170	26,320000000000	0,001708215941	0,003453277046
49556,204906889700	632,924528301887	26,980000000000	0,001772923432	0,003482562855
55602,976430699800	611,886792452830	28,060000000000	0,001851979252	0,003474284425
62387,565669362300	591,415094339623	28,830000000000	0,001930085565	0,003506462385
70000,000000000200	570,660377358491	29,540000000000	0,002014174920	0,003554250215
78541,291801137600	550,377358490566	30,500000000000	0,002108720655	0,003579897285
88124,778825591900	530,849056603774	31,500000000000	0,002209343093	0,003605320254
98877,628123593100	511,415094339623	32,400000000000	0,002315876013	0,003649236672
110942,523472278000	492,075471698113	33,320000000000	0,002431989578	0,003699535429
124479,558702725000	473,113207547170	34,350000000000	0,002560129751	0,003745983573
139668,362047822000	454,150943396226	35,410000000000	0,002701642962	0,003800176137
156710,479699784000	434,716981132075	36,550000000000	0,002863488008	0,003862727614

frequency [Hz]	measurement 2	phase difference [°]	real admittance Y´ [S m-1]	imaginary admittance Y´´ [S m-1]
175832,050205671000	413,962264150943	37,530000000000	0,003046121160	0,003965481524
197286,805188512000	394,811320754717	38,700000000000	0,003245459701	0,004050995898
221359,436211787000	376,320754716981	39,550000000000	0,003446263413	0,004173226498
248369,372463503000	358,018867924528	40,680000000000	0,003683134429	0,004285063463
278675,019387448000	343,396226415094	41,250000000000	0,003873282424	0,004416632131
312678,514505674000	324,150943396226	42,560000000000	0,004188311790	0,004561141724
350831,063539090000	306,226415094340	43,830000000000	0,004526709056	0,004715463716
393638,927633244000	290,754716981132	44,780000000000	0,004845371096	0,004882724485
441670,141136134000	275,188679245283	45,860000000000	0,005217974584	0,005063637725
495562,049068895000	261,037735849057	46,930000000000	0,005609770355	0,005244023541
556029,764306995000	246,037735849057	48,070000000000	0,006082433765	0,005463207053
623875,656693620000	232,169811320755	49,180000000000	0,006589096401	0,005691570375
699999,999999997000	212,924528301887	47,680000000000	0,006975649037	0,006351804702
785412,918011371000	204,433962264151	51,850000000000	0,007918695160	0,006220216719
881247,788255913000	190,283018867925	52,010000000000	0,008537977848	0,006668199938
988776,281235923000	179,056603773585	54,550000000000	0,009629138660	0,006855727389

frequency [Hz]	measurement 3	phase difference [°]	real impedance Z´ [Ω m]	imaginary impedance Z´´ [Ω m]
785,412918011374	1851,851851851850	9,690000000000	1825,431224110850	311,698776462586
881,247788255917	1838,383838383840	10,100000000000	1809,894734902500	322,391355037795
988,776281235928	1818,181818181820	10,500000000000	1787,736195570830	331,337319076632
1109,425234722780	1804,713804713800	11,000000000000	1771,556129050330	344,355628019622
1244,795587027250	1784,511784511780	11,400000000000	1749,305463129670	352,721853201807
1396,683620478220	1764,309764309760	11,900000000000	1726,392956879900	363,808057736814
1567,104796997840	1750,841750841750	12,500000000000	1709,339810445670	378,951512618900
1758,320502056710	1723,905723905720	13,000000000000	1679,722131885650	387,794410182016
1972,868051885120	1696,969696969700	13,500000000000	1650,082289159700	396,149708361537
2213,594362117870	1676,767676767680	14,000000000000	1626,960510725410	405,646814843888
2483,693724635030	1649,831649831650	14,600000000000	1596,557217293490	415,872005182241
2786,750193874480	1616,161616161620	15,200000000000	1559,622617328990	423,740086692308
3126,785145056740	1589,225589225590	15,700000000000	1529,934357957230	430,045153200699
3508,310635390910	1562,289562289560	16,300000000000	1499,493789483120	438,482669829109
3936,389276332440	1528,619528619530	16,900000000000	1462,603929838900	444,373050146824
4416,701411361350	1494,949494949490	17,500000000000	1425,758673845830	449,539983097296
4955,620490688970	1468,013468013470	18,100000000000	1395,369895588260	456,077182892253
5560,297643069970	1434,343434343430	18,700000000000	1358,624842827630	459,869138011777
6238,756566936220	1400,673400673400	19,300000000000	1321,956888412870	462,942718413134
7000,000000000000	1367,003367003370	19,900000000000	1285,377035576540	465,299991200332
7854,129180113750	1333,333333333330	20,500000000000	1248,896252331190	466,943175012622
8812,477882559180	1299,663299663300	21,100000000000	1212,525469503830	467,874639509562
9887,762812359290	1265,993265993270	21,800000000000	1175,456804401430	470,149179013093
11094,252347227800	1232,323232323230	22,400000000000	1139,339556572750	469,601877926600
12447,955870272500	1198,653198653200	23,000000000000	1103,366086966560	468,351116977042
13966,836204782200	1164,983164983160	23,600000000000	1067,547152958030	466,399883046078
15671,047969978400	1131,313131313130	24,300000000000	1031,082494779480	465,551597613860
17583,205020567100	1097,643097643100	25,000000000000	994,802486780971	463,884017937604
19728,680518851200	1063,973063973060	25,600000000000	959,525516309815	459,727598051939
22135,943621178700	1030,303030303030	26,300000000000	923,652685849605	456,497590546124
24836,937246350300	1003,367003367000	27,000000000000	894,006546155329	455,519087280756
27867,501938744900	969,696969696970	27,700000000000	858,563515883070	450,755923126904
31267,851450567500	942,760942760943	28,100000000000	831,634755841572	444,051605190016
35083,106353909100	902,356902356902	29,200000000000	787,687261644138	440,223530805321
39363,892763324500	875,420875420875	30,000000000000	758,136717117690	437,710437710437
44167,014113613600	841,750841750842	30,800000000000	723,030216271603	431,012512517316
49556,204906889700	808,080808080808	31,500000000000	689,002153013408	422,221062396726
55602,976430699800	781,144781144781	32,400000000000	659,542352580698	418,558304495378
62387,565669362300	754,208754208754	33,200000000000	631,094970420227	412,976976640846
70000,000000000200	722,020202020202	34,120000000000	597,734954366093	405,001353644970
78541,291801137600	693,265993265993	35,030000000000	567,681973423671	397,938329982034
88124,778825591900	665,185185185185	35,970000000000	538,350765256814	390,704215663527
98877,628123593100	638,249158249158	36,930000000000	510,197337868765	383,484894666510
110942,523472278000	612,659932659933	38,010000000000	482,716775617946	377,275373731029
124479,558702725000	587,609427609428	39,240000000000	455,105299885128	371,704190764574
139668,362047822000	562,356902356902	40,630000000000	426,789781851992	366,190889749021
156710,479699784000	536,026936026936	42,250000000000	396,776854868363	360,406719675418

frequency [Hz]	measurement 3	phase difference [°]	real impedance Z´ [Ω m]	imaginary impedance Z´´ [Ω m]
175832,050205671000	508,148148148148	43,680000000000	367,496940745425	350,942358527929
197286,805188512000	480,740740740741	45,220000000000	338,627278224155	341,237785496356
221359,436211787000	453,670033670034	46,620000000000	311,595934287521	329,733943029311
248369,372463503000	428,215488215488	48,110000000000	285,920611297477	318,775639569440
278675,019387448000	403,973063973064	49,590000000000	261,876671743586	307,595262012092
312678,514505674000	380,606060606061	51,170000000000	238,644485768427	296,495839401479
350831,063539090000	357,845117845118	52,850000000000	216,104019769710	285,223037297059
393638,927633244000	335,286195286195	54,610000000000	194,177277277758	273,334991793018
441670,141136134000	313,400673400673	56,480000000000	173,068637332648	261,279981743370
495562,049068895000	291,784511784512	58,460000000000	152,630637673743	248,680698407883
556029,764306995000	270,976430976431	60,440000000000	133,682082864558	235,706017881848
623875,656693620000	250,505050505050	62,380000000000	116,135481689805	221,957946965669
699999,999999997000	229,629629629630	63,920000000000	100,951080305981	206,248990758492
785412,918011371000	211,986531986532	66,160000000000	85,681556030284	193,899357141550
881247,788255913000	193,535353535354	67,700000000000	73,438181985614	179,060789942138
988776,281235923000	175,892255892256	69,700000000000		

frequency [Hz]	measurement 3	phase difference [°]	real admittance Y´ [S m-1]	imaginary admittance Y´´ [S m-1]
785,412918011374	1851,851851851850	9,690000000000	0,000547816	0,003208226
881,247788255917	1838,383838383840	10,100000000000	0,000552518	0,00310182
988,776281235928	1818,181818181820	10,500000000000	0,000559367	0,003018072
1109,425234722780	1804,713804713800	11,000000000000	0,000564475	0,002903975
1244,795587027250	1784,511784511780	11,400000000000	0,000571655	0,002835095
1396,683620478220	1764,309764309760	11,900000000000	0,000579242	0,002748702
1567,104796997840	1750,841750841750	12,500000000000	0,000585021	0,00263886
1758,320502056710	1723,905723905720	13,000000000000	0,000595337	0,002578686
1972,868051885120	1696,969696969700	13,500000000000	0,00060603	0,002524298
2213,594362117870	1676,767676767680	14,000000000000	0,000614643	0,002465199
2483,693724635030	1649,831649831650	14,600000000000	0,000626348	0,002404586
2786,750193874480	1616,161616161620	15,200000000000	0,000641181	0,002359937
3126,785145056740	1589,225589225590	15,700000000000	0,000653623	0,002325337
3508,310635390910	1562,289562289560	16,300000000000	0,000666892	0,002280592
3936,389276332440	1528,619528619530	16,900000000000	0,000683712	0,002250361
4416,701411361350	1494,949494949490	17,500000000000	0,000701381	0,002224496
4955,620490688970	1468,013468013470	18,100000000000	0,000716656	0,002192611
5560,297643069970	1434,343434343430	18,700000000000	0,000736038	0,002174532
6238,756566936220	1400,673400673400	19,300000000000	0,000756454	0,002160094
7000,000000000000	1367,003367003370	19,900000000000	0,000777982	0,002149151
7854,129180113750	1333,333333333330	20,500000000000	0,000800707	0,002141588
8812,477882559180	1299,663299663300	21,100000000000	0,000824725	0,002137325
9887,762812359290	1265,993265993270	21,800000000000	0,000850733	0,002126984
11094,252347227800	1232,323232323230	22,400000000000	0,000877701	0,002129463
12447,955870272500	1198,653198653200	23,000000000000	0,000906318	0,00213515
13966,836204782200	1164,983164983160	23,600000000000	0,000936727	0,002144083
15671,047969978400	1131,313131313130	24,300000000000	0,000969855	0,00214799
17583,205020567100	1097,643097643100	25,000000000000	0,001005225	0,002155711
19728,680518851200	1063,973063973060	25,600000000000	0,001042182	0,002175201
22135,943621178700	1030,303030303030	26,300000000000	0,001082658	0,002190592
24836,937246350300	1003,367003367000	27,000000000000	0,00111856	0,002195298
27867,501938744900	969,696969696970	27,700000000000	0,001164736	0,002218496
31267,851450567500	942,760942760943	28,100000000000	0,001202451	0,002251991
35083,106353909100	902,356902356902	29,200000000000	0,001269539	0,002271573
39363,892763324500	875,420875420875	30,000000000000	0,001319023	0,002284615
44167,014113613600	841,750841750842	30,800000000000	0,001383068	0,002320118
49556,204906889700	808,080808080808	31,500000000000	0,001451374	0,002368428
55602,976430699800	781,144781144781	32,400000000000	0,001516203	0,002389153
62387,565669362300	754,208754208754	33,200000000000	0,001584548	0,002421442
70000,000000000200	722,020202020202	34,120000000000	0,001672982	0,002469128
78541,291801137600	693,265993265993	35,030000000000	0,00176155	0,002512952
88124,778825591900	665,185185185185	35,970000000000	0,001857525	0,002559481
98877,628123593100	638,249158249158	36,930000000000	0,001960026	0,002607665
110942,523472278000	612,659932659933	38,010000000000	0,002071608	0,002650584
124479,558702725000	587,609427609428	39,240000000000	0,002197294	0,002690311
139668,362047822000	562,356902356902	40,630000000000	0,002343074	0,002730816
156710,479699784000	536,026936026936	42,250000000000	0,002520308	0,002774643

frequency [Hz]	measurement 3	phase difference [°]	real admittance Y´ [S m-1]	imaginary admittance Y´´ [S m-1]
175832,050205671000	508,148148148148	43,680000000000	0,002721111	0,002849471
197286,805188512000	480,740740740741	45,220000000000	0,002953099	0,002930508
221359,436211787000	453,670033670034	46,620000000000	0,003209284	0,003032748
248369,372463503000	428,215488215488	48,110000000000	0,003497474	0,003137003
278675,019387448000	403,973063973064	49,590000000000	0,003818591	0,003251025
312678,514505674000	380,606060606061	51,170000000000	0,004190334	0,003372729
350831,063539090000	357,845117845118	52,850000000000	0,004627401	0,003506028
393638,927633244000	335,286195286195	54,610000000000	0,005149933	0,003658514
441670,141136134000	313,400673400673	56,480000000000	0,005778054	0,003827312
495562,049068895000	291,784511784512	58,460000000000	0,006551765	0,004021221
556029,764306995000	270,976430976431	60,440000000000	0,007480434	0,004242573
623875,656693620000	250,505050505050	62,380000000000	0,008610633	0,004505358
699999,999999997000	229,629629629630	63,920000000000	0,009905788	0,004848509
785412,918011371000	211,986531986532	66,160000000000	0,011671123	0,005157315
881247,788255913000	193,535353535354	67,700000000000	0,013616895	0,005584696
988776,281235923000	175,892255892256	69,700000000000		

III.4 COMPLEX IMPEDANCE DATA FOR SAMPLE 17/08/00/11 CORE 1:

frequency [Hz]	real impedance at 0 bar Z´ [Ω m]	imaginary impedance at 0 bar Z´´ [Ω m]	real admittance at 0 bar Y´ [S m-1]	imaginary admittance at 0 bar Y´´ [S m-1]
785,412900	562,322400	91,834880	0,001778	0,010889
881,247800	555,725800	90,459010	0,001799	0,011055
988,776300	549,518700	89,547050	0,001820	0,011167
1109,425000	543,312000	88,632920	0,001841	0,011282
1244,796000	537,074800	87,904000	0,001862	0,011376
1396,684000	530,989700	87,193380	0,001883	0,011469
1567,105000	524,920400	86,384850	0,001905	0,011576
1758,320000	518,987800	85,687520	0,001927	0,011670
1972,868000	513,192300	85,098530	0,001949	0,011751
2213,594000	507,383000	84,590010	0,001971	0,011822
2483,694000	501,560300	84,158920	0,001994	0,011882
2786,750000	495,890000	83,741220	0,002017	0,011942
3126,785000	490,192000	83,482750	0,002040	0,011979
3508,311000	484,481200	83,293070	0,002064	0,012006
3936,389000	478,864800	83,445990	0,002088	0,011984
4416,701000	473,114200	83,464740	0,002114	0,011981
4955,620000	467,802800	83,622060	0,002138	0,011959
5560,297000	462,162900	83,862450	0,002164	0,011924
6238,757000	456,495600	84,233180	0,002191	0,011872
7000,000000	450,800700	84,728320	0,002218	0,011802
7854,129000	444,942500	85,235510	0,002247	0,011732
8812,479000	439,206500	85,885410	0,002277	0,011643
9887,763000	433,441900	86,643810	0,002307	0,011542
11094,250000	427,498400	87,473970	0,002339	0,011432
12447,960000	421,510100	88,472630	0,002372	0,011303
13966,840000	415,641200	89,590190	0,002406	0,011162
15671,050000	409,458000	90,652210	0,002442	0,011031
17583,200000	403,212100	91,929430	0,002480	0,010878
19728,680000	396,785100	93,235310	0,002520	0,010726
22135,940000	390,309200	94,664350	0,002562	0,010564
24836,940000	383,783200	96,206460	0,002606	0,010394
27867,500000	377,205700	97,851480	0,002651	0,010220
31267,850000	370,410200	99,614070	0,002700	0,010039
35083,110000	363,560700	101,453900	0,002751	0,009857
39363,890000	356,454700	103,504300	0,002805	0,009661
44167,020000	348,998200	105,511500	0,002865	0,009478
49556,210000	341,574800	107,771000	0,002928	0,009279
55602,980000	333,887900	110,169100	0,002995	0,009077
62387,570000	326,060300	112,783100	0,003067	0,008867
70000,000000	317,839300	115,369300	0,003146	0,008668
78541,290000	309,451800	118,164400	0,003232	0,008463
88124,780000	300,466200	120,962600	0,003328	0,008267
98877,620000	291,211900	123,722000	0,003434	0,008083
110942,500000	281,508300	126,442400	0,003552	0,007909

frequency [Hz]	real impedance at 0 bar Z´ [Ω m]	imaginary impedance at 0 bar Z´´ [Ω m]	real admittance at 0 bar Y´ [S m-1]	imaginary admittance at 0 bar Y´´ [S m-1]
124479,600000	271,477100	129,180400	0,003684	0,007741
139668,400000	260,917500	131,607100	0,003833	0,007598
156710,500000	249,914200	133,866500	0,004001	0,007470
175832,000000	238,506900	135,848600	0,004193	0,007361
197286,800000	226,812900	137,331300	0,004409	0,007282
221359,400000	214,636400	138,341600	0,004659	0,007228
248369,400000	202,365600	138,835300	0,004942	0,007203
278675,000000	189,882700	138,727300	0,005266	0,007208
312678,500000	177,301800	137,880500	0,005640	0,007253
350831,100000	164,737000	136,427200	0,006070	0,007330
393638,900000	152,345000	134,211000	0,006564	0,007451
441670,100000	140,249300	131,372200	0,007130	0,007612
495562,000000	128,521000	127,882200	0,007781	0,007820
556029,800000	117,181200	123,770100	0,008534	0,008079
623875,700000	106,495400	119,173700	0,009390	0,008391
700000,000000	96,365100	114,173000	0,010377	0,008759
785412,900000	86,921900	108,822600	0,011505	0,009189
881247,800000	78,163280	103,249900	0,012794	0,009685
988776,300000	70,098200	97,489000	0,014266	0,010258

frequency [Hz]	real impedance at 75 bar Z´ [Ω m]	imaginary impedance at 75 bar Z´´ [Ω m]	real admittance at 75 bar Y´ [S m-1]	imaginary admittance at 75 bar Y´´ [S m-1]
785,412900	550,811300	94,795620	0,001816	0,010549
881,247800	544,209500	93,463950	0,001838	0,010699
988,776300	537,574600	92,324460	0,001860	0,010831
1109,425000	531,058700	91,396160	0,001883	0,010941
1244,796000	524,694200	90,489320	0,001906	0,011051
1396,684000	518,346100	89,487630	0,001929	0,011175
1567,105000	512,133700	88,599130	0,001953	0,011287
1758,320000	506,072600	87,732430	0,001976	0,011398
1972,868000	499,997200	86,948740	0,002000	0,011501
2213,594000	494,058300	86,271190	0,002024	0,011591
2483,694000	488,090800	85,755710	0,002049	0,011661
2786,750000	482,441100	85,196930	0,002073	0,011738
3126,785000	476,461900	84,741110	0,002099	0,011801
3508,311000	470,469800	84,352890	0,002126	0,011855
3936,389000	464,887400	84,273060	0,002151	0,011866
4416,701000	459,020700	84,036880	0,002179	0,011900
4955,620000	453,413300	84,073430	0,002205	0,011894
5560,297000	447,657700	84,056740	0,002234	0,011897
6238,757000	442,025500	84,197180	0,002262	0,011877
7000,000000	436,230700	84,355820	0,002292	0,011855
7854,129000	430,394300	84,708020	0,002323	0,011805
8812,479000	424,545500	85,096530	0,002355	0,011751
9887,763000	418,819500	85,621990	0,002388	0,011679
11094,250000	412,915800	86,217620	0,002422	0,011599
12447,960000	406,999500	86,836330	0,002457	0,011516
13966,840000	401,024700	87,684960	0,002494	0,011404
15671,050000	395,036300	88,544300	0,002531	0,011294
17583,200000	389,003400	89,546980	0,002571	0,011167
19728,680000	382,791600	90,581560	0,002612	0,011040
22135,940000	376,550000	91,675060	0,002656	0,010908
24836,940000	370,245700	92,950190	0,002701	0,010758
27867,500000	363,745300	94,291960	0,002749	0,010605
31267,850000	357,344100	95,766050	0,002798	0,010442
35083,110000	350,728400	97,345570	0,002851	0,010273
39363,890000	344,026900	99,115170	0,002907	0,010089
44167,020000	336,978900	100,852100	0,002968	0,009916
49556,210000	329,953000	102,903000	0,003031	0,009718
55602,980000	322,706600	104,983700	0,003099	0,009525
62387,570000	315,183900	107,238800	0,003173	0,009325
70000,000000	307,545300	109,633200	0,003252	0,009121
78541,290000	299,481400	112,088200	0,003339	0,008922
88124,780000	291,115500	114,668100	0,003435	0,008721
98877,620000	282,486900	117,232700	0,003540	0,008530
110942,500000	273,395000	119,829900	0,003658	0,008345
124479,600000	264,025000	122,373700	0,003788	0,008172
139668,400000	254,085000	124,732100	0,003936	0,008017

frequency [Hz]	real impedance at 75 bar Z´ [Ω m]	imaginary impedance at 75 bar Z´´ [Ω m]	real admittance at 75 bar Y´ [S m-1]	imaginary admittance at 75 bar Y´´ [S m-1]
156710,500000	243,884400	126,936800	0,004100	0,007878
175832,000000	233,254600	128,951200	0,004287	0,007755
197286,800000	222,172500	130,475900	0,004501	0,007664
221359,400000	210,753500	131,610400	0,004745	0,007598
248369,400000	199,200200	132,313000	0,005020	0,007558
278675,000000	187,391200	132,494400	0,005336	0,007547
312678,500000	175,433700	132,012900	0,005700	0,007575
350831,100000	163,465800	130,962500	0,006117	0,007636
393638,900000	151,636500	129,187400	0,006595	0,007741
441670,100000	139,934800	126,745600	0,007146	0,007890
495562,000000	128,528200	123,718800	0,007780	0,008083
556029,800000	117,535600	120,052100	0,008508	0,008330
623875,700000	107,044700	115,946500	0,009342	0,008625
700000,000000	97,079630	111,383300	0,010301	0,008978
785412,900000	87,726700	106,475400	0,011399	0,009392
881247,800000	79,027740	101,273300	0,012654	0,009874
988776,300000	70,960200	95,837270	0,014092	0,010434

frequency [Hz]	real impedance at 100 bar Z´ [Ω m]	imaginary impedance at 100 bar Z´´ [Ω m]	real admittance at 100 bar Y´ [S m-1]	imaginary admittance at 100 bar Y´´ [S m-1]
785,412900	536,058900	98,237580	0,001865	0,010179
881,247800	529,002600	96,849060	0,001890	0,010325
988,776300	522,230100	95,609170	0,001915	0,010459
1109,425000	515,608200	94,396840	0,001939	0,010594
1244,796000	508,803300	93,334470	0,001965	0,010714
1396,684000	502,149500	92,295030	0,001991	0,010835
1567,105000	495,813500	91,219890	0,002017	0,010963
1758,320000	489,295900	90,285530	0,002044	0,011076
1972,868000	482,945500	89,287980	0,002071	0,011200
2213,594000	476,730800	88,397040	0,002098	0,011313
2483,694000	470,637100	87,691810	0,002125	0,011404
2786,750000	464,725600	86,842030	0,002152	0,011515
3126,785000	458,619800	86,197920	0,002180	0,011601
3508,311000	452,801600	85,676970	0,002208	0,011672
3936,389000	446,790400	85,347130	0,002238	0,011717
4416,701000	440,781800	84,996600	0,002269	0,011765
4955,620000	434,926000	84,654590	0,002299	0,011813
5560,297000	429,057900	84,367260	0,002331	0,011853
6238,757000	423,298700	84,309070	0,002362	0,011861
7000,000000	417,527600	84,296100	0,002395	0,011863
7854,129000	411,744800	84,325330	0,002429	0,011859
8812,479000	405,950400	84,393780	0,002463	0,011849
9887,763000	400,115100	84,638000	0,002499	0,011815
11094,250000	394,268200	84,911340	0,002536	0,011777
12447,960000	388,395100	85,278500	0,002575	0,011726
13966,840000	382,495500	85,733370	0,002614	0,011664
15671,050000	376,554400	86,335500	0,002656	0,011583
17583,200000	370,601400	86,946320	0,002698	0,011501
19728,680000	364,606200	87,689970	0,002743	0,011404
22135,940000	358,583600	88,494570	0,002789	0,011300
24836,940000	352,369500	89,377720	0,002838	0,011188
27867,500000	346,259800	90,404210	0,002888	0,011061
31267,850000	340,105400	91,527840	0,002940	0,010926
35083,110000	333,741900	92,756360	0,002996	0,010781
39363,890000	327,463000	94,157470	0,003054	0,010621
44167,020000	320,809300	95,647030	0,003117	0,010455
49556,210000	314,090500	97,234910	0,003184	0,010284
55602,980000	307,433700	99,007800	0,003253	0,010100
62387,570000	300,364600	100,912200	0,003329	0,009910
70000,000000	293,189500	102,961900	0,003411	0,009712
78541,290000	285,743400	105,131700	0,003500	0,009512
88124,780000	278,025100	107,388500	0,003597	0,009312
98877,620000	270,053000	109,650500	0,003703	0,009120
110942,500000	261,629600	111,963000	0,003822	0,008932
124479,600000	252,957300	114,202300	0,003953	0,008756
139668,400000	243,842100	116,395800	0,004101	0,008591

frequency [Hz]	real impedance at 100 bar Z´ [Ω m]	imaginary impedance at 100 bar Z´´ [Ω m]	real admittance at 100 bar Y´ [S m-1]	imaginary admittance at 100 bar Y´´ [S m-1]
156710,500000	234,333400	118,403200	0,004267	0,008446
175832,000000	224,558700	120,284800	0,004453	0,008314
197286,800000	214,438200	121,842500	0,004663	0,008207
221359,400000	203,862200	122,949500	0,004905	0,008133
248369,400000	193,141800	123,678200	0,005178	0,008085
278675,000000	182,256700	124,059900	0,005487	0,008061
312678,500000	171,217100	123,812100	0,005841	0,008077
350831,100000	159,973500	123,022600	0,006251	0,008129
393638,900000	148,953000	121,656800	0,006714	0,008220
441670,100000	137,998900	119,703900	0,007246	0,008354
495562,000000	127,298000	117,213900	0,007856	0,008531
556029,800000	116,890300	114,138200	0,008555	0,008761
623875,700000	106,850500	110,595400	0,009359	0,009042
700000,000000	97,309770	106,627000	0,010276	0,009378
785412,900000	88,267470	102,277000	0,011329	0,009777
881247,800000	79,776200	97,621240	0,012535	0,010244
988776,300000	71,868450	92,730800	0,013914	0,010784

frequency [Hz]	real impedance at 150 bar Z´ [Ω m]	imaginary impedance at 150 bar Z´´ [Ω m]	real admittance at 150 bar Y´ [S m-1]	imaginary admittance at 150 bar Y´´ [S m-1]
785,412900	524,461200	101,132600	0,001907	0,009888
881,247800	517,435100	99,590530	0,001933	0,010041
988,776300	510,240600	98,113510	0,001960	0,010192
1109,425000	503,329200	96,784520	0,001987	0,010332
1244,796000	496,384500	95,628730	0,002015	0,010457
1396,684000	489,757500	94,440670	0,002042	0,010589
1567,105000	482,997100	93,137030	0,002070	0,010737
1758,320000	476,521100	91,974480	0,002099	0,010873
1972,868000	470,029600	90,891650	0,002128	0,011002
2213,594000	463,657800	89,995180	0,002157	0,011112
2483,694000	457,468700	88,959520	0,002186	0,011241
2786,750000	451,280400	87,919550	0,002216	0,011374
3126,785000	445,347700	87,166980	0,002245	0,011472
3508,311000	439,266500	86,374600	0,002277	0,011577
3936,389000	433,127200	85,873930	0,002309	0,011645
4416,701000	427,170300	85,235150	0,002341	0,011732
4955,620000	421,486100	84,789260	0,002373	0,011794
5560,297000	415,504600	84,264920	0,002407	0,011867
6238,757000	409,781600	83,997760	0,002440	0,011905
7000,000000	403,911700	83,675970	0,002476	0,011951
7854,129000	398,315400	83,531660	0,002511	0,011972
8812,479000	392,558100	83,397230	0,002547	0,011991
9887,763000	386,775100	83,368190	0,002585	0,011995
11094,250000	380,981300	83,372080	0,002625	0,011994
12447,960000	375,297000	83,570000	0,002665	0,011966
13966,840000	369,601800	83,791870	0,002706	0,011934
15671,050000	363,881300	84,098240	0,002748	0,011891
17583,200000	357,986300	84,448040	0,002793	0,011842
19728,680000	352,348800	85,002120	0,002838	0,011764
22135,940000	346,403100	85,488530	0,002887	0,011697
24836,940000	340,698600	86,227700	0,002935	0,011597
27867,500000	334,671300	86,942180	0,002988	0,011502
31267,850000	328,883000	87,892720	0,003041	0,011378
35083,110000	322,772000	88,798360	0,003098	0,011261
39363,890000	316,718900	89,992430	0,003157	0,011112
44167,020000	310,621100	91,254040	0,003219	0,010958
49556,210000	304,299200	92,635440	0,003286	0,010795
55602,980000	297,882100	94,214000	0,003357	0,010614
62387,570000	291,383500	95,919000	0,003432	0,010425
70000,000000	284,605400	97,832920	0,003514	0,010222
78541,290000	277,614500	99,728380	0,003602	0,010027
88124,780000	270,449100	101,922000	0,003698	0,009811
98877,620000	262,926700	103,988900	0,003803	0,009616
110942,500000	255,102300	106,181200	0,003920	0,009418
124479,600000	246,993700	108,412300	0,004049	0,009224
139668,400000	238,483100	110,535200	0,004193	0,009047

frequency [Hz]	real impedance at 150 bar Z´ [Ω m]	imaginary impedance at 150 bar Z´´ [Ω m]	real admittance at 150 bar Y´ [S m-1]	imaginary admittance at 150 bar Y´´ [S m-1]
156710,500000	229,559500	112,543300	0,004356	0,008885
175832,000000	220,349500	114,492100	0,004538	0,008734
197286,800000	210,808000	116,110100	0,004744	0,008613
221359,400000	200,893400	117,461400	0,004978	0,008513
248369,400000	190,668700	118,421700	0,005245	0,008444
278675,000000	180,288600	119,027600	0,005547	0,008401
312678,500000	169,693300	119,095300	0,005893	0,008397
350831,100000	159,019500	118,708200	0,006289	0,008424
393638,900000	148,280500	117,612100	0,006744	0,008503
441670,100000	137,687800	116,065700	0,007263	0,008616
495562,000000	127,325500	113,997300	0,007854	0,008772
556029,800000	117,057100	111,230400	0,008543	0,008990
623875,700000	107,197400	108,050400	0,009329	0,009255
700000,000000	97,770840	104,429800	0,010228	0,009576
785412,900000	88,817700	100,373900	0,011259	0,009963
881247,800000	80,371640	96,036860	0,012442	0,010413
988776,300000	72,474500	91,419830	0,013798	0,010939

frequency [Hz]	real impedance at 200 bar Z´ [Ω m]	imaginary impedance at 200 bar Z´´ [Ω m]	real admittance at 200 bar Y´ [S m-1]	imaginary admittance at 200 bar Y´´ [S m-1]
785,412900	524,054700	101,623300	0,001908	0,009840
881,247800	516,879900	100,044800	0,001935	0,009996
988,776300	509,837100	98,589400	0,001961	0,010143
1109,425000	502,927200	97,253200	0,001988	0,010282
1244,796000	495,983700	96,090030	0,002016	0,010407
1396,684000	489,074200	94,751400	0,002045	0,010554
1567,105000	482,448700	93,555140	0,002073	0,010689
1758,320000	475,973900	92,385720	0,002101	0,010824
1972,868000	469,499600	91,214050	0,002130	0,010963
2213,594000	462,994200	90,201650	0,002160	0,011086
2483,694000	456,790300	89,241160	0,002189	0,011206
2786,750000	450,753100	88,224970	0,002219	0,011335
3126,785000	444,536100	87,330240	0,002250	0,011451
3508,311000	438,605700	86,562590	0,002280	0,011552
3936,389000	432,481900	85,981250	0,002312	0,011630
4416,701000	426,525600	85,338620	0,002345	0,011718
4955,620000	420,691800	84,858570	0,002377	0,011784
5560,297000	414,846000	84,432780	0,002411	0,011844
6238,757000	409,002900	83,986840	0,002445	0,011907
7000,000000	403,268700	83,762880	0,002480	0,011938
7854,129000	397,537600	83,513340	0,002515	0,011974
8812,479000	391,780700	83,374950	0,002552	0,011994
9887,763000	385,998300	83,341680	0,002591	0,011999
11094,250000	380,190400	83,407520	0,002630	0,011989
12447,960000	374,521200	83,534390	0,002670	0,011971
13966,840000	368,677400	83,717540	0,002712	0,011945
15671,050000	362,957500	84,018170	0,002755	0,011902
17583,200000	357,212300	84,397030	0,002799	0,011849
19728,680000	351,441700	84,848150	0,002845	0,011786
22135,940000	345,630600	85,425830	0,002893	0,011706
24836,940000	339,793700	86,061740	0,002943	0,011620
27867,500000	333,900600	86,866340	0,002995	0,011512
31267,850000	327,980900	87,712920	0,003049	0,011401
35083,110000	322,019000	88,651600	0,003105	0,011280
39363,890000	315,967400	89,838460	0,003165	0,011131
44167,020000	309,871200	91,092470	0,003227	0,010978
49556,210000	303,551200	92,465600	0,003294	0,010815
55602,980000	297,152700	93,983310	0,003365	0,010640
62387,570000	290,640100	95,730500	0,003441	0,010446
70000,000000	283,899000	97,534730	0,003522	0,010253
78541,290000	276,894500	99,469740	0,003611	0,010053
88124,780000	269,751000	101,605200	0,003707	0,009842
98877,620000	262,233500	103,661800	0,003813	0,009647
110942,500000	254,414500	105,842900	0,003931	0,009448
124479,600000	246,330900	108,018900	0,004060	0,009258
139668,400000	237,808200	110,172000	0,004205	0,009077

frequency [Hz]	real impedance at 200 bar Z´ [Ω m]	imaginary impedance at 200 bar Z´´ [Ω m]	real admittance at 200 bar Y´ [S m-1]	imaginary admittance at 200 bar Y´´ [S m-1]
156710,500000	229,049200	112,194000	0,004366	0,008913
175832,000000	219,846300	114,133200	0,004549	0,008762
197286,800000	210,332500	115,704800	0,004754	0,008643
221359,400000	200,426400	117,047600	0,004989	0,008544
248369,400000	190,361200	118,046700	0,005253	0,008471
278675,000000	180,009000	118,617800	0,005555	0,008430
312678,500000	169,421200	118,683900	0,005902	0,008426
350831,100000	158,754900	118,295200	0,006299	0,008453
393638,900000	148,163600	117,267000	0,006749	0,008528
441670,100000	137,575000	115,724500	0,007269	0,008641
495562,000000	127,102400	113,558100	0,007868	0,008806
556029,800000	116,951400	110,897200	0,008551	0,009017
623875,700000	107,156600	107,745900	0,009332	0,009281
700000,000000	97,751720	104,154200	0,010230	0,009601
785412,900000	88,811040	100,155000	0,011260	0,009985
881247,800000	80,380680	95,809710	0,012441	0,010437
988776,300000	72,484490	91,236110	0,013796	0,010961

frequency [Hz]	real impedance at 200 bar Z´ [Ω m]	imaginary impedance at 200 bar Z´´ [Ω m]	real admittance at 200 bar Y´ [S m-1]	imaginary admittance at 200 bar Y´´ [S m-1]
785,412900	524,054700	101,623300	0,001908	0,009840
881,247800	516,879900	100,044800	0,001935	0,009996
988,776300	509,837100	98,589400	0,001961	0,010143
1109,425000	502,927200	97,253200	0,001988	0,010282
1244,796000	495,983700	96,090030	0,002016	0,010407
1396,684000	489,074200	94,751400	0,002045	0,010554
1567,105000	482,448700	93,555140	0,002073	0,010689
1758,320000	475,973900	92,385720	0,002101	0,010824
1972,868000	469,499600	91,214050	0,002130	0,010963
2213,594000	462,994200	90,201650	0,002160	0,011086
2483,694000	456,790300	89,241160	0,002189	0,011206
2786,750000	450,753100	88,224970	0,002219	0,011335
3126,785000	444,536100	87,330240	0,002250	0,011451
3508,311000	438,605700	86,562590	0,002280	0,011552
3936,389000	432,481900	85,981250	0,002312	0,011630
4416,701000	426,525600	85,338620	0,002345	0,011718
4955,620000	420,691800	84,858570	0,002377	0,011784
5560,297000	414,846000	84,432780	0,002411	0,011844
6238,757000	409,002900	83,986840	0,002445	0,011907
7000,000000	403,268700	83,762880	0,002480	0,011938
7854,129000	397,537600	83,513340	0,002515	0,011974
8812,479000	391,780700	83,374950	0,002552	0,011994
9887,763000	385,998300	83,341680	0,002591	0,011999
11094,250000	380,190400	83,407520	0,002630	0,011989
12447,960000	374,521200	83,534390	0,002670	0,011971
13966,840000	368,677400	83,717540	0,002712	0,011945
15671,050000	362,957500	84,018170	0,002755	0,011902
17583,200000	357,212300	84,397030	0,002799	0,011849
19728,680000	351,441700	84,848150	0,002845	0,011786
22135,940000	345,630600	85,425830	0,002893	0,011706
24836,940000	339,793700	86,061740	0,002943	0,011620
27867,500000	333,900600	86,866340	0,002995	0,011512
31267,850000	327,980900	87,712920	0,003049	0,011401
35083,110000	322,019000	88,651600	0,003105	0,011280
39363,890000	315,967400	89,838460	0,003165	0,011131
44167,020000	309,871200	91,092470	0,003227	0,010978
49556,210000	303,551200	92,465600	0,003294	0,010815
55602,980000	297,152700	93,983310	0,003365	0,010640
62387,570000	290,640100	95,730500	0,003441	0,010446
70000,000000	283,899000	97,534730	0,003522	0,010253
78541,290000	276,894500	99,469740	0,003611	0,010053
88124,780000	269,751000	101,605200	0,003707	0,009842
98877,620000	262,233500	103,661800	0,003813	0,009647
110942,500000	254,414500	105,842900	0,003931	0,009448
124479,600000	246,330900	108,018900	0,004060	0,009258
139668,400000	237,808200	110,172000	0,004205	0,009077
156710,500000	229,049200	112,194000	0,004366	0,008913

frequency [Hz]	real impedance at 200 bar Z´ [Ω m]	imaginary impedance at 200 bar Z´´ [Ω m]	real admittance at 200 bar Y´ [S m-1]	imaginary admittance at 200 bar Y´´ [S m-1]
175832,000000	219,846300	114,133200	0,004549	0,008762
197286,800000	210,332500	115,704800	0,004754	0,008643
221359,400000	200,426400	117,047600	0,004989	0,008544
248369,400000	190,361200	118,046700	0,005253	0,008471
278675,000000	180,009000	118,617800	0,005555	0,008430
312678,500000	169,421200	118,683900	0,005902	0,008426
350831,100000	158,754900	118,295200	0,006299	0,008453
393638,900000	148,163600	117,267000	0,006749	0,008528
441670,100000	137,575000	115,724500	0,007269	0,008641
495562,000000	127,102400	113,558100	0,007868	0,008806
556029,800000	116,951400	110,897200	0,008551	0,009017
623875,700000	107,156600	107,745900	0,009332	0,009281
700000,000000	97,751720	104,154200	0,010230	0,009601
785412,900000	88,811040	100,155000	0,011260	0,009985
881247,800000	80,380680	95,809710	0,012441	0,010437
988776,300000	72,484490	91,236110	0,013796	0,010961

frequency [Hz]	real impedance at 250 bar Z´ [Ω m]	imaginary impedance at 250 bar Z´´ [Ω m]	real admittance at 250 bar Y´ [S m-1]	imaginary admittance at 250 bar Y´´ [S m-1]
785,412900	522,764500	101,846200	0,001913	0,009819
881,247800	515,440800	100,232800	0,001940	0,009977
988,776300	508,399300	98,771450	0,001967	0,010124
1109,425000	501,323200	97,487480	0,001995	0,010258
1244,796000	494,414600	96,144040	0,002023	0,010401
1396,684000	487,623100	94,999920	0,002051	0,010526
1567,105000	481,015400	93,712590	0,002079	0,010671
1758,320000	474,391400	92,508000	0,002108	0,010810
1972,868000	467,918200	91,330410	0,002137	0,010949
2213,594000	461,413800	90,311570	0,002167	0,011073
2483,694000	455,226500	89,265460	0,002197	0,011203
2786,750000	449,040000	88,215040	0,002227	0,011336
3126,785000	442,808600	87,392070	0,002258	0,011443
3508,311000	436,894200	86,541600	0,002289	0,011555
3936,389000	430,906400	86,058790	0,002321	0,011620
4416,701000	424,965900	85,335010	0,002353	0,011719
4955,620000	418,983000	84,818160	0,002387	0,011790
5560,297000	413,152700	84,313350	0,002420	0,011861
6238,757000	407,460300	83,892330	0,002454	0,011920
7000,000000	401,577100	83,630780	0,002490	0,011957
7854,129000	395,847000	83,374510	0,002526	0,011994
8812,479000	390,091100	83,228800	0,002564	0,012015
9887,763000	384,473700	83,152920	0,002601	0,012026
11094,250000	378,666900	83,211760	0,002641	0,012018
12447,960000	373,013400	83,266390	0,002681	0,012010
13966,840000	367,185300	83,378740	0,002723	0,011993
15671,050000	361,616000	83,707630	0,002765	0,011946
17583,200000	355,723300	84,045230	0,002811	0,011898
19728,680000	349,954400	84,489080	0,002858	0,011836
22135,940000	344,308600	85,035380	0,002904	0,011760
24836,940000	338,473800	85,664610	0,002954	0,011673
27867,500000	332,598100	86,403600	0,003007	0,011574
31267,850000	326,696300	87,186210	0,003061	0,011470
35083,110000	320,869700	88,214780	0,003117	0,011336
39363,890000	314,836900	89,338960	0,003176	0,011193
44167,020000	308,597500	90,542630	0,003240	0,011045
49556,210000	302,428500	91,950670	0,003307	0,010875
55602,980000	296,034600	93,459300	0,003378	0,010700
62387,570000	289,544000	95,145570	0,003454	0,010510
70000,000000	282,953800	96,989330	0,003534	0,010310
78541,290000	275,955700	98,915120	0,003624	0,010110
88124,780000	268,836900	100,993200	0,003720	0,009902
98877,620000	261,469800	103,096300	0,003825	0,009700
110942,500000	253,658900	105,269000	0,003942	0,009499
124479,600000	245,584000	107,436100	0,004072	0,009308
139668,400000	237,248100	109,560800	0,004215	0,009127
156710,500000	228,498600	111,578500	0,004376	0,008962

frequency [Hz]	real impedance at 250 bar Z´ [Ω m]	imaginary impedance at 250 bar Z´´ [Ω m]	real admittance at 250 bar Y´ [S m-1]	imaginary admittance at 250 bar Y´´ [S m-1]
175832,000000	219,306100	113,513000	0,004560	0,008810
197286,800000	209,802900	115,080000	0,004766	0,008690
221359,400000	200,060600	116,459900	0,004998	0,008587
248369,400000	189,984700	117,492300	0,005264	0,008511
278675,000000	179,662900	118,030400	0,005566	0,008472
312678,500000	169,210300	118,184500	0,005910	0,008461
350831,100000	158,572000	117,772100	0,006306	0,008491
393638,900000	147,966800	116,775700	0,006758	0,008563
441670,100000	137,404800	115,213500	0,007278	0,008680
495562,000000	127,052000	113,154900	0,007871	0,008837
556029,800000	116,914100	110,513800	0,008553	0,009049
623875,700000	107,123200	107,412100	0,009335	0,009310
700000,000000	97,739690	103,850500	0,010231	0,009629
785412,900000	88,818550	99,882300	0,011259	0,010012
881247,800000	80,415810	95,580370	0,012435	0,010462
988776,300000	72,525930	91,027170	0,013788	0,010986

frequency [Hz]	real impedance at 300 bar Z´ [Ω m]	imaginary impedance at 300 bar Z´´ [Ω m]	real admittance at 300 bar Y´ [S m-1]	imaginary admittance at 300 bar Y´´ [S m-1]
785,412900	521,978000	101,882100	0,001916	0,009815
881,247800	514,654900	100,266300	0,001943	0,009973
988,776300	507,596600	98,891210	0,001970	0,010112
1109,425000	500,538300	97,516090	0,001998	0,010255
1244,796000	493,613400	96,256350	0,002026	0,010389
1396,684000	486,839100	95,023500	0,002054	0,010524
1567,105000	480,081600	93,704540	0,002083	0,010672
1758,320000	473,608400	92,526830	0,002111	0,010808
1972,868000	467,119600	91,428340	0,002141	0,010938
2213,594000	460,631600	90,325340	0,002171	0,011071
2483,694000	454,429100	89,356090	0,002201	0,011191
2786,750000	448,258600	88,223980	0,002231	0,011335
3126,785000	442,177700	87,427850	0,002262	0,011438
3508,311000	436,113600	86,545100	0,002293	0,011555
3936,389000	430,141200	85,984010	0,002325	0,011630
4416,701000	424,036100	85,302220	0,002358	0,011723
4955,620000	418,203600	84,812290	0,002391	0,011791
5560,297000	412,373800	84,304260	0,002425	0,011862
6238,757000	406,531900	83,849040	0,002460	0,011926
7000,000000	400,813600	83,544730	0,002495	0,011970
7854,129000	395,083900	83,285770	0,002531	0,012007
8812,479000	389,328400	83,137080	0,002569	0,012028
9887,763000	383,711500	83,058140	0,002606	0,012040
11094,250000	377,919800	83,047580	0,002646	0,012041
12447,960000	372,252200	83,164660	0,002686	0,012024
13966,840000	366,574000	83,307170	0,002728	0,012004
15671,050000	360,707100	83,563530	0,002772	0,011967
17583,200000	354,978800	83,869330	0,002817	0,011923
19728,680000	349,210800	84,309550	0,002864	0,011861
22135,940000	343,551100	84,911890	0,002911	0,011777
24836,940000	337,732200	85,476910	0,002961	0,011699
27867,500000	331,872700	86,153370	0,003013	0,011607
31267,850000	326,089800	87,085300	0,003067	0,011483
35083,110000	320,132000	88,011990	0,003124	0,011362
39363,890000	314,100900	89,130130	0,003184	0,011220
44167,020000	308,010300	90,370330	0,003247	0,011066
49556,210000	301,859000	91,719990	0,003313	0,010903
55602,980000	295,467300	93,223510	0,003384	0,010727
62387,570000	288,979200	94,904100	0,003460	0,010537
70000,000000	282,391800	96,741620	0,003541	0,010337
78541,290000	275,396800	98,660580	0,003631	0,010136
88124,780000	268,281600	100,731200	0,003727	0,009927
98877,620000	260,918400	102,826300	0,003833	0,009725
110942,500000	253,130200	104,946200	0,003951	0,009529
124479,600000	245,200900	107,166500	0,004078	0,009331
139668,400000	236,730600	109,221700	0,004224	0,009156
156710,500000	227,987500	111,230500	0,004386	0,008990

frequency [Hz]	real impedance at 300 bar Z´ [Ω m]	imaginary impedance at 300 bar Z´´ [Ω m]	real admittance at 300 bar Y´ [S m-1]	imaginary admittance at 300 bar Y´´ [S m-1]
175832,000000	218,957700	113,187400	0,004567	0,008835
197286,800000	209,460500	114,749600	0,004774	0,008715
221359,400000	199,724700	116,124500	0,005007	0,008611
248369,400000	189,676100	117,118500	0,005272	0,008538
278675,000000	179,340900	117,684600	0,005576	0,008497
312678,500000	168,916300	117,803900	0,005920	0,008489
350831,100000	158,408300	117,479100	0,006313	0,008512
393638,900000	147,807900	116,483100	0,006766	0,008585
441670,100000	137,367900	115,019300	0,007280	0,008694
495562,000000	127,016600	112,964600	0,007873	0,008852
556029,800000	116,843600	110,254300	0,008558	0,009070
623875,700000	107,076300	107,177900	0,009339	0,009330
700000,000000	97,704280	103,631700	0,010235	0,009650
785412,900000	88,803860	99,690540	0,011261	0,010031
881247,800000	80,410400	95,404900	0,012436	0,010482
988776,300000	72,528950	90,868220	0,013788	0,011005

frequency [Hz]	real impedance at 400 bar Z´ [Ω m]	imaginary impedance at 400 bar Z´´ [Ω m]	real admittance at 400 bar Y´ [S m-1]	imaginary admittance at 400 bar Y´´ [S m-1]
785,412900	519,654700	101,805100	0,001924355	0,009822691
881,247800	512,332500	100,185000	0,001951857	0,009981534
988,776300	505,275100	98,804920	0,00197912	0,010120953
1109,425000	498,401900	97,280380	0,002006413	0,010279565
1244,796000	491,293900	96,159920	0,002035442	0,010399343
1396,684000	484,520500	94,921950	0,002063896	0,010534971
1567,105000	477,930400	93,544330	0,002092355	0,010690119
1758,320000	471,307700	92,333440	0,002121756	0,010830312
1972,868000	464,819600	91,230770	0,002151372	0,010961214
2213,594000	458,498200	90,073130	0,002181034	0,01110209
2483,694000	452,280800	89,179510	0,002211016	0,011213338
2786,750000	446,110900	88,043820	0,002241595	0,011357981
3126,785000	439,880700	87,212920	0,002273344	0,011466191
3508,311000	433,967500	86,355300	0,00230432	0,011580065
3936,389000	427,860800	85,683420	0,002337209	0,011670869
4416,701000	421,906500	85,026990	0,002370193	0,011760971
4955,620000	416,074900	84,531730	0,002403413	0,011829877
5560,297000	410,260500	83,946790	0,002437476	0,011912308
6238,757000	404,554800	83,588420	0,002471853	0,01196338
7000,000000	398,837400	83,278020	0,002507287	0,01200797
7854,129000	393,123200	82,944080	0,002543732	0,012056316
8812,479000	387,368800	82,789290	0,002581519	0,012078857
9887,763000	381,603600	82,671550	0,00262052	0,01209606
11094,250000	375,962700	82,686270	0,002659838	0,012093906
12447,960000	370,311100	82,731000	0,002700432	0,012087367
13966,840000	364,634500	82,866390	0,002742472	0,012067619
15671,050000	358,933000	83,086560	0,002786035	0,012035641
17583,200000	353,206500	83,385550	0,002831205	0,011992486
19728,680000	347,589400	83,853930	0,002876958	0,011925499
22135,940000	341,798200	84,352110	0,002925703	0,011855068
24836,940000	336,130300	84,946720	0,002975037	0,011772085
27867,500000	330,273600	85,615260	0,003027793	0,011680161
31267,850000	324,509100	86,481250	0,003081578	0,0115632
35083,110000	318,702600	87,439630	0,003137721	0,011436462
39363,890000	312,690800	88,494290	0,003198047	0,011300164
44167,020000	306,604900	89,725660	0,003261526	0,011145084
49556,210000	300,458700	91,065550	0,003328244	0,010981101
55602,980000	294,218800	92,603900	0,003398831	0,010798681
62387,570000	287,736700	94,273690	0,0034754	0,010607413
70000,000000	281,172900	96,050160	0,003556531	0,010411227
78541,290000	274,330100	98,008540	0,003645243	0,010203192
88124,780000	267,223100	100,067900	0,003742191	0,009993215
98877,620000	259,886600	102,105600	0,003847832	0,009793782
110942,500000	252,250200	104,272000	0,003964318	0,009590302
124479,600000	244,331100	106,482000	0,004092807	0,009391259
139668,400000	236,010800	108,590100	0,004237094	0,009208943
156710,500000	227,278300	110,590100	0,004399892	0,009042401

frequency [Hz]	real impedance at 400 bar Z´ [Ω m]	imaginary impedance at 400 bar Z´´ [Ω m]	real admittance at 400 bar Y´ [S m-1]	imaginary admittance at 400 bar Y´´ [S m-1]
175832,000000	218,260100	112,537500	0,004581689	0,008885927
197286,800000	208,929100	114,127100	0,004786313	0,008762161
221359,400000	199,204600	115,496800	0,005019964	0,008658249
248369,400000	189,167600	116,485700	0,005286318	0,008584745
278675,000000	178,992800	117,099100	0,005586817	0,008539775
312678,500000	168,578000	117,218700	0,005931972	0,008531062
350831,100000	158,080000	116,894100	0,006325911	0,008554752
393638,900000	147,629700	115,967300	0,006773705	0,00862312
441670,100000	137,175900	114,533400	0,00728991	0,008731078
495562,000000	126,850400	112,460500	0,007883302	0,008892011
556029,800000	116,741000	109,849900	0,008565971	0,009103331
623875,700000	106,987500	106,790600	0,009346886	0,00936412
700000,000000	97,659600	103,295100	0,010239649	0,009681001
785412,900000	88,779820	99,383960	0,011263821	0,010061986
881247,800000	80,398480	95,154710	0,012438046	0,010509201
988776,300000	72,525140	90,636230	0,013788322	0,011033116

III.5 CALCULATIONS OF BULK CONDUCTIVITIES OF SAMPLE 17/08/00/11 CORE 1:

pressure measurement 1 [bar]	resistivity R1-1of elem. cell 1 [Ω]	capacity C1-1 * E^{-7} of elem. cell 1 [F]	resistivity R2-1 of elem. cell 2 [Ω]	capacity C2-1 * E^{-9} of elem. cell 2 [F]
0	174	2,49	209	7,72
75	177	2,61	196	8,54
100	181	2,7	184	9,39
150	184	2,86	173	10,4
200	185	2,87	173	10,5
250	185	2,88	172	10,6
300	185	2,89	171	10,6
400	185	2,91	170	10,7

resistivity R3-1 of elem. cell 3 [Ω]	capacity C3-1 * E^{-9} of elem. cell 3 [F]	X2-1
186	1,22	0,142
186	1,2	0,147
182	1,19	0,156
183	1,18	0,161
182	1,18	0,161
182	1,18	0,162
182	1,18	0,162
181	1,18	0,162
surface resistivity	surface resistivity	

III.6 COMPLEX IMPEDANCE DATA FOR SAMPLE 17/08/00/11 CORE 2:

frequency [Hz]	real impedance at 0 bar Z´ [Ω m]	imaginary impedance at 0 bar Z´´ [Ω m]	real admittance at 0 bar Y´ [S m1]	imaginary admittance at 0 bar Y´´ [S m1]
785,412900	407,578400	40,158380	0,002454	0,024901
881,247700	404,739100	39,807340	0,002471	0,025121
988,776200	401,892900	39,527400	0,002488	0,025299
1109,425000	399,338000	39,205800	0,002504	0,025506
1244,796000	396,478100	39,064690	0,002522	0,025599
1396,684000	393,909800	38,881010	0,002539	0,025719
1567,105000	391,043300	38,804730	0,002557	0,025770
1758,320000	388,488600	38,482780	0,002574	0,025986
1972,868000	385,907100	38,431010	0,002591	0,026021
2213,594000	383,332500	38,309680	0,002609	0,026103
2483,694000	380,744600	38,319390	0,002626	0,026096
2786,750000	378,156800	38,325520	0,002644	0,026092
3126,785000	375,847100	38,422650	0,002661	0,026026
3508,311000	373,246300	38,551560	0,002679	0,025939
3936,389000	370,632200	38,804380	0,002698	0,025770
4416,701000	368,024800	38,985790	0,002717	0,025650
4955,620000	365,403900	39,288360	0,002737	0,025453
5560,297000	362,776100	39,646100	0,002757	0,025223
6238,757000	359,863800	39,963210	0,002779	0,025023
7000,000000	357,498800	40,521510	0,002797	0,024678
7854,129000	355,140300	41,007340	0,002816	0,024386
8812,479000	352,482800	41,573050	0,002837	0,024054
9887,763000	349,518700	42,274760	0,002861	0,023655
11094,250000	346,837300	42,994430	0,002883	0,023259
12447,960000	343,855800	43,782530	0,002908	0,022840
13966,840000	341,125400	44,826440	0,002931	0,022308
15671,050000	338,116600	45,751770	0,002958	0,021857
17583,210000	335,356500	46,928120	0,002982	0,021309
19728,680000	332,301200	48,097430	0,003009	0,020791
22135,950000	329,225300	49,353880	0,003037	0,020262
24836,940000	326,118700	50,751130	0,003066	0,019704
27867,500000	322,952000	52,453290	0,003096	0,019065
31267,850000	319,514200	53,956540	0,003130	0,018533
35083,110000	316,002400	55,804610	0,003165	0,017920
39363,890000	312,460900	57,712070	0,003200	0,017327
44167,020000	308,471200	59,873730	0,003242	0,016702
49556,210000	304,334600	62,051190	0,003286	0,016116
55602,980000	300,212400	64,435890	0,003331	0,015519
62387,570000	295,983000	66,884740	0,003379	0,014951
70000,000000	291,388800	69,596980	0,003432	0,014368
78541,290000	286,667200	72,393230	0,003488	0,013813
88124,780000	281,568900	75,406110	0,003552	0,013262
98877,630000	276,265100	78,289600	0,003620	0,012773

frequency [Hz]	real impedance at 0 bar Z´ [Ω m]	imaginary impedance at 0 bar Z´´ [Ω m]	real admittance at 0 bar Y´ [S m1]	imaginary admittance at 0 bar Y´´ [S m1]
110942,500000	270,508900	81,370230	0,003697	0,012290
124479,600000	264,444900	84,603680	0,003782	0,011820
139668,400000	258,043200	87,847400	0,003875	0,011383
156710,500000	251,228700	91,190960	0,003980	0,010966
175832,000000	243,897200	94,450990	0,004100	0,010588
197286,800000	236,280600	97,477740	0,004232	0,010259
221359,400000	228,135200	100,467200	0,004383	0,009953
248369,400000	219,642200	103,249200	0,004553	0,009685
278675,000000	210,692500	105,766900	0,004746	0,009455
312678,500000	201,341500	107,893700	0,004967	0,009268
350831,100000	191,599800	109,663100	0,005219	0,009119
393638,900000	181,662900	110,905200	0,005505	0,009017
441670,100000	171,501100	111,686000	0,005831	0,008954
495562,000000	161,187700	111,954700	0,006204	0,008932
556029,800000	150,804500	111,758500	0,006631	0,008948
623875,700000	140,419200	110,699900	0,007122	0,009033
700000,000000	130,117300	109,180300	0,007685	0,009159
785412,900000	120,040200	107,060300	0,008331	0,009341
881247,800000	110,252100	104,398700	0,009070	0,009579
988776,300000	100,808500	101,221400	0,009920	0,009879

frequency [Hz]	real impedance at 25 bar Z´ [Ω m]	imaginary impedance at 25 bar Z´´ [Ω m]	real admittance at 25 bar Y´ [S m1]	imaginary admittance at 25 bar Y´´ [S m1]
785,412900	435,246100	59,513350	0,002298	0,016803
881,247700	430,702000	58,968550	0,002322	0,016958
988,776200	426,451600	58,386620	0,002345	0,017127
1109,425000	422,768000	57,882290	0,002365	0,017276
1244,796000	418,791000	57,412210	0,002388	0,017418
1396,684000	414,530800	56,901860	0,002412	0,017574
1567,105000	410,573900	56,285720	0,002436	0,017766
1758,320000	406,568000	56,025600	0,002460	0,017849
1972,868000	402,591800	55,549240	0,002484	0,018002
2213,594000	398,899000	55,110640	0,002507	0,018145
2483,694000	395,480300	54,778930	0,002529	0,018255
2786,750000	391,759400	54,542180	0,002553	0,018334
3126,785000	388,048600	54,232580	0,002577	0,018439
3508,311000	384,310000	54,120240	0,002602	0,018477
3936,389000	380,590800	53,867360	0,002627	0,018564
4416,701000	376,853500	53,740780	0,002654	0,018608
4955,620000	373,126100	53,541360	0,002680	0,018677
5560,297000	369,352800	53,657660	0,002707	0,018637
6238,757000	365,872500	53,738740	0,002733	0,018609
7000,000000	362,374100	53,935460	0,002760	0,018541
7854,129000	358,866900	54,181550	0,002787	0,018456
8812,479000	355,077500	54,369920	0,002816	0,018393
9887,763000	350,996800	54,560010	0,002849	0,018328
11094,250000	347,745500	54,986910	0,002876	0,018186
12447,960000	343,919900	55,366340	0,002908	0,018062
13966,840000	340,338200	56,008610	0,002938	0,017854
15671,050000	336,202000	56,473050	0,002974	0,017708
17583,210000	332,590500	57,239420	0,003007	0,017470
19728,680000	328,404800	57,935740	0,003045	0,017261
22135,950000	324,761600	58,813060	0,003079	0,017003
24836,940000	320,804800	59,774190	0,003117	0,016730
27867,500000	317,106400	60,861260	0,003154	0,016431
31267,850000	313,092700	62,018540	0,003194	0,016124
35083,110000	308,752200	63,288590	0,003239	0,015801
39363,890000	304,145400	64,780720	0,003288	0,015437
44167,020000	299,813400	66,267650	0,003335	0,015090
49556,210000	295,540800	67,923720	0,003384	0,014722
55602,980000	291,077700	69,791100	0,003436	0,014328
62387,570000	286,235500	71,647140	0,003494	0,013957
70000,000000	281,487400	73,702770	0,003553	0,013568
78541,290000	276,317400	75,758950	0,003619	0,013200
88124,780000	270,836900	78,028900	0,003692	0,012816
98877,630000	265,179600	80,221370	0,003771	0,012466
110942,500000	259,368800	82,730380	0,003856	0,012087
124479,600000	253,173400	85,106740	0,003950	0,011750
139668,400000	246,672600	87,545620	0,004054	0,011423
156710,500000	239,849500	90,055850	0,004169	0,011104

frequency [Hz]	real impedance at 25 bar Z´ [Ω m]	imaginary impedance at 25 bar Z´´ [Ω m]	real admittance at 25 bar Y´ [S m1]	imaginary admittance at 25 bar Y´´ [S m1]
175832,000000	232,926100	92,734860	0,004293	0,010783
197286,800000	225,491400	94,965810	0,004435	0,010530
221359,400000	217,683100	97,227550	0,004594	0,010285
248369,400000	209,754400	99,406510	0,004767	0,010060
278675,000000	201,410400	101,371400	0,004965	0,009865
312678,500000	192,702000	103,004500	0,005189	0,009708
350831,100000	183,599600	104,235500	0,005447	0,009594
393638,900000	174,373800	104,999200	0,005735	0,009524
441670,100000	165,086700	105,591400	0,006057	0,009470
495562,000000	155,578800	105,622800	0,006428	0,009468
556029,800000	145,993900	105,107800	0,006850	0,009514
623875,700000	136,487800	104,243600	0,007327	0,009593
700000,000000	127,049800	102,920400	0,007871	0,009716
785412,900000	117,731200	101,012700	0,008494	0,009900
881247,800000	108,627000	98,664830	0,009206	0,010135
988776,300000	99,832940	95,929710	0,010017	0,010424

frequency [Hz]	real impedance at 50 bar Z´ [Ω m]	imaginary impedance at 50 bar Z´´ [Ω m]	real admittance at 50 bar Y´ [S m1]	imaginary admittance at 50 bar Y´´ [S m1]
785,412900	444,491500	71,238820	0,002250	0,014037
881,247700	439,113600	70,455490	0,002277	0,014193
988,776200	434,006300	69,791350	0,002304	0,014328
1109,425000	429,169800	69,244030	0,002330	0,014442
1244,796000	424,063700	68,571980	0,002358	0,014583
1396,684000	419,240300	67,942150	0,002385	0,014718
1567,105000	414,123400	67,335340	0,002415	0,014851
1758,320000	409,312900	66,626440	0,002443	0,015009
1972,868000	404,479500	66,056990	0,002472	0,015138
2213,594000	399,658300	65,412790	0,002502	0,015288
2483,694000	395,390700	64,926780	0,002529	0,015402
2786,750000	390,570500	64,275220	0,002560	0,015558
3126,785000	386,010800	63,801510	0,002591	0,015674
3508,311000	381,452000	63,321480	0,002622	0,015792
3936,389000	377,165100	62,947940	0,002651	0,015886
4416,701000	372,586300	62,584650	0,002684	0,015978
4955,620000	368,041100	62,019240	0,002717	0,016124
5560,297000	363,735600	61,750580	0,002749	0,016194
6238,757000	359,431300	61,471500	0,002782	0,016268
7000,000000	355,096200	61,367850	0,002816	0,016295
7854,129000	350,762600	61,249260	0,002851	0,016327
8812,479000	346,722700	61,104940	0,002884	0,016365
9887,763000	342,381400	61,017470	0,002921	0,016389
11094,250000	338,301800	61,082310	0,002956	0,016371
12447,960000	333,931800	61,135770	0,002995	0,016357
13966,840000	329,823300	61,335520	0,003032	0,016304
15671,050000	325,424700	61,516510	0,003073	0,016256
17583,210000	321,276300	61,894060	0,003113	0,016157
19728,680000	317,129400	62,243420	0,003153	0,016066
22135,950000	312,962200	62,673810	0,003195	0,015956
24836,940000	308,763300	63,234720	0,003239	0,015814
27867,500000	304,062000	63,931690	0,003289	0,015642
31267,850000	299,736700	64,607330	0,003336	0,015478
35083,110000	295,299600	65,486120	0,003386	0,015270
39363,890000	290,990600	66,397130	0,003437	0,015061
44167,020000	286,495400	67,425270	0,003490	0,014831
49556,210000	281,936300	68,536170	0,003547	0,014591
55602,980000	277,216900	69,749550	0,003607	0,014337
62387,570000	272,336300	71,052930	0,003672	0,014074
70000,000000	267,433700	72,571420	0,003739	0,013780
78541,290000	262,419500	74,069310	0,003811	0,013501
88124,780000	257,146800	75,836860	0,003889	0,013186
98877,630000	251,773300	77,413890	0,003972	0,012918
110942,500000	246,219300	79,341330	0,004061	0,012604
124479,600000	240,359100	81,219300	0,004160	0,012312
139668,400000	234,328200	83,164520	0,004268	0,012024
156710,500000	228,018100	85,114680	0,004386	0,011749

frequency [Hz]	real impedance at 50 bar Z´ [Ω m]	imaginary impedance at 50 bar Z´´ [Ω m]	real admittance at 50 bar Y´ [S m1]	imaginary admittance at 50 bar Y´´ [S m1]
175832,000000	221,411300	87,167580	0,004516	0,011472
197286,800000	214,642100	89,033120	0,004659	0,011232
221359,400000	207,638000	90,878880	0,004816	0,011004
248369,400000	200,178000	92,611470	0,004996	0,010798
278675,000000	192,527500	94,179840	0,005194	0,010618
312678,500000	184,618800	95,517990	0,005417	0,010469
350831,100000	176,406500	96,641500	0,005669	0,010348
393638,900000	168,138300	97,563330	0,005947	0,010250
441670,100000	159,552400	97,942440	0,006268	0,010210
495562,000000	150,924500	98,211020	0,006626	0,010182
556029,800000	142,204800	98,072880	0,007032	0,010196
623875,700000	133,427000	97,445380	0,007495	0,010262
700000,000000	124,695900	96,448510	0,008020	0,010368
785412,900000	115,998400	94,977600	0,008621	0,010529
881247,800000	107,456000	93,046030	0,009306	0,010747
988776,300000	99,133700	90,738960	0,010087	0,011021

frequency [Hz]	real impedance at 75 bar Z´ [Ω m]	imaginary impedance at 75 bar Z´´ [Ω m]	real admittance at 75 bar Y´ [S m1]	imaginary admittance at 75 bar Y´´ [S m1]
785,412900	443,535400	73,547900	0,002255	0,013597
881,247700	438,418700	72,935200	0,002281	0,013711
988,776200	433,045800	72,119000	0,002309	0,013866
1109,425000	427,673100	71,300930	0,002338	0,014025
1244,796000	422,570600	70,601780	0,002366	0,014164
1396,684000	417,468700	69,899090	0,002395	0,014306
1567,105000	412,355100	69,264770	0,002425	0,014437
1758,320000	407,524400	68,672640	0,002454	0,014562
1972,868000	402,718200	67,934980	0,002483	0,014720
2213,594000	397,900500	67,265060	0,002513	0,014867
2483,694000	393,060000	66,728930	0,002544	0,014986
2786,750000	388,243600	66,050610	0,002576	0,015140
3126,785000	383,686800	65,550890	0,002606	0,015255
3508,311000	379,130800	65,044830	0,002638	0,015374
3936,389000	374,575800	64,532450	0,002670	0,015496
4416,701000	369,999300	64,142840	0,002703	0,015590
4955,620000	365,446200	63,616210	0,002736	0,015719
5560,297000	360,861000	63,272130	0,002771	0,015805
6238,757000	356,558900	62,966690	0,002805	0,015881
7000,000000	352,236100	62,773730	0,002839	0,015930
7854,129000	347,644300	62,456080	0,002877	0,016011
8812,479000	343,606000	62,287620	0,002910	0,016055
9887,763000	339,266100	62,173540	0,002948	0,016084
11094,250000	334,917100	62,101470	0,002986	0,016103
12447,960000	330,559100	62,069130	0,003025	0,016111
13966,840000	326,473100	62,127710	0,003063	0,016096
15671,050000	322,086300	62,224930	0,003105	0,016071
17583,210000	317,949600	62,519600	0,003145	0,015995
19728,680000	313,814400	62,787540	0,003187	0,015927
22135,950000	309,389800	63,025690	0,003232	0,015867
24836,940000	304,777900	63,582730	0,003281	0,015728
27867,500000	300,542600	64,122970	0,003327	0,015595
31267,850000	296,258100	64,723370	0,003375	0,015450
35083,110000	291,885100	65,423770	0,003426	0,015285
39363,890000	287,506600	66,235650	0,003478	0,015098
44167,020000	283,026300	67,182260	0,003533	0,014885
49556,210000	278,506600	68,114230	0,003591	0,014681
55602,980000	273,887500	69,267570	0,003651	0,014437
62387,570000	269,107800	70,511540	0,003716	0,014182
70000,000000	264,304700	71,870860	0,003784	0,013914
78541,290000	259,351500	73,252190	0,003856	0,013651
88124,780000	254,266400	74,987400	0,003933	0,013336
98877,630000	248,916300	76,487910	0,004017	0,013074
110942,500000	243,470100	78,267960	0,004107	0,012777
124479,600000	237,773800	80,114690	0,004206	0,012482
139668,400000	231,882200	81,932240	0,004313	0,012205
156710,500000	225,711700	83,850250	0,004430	0,011926

frequency [Hz]	real impedance at 75 bar Z´ [Ω m]	imaginary impedance at 75 bar Z´´ [Ω m]	real admittance at 75 bar Y´ [S m1]	imaginary admittance at 75 bar Y´´ [S m1]
175832,000000	219,287800	85,845940	0,004560	0,011649
197286,800000	212,664100	87,604490	0,004702	0,011415
221359,400000	205,708600	89,436440	0,004861	0,011181
248369,400000	198,512500	91,169100	0,005037	0,010969
278675,000000	191,046800	92,713260	0,005234	0,010786
312678,500000	183,289400	94,101810	0,005456	0,010627
350831,100000	175,302000	95,322030	0,005704	0,010491
393638,900000	167,156000	96,176520	0,005982	0,010398
441670,100000	158,801500	96,758290	0,006297	0,010335
495562,000000	150,250100	96,990500	0,006656	0,010310
556029,800000	141,652800	96,855830	0,007060	0,010325
623875,700000	133,006200	96,322140	0,007518	0,010382
700000,000000	124,355700	95,390390	0,008041	0,010483
785412,900000	115,795500	94,004430	0,008636	0,010638
881247,800000	107,351100	92,204190	0,009315	0,010845
988776,300000	99,094670	89,975200	0,010091	0,011114

frequency [Hz]	real impedance at 100 bar Z´ [Ω m]	imaginary impedance at 100 bar Z´´ [Ω m]	real admittance at 100 bar Y´ [S m1]	imaginary admittance at 100 bar Y´´ [S m1]
785,412900	443,662500	74,523580	0,002254	0,013419
881,247700	438,265000	73,852790	0,002282	0,013540
988,776200	432,893900	73,025350	0,002310	0,013694
1109,425000	427,779700	72,392910	0,002338	0,013814
1244,796000	422,409500	71,559900	0,002367	0,013974
1396,684000	417,309100	70,845630	0,002396	0,014115
1567,105000	412,197000	70,199710	0,002426	0,014245
1758,320000	407,097900	69,477460	0,002456	0,014393
1972,868000	402,269200	68,870050	0,002486	0,014520
2213,594000	397,183100	68,070610	0,002518	0,014691
2483,694000	392,344000	67,523110	0,002549	0,014810
2786,750000	387,517500	66,901280	0,002581	0,014947
3126,785000	382,691700	66,274420	0,002613	0,015089
3508,311000	378,137000	65,757450	0,002645	0,015207
3936,389000	373,583300	65,234150	0,002677	0,015329
4416,701000	368,737400	64,719460	0,002712	0,015451
4955,620000	364,456100	64,295750	0,002744	0,015553
5560,297000	359,883000	63,877450	0,002779	0,015655
6238,757000	355,300100	63,511650	0,002815	0,015745
7000,000000	350,989100	63,246640	0,002849	0,015811
7854,129000	346,679600	62,969720	0,002885	0,015881
8812,479000	342,360600	62,740630	0,002921	0,015939
9887,763000	337,751000	62,505050	0,002961	0,015999
11094,250000	333,683800	62,475080	0,002997	0,016006
12447,960000	329,326400	62,432590	0,003037	0,016017
13966,840000	324,959900	62,427350	0,003077	0,016019
15671,050000	320,865400	62,511770	0,003117	0,015997
17583,210000	316,459300	62,685400	0,003160	0,015953
19728,680000	312,324700	62,942920	0,003202	0,015887
22135,950000	307,604400	63,332930	0,003251	0,015790
24836,940000	303,328600	63,666980	0,003297	0,015707
27867,500000	299,049100	64,131650	0,003344	0,015593
31267,850000	294,737700	64,714490	0,003393	0,015452
35083,110000	290,349200	65,345500	0,003444	0,015303
39363,890000	285,999800	66,151250	0,003497	0,015117
44167,020000	281,504800	67,028620	0,003552	0,014919
49556,210000	277,014700	67,954230	0,003610	0,014716
55602,980000	272,409600	69,045500	0,003671	0,014483
62387,570000	267,672400	70,235230	0,003736	0,014238
70000,000000	262,927500	71,594870	0,003803	0,013967
78541,290000	257,962600	72,908510	0,003877	0,013716
88124,780000	252,867400	74,574800	0,003955	0,013409
98877,630000	247,617300	76,041480	0,004038	0,013151
110942,500000	242,190300	77,763330	0,004129	0,012860
124479,600000	236,568700	79,570820	0,004227	0,012567
139668,400000	230,684400	81,373240	0,004335	0,012289
156710,500000	224,604800	83,216160	0,004452	0,012017

frequency [Hz]	real impedance at 100 bar Z´ [Ω m]	imaginary impedance at 100 bar Z´´ [Ω m]	real admittance at 100 bar Y´ [S m1]	imaginary admittance at 100 bar Y´´ [S m1]
175832,000000	218,258500	85,179660	0,004582	0,011740
197286,800000	211,671000	86,936370	0,004724	0,011503
221359,400000	204,809600	88,705960	0,004883	0,011273
248369,400000	197,719000	90,429080	0,005058	0,011058
278675,000000	190,332700	91,956830	0,005254	0,010875
312678,500000	182,680200	93,346510	0,005474	0,010713
350831,100000	174,755200	94,590650	0,005722	0,010572
393638,900000	166,703500	95,413610	0,005999	0,010481
441670,100000	158,433500	96,042100	0,006312	0,010412
495562,000000	149,964300	96,324940	0,006668	0,010382
556029,800000	141,463200	96,220060	0,007069	0,010393
623875,700000	132,846600	95,712800	0,007527	0,010448
700000,000000	124,270000	94,843480	0,008047	0,010544
785412,900000	115,757700	93,505680	0,008639	0,010695
881247,800000	107,320800	91,756050	0,009318	0,010898
988776,300000	99,070650	89,575740	0,010094	0,011164

frequency [Hz]	real impedance at 150 bar Z´ [Ω m]	imaginary impedance at 150 bar Z´´ [Ω m]	real admittance at 150 bar Y´ [S m1]	imaginary admittance at 150 bar Y´´ [S m1]
785,412900	443,892500	74,880710	0,002253	0,013355
881,247700	438,226300	74,082150	0,002282	0,013499
988,776200	433,124800	73,375170	0,002309	0,013629
1109,425000	427,754500	72,542150	0,002338	0,013785
1244,796000	422,359400	71,854630	0,002368	0,013917
1396,684000	417,271900	71,064010	0,002397	0,014072
1567,105000	412,160200	70,415420	0,002426	0,014201
1758,320000	407,049300	69,761510	0,002457	0,014335
1972,868000	401,951200	69,032150	0,002488	0,014486
2213,594000	397,123600	68,417020	0,002518	0,014616
2483,694000	392,308600	67,728420	0,002549	0,014765
2786,750000	387,470700	67,171670	0,002581	0,014887
3126,785000	382,657000	66,474690	0,002613	0,015043
3508,311000	378,102600	65,955330	0,002645	0,015162
3936,389000	373,256000	65,445420	0,002679	0,015280
4416,701000	368,692200	64,976740	0,002712	0,015390
4955,620000	364,140700	64,436630	0,002746	0,015519
5560,297000	359,567900	64,015660	0,002781	0,015621
6238,757000	355,266800	63,697580	0,002815	0,015699
7000,000000	350,674500	63,379440	0,002852	0,015778
7854,129000	346,365200	63,099890	0,002887	0,015848
8812,479000	342,046400	62,868090	0,002924	0,015906
9887,763000	337,718300	62,681800	0,002961	0,015954
11094,250000	333,370000	62,596930	0,003000	0,015975
12447,960000	329,012700	62,551520	0,003039	0,015987
13966,840000	324,646400	62,543300	0,003080	0,015989
15671,050000	320,541000	62,680760	0,003120	0,015954
17583,210000	316,145900	62,795280	0,003163	0,015925
19728,680000	311,731000	62,993060	0,003208	0,015875
22135,950000	307,274200	63,376690	0,003254	0,015779
24836,940000	302,987300	63,760930	0,003300	0,015684
27867,500000	298,707900	64,222020	0,003348	0,015571
31267,850000	294,424400	64,807240	0,003396	0,015430
35083,110000	290,008000	65,428220	0,003448	0,015284
39363,890000	285,602900	66,216940	0,003501	0,015102
44167,020000	281,191500	67,109550	0,003556	0,014901
49556,210000	276,685400	67,975810	0,003614	0,014711
55602,980000	272,025100	69,049060	0,003676	0,014482
62387,570000	267,343600	70,248660	0,003741	0,014235
70000,000000	262,516200	71,581270	0,003809	0,013970
78541,290000	257,579400	72,897260	0,003882	0,013718
88124,780000	252,512200	74,565810	0,003960	0,013411
98877,630000	247,235400	76,018590	0,004045	0,013155
110942,500000	241,836400	77,742790	0,004135	0,012863
124479,600000	236,148200	79,475250	0,004235	0,012583
139668,400000	230,292600	81,280220	0,004342	0,012303
156710,500000	224,214800	83,116170	0,004460	0,012031

frequency [Hz]	real impedance at 150 bar Z´ [Ω m]	imaginary impedance at 150 bar Z´´ [Ω m]	real admittance at 150 bar Y´ [S m1]	imaginary admittance at 150 bar Y´´ [S m1]
175832,000000	217,870700	85,072090	0,004590	0,011755
197286,800000	211,327000	86,795120	0,004732	0,011521
221359,400000	204,494700	88,569560	0,004890	0,011291
248369,400000	197,370700	90,228120	0,005067	0,011083
278675,000000	190,014000	91,761960	0,005263	0,010898
312678,500000	182,390800	93,158530	0,005483	0,010734
350831,100000	174,511500	94,380020	0,005730	0,010595
393638,900000	166,447000	95,228300	0,006008	0,010501
441670,100000	158,198000	95,823840	0,006321	0,010436
495562,000000	149,774000	96,092000	0,006677	0,010407
556029,800000	141,260300	96,009930	0,007079	0,010416
623875,700000	132,694300	95,532760	0,007536	0,010468
700000,000000	124,137700	94,639720	0,008056	0,010566
785412,900000	115,628600	93,301400	0,008648	0,010718
881247,800000	107,254300	91,569720	0,009324	0,010921
988776,300000	99,027000	89,410770	0,010098	0,011184

frequency [Hz]	real impedance at 200 bar Z´ [Ω m]	imaginary impedance at 200 bar Z´´ [Ω m]	real admittance at 200 bar Y´ [S m1]	imaginary admittance at 200 bar Y´´ [S m1]
785,412900	443,020300	74,892570	0,002257	0,013352
881,247700	437,649400	74,063150	0,002285	0,013502
988,776200	432,535200	73,430540	0,002312	0,013618
1109,425000	426,883200	72,547630	0,002343	0,013784
1244,796000	421,783000	71,832270	0,002371	0,013921
1396,684000	416,670900	71,186040	0,002400	0,014048
1567,105000	411,559500	70,534480	0,002430	0,014177
1758,320000	406,473300	69,735790	0,002460	0,014340
1972,868000	401,363400	69,075370	0,002492	0,014477
2213,594000	396,548000	68,389080	0,002522	0,014622
2483,694000	391,439500	67,719030	0,002555	0,014767
2786,750000	386,907100	67,073970	0,002585	0,014909
3126,785000	382,058600	66,576740	0,002617	0,015020
3508,311000	377,527600	65,922890	0,002649	0,015169
3936,389000	372,681100	65,411640	0,002683	0,015288
4416,701000	368,117500	64,941690	0,002717	0,015398
4955,620000	363,555000	64,463810	0,002751	0,015513
5560,297000	358,982500	64,040640	0,002786	0,015615
6238,757000	354,681600	63,720380	0,002819	0,015694
7000,000000	350,100600	63,338790	0,002856	0,015788
7854,129000	345,780500	63,118010	0,002892	0,015843
8812,479000	341,461900	62,883820	0,002929	0,015902
9887,763000	337,134000	62,695050	0,002966	0,015950
11094,250000	332,786000	62,607470	0,003005	0,015973
12447,960000	328,429000	62,559270	0,003045	0,015985
13966,840000	324,062900	62,548160	0,003086	0,015988
15671,050000	319,688000	62,571870	0,003128	0,015982
17583,210000	315,573900	62,738900	0,003169	0,015939
19728,680000	311,439700	62,990740	0,003211	0,015875
22135,950000	306,731000	63,320430	0,003260	0,015793
24836,940000	302,388500	63,690000	0,003307	0,015701
27867,500000	298,137500	64,153790	0,003354	0,015588
31267,850000	293,798700	64,723240	0,003404	0,015450
35083,110000	289,438700	65,352820	0,003455	0,015302
39363,890000	285,006300	66,131010	0,003509	0,015121
44167,020000	280,579500	66,963480	0,003564	0,014934
49556,210000	276,007000	67,860200	0,003623	0,014736
55602,980000	271,403200	68,941610	0,003685	0,014505
62387,570000	266,750500	70,142560	0,003749	0,014257
70000,000000	261,936700	71,423260	0,003818	0,014001
78541,290000	257,001500	72,733710	0,003891	0,013749
88124,780000	251,936200	74,395720	0,003969	0,013442
98877,630000	246,688700	75,850490	0,004054	0,013184
110942,500000	241,278200	77,516890	0,004145	0,012900
124479,600000	235,606100	79,292800	0,004244	0,012611
139668,400000	229,821300	81,068790	0,004351	0,012335
156710,500000	223,732100	82,937230	0,004470	0,012057

frequency [Hz]	real impedance at 200 bar Z´ [Ω m]	imaginary impedance at 200 bar Z´´ [Ω m]	real admittance at 200 bar Y´ [S m1]	imaginary admittance at 200 bar Y´´ [S m1]
175832,000000	217,432600	84,857330	0,004599	0,011784
197286,800000	210,839500	86,551890	0,004743	0,011554
221359,400000	204,079400	88,305140	0,004900	0,011324
248369,400000	196,985900	89,969140	0,005077	0,011115
278675,000000	189,617900	91,529880	0,005274	0,010925
312678,500000	182,015700	92,886890	0,005494	0,010766
350831,100000	174,183400	94,084790	0,005741	0,010629
393638,900000	166,149200	94,942530	0,006019	0,010533
441670,100000	157,930000	95,548570	0,006332	0,010466
495562,000000	149,535300	95,828430	0,006687	0,010435
556029,800000	141,066900	95,734680	0,007089	0,010446
623875,700000	132,528700	95,273210	0,007546	0,010496
700000,000000	123,998900	94,397160	0,008065	0,010594
785412,900000	115,515500	93,077160	0,008657	0,010744
881247,800000	107,138200	91,309170	0,009334	0,010952
988776,300000	98,956220	89,190320	0,010105	0,011212

frequency [Hz]	real impedance at 250 bar Z´ [Ω m]	imaginary impedance at 250 bar Z´´ [Ω m]	real admittance at 250 bar Y´ [S m1]	imaginary admittance at 250 bar Y´´ [S m1]
785,412900	442,148200	74,903820	0,002262	0,013350
881,247700	436,790500	73,996180	0,002289	0,013514
988,776200	431,394600	73,314320	0,002318	0,013640
1109,425000	426,012100	72,552510	0,002347	0,013783
1244,796000	420,630200	71,786960	0,002377	0,013930
1396,684000	415,812700	71,114090	0,002405	0,014062
1567,105000	410,419700	70,412830	0,002437	0,014202
1758,320000	405,333700	69,613060	0,002467	0,014365
1972,868000	400,517800	68,929840	0,002497	0,014508
2213,594000	395,678600	68,381320	0,002527	0,014624
2483,694000	390,594100	67,572770	0,002560	0,014799
2786,750000	386,038300	67,062100	0,002590	0,014912
3126,785000	381,213300	66,429450	0,002623	0,015054
3508,311000	376,377700	65,857430	0,002657	0,015184
3936,389000	371,824600	65,328190	0,002689	0,015307
4416,701000	367,261300	64,856690	0,002723	0,015419
4955,620000	362,406200	64,390520	0,002759	0,015530
5560,297000	358,126600	63,952430	0,002792	0,015637
6238,757000	353,544600	63,579770	0,002828	0,015728
7000,000000	349,245300	63,246970	0,002863	0,015811
7854,129000	344,925400	63,024110	0,002899	0,015867
8812,479000	340,325900	62,736000	0,002938	0,015940
9887,763000	335,998400	62,544500	0,002976	0,015989
11094,250000	331,650800	62,453820	0,003015	0,016012
12447,960000	327,575200	62,455870	0,003053	0,016011
13966,840000	323,209600	62,441940	0,003094	0,016015
15671,050000	318,835100	62,462680	0,003136	0,016010
17583,210000	314,721500	62,626500	0,003177	0,015968
19728,680000	310,307400	62,818080	0,003223	0,015919
22135,950000	305,823600	63,188760	0,003270	0,015826
24836,940000	301,576900	63,519050	0,003316	0,015743
27867,500000	297,298700	63,973300	0,003364	0,015632
31267,850000	292,988700	64,544800	0,003413	0,015493
35083,110000	288,629600	65,170140	0,003465	0,015344
39363,890000	284,237700	65,900420	0,003518	0,015174
44167,020000	279,816700	66,833040	0,003574	0,014963
49556,210000	275,312700	67,689490	0,003632	0,014773
55602,980000	270,710200	68,765570	0,003694	0,014542
62387,570000	266,031300	69,953450	0,003759	0,014295
70000,000000	261,219300	71,227650	0,003828	0,014039
78541,290000	256,313500	72,539010	0,003901	0,013786
88124,780000	251,235900	74,141310	0,003980	0,013488
98877,630000	246,005200	75,640350	0,004065	0,013220
110942,500000	240,597400	77,298190	0,004156	0,012937
124479,600000	235,010200	79,000990	0,004255	0,012658
139668,400000	229,202200	80,760500	0,004363	0,012382
156710,500000	223,158600	82,591800	0,004481	0,012108

frequency [Hz]	real impedance at 250 bar Z´ [Ω m]	imaginary impedance at 250 bar Z´´ [Ω m]	real admittance at 250 bar Y´ [S m1]	imaginary admittance at 250 bar Y´´ [S m1]
175832,000000	216,849300	84,542520	0,004611	0,011828
197286,800000	210,340400	86,261280	0,004754	0,011593
221359,400000	203,532600	87,984260	0,004913	0,011366
248369,400000	196,486500	89,616810	0,005089	0,011159
278675,000000	189,192100	91,161660	0,005286	0,010970
312678,500000	181,621800	92,526180	0,005506	0,010808
350831,100000	173,795900	93,718890	0,005754	0,010670
393638,900000	165,793100	94,585650	0,006032	0,010572
441670,100000	157,604900	95,201740	0,006345	0,010504
495562,000000	149,281500	95,482220	0,006699	0,010473
556029,800000	140,818800	95,387050	0,007101	0,010484
623875,700000	132,326200	94,917730	0,007557	0,010535
700000,000000	123,824300	94,059730	0,008076	0,010632
785412,900000	115,390000	92,776980	0,008666	0,010779
881247,800000	107,043600	91,067440	0,009342	0,010981
988776,300000	98,879410	88,933710	0,010113	0,011244

frequency [Hz]	real impedance at 300 bar Z´ [Ω m]	imaginary impedance at 300 bar Z´´ [Ω m]	real admittance at 300 bar Y´ [S m1]	imaginary admittance at 300 bar Y´´ [S m1]
785,412900	441,597300	74,731240	0,002265	0,013381
881,247700	435,918800	74,004970	0,002294	0,013513
988,776200	430,805100	73,368790	0,002321	0,013630
1109,425000	425,435600	72,530700	0,002351	0,013787
1244,796000	420,348300	71,738850	0,002379	0,013939
1396,684000	414,967000	70,969450	0,002410	0,014091
1567,105000	409,855900	70,316120	0,002440	0,014221
1758,320000	405,051800	69,564650	0,002469	0,014375
1972,868000	399,660200	68,854030	0,002502	0,014523
2213,594000	394,833200	68,235210	0,002533	0,014655
2483,694000	390,006900	67,611340	0,002564	0,014790
2786,750000	385,181300	66,982440	0,002596	0,014929
3126,785000	380,356500	66,348500	0,002629	0,015072
3508,311000	375,814200	65,758830	0,002661	0,015207
3936,389000	371,249900	65,293960	0,002694	0,015315
4416,701000	366,686700	64,821170	0,002727	0,015427
4955,620000	361,843000	64,290460	0,002764	0,015554
5560,297000	357,552400	63,914260	0,002797	0,015646
6238,757000	352,970500	63,540100	0,002833	0,015738
7000,000000	348,671400	63,205860	0,002868	0,015821
7854,129000	344,070500	62,929920	0,002906	0,015891
8812,479000	339,752400	62,691570	0,002943	0,015951
9887,763000	335,436000	62,439830	0,002981	0,016015
11094,250000	331,077800	62,405720	0,003020	0,016024
12447,960000	327,013300	62,348740	0,003058	0,016039
13966,840000	322,648000	62,333440	0,003099	0,016043
15671,050000	318,273800	62,352710	0,003142	0,016038
17583,210000	314,160500	62,514870	0,003183	0,015996
19728,680000	309,746800	62,704590	0,003228	0,015948
22135,950000	305,235500	63,067230	0,003276	0,015856
24836,940000	301,006100	63,453680	0,003322	0,015760
27867,500000	296,711600	63,846950	0,003370	0,015662
31267,850000	292,441300	64,370720	0,003419	0,015535
35083,110000	288,083000	64,993910	0,003471	0,015386
39363,890000	283,724700	65,833640	0,003525	0,015190
44167,020000	279,299800	66,658080	0,003580	0,015002
49556,210000	274,796800	67,511820	0,003639	0,014812
55602,980000	270,223200	68,591690	0,003701	0,014579
62387,570000	265,545600	69,776210	0,003766	0,014332
70000,000000	260,735000	71,046740	0,003835	0,014075
78541,290000	255,830800	72,354190	0,003909	0,013821
88124,780000	250,755100	73,951860	0,003988	0,013522
98877,630000	245,539500	75,403390	0,004073	0,013262
110942,500000	240,161500	77,065690	0,004164	0,012976
124479,600000	234,590200	78,814270	0,004263	0,012688
139668,400000	228,784700	80,568510	0,004371	0,012412
156710,500000	222,758200	82,355260	0,004489	0,012143

frequency [Hz]	real impedance at 300 bar Z´ [Ω m]	imaginary impedance at 300 bar Z´´ [Ω m]	real admittance at 300 bar Y´ [S m1]	imaginary admittance at 300 bar Y´´ [S m1]
175832,000000	216,493800	84,273410	0,004619	0,011866
197286,800000	210,015000	85,999470	0,004762	0,011628
221359,400000	203,237300	87,730390	0,004920	0,011399
248369,400000	196,179400	89,394090	0,005097	0,011186
278675,000000	188,930600	90,913820	0,005293	0,010999
312678,500000	181,364300	92,275480	0,005514	0,010837
350831,100000	173,567900	93,478750	0,005761	0,010698
393638,900000	165,610500	94,328380	0,006038	0,010601
441670,100000	157,426400	94,944050	0,006352	0,010533
495562,000000	149,107100	95,224100	0,006707	0,010502
556029,800000	140,695800	95,160570	0,007108	0,010509
623875,700000	132,206400	94,692150	0,007564	0,010561
700000,000000	123,753200	93,869600	0,008081	0,010653
785412,900000	115,298600	92,571110	0,008673	0,010803
881247,800000	106,992200	90,862970	0,009346	0,011006
988776,300000	98,813770	88,750020	0,010120	0,011268

frequency [Hz]	real impedance at 400 bar Z´ [Ω m]	imaginary impedance at 400 bar Z´´ [Ω m]	real admittance at 400 bar Y´ [S m1]	imaginary admittance at 400 bar Y´´ [S m1]
785,412900	439,007400	74,608100	0,002278	0,013403
881,247700	433,932200	73,745570	0,002305	0,013560
988,776200	428,549600	72,984660	0,002333	0,013702
1109,425000	423,449400	72,268100	0,002362	0,013837
1244,796000	418,055500	71,572720	0,002392	0,013972
1396,684000	412,956600	70,848080	0,002422	0,014115
1567,105000	407,858300	70,119900	0,002452	0,014261
1758,320000	402,760600	69,388160	0,002483	0,014412
1972,868000	397,651400	68,722250	0,002515	0,014551
2213,594000	392,836700	68,031330	0,002546	0,014699
2483,694000	388,022500	67,337060	0,002577	0,014851
2786,750000	383,197300	66,706280	0,002610	0,014991
3126,785000	378,654500	66,119670	0,002641	0,015124
3508,311000	373,819400	65,544200	0,002675	0,015257
3936,389000	369,266800	65,011600	0,002708	0,015382
4416,701000	364,704000	64,536300	0,002742	0,015495
4955,620000	360,142300	64,053090	0,002777	0,015612
5560,297000	355,570600	63,624000	0,002812	0,015717
6238,757000	351,270600	63,297360	0,002847	0,015798
7000,000000	346,690600	62,909240	0,002884	0,015896
7854,129000	342,371500	62,680910	0,002921	0,015954
8812,479000	338,054000	62,439160	0,002958	0,016016
9887,763000	333,727300	62,242230	0,002996	0,016066
11094,250000	329,391500	62,087860	0,003036	0,016106
12447,960000	325,316800	62,084110	0,003074	0,016107
13966,840000	320,963100	62,007940	0,003116	0,016127
15671,050000	316,578900	62,078030	0,003159	0,016109
17583,210000	312,466600	62,234480	0,003200	0,016068
19728,680000	307,892100	62,496880	0,003248	0,016001
22135,950000	303,695000	62,748940	0,003293	0,015937
24836,940000	299,466900	63,129210	0,003339	0,015841
27867,500000	295,229700	63,528080	0,003387	0,015741
31267,850000	290,933000	64,038730	0,003437	0,015616
35083,110000	286,604400	64,660320	0,003489	0,015465
39363,890000	282,271000	65,392560	0,003543	0,015292
44167,020000	277,864800	66,264370	0,003599	0,015091
49556,210000	273,392000	67,116130	0,003658	0,014900
55602,980000	268,837200	68,239870	0,003720	0,014654
62387,570000	264,186800	69,320630	0,003785	0,014426
70000,000000	259,450500	70,648090	0,003854	0,014155
78541,290000	254,562400	71,899550	0,003928	0,013908
88124,780000	249,546300	73,500740	0,004007	0,013605
98877,630000	244,348400	74,897710	0,004093	0,013352
110942,500000	238,990000	76,597820	0,004184	0,013055
124479,600000	233,438400	78,291340	0,004284	0,012773
139668,400000	227,707500	80,010650	0,004392	0,012498
156710,500000	221,715400	81,793960	0,004510	0,012226

frequency [Hz]	real impedance at 400 bar Z´ [Ω m]	imaginary impedance at 400 bar Z´´ [Ω m]	real admittance at 400 bar Y´ [S m1]	imaginary admittance at 400 bar Y´´ [S m1]
175832,000000	215,486200	83,708080	0,004641	0,011946
197286,800000	209,057400	85,394470	0,004783	0,011710
221359,400000	202,341800	87,134540	0,004942	0,011477
248369,400000	195,361600	88,774590	0,005119	0,011264
278675,000000	188,149000	90,295300	0,005315	0,011075
312678,500000	180,660600	91,639940	0,005535	0,010912
350831,100000	172,926000	92,860820	0,005783	0,010769
393638,900000	165,045600	93,701810	0,006059	0,010672
441670,100000	156,921400	94,341120	0,006373	0,010600
495562,000000	148,660800	94,647280	0,006727	0,010566
556029,800000	140,283100	94,596360	0,007128	0,010571
623875,700000	131,866100	94,135510	0,007583	0,010623
700000,000000	123,460400	93,308680	0,008100	0,010717
785412,900000	115,080200	92,066100	0,008690	0,010862
881247,800000	106,785400	90,399200	0,009365	0,011062
988776,300000	98,670090	88,310470	0,010135	0,011324

frequency [Hz]	real impedance at 500 bar Z´ [Ω m]	imaginary impedance at 500 bar Z´´ [Ω m]	real admittance at 500 bar Y´ [S m1]	imaginary admittance at 500 bar Y´´ [S m1]
785,412900	437,315700	74,320590	0,002287	0,013455
881,247700	432,201900	73,684270	0,002314	0,013571
988,776200	426,550600	72,797360	0,002344	0,013737
1109,425000	421,168900	72,030140	0,002374	0,013883
1244,796000	416,069800	71,307460	0,002403	0,014024
1396,684000	410,958800	70,652950	0,002433	0,014154
1567,105000	406,142700	69,970850	0,002462	0,014292
1758,320000	401,057400	69,166790	0,002493	0,014458
1972,868000	395,960400	68,430020	0,002526	0,014613
2213,594000	391,134000	67,806740	0,002557	0,014748
2483,694000	386,308400	67,178430	0,002589	0,014886
2786,750000	381,471900	66,611640	0,002621	0,015012
3126,785000	376,941100	65,956020	0,002653	0,015162
3508,311000	372,106400	65,377680	0,002687	0,015296
3936,389000	367,554200	64,842310	0,002721	0,015422
4416,701000	363,003000	64,300620	0,002755	0,015552
4955,620000	358,441700	63,815140	0,002790	0,015670
5560,297000	353,859300	63,445210	0,002826	0,015762
6238,757000	349,559800	63,115010	0,002861	0,015844
7000,000000	345,261700	62,774400	0,002896	0,015930
7854,129000	340,683600	62,371880	0,002935	0,016033
8812,479000	336,355700	62,186160	0,002973	0,016081
9887,763000	332,310800	62,038020	0,003009	0,016119
11094,250000	327,975500	61,880200	0,003049	0,016160
12447,960000	323,631300	61,762420	0,003090	0,016191
13966,840000	319,267500	61,738130	0,003132	0,016197
15671,050000	315,175700	61,802870	0,003173	0,016180
17583,210000	311,075000	61,900880	0,003215	0,016155
19728,680000	306,462700	62,206730	0,003263	0,016075
22135,950000	302,238600	62,448010	0,003309	0,016013
24836,940000	298,050700	62,776350	0,003355	0,015930
27867,500000	293,831700	63,227250	0,003403	0,015816
31267,850000	289,564400	63,737460	0,003453	0,015689
35083,110000	285,293100	64,364490	0,003505	0,015537
39363,890000	280,961500	65,089190	0,003559	0,015364
44167,020000	276,596600	65,910930	0,003615	0,015172
49556,210000	272,114300	66,802470	0,003675	0,014970
55602,980000	267,597600	67,776160	0,003737	0,014754
62387,570000	263,009300	68,962630	0,003802	0,014501
70000,000000	258,300600	70,189810	0,003871	0,014247
78541,290000	253,433900	71,580830	0,003946	0,013970
88124,780000	248,419600	73,074690	0,004025	0,013685
98877,630000	243,280700	74,477580	0,004110	0,013427
110942,500000	237,980900	76,091340	0,004202	0,013142
124479,600000	232,462300	77,783580	0,004302	0,012856
139668,400000	226,737700	79,492180	0,004410	0,012580
156710,500000	220,859900	81,303310	0,004528	0,012300

frequency [Hz]	real impedance at 500 bar Z´ [Ω m]	imaginary impedance at 500 bar Z´´ [Ω m]	real admittance at 500 bar Y´ [S m1]	imaginary admittance at 500 bar Y´´ [S m1]
175832,000000	214,637900	83,206220	0,004659	0,012018
197286,800000	208,204800	84,834380	0,004803	0,011788
221359,400000	201,576900	86,596790	0,004961	0,011548
248369,400000	194,672900	88,215920	0,005137	0,011336
278675,000000	187,469400	89,727900	0,005334	0,011145
312678,500000	180,041900	91,089270	0,005554	0,010978
350831,100000	172,399800	92,268510	0,005800	0,010838
393638,900000	164,562600	93,162040	0,006077	0,010734
441670,100000	156,488700	93,783880	0,006390	0,010663
495562,000000	148,285700	94,117870	0,006744	0,010625
556029,800000	139,980500	94,072910	0,007144	0,010630
623875,700000	131,594200	93,629920	0,007599	0,010680
700000,000000	123,225100	92,860900	0,008115	0,010769
785412,900000	114,895600	91,655720	0,008704	0,010910
881247,800000	106,643100	89,991660	0,009377	0,011112
988776,300000	98,558520	87,963200	0,010146	0,011368

frequency [Hz]	real impedance at 600 bar Z´ [Ω m]	imaginary impedance at 600 bar Z´´ [Ω m]	real admittance at 600 bar Y´ [S m1]	imaginary admittance at 600 bar Y´´ [S m1]
785,412900	435,060000	73,937250	0,002299	0,013525
881,247700	429,946500	73,299740	0,002326	0,013643
988,776200	424,564500	72,534630	0,002355	0,013787
1109,425000	419,465000	71,814030	0,002384	0,013925
1244,796000	414,071700	71,113760	0,002415	0,014062
1396,684000	408,985700	70,313740	0,002445	0,014222
1567,105000	403,888000	69,582390	0,002476	0,014371
1758,320000	398,790700	68,847500	0,002508	0,014525
1972,868000	393,963900	68,226540	0,002538	0,014657
2213,594000	388,867900	67,483760	0,002572	0,014818
2483,694000	384,324300	66,902480	0,002602	0,014947
2786,750000	379,511300	66,201070	0,002635	0,015105
3126,785000	374,969100	65,610950	0,002667	0,015241
3508,311000	370,416200	65,080730	0,002700	0,015366
3936,389000	365,582700	64,494500	0,002735	0,015505
4416,701000	361,009400	64,077380	0,002770	0,015606
4955,620000	356,459600	63,526410	0,002805	0,015741
5560,297000	352,181200	63,080940	0,002839	0,015853
6238,757000	347,589700	62,759280	0,002877	0,015934
7000,000000	343,292000	62,416280	0,002913	0,016021
7854,129000	338,984800	62,121990	0,002950	0,016097
8812,479000	334,679100	61,815810	0,002988	0,016177
9887,763000	330,353500	61,612990	0,003027	0,016230
11094,250000	326,289200	61,562050	0,003065	0,016244
12447,960000	321,945700	61,440750	0,003106	0,016276
13966,840000	317,863500	61,466640	0,003146	0,016269
15671,050000	313,502500	61,417980	0,003190	0,016282
17583,210000	309,392000	61,565980	0,003232	0,016243
19728,680000	304,942700	61,787430	0,003279	0,016185
22135,950000	300,765000	62,088840	0,003325	0,016106
24836,940000	296,578300	62,412200	0,003372	0,016023
27867,500000	292,399700	62,812390	0,003420	0,015920
31267,850000	288,150900	63,373650	0,003470	0,015779
35083,110000	283,937300	64,006550	0,003522	0,015623
39363,890000	279,551800	64,711230	0,003577	0,015453
44167,020000	275,284100	65,496680	0,003633	0,015268
49556,210000	270,859900	66,394310	0,003692	0,015062
55602,980000	266,334000	67,406680	0,003755	0,014835
62387,570000	261,732900	68,530380	0,003821	0,014592
70000,000000	257,027900	69,747660	0,003891	0,014337
78541,290000	252,232700	71,099020	0,003965	0,014065
88124,780000	247,305200	72,606300	0,004044	0,013773
98877,630000	242,170800	73,999220	0,004129	0,013514
110942,500000	236,903700	75,610250	0,004221	0,013226
124479,600000	231,445000	77,308530	0,004321	0,012935
139668,400000	225,726500	79,005030	0,004430	0,012657
156710,500000	219,869600	80,764580	0,004548	0,012382

frequency [Hz]	real impedance at 600 bar Z´ [Ω m]	imaginary impedance at 600 bar Z´´ [Ω m]	real admittance at 600 bar Y´ [S m1]	imaginary admittance at 600 bar Y´´ [S m1]
175832,000000	213,723400	82,637350	0,004679	0,012101
197286,800000	207,389600	84,333550	0,004822	0,011858
221359,400000	200,799800	86,014130	0,004980	0,011626
248369,400000	193,931100	87,635240	0,005156	0,011411
278675,000000	186,788900	89,162030	0,005354	0,011216
312678,500000	179,438000	90,508710	0,005573	0,011049
350831,100000	171,799100	91,754330	0,005821	0,010899
393638,900000	164,028700	92,595480	0,006096	0,010800
441670,100000	156,013900	93,240590	0,006410	0,010725
495562,000000	147,861000	93,559110	0,006763	0,010688
556029,800000	139,612700	93,543150	0,007163	0,010690
623875,700000	131,281600	93,131770	0,007617	0,010737
700000,000000	122,959100	92,358150	0,008133	0,010827
785412,900000	114,658800	91,172610	0,008722	0,010968
881247,800000	106,477800	89,566380	0,009392	0,011165
988776,300000	98,418720	87,561230	0,010161	0,011421

frequency [Hz]	real impedance at 700 bar Z´ [Ω m]	imaginary impedance at 700 bar Z´´ [Ω m]	real admittance at 700 bar Y´ [S m1]	imaginary admittance at 700 bar Y´´ [S m1]
785,412900	433,342500	73,800930	0,002308	0,013550
881,247700	427,960200	73,037940	0,002337	0,013692
988,776200	422,847700	72,393180	0,002365	0,013813
1109,425000	417,479200	71,549030	0,002395	0,013976
1244,796000	412,380500	70,823300	0,002425	0,014120
1396,684000	407,282300	70,094030	0,002455	0,014267
1567,105000	402,184800	69,361210	0,002486	0,014417
1758,320000	397,357600	68,742860	0,002517	0,014547
1972,868000	392,261200	68,002150	0,002549	0,014705
2213,594000	387,435500	67,374440	0,002581	0,014842
2483,694000	382,903900	66,724040	0,002612	0,014987
2786,750000	378,079500	66,087240	0,002645	0,015132
3126,785000	373,256000	65,445420	0,002679	0,015280
3508,311000	368,714800	64,848100	0,002712	0,015421
3936,389000	364,152000	64,373100	0,002746	0,015534
4416,701000	359,590200	63,890200	0,002781	0,015652
4955,620000	355,040700	63,337450	0,002817	0,015788
5560,297000	350,751700	62,951190	0,002851	0,015885
6238,757000	346,182400	62,505200	0,002889	0,015999
7000,000000	341,874200	62,220100	0,002925	0,016072
7854,129000	337,567400	61,923110	0,002962	0,016149
8812,479000	333,251400	61,672350	0,003001	0,016215
9887,763000	328,937000	61,408190	0,003040	0,016284
11094,250000	324,873300	61,353600	0,003078	0,016299
12447,960000	320,530400	61,228590	0,003120	0,016332
13966,840000	316,459500	61,195140	0,003160	0,016341
15671,050000	312,088500	61,197500	0,003204	0,016341
17583,210000	307,687600	61,338430	0,003250	0,016303
19728,680000	303,586500	61,567780	0,003294	0,016242
22135,950000	299,420500	61,811290	0,003340	0,016178
24836,940000	295,234900	62,129510	0,003387	0,016095
27867,500000	291,074600	62,580850	0,003436	0,015979
31267,850000	286,849100	63,034870	0,003486	0,015864
35083,110000	282,648200	63,612340	0,003538	0,015720
39363,890000	278,364900	64,385320	0,003592	0,015531
44167,020000	274,059800	65,205400	0,003649	0,015336
49556,210000	269,677000	66,054490	0,003708	0,015139
55602,980000	265,181200	67,065700	0,003771	0,014911
62387,570000	260,594700	68,135210	0,003837	0,014677
70000,000000	255,920400	69,351290	0,003907	0,014419
78541,290000	251,128700	70,693280	0,003982	0,014146
88124,780000	246,205300	72,190080	0,004062	0,013852
98877,630000	241,157200	73,597500	0,004147	0,013587
110942,500000	235,907700	75,156360	0,004239	0,013306
124479,600000	230,481600	76,852670	0,004339	0,013012
139668,400000	224,863600	78,526910	0,004447	0,012734
156710,500000	218,986100	80,266650	0,004566	0,012458

frequency [Hz]	real impedance at 700 bar Z´ [Ω m]	imaginary impedance at 700 bar Z´´ [Ω m]	real admittance at 700 bar Y´ [S m1]	imaginary admittance at 700 bar Y´´ [S m1]
175832,000000	212,900400	82,148450	0,004697	0,012173
197286,800000	206,603100	83,761830	0,004840	0,011939
221359,400000	200,033200	85,479320	0,004999	0,011699
248369,400000	193,199200	87,101660	0,005176	0,011481
278675,000000	186,159100	88,622250	0,005372	0,011284
312678,500000	178,817300	89,960950	0,005592	0,011116
350831,100000	171,254700	91,194950	0,005839	0,010966
393638,900000	163,518600	92,044390	0,006116	0,010864
441670,100000	155,603300	92,700740	0,006427	0,010787
495562,000000	147,507600	93,047500	0,006779	0,010747
556029,800000	139,291200	93,046380	0,007179	0,010747
623875,700000	131,037800	92,684230	0,007631	0,010789
700000,000000	122,721600	91,912150	0,008149	0,010880
785412,900000	114,472200	90,763760	0,008736	0,011018
881247,800000	106,317800	89,178760	0,009406	0,011213
988776,300000	98,320710	87,197870	0,010171	0,011468

frequency [Hz]	real impedance at 800 bar Z´ [Ω m]	imaginary impedance at 800 bar Z´´ [Ω m]	real admittance at 800 bar Y´ [S m1]	imaginary admittance at 800 bar Y´´ [S m1]
785,412900	453,628800	77,337240	0,002204	0,012930
881,247700	447,976800	76,454080	0,002232	0,013080
988,776200	442,607100	75,617110	0,002259	0,013225
1109,425000	437,224600	74,854550	0,002287	0,013359
1244,796000	431,829800	74,163570	0,002316	0,013484
1396,684000	426,461400	73,318180	0,002345	0,013639
1567,105000	421,387800	72,445920	0,002373	0,013803
1758,320000	416,276700	71,791530	0,002402	0,013929
1972,868000	411,216000	70,844870	0,002432	0,014115
2213,594000	406,081500	70,325070	0,002463	0,014220
2483,694000	401,009100	69,446620	0,002494	0,014400
2786,750000	396,194400	68,755200	0,002524	0,014544
3126,785000	391,380300	68,060420	0,002555	0,014693
3508,311000	386,566700	67,362310	0,002587	0,014845
3936,389000	381,742000	66,727430	0,002620	0,014986
4416,701000	377,188200	66,202710	0,002651	0,015105
4955,620000	372,365200	65,557080	0,002686	0,015254
5560,297000	367,813200	65,020320	0,002719	0,015380
6238,757000	363,262200	64,477240	0,002753	0,015509
7000,000000	358,689800	64,052990	0,002788	0,015612
7854,129000	354,129700	63,557460	0,002824	0,015734
8812,479000	349,852300	63,104790	0,002858	0,015847
9887,763000	345,543100	62,825560	0,002894	0,015917
11094,250000	341,235300	62,534420	0,002931	0,015991
12447,960000	336,669500	62,061980	0,002970	0,016113
13966,840000	332,624400	61,916450	0,003006	0,016151
15671,050000	328,299700	61,704160	0,003046	0,016206
17583,210000	323,966000	61,533490	0,003087	0,016251
19728,680000	319,623500	61,402180	0,003129	0,016286
22135,950000	315,542400	61,417600	0,003169	0,016282
24836,940000	311,182500	61,358130	0,003214	0,016298
27867,500000	306,753900	61,486200	0,003260	0,016264
31267,850000	302,562600	61,579960	0,003305	0,016239
35083,110000	298,295900	61,741900	0,003352	0,016196
39363,890000	294,037900	61,984730	0,003401	0,016133
44167,020000	289,721600	62,342830	0,003452	0,016040
49556,210000	285,390500	62,609980	0,003504	0,015972
55602,980000	281,018100	63,039490	0,003558	0,015863
62387,570000	276,581300	63,464690	0,003616	0,015757
70000,000000	272,085800	63,983940	0,003675	0,015629
78541,290000	267,542600	64,543100	0,003738	0,015494
88124,780000	262,817800	65,201170	0,003805	0,015337
98877,630000	258,068200	65,793940	0,003875	0,015199
110942,500000	253,232000	66,446180	0,003949	0,015050
124479,600000	248,316600	67,011840	0,004027	0,014923
139668,400000	243,276100	67,659050	0,004111	0,014780
156710,500000	238,079200	68,276580	0,004200	0,014646

frequency [Hz]	real impedance at 800 bar Z´ [Ω m]	imaginary impedance at 800 bar Z´´ [Ω m]	real admittance at 800 bar Y´ [S m1]	imaginary admittance at 800 bar Y´´ [S m1]
175832,000000	232,785500	68,961400	0,004296	0,014501
197286,800000	227,370500	69,390010	0,004398	0,014411
221359,400000	221,806700	69,855080	0,004508	0,014315
248369,400000	216,131900	70,229130	0,004627	0,014239
278675,000000	210,279100	70,442500	0,004756	0,014196
312678,500000	204,305500	70,508980	0,004895	0,014183
350831,100000	198,189100	70,494310	0,005046	0,014186
393638,900000	192,040700	70,010390	0,005207	0,014284
441670,100000	185,766300	69,416770	0,005383	0,014406
495562,000000	179,452400	68,488200	0,005573	0,014601
556029,800000	173,178000	67,273000	0,005774	0,014865
623875,700000	166,933000	65,652700	0,005990	0,015232
700000,000000	160,951300	63,592140	0,006213	0,015725
785412,900000	155,126100	61,290590	0,006446	0,016316
881247,800000	149,477300	58,697290	0,006690	0,017037
988776,300000	144,054400	55,757240	0,006942	0,017935

III.7 CALCULATIONS OF BULK CONDUCTIVITIES OF SAMPLE 17/08/00/11 CORE 2:

pressure measurement 2 [bar]	resistivity R1-1of elem. cell 1 [Ω]	capacity C1-1 * E^{-7} of elem. cell 1 [F]	resistivity R2-1 of elem. cell 2 [Ω]	capacity C2-1 * E^{-9} of elem. cell 2 [F]
0	82	3,58	142	0,699
25	115	3,59	141	0,917
50	136	3,44	135	1,11
75	139	3,45	132	1,17
100	141	3,46	131	1,2
150	142	3,46	131	1,2
200	142	3,46	131	1,21
250	141	3,47	130	1,21
300	141	3,47	130	1,22
400	141	3,5	129	1,3
500	140	3,52	129	1,24
600	140	3,55	128	1,25
700	140	3,55	128	1,25
800	148	2,66	138	0,772

resistivity R3-1 of elem. cell 3 [Ω]	capacity C3-1 * E^{-9} of elem. cell 3 [F]	X2-2
178	8,15	0,0644
182	8,24	0,104
180	8,27	0,124
180	8,28	0,128
180	8,29	0,13
179	8,29	0,13
179	8,3	0,131
179	8,3	0,13
178	8,3	0,13
178	8,31	0,131
177	8,31	0,131
176	8,32	0,13
176	8,32	0,13
176	2,84	0,176
surface resisitivity	surface resisitivity	

III.8 STATISTICAL ANALYSIS OF BULK CONDUCTIVITIES OF SAMPLE 17/08/00/11

pressure core 1 [bar]	bulk resistivity core 1 R [Ω m]	pressure core 2 [bar]	bulk resistivity core 2 R [Ω m]
0,000000	542,691000	25,000000	400,972000
75,000000	537,642000	50,000000	425,854000
100,000000	523,260000	75,000000	433,862000
150,000000	511,326000	100,000000	433,004000
200,000000	511,020000	150,000000	432,718000
250,000000	509,490000	200,000000	433,290000
300,000000	508,878000	250,000000	432,432000
400,000000	506,430000	300,000000	431,288000
		400,000000	430,716000
		500,000000	428,714000
		600,000000	426,712000
		700,000000	424,424000
		800,000000	422,994000
			413,842000

measurement 1		measurement 2	
sum of bulk resistivity [Ω m]	4150,737000	sum of bulk resistivity [Ω m]	5970,822000
av. bulk resistivity [Ω m]	518,842125	av. bulk resistivity [Ω m]	426,4872857
av. bulk conductivity [S m^{-1}]	0,001927369	av. bulk conductivity [S m^{-1}]	0,002344736

IV. STABLE ISOTOPE ANALYSIS

IV.1 OWN MEASUREMENT DATA AND CALCULATIONS:

samples	$d^{13}C_{calcite}$ V-PDB mean [‰]	$d^{18}O_{calcite}$ V-PDB mean [‰]	$d^{13}C_{graphite}$ V-PDB [‰]	Δ (cal-gr) [‰]
12/08/00/02	9,64	-13,99	6,46	3,19
12/08/00/03	9,53	-13,55		
15/08/00/01	10,34	-12,20	6,85	3,49
17/08/00/04	7,80	-11,45	4,84	2,96
17/08/00/05	10,43	-10,10	7,27	3,16
17/08/00/10	9,87	-11,20	6,68	3,19
17/08/00/11	11,20	-10,23	8,03	3,16
17/08/00/12	9,97	-11,02	6,76	3,20
17/08/00/13	10,50	-8,49	7,20	3,31
17/08/00/15	11,07	-10,89	7,92	3,16
17/08/00/16	6,61	-9,80	3,86	2,75
17/08/00/17	10,34	-10,34	7,58	2,76
17/08/00/19	9,82	-12,51	6,98	2,84
17/08/00/20	10,77	-7,15	7,52	3,25
17/08/00/21	9,94	-11,65	7,26	2,67
18/08/00/02	9,61	-11,70	6,01	3,60
3/10/01/3	9,30	-11,38	6,60	2,70
3/10/01/4	6,95	-11,68	4,42	2,53
3/10/01/5	7,26	-9,46	4,77	2,49
Elim Am	11,08	-7,46	7,06	4,02
Omaruru Sp	8,63	-7,51	6,18	2,45
17/08/00/16 II			3,72	
17/08/00/21 II			7,29	
sum	200,66	-223,74	141,26	60,87
mean	9,555047619	-10,65447619	6,421045455	3,04355
min	6,61	-13,99	3, 72	2,45
max	11,2	-7,15	8,03	4,02
standard deviation	1,358982725	1,870403796	1,284107527	0,402266012

samples	$^{13}C/^{12}C$ calcite	$^{13}C/^{12}C$ graphite	$\alpha_{cc\text{-}gr}$	10^3 x ln α
12/08/00/02	0,0113455491	0,0113097586	1,0031645664	3,159569693
12/08/00/03				
15/08/00/01	0,0113534151	0,0113141748	1,0034682425	3,462242056
17/08/00/04	0,0113248052	0,0112915880	1,0029417619	2,937443358
17/08/00/05	0,0113544377	0,0113189282	1,0031371833	3,132272574
17/08/00/10	0,0113481449	0,0113122645	1,0031718123	3,166792709
17/08/00/11	0,0113630005	0,0113274684	1,0031368021	3,131892569
17/08/00/12	0,0113491787	0,0113131972	1,0031804903	3,175443283
17/08/00/13	0,0113552243	0,0113180854	1,0032813806	3,276008641
17/08/00/15	0,0113616295	0,0113261761	1,0031302150	3,125326035
17/08/00/16	0,0113114779	0,0112805756	1,0027394258	2,735680428
17/08/00/17	0,0113533814	0,0113223780	1,0027382441	2,734501949
17/08/00/19	0,0113475830	0,0113156357	1,0028232934	2,819315405
17/08/00/20	0,0113582022	0,0113216925	1,0032247531	3,219564716
17/08/00/21	0,0113488641	0,0113188270	1,0026537234	2,650208447
18/08/00/02	0,0113452344	0,0113047356	1,0035824694	3,576067601
3/10/01/3	0,0113416947	0,0113113768	1,0026803073	2,676721674
3/10/01/4	0,0113152536	0,0112868235	1,0025188766	2,515709588
3/10/01/5	0,0113188158	0,0112908014	1,0024811648	2,478091836
Elim Am	0,0113616632	0,0113165346	1,0039878458	3,979915428
Omaruru Sp	0,0113341321	0,0113066459	1,0024309766	2,428026521
17/08/00/16 II				
17/08/00/21 II				
sum				60,38079451
mean				3,019039726
min				2,428026521
max				3,979915428
standard deviation				0,397055763

IV.2 TYPES OF GRAPHITE-BEARING MARBLES:

Type I	Type II	Type III
Elim Am	12/08/00/02	3/10/01/4
Omaruru Sp	12/08/00/03	3/10/01/5
	15/08/00/01	
	17/08/00/04	
	17/08/00/05	
	17/08/00/10	
	17/08/00/11	
	17/08/00/12	
	17/08/00/13	
	17/08/00/15	
	17/08/00/16	
	17/08/00/17	
	17/08/00/19	
	17/08/00/20	
	17/08/00/21	
	18/08/00/02	
	3/10/01/3	

IV.3 GEOTHERMOMETRY CALCULATIONS:

Δ (cc-gr)	10^3 x ln α	Thermometer Valley & O´Neil 1981 [° C] (610-760° C)	Thermometer Wada & Suzuki 1982 [° C] (400-680° C)	Thermometer Morikiyo 1984 [° C] (270-650° C)
1	1	1027	1153	775
1,1	1,1	1013	1129	769
1,2	1,2	1000	1106	762
1,3	1,3	987	1085	756
1,4	1,4	973	1064	750
1,5	1,5	960	1044	744
1,6	1,6	947	1025	738
1,7	1,7	933	1007	733
1,8	1,8	920	990	727
1,9	1,9	906	973	721
2	2	893	957	716
2,1	2,1	880	941	710
2,2	2,2	866	926	705
2,3	2,3	853	912	700
2,4	2,4	840	898	695
2,5	2,5	826	885	690
2,6	2,6	813	872	685
2,7	2,7	799	859	680
2,8	2,8	786	847	675
2,9	2,9	773	836	670
3	**3**	**759**	**824**	**666**
3,1	**3,1**	**746**	**813**	**661**
3,2	3,2	733	802	656
3,3	3,3	719	792	652
3,4	3,4	706	782	648
3,5	3,5	693	772	643
3,6	3,6	679	763	639
3,7	3,7	666	753	635
3,8	3,8	652	744	630
3,9	3,9	639	735	626
4	4	626	727	622
4,1	4,1	612	718	618
4,2	4,2	599	710	614
4,3	4,3	586	702	610
4,4	4,4		695	607
4,5	4,5		687	603
4,6	4,6		680	599
4,7	4,7		672	595
4,8	4,8		665	592
4,9	4,9		658	588
5	5		652	584
5,1	5,1		645	581
5,2	5,2		638	577
5,3	5,3		632	574
5,4	5,4		626	571

Δ (cc-gr)	10^3 x ln α	Thermometer Valley & O´Neil 1981 [° C] (610-760° C)	Thermometer Wada & Suzuki 1982 [° C] (400-680° C)	Thermometer Morikiyo 1984 [° C] (270-650° C)
5,5	5,5		620	567
5,6	5,6		614	564
5,7	5,7		608	561
5,8	5,8		602	557
5,9	5,9		597	554
6	6		591	551
6,1	6,1		586	548
6,2	6,2		580	545
6,3	6,3		575	542
6,4	6,4		570	539
6,5	6,5		565	536
6,6	6,6		560	533
6,7	6,7		555	530
6,8	6,8		550	527
6,9	6,9		546	524
7	7		541	521
7,1	7,1		537	519
7,2	7,2		532	516
7,3	7,3		528	513
7,4	7,4		523	510
7,5	7,5		519	508
7,6	7,6		515	505
7,7	7,7		511	502
7,8	7,8		507	500
7,9	7,9		503	497
8	8		499	495
8,1	8,1		495	492
8,2	8,2		491	490
8,3	8,3		487	487
8,4	8,4		484	485
8,5	8,5		480	482
8,6	8,6		476	480
8,7	8,7		473	477
8,8	8,8		469	475
8,9	8,9		466	473
9	9		463	470
9,1	9,1		459	468
9,2	9,2		456	466
9,3	9,3		453	464
9,4	9,4		449	461
9,5	9,5		446	459
9,6	9,6		443	457
9,7	9,7		440	455
9,8	9,8		437	453
9,9	9,9		434	450
10	10		431	448
10,1	10,1		428	446

Δ (cc-gr)	10^3 x ln α	Thermometer Valley & O´Neil 1981 [° C] (610-760° C)	Thermometer Wada & Suzuki 1982 [° C] (400-680° C)	Thermometer Morikiyo 1984 [° C] (270-650° C)
10,2	10,2		425	444
10,3	10,3		422	442
10,4	10,4		419	440
10,5	10,5		417	438
10,6	10,6		414	436
10,7	10,7		411	434
10,8	10,8		408	432
10,9	10,9		406	430
11	11		403	428
11,1	11,1		401	426
11,2	11,2			424
11,3	11,3			422
11,4	11,4			420
11,5	11,5			419
11,6	11,6			417
11,7	11,7			415
11,8	11,8			413
11,9	11,9			411
12	12			409
12,1	12,1			408
12,2	12,2			406
12,3	12,3			404
12,4	12,4			402
12,5	12,5			401
12,6	12,6			399
12,7	12,7			397
12,8	12,8			396
12,9	12,9			394
13	13			392
13,1	13,1			391
13,2	13,2			389
13,3	13,3			387
13,4	13,4			386
13,5	13,5			384
13,6	13,6			383
13,7	13,7			381
13,8	13,8			379
13,9	13,9			378
14	14			376
14,1	14,1			375
14,2	14,2			373
14,3	14,3			372
14,4	14,4			370
14,5	14,5			369
14,6	14,6			367
14,7	14,7			366
14,8	14,8			364

Δ (cc-gr)	10^3 x ln α	Thermometer Dunn & Valley 1992 [° C] (400-800° C)	Thermometer Kitchen & Valley 1995 [° C] (650-850° C)	Thermometer Chako et al 1991 [° C] (400-700° C)
1	1	995		1710
1,1	1,1	978		1616
1,2	1,2	962		1533
1,3	1,3	946		1461
1,4	1,4	931		1396
1,5	1,5	916		1338
1,6	1,6	902		1285
1,7	1,7	888		1237
1,8	1,8	875		1193
1,9	1,9	862		1153
2	2	849		1115
2,1	2,1	838		1080
2,2	2,2	826		1048
2,3	2,3	815		1018
2,4	2,4	804	945	989
2,5	2,5	793	920	962
2,6	2,6	783	897	937
2,7	2,7	773	875	913
2,8	2,8	763	854	891
2,9	2,9	754	835	869
3	**3**	**745**	**816**	**849**
3,1	**3,1**	**736**	**798**	**829**
3,2	3,2	727	782	811
3,3	3,3	718	765	793
3,4	3,4	710	750	776
3,5	3,5	702	735	760
3,6	3,6	694	721	745
3,7	3,7	686	708	730
3,8	3,8	679	695	715
3,9	3,9	672	682	702
4	4	664	670	688
4,1	4,1	657	659	675
4,2	4,2	651	648	663
4,3	4,3	644	637	651
4,4	4,4	637	626	640
4,5	4,5	631	616	628
4,6	4,6	625	607	618
4,7	4,7	618	597	607
4,8	4,8	612	588	597
4,9	4,9	606	579	587
5	5	601	571	577
5,1	5,1	595	562	568
5,2	5,2	589	554	559
5,3	5,3	584	546	550
5,4	5,4	579	539	542
5,5	5,5	573	531	533
5,6	5,6	568	524	525

Δ (cc-gr)	10^3 x ln α	Thermometer Dunn & Valley 1992 [° C] (400-800° C)	Thermometer Kitchen & Valley 1995 [° C] (650-850° C)	Thermometer Chako et al 1991 [° C] (400-700° C)
5,7	5,7	563	517	517
5,8	5,8	558	510	509
5,9	5,9	553	504	502
6	6	548	497	495
6,1	6,1	544	491	487
6,2	6,2	539	485	480
6,3	6,3	534	479	473
6,4	6,4	530	473	467
6,5	6,5	525	467	460
6,6	6,6	521	461	454
6,7	6,7	517	456	447
6,8	6,8	513	450	441
6,9	6,9	508	445	435
7	7	504	440	429
7,1	7,1	500	435	424
7,2	7,2	496	430	418
7,3	7,3	493	425	412
7,4	7,4	489	420	407
7,5	7,5	485	416	401
7,6	7,6	481	411	396
7,7	7,7	478	407	391
7,8	7,8	474	402	386
7,9	7,9	470	398	381
8	8	467		376
8,1	8,1	463		371
8,2	8,2	460		366
8,3	8,3	457		362
8,4	8,4	453		357
8,5	8,5	450		353
8,6	8,6	447		348
8,7	8,7	444		344
8,8	8,8	440		340
8,9	8,9	437		335
9	9	434		331
9,1	9,1	431		327
9,2	9,2	428		323
9,3	9,3	425		319
9,4	9,4	422		315
9,5	9,5	420		311
9,6	9,6	417		307
9,7	9,7	414		304
9,8	9,8	411		300
9,9	9,9	408		296
10	10	406		293
10,1	10,1	403		289
10,2	10,2	400		286
10,3	10,3	398		282

Δ (cc-gr)	10^3 x ln α	Thermometer Dunn & Valley 1992 [° C] (400-800° C	Thermometer Kitchen & Valley 1995 [° C] (650-850° C	Thermometer Chako et al 1991 [° C] (400-700° C
10,4	10,4	395		279
10,5	10,5	393		275
10,6	10,6	390		272
10,7	10,7	388		269
10,8	10,8	385		266
10,9	10,9	383		262
11	11	380		259

Δ (cc-gr)	10^3 x ln α	Thermometer Polyakov & Kharlashina 1995 [° C] (600-1200° C)	Thermometer Scheele & Hoefs 1992 [° C] (600-1200° C)
1	1	1625	
1,1	1,1	1536	
1,2	1,2	1457	
1,3	1,3	1388	
1,4	1,4	1326	
1,5	1,5	1271	
1,6	1,6	1220	
1,7	1,7	1175	
1,8	1,8	1133	
1,9	1,9	1094	
2	2	1058	
2,1	2,1	1025	
2,2	2,2	994	
2,3	2,3	965	
2,4	2,4	938	
2,5	2,5	913	
2,6	2,6	889	
2,7	2,7	866	
2,8	2,8	845	
2,9	2,9	824	
3	**3**	**805**	**1120**
3,1	**3,1**	**787**	**1039**
3,2	3,2	769	982
3,3	3,3	752	937
3,4	3,4	736	900
3,5	3,5	721	868
3,6	3,6	706	841
3,7	3,7	692	816
3,8	3,8	679	794
3,9	3,9	666	774
4	4	653	755
4,1	4,1	641	738
4,2	4,2	629	722
4,3	4,3	618	707
4,4	4,4	607	694
4,5	4,5	597	680
4,6	4,6	586	668
4,7	4,7	577	657
4,8	4,8	567	645
4,9	4,9	558	635
5	5	549	625
5,1	5,1	540	615
5,2	5,2	531	606
5,3	5,3	523	
5,4	5,4	515	
5,5	5,5	507	

Δ (cc-gr)	10^3 x ln α	Thermometer Polyakov & Kharlashina 1995 [° C] (600-1200° C)	Thermometer Scheele & Hoefs 1992 [° C] (600-1200° C)
5,6	5,6	500	
5,7	5,7	492	
5,8	5,8	485	
5,9	5,9	478	
6	6	471	
6,1	6,1	464	
6,2	6,2	458	
6,3	6,3	451	
6,4	6,4	445	
6,5	6,5	439	
6,6	6,6	433	
6,7	6,7	427	
6,8	6,8	422	
6,9	6,9	416	
7	7	411	
7,1	7,1	405	
7,2	7,2	400	
7,3	7,3	395	
7,4	7,4	390	
7,5	7,5	385	
7,6	7,6	380	
7,7	7,7	375	
7,8	7,8	371	
7,9	7,9	366	
8	8	361	
8,1	8,1	357	
8,2	8,2	353	
8,3	8,3	348	
8,4	8,4	344	
8,5	8,5	340	
8,6	8,6	336	
8,7	8,7	332	
8,8	8,8	328	
8,9	8,9	324	
9	9	321	
9,1	9,1	317	
9,2	9,2	313	
9,3	9,3	310	
9,4	9,4	306	
9,5	9,5	303	
9,6	9,6	299	
9,7	9,7	296	
9,8	9,8	293	
9,9	9,9	289	
10	10	286	
10,1	10,1	283	

Δ (cc-gr)	10^3 x ln α	Thermometer Polyakov & Kharlashina 1995 [° C] (600-1200° C)	Thermometer Scheele & Hoefs 1992 [° C] (600-1200° C)
10,2	10,2	280	
10,3	10,3	277	
10,4	10,4	274	
10,5	10,5	271	
10,6	10,6	268	
10,7	10,7	265	
10,8	10,8	262	
10,9	10,9	259	
11	11	256	

LEBENSLAUF:

Am 16. Mai 1972 wurde ich als Sohn von Hiltrut Walter geb. Gellert und Joachim Walter in Windhoek, Namibia geboren. Dort wurde ich Anfang 1979 in die Deutsche Höhere Privatschule Windhoek eingeschult, an der ich dann zunächst 1990 den südafrikanischen Schulabschluss, das Matriculation Certificate, absolvierte. Im November des folgenden Jahres schloss ich dann ebenfalls an der Deutschen Höheren Privatschule Windhoek mit der deutschen Allgemeinen Hochschulreife ab.

Zum WS 1992/93 begann ich an der Georg-August-Universität Göttingen das Studium der Geologie/Paläontologie, an der ich am 18. April 1997 die Diplomvorprüfung absolvierte. Nach der Diplomkartierung und –arbeit am Institut für Geologie und Dynamik der Lithosphäre (IGDL der Universität Göttingen schloss ich das Studium am 28.10.1999 mit dem Diplom ab.

Im September 2000 begann ich mit der Promotion ebenfalls am IGDL in der ich vom 01. September 2000 bis 31. August 2001 und vom 01. September 2002 bis 31. August 2003 über das DFG Projekt WE 488/50-1 am IGDL und am Geowissenschaftlichen Zentrum der Universität Göttingen angestellt war. Im Juni 2000 heiratete ich meine Frau Maria Elisabeth Walter geborene Rogge. Im Juli 2002 wurde unsere Tochter Franziska Leoni Walter geboren.